MEMBRANE AND ELECTRODE MODIFICATIONS FOR IMPROVING POWER DENSITY IN AQUEOUS REDOX FLOW BATTERIES

A Dissertation

Presented to the Faculty of the Graduate School

of Cornell University

In Partial Fulfillment of the Requirements for the Degree of

Doctor of Philosophy

by

Andrew Brady Shah

August 2018

MEMBRANE AND ELECTRODE MODIFICATIONS FOR IMPROVING POWER DENSITY IN AQUEOUS REDOX FLOW BATTERIES

Andrew Brady Shah, Ph. D.

Cornell University 2018

Global electricity production from renewable sources has grown dramatically in recent years. While this has fostered lower dependence on carbon-based energy generation, the intermittent nature of these renewable energy resources has introduced new technical challenges to regional electrical grids. One approach to address intermittent energy generation and associated inefficiencies is to introduce grid-scale electricity storage using redox flow batteries. Redox flow batteries provide a reasonably stable, long-term means to store renewable energy. Vanadium redox flow batteries (VRBs) have been of particular interest due to their chemical stability, long life cyclability, and potential for high capacity electrical storage. VRBs also have a number of research challenges. One key factor limiting market penetration of redox flow batteries in energy storage portfolios is the high capital cost associated with a comparatively low power density technology. To this end, current research efforts focus on improving the energy density of VRBs to warrant this cost in the long term.

This work focuses on four approaches to improve the power density of VRBs: the use of conductive membrane coatings, the generation of electroactive hydrophilic surface functional groups, use of drop-in electrocatalysts via direct reduction of metal salts, and chemical synthesis of lead oxide particles on the VRB anode. First, it is

demonstrated that the rate capability of VRBs can be improved by electrospray deposition of a conductive carbon/binder mixture onto the surface of the ion-exchange membrane in a VRB. This work goes on to show dramatic rate improvements by hydrothermally treating graphite felt electrodes with various surface modifiers, most notably ammonium persulfate. Alternative approaches to improve the current density of a VRB involve the use of electrocatalysts on the surface of the anode. This work shows that the use of drop-in metal salts and the chemical synthesis of lead oxides are both facile routes to form catalytically-active nanoparticles on the surface of the VRB anode, which significantly accelerate the kinetics of otherwise sluggish anodic reactions in VRBs. These four methods each offer a commercially scalable and inexpensive pathway to increasing the capacity and power density of aqueous vanadium redox flow batteries.

BIOGRAPHICAL SKETCH

Andrew Brady Shah was born in Princeton, NJ in 1991 to Nilesh Shah and Jean Brady. He grew up in Maple Glen, PA. He attended Jarrettown Elementary School, Sandy Run Middle School, and Upper Dublin High School. He went on to earn an Honors Bachelor's degree with Distinction in Chemical Engineering at the University of Delaware in 2013. During his time at Delaware, he researched catalysis related to converting bio-based feedstocks to platform chemicals in the Vlachos Research Group. He started his doctoral work at Cornell in 2013 after joining the Joo Research Group in the Robert Frederick Smith School and Chemical and Biomolecular Engineering. He focused most of his work on studying large-scale energy storage from a materials perspective.

ACKNOWLEDGMENTS

There are quite a few people who have been instrumental to my academic development and personal happiness throughout my time at Cornell. First and foremost, I would like to thank Prof. Yong Lak Joo for his support and guidance throughout the past five years. His practical suggestions and comments would always energize me, and consistently helped to motivate and focus my work. I most appreciated his flexibility and encouragement when I would suggest new and different project ideas. I would also like to thank my thesis committee members, Prof. Uli Wiesner and Prof. Claude Cohen for their time and helpful guidance. I would like to acknowledge Prof. Jeff Tester and members of the Earth-Energy IGERT program – I enjoyed attending and participating in weekly seminars outside of my field, and greatly enjoyed the company of the group itself. I would like to thank Prof. A. Brad Anton for his unique perspectives on science education, and for always keeping my TA duties interesting. I would like to acknowledge Prof. Susan Daniel for her enthusiastic efforts as Director of Graduate Studies, which have made a noticeable positive impact on the department. I would like to acknowledge Prof. Tobias Hanrath for spearheading the effort to improve the safety culture in our department. I would like to thank the many helpful staff at the Cornell Center for Materials Research for their guidance and patience. I would like to thank those who have directly contributed to my research, including Xuechen Zhou, Maharshi Thakker, Meghan Pierson, and Camelia Wu – you were all a pleasure to work with, and your tireless efforts were extremely helpful to this work. I would like to thank all members of the Joo Group, past and present, who have helped me during my time at Cornell. I would especially like to acknowledge Dr. Bryan Rolfe, Dr. Brian Williams, Dr. Joe Carlin, Dr. Jangwoo Kim, Ghazal Shoorideh, George Shebert, Shubham Pinge, Mohammed AlAmer,

Mounica Divvela, Chris Klaassen, Prof. Ling Fei, and Dr. Seung Wan Kim for all of their help, conversation, commiseration, and company during my time in the Joo Group. I want to thank my group of close friends, especially Joey Brown, Yaset Acevedo, Joe Mattson, Dana Thornlow, Morgan Baltz, Jon Ludwicki, Winston Black, Arna Pálsdóttir, Laura Sinclair, and Carolyn Shurer. You have helped make my time at Cornell some of the most interesting and entertaining years of my life, and I love you all. I would also like to thank Mary Reinthal for her constant love and support during my thesis work. Finally, I would like to thank my family for their unwavering support throughout my entire educational journey. To my wonderful grandparents, Sushila and Kishor Shah, for their warm and loving encouragement throughout my life. To my Uncle Ashish Shah, for his indomitable optimism and support. To my sister Jennifer, who has always grounded me, who has perpetually been my most reliable sounding board, and who continues to be one of my best friends. And to my parents, for instilling in me a sense of curiosity, for their continual encouragement and love throughout my life, and for providing the means to help me to achieve this dream. You have inspired me to pursue a career in science, and have quite simply been incredible parents. I thank you and I love you.

TABLE OF CONTENTS

LIST OF FIGURES

LIST OF TABLES

LIST OF ABBREVIATIONS

RFB	Redox Flow Battery
VRB	Vanadium Redox Flow Battery
CNT	Carbon Nanotube
DOE	U.S. Department of Energy
V(II)	Vanadium +2
V(III)	Vanadium +3
V(IV)	Vanadium +4
V(V)	Vanadium +5
SHE	Standard Hydrogen Electrode
DI	De-ionized
CV	Cyclic Voltammetry
EIS	Electrical Impedance Spectroscopy
GCE	Glassy Carbon Electrode
UV	Ultra-violet
ID	Inner Diameter
HDPE	High Density Polyethylene
PAN	Polyacrylonitrile
SEM	Scanning Electron Microscopy
FT-IR	Fourier Transform Infrared Spectroscopy
APS	Ammonium Persulfate
AC	Alternating Current
Hz	Hertz
XPS	X-ray Photoelectron Spectroscopy
eV	Electron-volts

GF	Graphite Felt
XRD	X-ray Diffraction
EDX	Energy Dispersive X-ray Spectroscopy

INTRODUCTION

The Case for Large-Scale Energy Storage

Global electricity production from renewable sources has grown dramatically in recent years. With both solar and wind energy generation technologies growing at a rapid pace, the need to better integrate these technologies into larger electrical grids has become more apparent. These generation sources are, by nature, intermittent – the weather is only so predictable, and this can cause large differences in power generation day-to-day. This is an inherent barrier to entry for widespread adoption of these renewable technologies in place of cheaper carbon-based fuels. As societies begin to appreciate the need to move past the combustion of fossil fuels to power the modern world, it is very likely that solutions for managing this intermittency will become more critical.[1-3]

The solution to this issue is clear: there is a growing need for the development of large-scale energy storage technologies. These are classified as technologies that do not generate electricity themselves, but can temporarily store energy generated at grid-scale or sub-grid-scale levels. The main idea hinges on the principle that renewable sources should generate as much electricity as possible. This "fate" of this electricity is then dictated by the grid power needs at the time of generation. Should the renewable sources generate more power than is required at the time, electricity can be temporarily stored as potential energy by these large-scale storage technologies. In that way, when there is a deficiency of production from renewable generators, these sources can help to make up the difference in production by contributing to the grid at

the time additional power is required. Large-scale electrical storage can also help to buffer temporal fluctuations in power production on a daily basis, meaning that the overall impact of unpredictable weather could be limited via peak-shaving assistance. As the world population grows and a greater fraction of countries industrialize, global power consumption will undoubtedly increase, and the need for large-scale electricity storage will become more and more necessary.

Redox Flow Batteries for Large-Scale Energy Storage

There are quite a few existing methods of large-scale energy storage that are currently in use around the world. These include a series of mechanical storage techniques: pumped hydroelectric, compressed air, and flywheel storage have all been used for some time. These technologies are useful largely due to their simplicity, reliability, and potential for storing large amounts of energy. As of 2017, the United States Department of Energy estimated that over 95% of large-scale electrical storage capacity in the United States consisted of a combination of these three mechanical storage technologies.[1] The DOE also reported that the United States can currently only store about 2.3% of it's total annual energy production capacity. Of the remaining ~5% of energy storage capability in the United States, about 1.3% currently consists of electrochemical storage.[1]

Redox Flow Batteries (RFB) are one type of electrochemical storage technology that have garnered great interest in recent years. They have the potential to make substantial contributions to large-scale energy storage portfolios worldwide.[2] A redox flow battery is a type of battery that differs from consumer-grade batteries in

two major ways: it is an open system, and the electrochemical energy is stored in the electrolyte, rather than the electrodes. A schematic of a redox flow battery is seen in Figure I.1. During the use of a redox flow battery, liquid electrolyte is pumped through two compartments (the anode on the negative side, the cathode on the positive side) separated by an ion-exchange membrane. This electrolyte consists of some sort of electroactive material (usually a metal salt) dissolved in a solvent. In aqueous redox flow batteries, this solvent is usually a dilute acid. A load is connected to the battery, and a redox reaction occurs. During charging, the catholyte is oxidized and the anolyte is reduced, a process that occurs from the addition of electricity to the system. Upon discharging, the catholyte is reduced and the anolyte is oxidized, generating electrons available for use, and returning the electrolyte to its ground state.

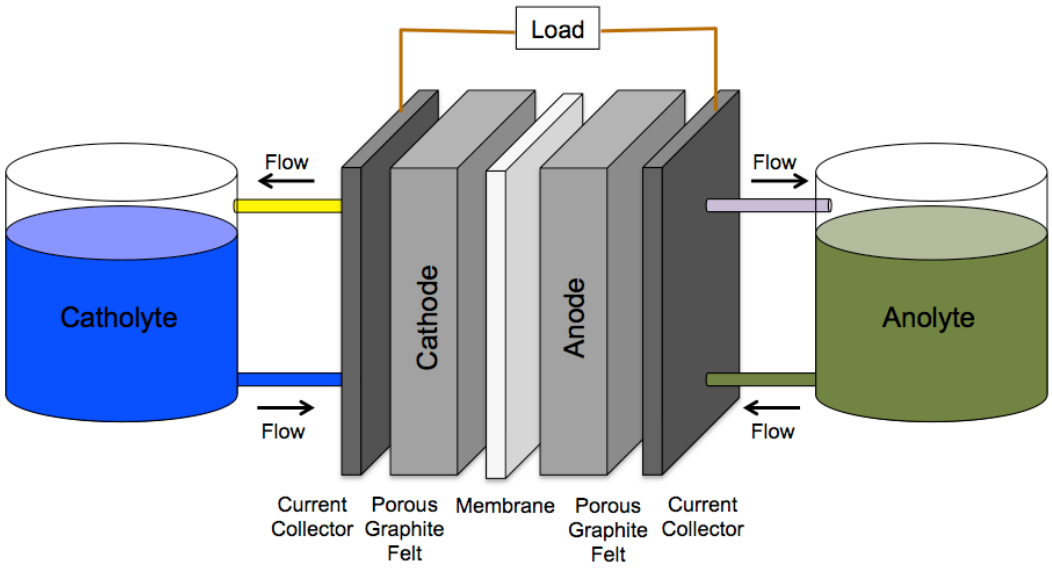

Figure I.1. Schematic of a redox flow battery.

The true appeal of this technology is found in the scalability of these batteries. The electrochemical energy is stored in the liquid electrolyte, allowing for a theoretically limitless volume of electrolyte, and therefore capacity, to be stored in each cell. These types of batteries avoid the issues observed in scaling up conventional closed-cell batteries, as they do not have complex substructures with hierarchical morphologies that can be easily altered upon battery cycling. The main drawbacks of these technologies are typically due to the comparatively low energy density of these batteries. Much of the mass of the electrolyte is in the form of solvent, and the total amount of electroactive material that can be dissolved in the solvent is limited. The initial installation costs can also be high, as pumps, electrolytes, electrodes, and membranes can all add to the overall total cost. Still, the promise of these devices to play a role in large-scale energy storage portfolios is feasible with technological improvements that drive down the cost and increase the power density.

Aqueous Vanadium Redox Flow Batteries

The majority of the work contained in this thesis relates directly to improvements and modifications to the Aqueous All-Vanadium Redox Flow Battery (VRB) system. VRBs have been of particular interest due to their chemical stability, long life cyclability, and potential for high capacity electrical storage. Originally invented in the 1980s, these batteries did not garner much attention until after the year 2000, when large-scale electrochemical storage methods began to become of greater interest to the scientific community. A journal search using Web of Science for the number of

publications containing the phrase “vanadium redox flow battery” by year is shown in Figure I.2, illustrating this point.

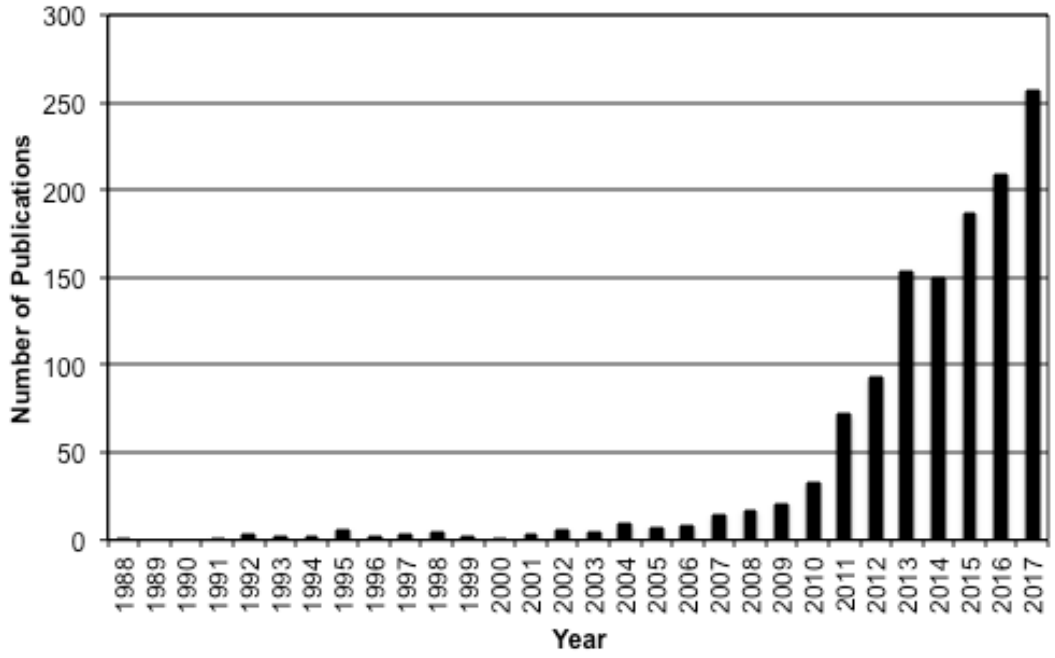

Figure I.2. A plot generated by searching Web of Science for the number of articles containing the phrase “vanadium redox flow battery” in their title, shown by year of publication.

VRBs operate by utilizing four oxidation states of vanadium: V(II), V(III), V(IV), and V(V). A vanadium salt can be dissolved into a supporting acid, in most cases sulfuric acid, the differences in reduction potential of the various oxidation states can be exploited. More specifically:

Anolyte reaction:

$$V^{3+}{}_{(aq)} + e^{-} \leftrightarrow V^{2+}{}_{(aq)} \qquad \text{E = -0.255V vs. SHE}$$

Catholyte reaction:

$$[VO_2]^+_{(aq)} + 2H^+ + e^- \leftrightarrow [VO]^{2+}_{(aq)} + H_2O \qquad E = 1.00V \text{ vs. SHE}$$

Each of these reactions generates one electron, and can be coupled to yield a nominal cell voltage of 1.00V – (-0.255V) = 1.255V when fully charged. One of the positive aspects of the VRB is that the two half-cells use what is effectively the same electrolyte, so the consequences of diffusion of vanadium species through the ion-exchange membrane is only a reduction in the total capacity of the battery. This is in contrast to some other redox flow battery technologies, in which electrolyte crossover can cause the formation of insoluble precipitates and other undesirable products.

VRBs come with a number of research challenges. One key factor limiting market penetration of redox flow batteries in energy storage portfolios is the high capital cost associated with a comparatively low energy density technology. To this end, current research efforts focus on improving the energy density of VRBs to warrant this cost in the long term.[4,5]

Membranes for Aqueous Vanadium Redox Flow Batteries

One main contributor to the total overall cost of VRBs is the cost of the ion-exchange membrane necessary for separating the anolyte and catholyte. The type of membrane most widely used in existing VRBs is typically some sort of perfluorinated sulfonated membrane. Nafion membranes are most commonly reported on in literature. While Nafion membranes have a high proton conductivity, and generally work well for this application, they add a significant fraction of the overall cost of a

VRB setup. Some work has been conducted to synthesize new types of membranes, in addition to modifying Nafion membranes to improve their performance in VRBs.

Electrodes for Aqueous Vanadium Redox Flow Batteries

In order for VRBs to be considered viable platforms for large-scale energy storage, the power density deficiencies must be addressed. Power density can be thought of as the product of current density multiplied by cell voltage. The voltage of a VRB system is fixed by the chemistry of the system, and thus the current density must be increased to increase power density. Current density is measured by the total current input to or output from the battery, scaled by the surface area of the membrane in the battery. This gives a scaled estimate for what currents can be reached in the battery in any given membrane or electrode configuration. Most VRBs use some sort of porous, high surface area conductive material as and electrode to provide many reaction surface sites for the vanadium redox reaction to occur. This is often in the form of a carbon or graphite felt. In many cases, this felt will be pre-treated with some sort of heat-treatment to increase the surface area and improve the wettability via oxidation. The surface hydrophilicity of the surface is important, as this likely plays a role in the redox reaction mechanism.

This thesis explores a variety of methods aimed at improving the power density in aqueous vanadium redox flow batteries. This is demonstrated through a series of conductive membrane coatings, graphite felt surface modifications, metal catalysts, and metal oxide catalysts. Each approach uses a different strategy to work towards the overall goal of improving the power density of VRBs. Some preliminary

work is then discussed on metal-free aqueous organic redox flow batteries and some of the potential opportunities in membrane development for these systems.

References

(1) U.S. Department of Energy. *Grid Energy Storage*; 2013.

(2) Alotto, P.; Guarnieri, M.; Moro, F. Redox flow batteries for the storage of renewable energy : A review. *Renew. Sustain. Energy Rev.* **2014**, *29*, 325–335.

(3) Liu, J.; Zhang, J.; Yang, Z.; Lemmon, J. P.; Imhoff, C.; Graff, G. L.; Li, L.; Hu, J.; Wang, C.; Xiao, J.; et al. Materials Science and Materials Chemistry for Large Scale Electrochemical Energy Storage : From Transportation to Electrical Grid. *Adv. Funct. Mater.* **2013**, *23*, 929–946.

(4) Weber, A. Z.; Mench, M. M.; Meyers, J. P.; Ross, P. N.; Gostick, J. T.; Liu, Q. Redox flow batteries: a review. *J. Appl. Electrochem.* **2011**, *41* (10), 1137–1164.

(5) Ulaganathan, M.; Aravindan, V.; Yan, Q.; Madhavi, S.; Skyllas-Kazacos, M.; Lim, T. M. Recent Advancements in All-Vanadium Redox Flow Batteries. *Adv. Energy Mater.* **2016**, *3*, 1–22.

CHAPTER 1

CONDUCTIVE MEMBRANE COATINGS FOR HIGH RATE VANADIUM REDOX FLOW BATTERIES

1.1. Introduction

Global electricity production from renewable sources has grown dramatically in recent years.[1,2] While this new production ultimately drives energy generation portfolios towards a lower dependence on carbon-based electricity, the intermittent nature of renewable forms of electricity generation have proven difficult to incorporate into regional electrical grids. Grid-scale electricity storage methods are a promising solution to the inefficiencies associated with unpredictable electricity generation. Redox flow batteries have demonstrated the ability to be used as a reasonably low-cost, long-term electrical storage method. Specifically, vanadium redox flow batteries have been of special interest due to their chemical stability, long life cyclability, and potential for high electrical capacity.[3-5]

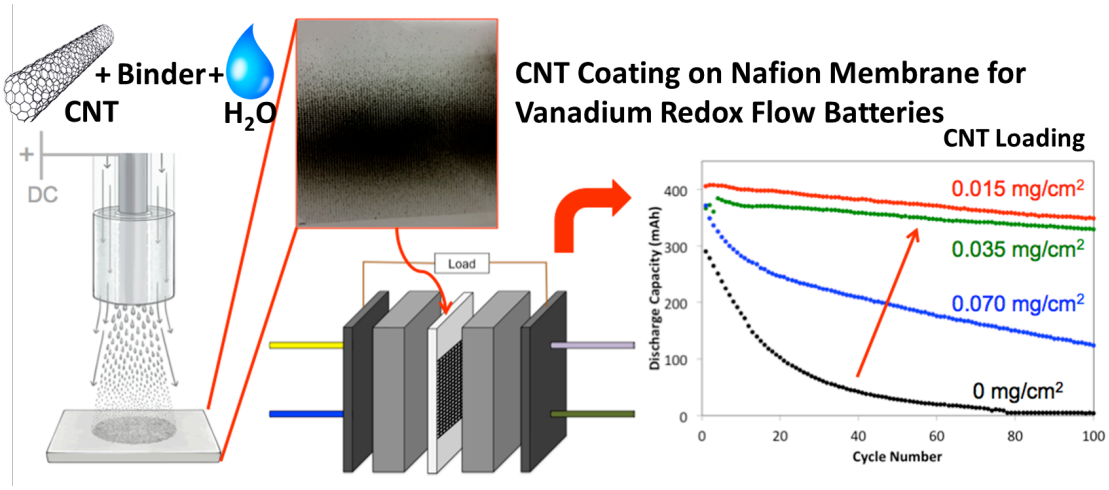

Abstract Image: Scheme of conductive coating process.

VRBs take advantage of the four adjacent oxidation states of vanadium for the transfer of electrons via a redox reaction. The positive half-cell contains VO^{2+}, which can be oxidized to VO_2^+ during charging; the negative half-cell contains V^{3+} which can be reduced to V^{2+} during charging. The vanadium salts are typically dissolved in sulfuric acid. Accompanying these advantages are some research challenges. There have been a number of efforts to improve the electrical conductivity of VRBs by physically or chemically altering the electrodes of the cell. Most VRBs use a carbon or graphite felt as porous cathodes and anodes – the large surface area from the felt is used to increase the number of reaction sites at which the redox reaction can occur. Many modifications to the electrodes have been investigated, including using various highly conductive carbons[6-16], metal catalysts[17-19], and doping the carbon felt with hydrophilic surface groups[20-23]. Some work on casting membranes with conductive carbons incorporated into the bulk of the membrane has also been explored, typically focusing on graphene oxide or graphite as the carbon source.[24-28] Substantial work has focused on selection and pretreatment methods for the Nafion family of membranes in VRBs.[29-32] To our knowledge, little work has been conducted investigating the application of conductive carbons to the surface of premade membranes themselves. While other membrane modification techniques involve poorly scalable casting or pretreatment techniques, our goal was to create a fast and inexpensive process to improve VRB performance. To this end, a new approach to improve the rate capability of VRBs involves increasing the electrical conductivity of the membrane itself using the electrospray deposition of conductive carbon mixed with a binder directly onto the

membrane. In this method, a very small amount of highly conductive carbon can be deposited directly onto the surface of the cation exchange membrane, thereby increasing the electrical conductivity near the surface of the membrane without impeding proton transport through the membrane. This technique was investigated for use as both a stand-alone pretreatment of VRB membranes and as a complementary feature to existing electrode modifications.

1.2. Experimental Section

1.2.1 Preparation of the Conductive Ink. The conductive ink consisted of three primary components – Multi-walled CNTs (Sigma), 20 wt% Nafion Dispersion (Ion Power, Newcastle, DE), and DI water. The CNTs add a highly conductive component to the spray, which improves the electrical conductivity across the surface of the membrane. The Nafion dispersion acted as a binder for the CNTs and the Nafion 117 membrane (Ion Power, Newcastle, DE) and was also a good surfactant when mixing the CNTs in water. The ink composition was important to both improve the rate capability of the battery and to allow for good processability when electrospraying. An ideal spray condition is realized when the conductive ink is able to be electrosprayed in a well-dispersed manner, while hitting the membrane without complete solvent evaporation. This allows time for the remaining solvent to evaporate while the Nafion dispersion has a chance to relax and form a thin film. It was found that ink compositions with high water content would result in the spray collecting as a dry powder, which could be easily removed with abrasion. Some ink compositions with too much Nafion dispersion added would result in the spray not drying fast enough on

the membrane, causing uneven distribution and dripping of the carbon ink down the substrate membrane. It was found that a carbon ink composition of 0.5wt% CNTs, 15.0 wt% Nafion dispersion (20wt% polymer), and 84.5wt% DI water created a carbon ink with both good processability and performance. The coating after spraying was assumed to have no residual water, leading to a coating composition of about 14 wt% CNTs and 86 wt% Nafion polymer.

1.2.2 Processing Conditions. The carbon ink was ultrasonicated for 1 hr before use. The solution was placed in a 5mL syringe and sprayed through a homemade coaxial needle (tube gauge of 10, shell gauge of 17) using a syringe pump (Harvard Apparatus). Dry air was applied through the shell of the coaxial needle at 10 psig. The use of air-controlled electrospraying helped increase the rate of spraying, as has been demonstrated elsewhere (see Figure 1.1).

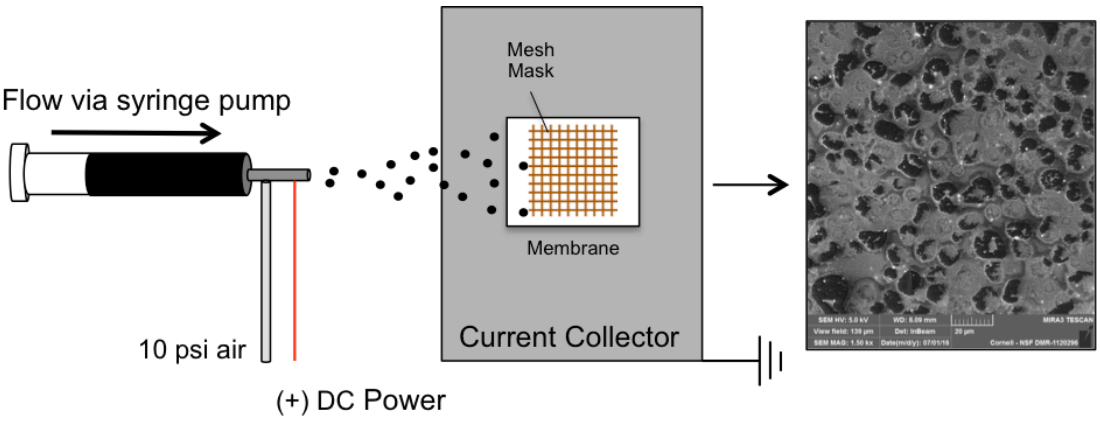

Figure 1.1 Schematic of air-controlled electrospraying process for creating conductive coatings.

The Nafion 117 membrane (dry) was placed on a grounded copper current collector at a distance of 18 cm from the tip of the needle. A positive lead was attached to the

needle, and the voltage was set to 18 kV. It was found that a flow rate of 0.05 mL/min was appropriate to balance deposition and solvent evaporation rates. The membranes seem to perform best when they were not completely covered by the carbon spray, so a copper mesh was used as a mask during spraying. The mesh had a series of 1 mm square holes, which allowed spray through to hit the Nafion 117 membrane. Spray that did not go through the holes was stopped by the mask, creating a uniformly patterned series of domains with and without the carbon ink spray. Both sides of each membrane were sprayed in every case. Spray loadings of 0.015 mg CNT/cm^2, 0.035 mg CNT/cm^2, and 0.070 mg CNT/cm^2 per side were tested.

1.2.3 Electrochemical Measurements. The spray-coated membranes were tested using in-situ Electrical Impedance Spectroscopy (EIS) testing, in order to measure the changes in resistance in the cell with the inclusion of the conductive membrane coating. An electrolyte consisting of 4M H_2SO_4 and 1M $VOSO_4$ was used for all testing. An AC voltage of 1mV amplitude was used over a frequency range of 10^4 Hz to 10^{-3} Hz to generate Nyquist plots of the pristine and coated membranes. Cyclic voltammetry (CV) was performed at rates of 20 mV/s, 50 mV/s, and 100 mV/s in a three-electrode glass cell, using the above-mentioned electrolyte. The reference electrode used was Ag/AgCl and the counter electrode used was a platinum wire. A 3.0 mm diameter circle of polished Glassy Carbon Electrode (GCE) was coated with both the conductive coating and the Nafion dispersion alone, to observe the difference in electrochemical activity at the membrane. A potential range between -0.85 V and 1.5 V was explored. Four-point probe surface conductivity tests were also used to

determine changes in surface electrical resistance with and without membrane coatings, and with and without the use of a mesh mask.

1.2.4 Diffusion Tests. A 2-chamber side-by-side diffusion cell (Permegear) was used to measure the diffusivity of both vanadium ions and hydrogen ions across the Nafion 117 membrane. Vanadium diffusion rates were measured by placing 3.4 mL of the 1M $VOSO_4$ in 4M H_2SO_4 in the donor chamber of the diffusion cell, and 3.4 mL of 1M $MgSO_4$ in 4M H_2SO_4 in the receptor chamber of the cell. The $MgSO_4$ was added to balance the contribution of osmotic pressure from the added vanadium salt that could impact the perceived diffusion rate. 200 μL samples of the receptor chamber were taken at periodic time intervals as the V(IV) ions diffused across the membrane, and were replaced with fresh receptor solution. These samples were analyzed using UV-Visible Spectroscopy to determine the increase in concentration of V(IV) over time.

1.2.5 Single-Cell Testing. Membrane coatings were assessed using single-cell testing in an in-house flow cell system. Included in the system were two glass chambers for electrolyte storage, from which electrolyte was pumped through ¼" I.D. tubing to and from the flow cell (Tygon 2375 Ultra tubing, Watson-Marlow 323E Pump). Each side of the cell consisted of symmetric acrylic end plates with push-to-connect tube fittings, a graphite current collector, a Viton gasket, a polypropylene flow frame, and an HDPE gasket. These parts were separated by a Nafion 117 membrane, with or without a coating. The total exposed area of the membrane and graphite current collector was a 7 cm by 5 cm rectangle, totaling 35 cm^2. Each side of the cell had a 2

mm space between the membrane and current collector, in which a piece of 3 mm thick porous graphite felt (PAN-based, AVCarb) was compressed for good electrical contact. The felt was used as received, and was not pre-treated in any way. The electrolyte used in all tests was 1M $VOSO_4$ (Alfa Aesar) in 4M H_2SO_4. This was prepared by first dissolving the appropriate mass of $VOSO_4$ into 4M H_2SO_4. This solution, containing V(IV), was then electrochemically oxidized while being pumped through the flow cell. This was accomplished by using a constant current charge of 15 mA/cm^2 and an upper cutoff voltage of 1.7 V. This cycle was repeated 5 times to ensure maximum conversion to V(V) in the cathode and V(III) in the anode. The V(V) was then removed from the system and replaced with more of the original V(IV) solution, and the process was repeated. This generated more V(V) at the cathode and V(II) at the anode. The single-cell tests were then run using these freshly generated electrolyte solutions. The electrolyte volume used was 25 mL for the catholyte and anolyte, with a flow rate of 30 mL/min. Current densities between 30 mA/cm^2 and 50 mA/cm^2 were explored. All single-cell cycling testing was carried out using a battery analyzer (3A/5V, MTI). Cycling involved charging and discharging repeatedly at a specified constant current density. The upper cutoff voltage was set at 1.7 V, the lower cutoff voltage was set at 0.8 V. Cycling tests were assessed by coulombic efficiency, voltaic efficiency, energy efficiency, and capacity retention.

1.3. Results and Discussion

The coated membranes and the coating itself were thoroughly analyzed to investigate the impact of the coating on electrochemical activity and overall performance of the battery.

1.3.1. Optical Analysis.

SEM was used to analyze the surface of the membrane (1.2). The thickness and homogeneity of the coating were considered as important aspects regarding the reproducibility of membrane coatings using these methods. Both surface and cross-section imaging was conducted. It was found that the carbon coatings were typically between 3 and 5 microns in thickness. The coatings seemed to form discrete regions of CNT aggregates, connected together with the Nafion dispersion binder. These regions are likely formed due to the rapid evaporation of small amounts of residual water left in the ink after it hits the surface of the membrane. The coatings showed that the CNTs were predominantly encapsulated in droplets of Nafion dispersion, providing anchoring sites that proved to be resistant to delamination or degradation during cycling.

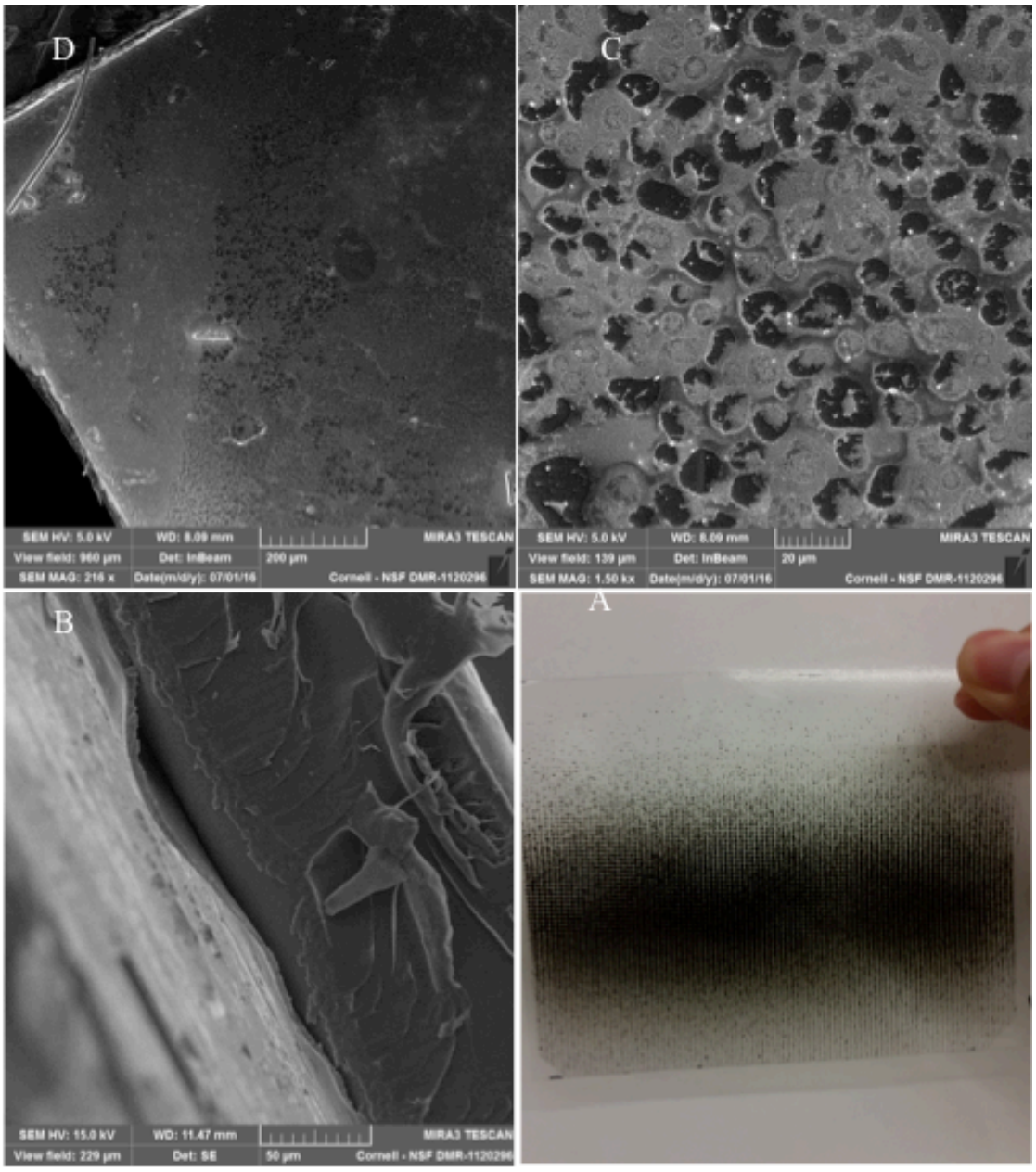

Figure 1.2. SEM images of Nafion 117 membrane coated with conductive ink. A: flat, showing uncoated domain from use of copper mesh; B: flat, showing discrete domains of conductive coating; C: cross-section with coating partially removed on left side; D: Photo of coated membrane with use of mesh.

1.3.2. Electrochemical Measurements.

Cyclic Voltammetry

Three-probe cyclic voltammetry tests were conducted at different scan rates to measure the impact of the conductive ink on the electrochemical activity of the vanadium redox reaction in the catholyte. The conductive ink was used to coat a glassy carbon electrode, and was compared to a glassy carbon electrode coated with only the Nafion dispersion. This test was run to compare the electrochemical activity of the coated Nafion membrane and the pristine Nafion membrane. The standard reduction potential of the oxidation of VO^{2+} to VO_2^+ (cathodic reaction) is about 1.00 V, while the standard reduction potential of the reduction of V^{3+} to V^{2+} (anodic reaction) is about -0.26 V, compared to the Standard Hydrogen Electrode. These two coatings were tested over a series of potential scan rates, ranging from 20 mV/s to 100 mV/s (see Figures 1.3a and 1.3b). It was found that when compared to the Nafion dispersion coating, the conductive ink peak current increased during both the cathodic and anodic reactions. This larger induced current is indicative of greater electrochemical activity of both relevant vanadium redox reactions in the on the surface of the electrodes. It should also be noted that no anodic peak was observed at both high and low scan rates with the Nafion coating. This shows that the kinetics of the anodic reaction are slow compared to the cathodic reaction, as is consistent with other literature. A small peak appears for the anodic reaction in the case of the conductive ink, showing that the addition of CNTs helps facilitate the anodic reaction. When current density is increased, the overpotential (peak voltage difference from standard reduction potential) will typically increase accordingly. When comparing a lower scan rate (20 mV/s) to a higher scan rate (100 mV/s), the observed increase in overpotential for the electrode coated with conductive ink is much lower than the

electrode coated with Nafion dispersion. This indicates the ability of the CNT-based conductive ink to allow for a highly efficient redox reaction, even at higher current densities.

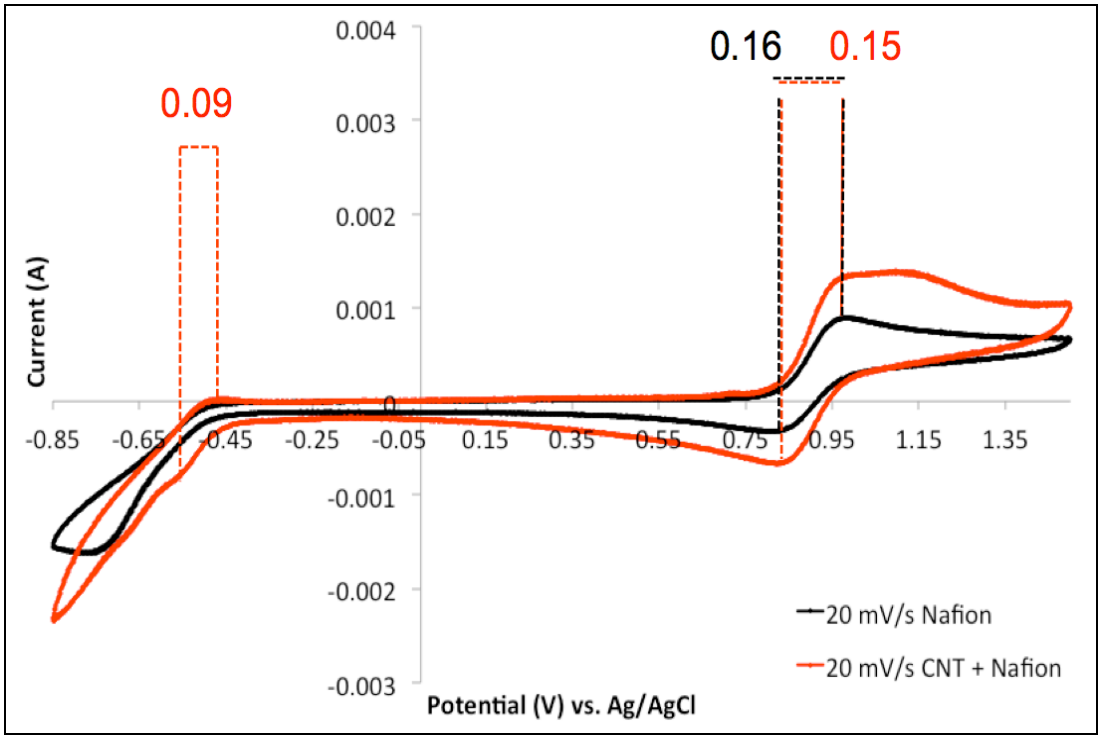

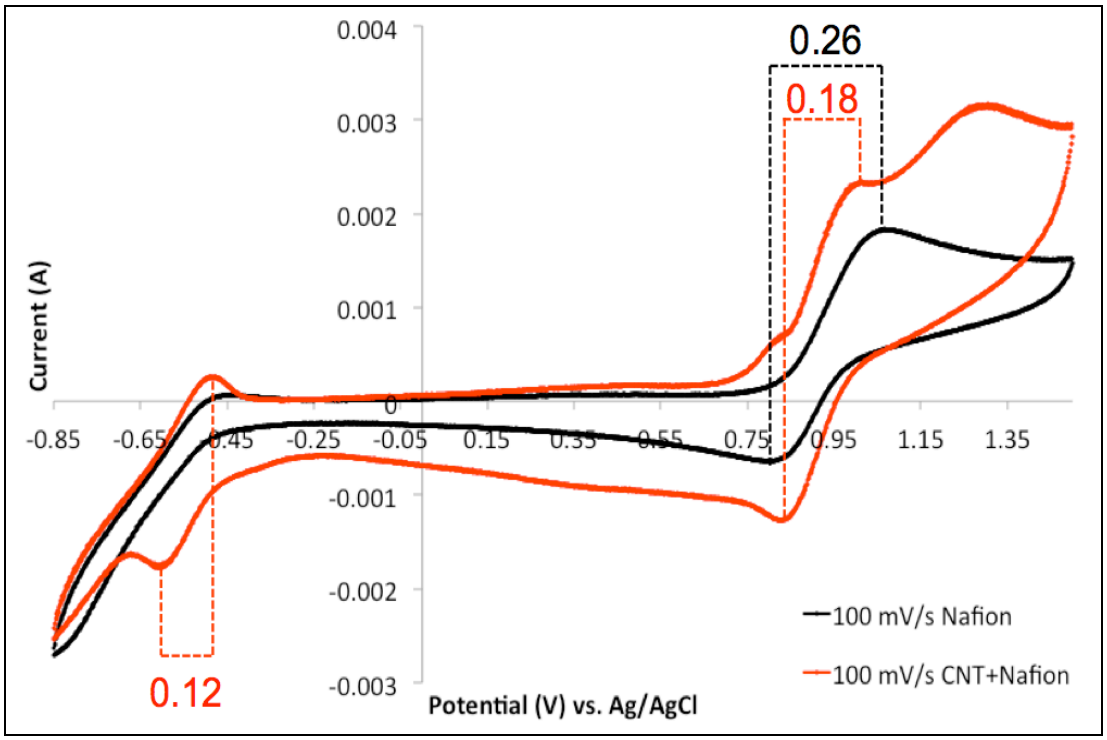

Figure 1.3. CV Curves of Nafion and CNT+Nafion coated glassy carbon electrode at a) 20 mV/s scan rate and b) 100 mV/s scan rate.

Electrical Impedance Spectroscopy

EIS testing was also conducted on the in-situ cell, probing the resistance of the membranes with different coating thicknesses, with and without the use of a mesh mask. This test was used primarily to test if the proton conductivity through the membrane was impacted with the use of the coating. It was found that the proton conductivity, and hence resistance contribution from the membrane, was nearly unchanged with the addition of the conductive ink. There was a very low ohmic resistance, on the order of 0.1 Ohms, as shown at the high frequency intercept of the real axis in the Nyquist plots (Figure 1.4). When the conductive ink coating was applied to the Nafion membrane, the charge transfer resistance did not change

noticeably. The charge transfer resistance was difficult to estimate precisely in the both and coated and pristine cases, as the system was difficult to keep at steady state in the slower, low frequency regime of the test. It is likely the charge transfer resistance was effectively the same in both cases due to the fact that the majority of the battery setup (electrodes and electrolyte) was unchanged during these tests. Thus, any improvement in performance in the battery can likely be attributed to the formation of a highly electrically conductive network (CNTs) with tethered reaction sites (end groups of CNTs) focused the interface between the membrane and the felt electrodes. The key message from these data is that despite the addition of a layer of conductive ink to the surface of the membrane, the observed resistance to proton transport through the membrane was largely unhindered.

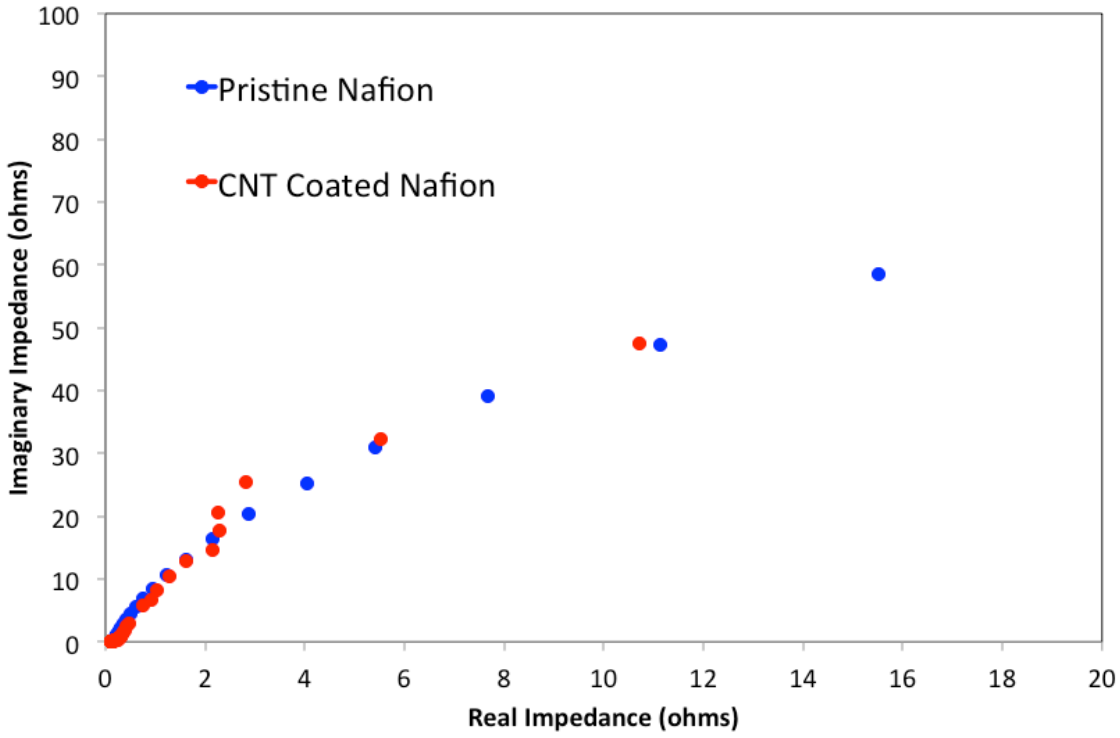

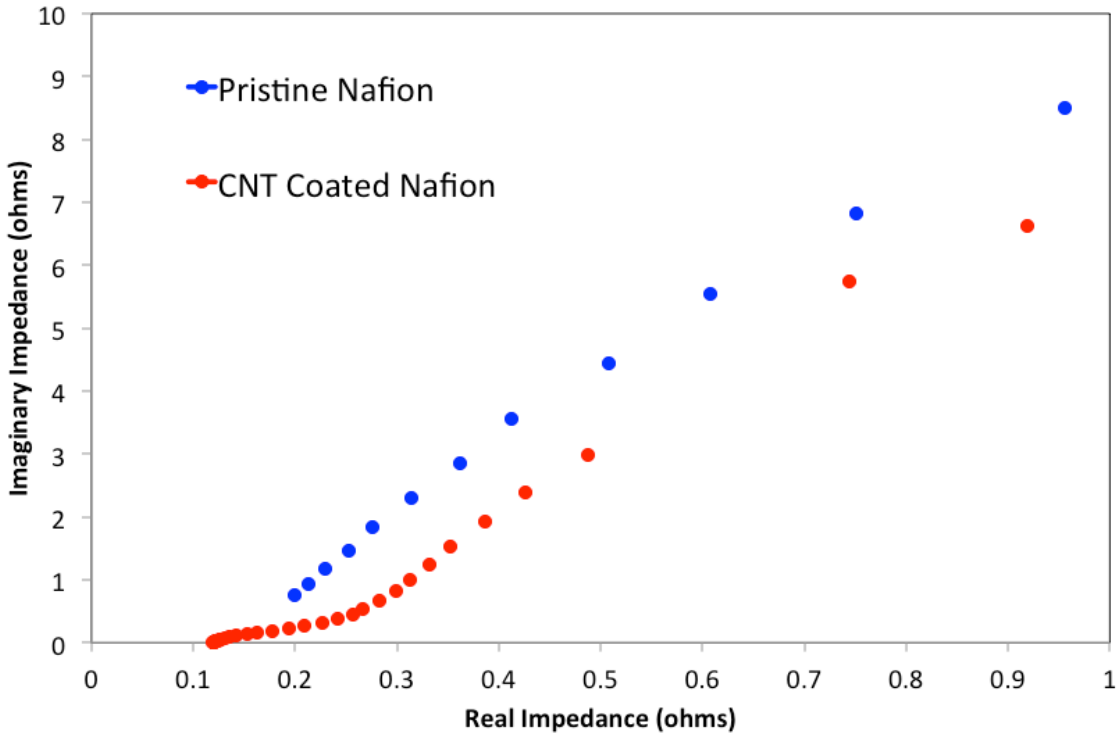

Figure 1.4. In-situ EIS data comparing the pristine Nafion membrane to a Nafion membrane coated with 0.10 mL of conductive ink. The bottom plot is a closer look at the high-frequency intercept shown in the top plot.

Surface Resistivity Measurements

Four-probe surface resistivity measurements of each membrane were also conducted to test the resistance to electron transport across the surface of the membrane with different coating masses. The surface resistivity of each membrane was measured and is shown in Figure 1.5. The addition of conductive ink at a deposition mass of ~ 0.01 mg CNT/cm^2 caused the electrical surface resistivity to decrease by about half, when compared to the pristine Nafion membrane. The surface resistivity decreased further when larger masses of conductive ink were added. Membranes coated without the mesh mask showed a slightly lower resistivity than those coated with the mask. This was expected, as there was a larger mass of conductive carbons reaching the

membrane in a continuous film, as compared to the discontinuous masked membrane. The main results from these tests show that there is a noticeable improvement in electrical conductivity across the surface of the membrane with the addition of the coating, and a greater mass of coating leads to lower electrical resistance across the surface. This is relevant to the vanadium battery performance, as electrons can be effectively transferred to the current collector when the vanadium redox reactions occur, especially closer to the interface of the membrane and the felt electrode. Ideally the surface of the membrane would have a very low electrical resistance, but this must be balanced with diffusive restrictions of protons imposed by the addition of the coating.

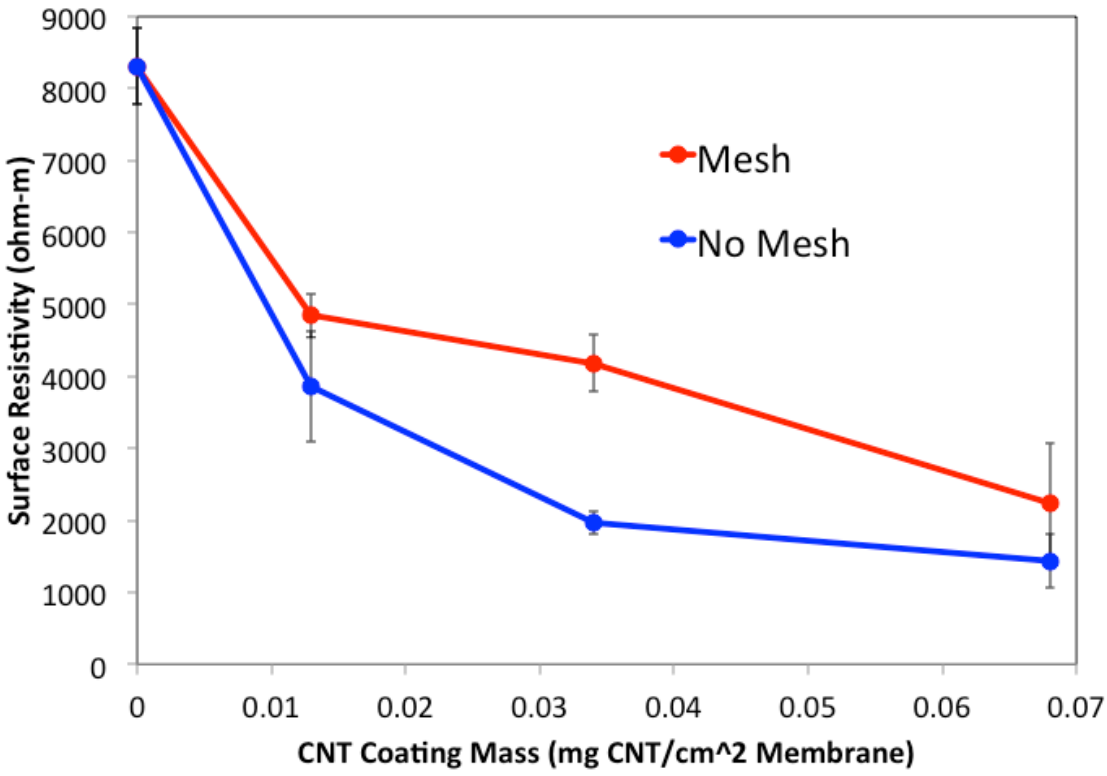

Figure 1.5. Surface resistivity measurements for differing amounts of added CNTs, with and without the use of a mesh mask.

1.3.3 Diffusion Testing. Membranes coated with varying amounts of conductive ink were assessed for ionic permeability using diffusion testing. These tests used the diffusion of vanadium (IV) ions through the membrane as an analogue for proton diffusion through the membrane, as proton diffusion proved difficult to measure accurately due to the protonated nature of the Nafion membrane. Figure 1.6 shows the change in measured vanadium ion concentration in the receptor chamber of the diffusion cell as a function of time. There was very little observed difference in the vanadium ion concentration between differently coated membranes. The vanadium ion concentration may have been somewhat reduced in the "0.035 mg CNT/cm^2, no mesh" case as compared to the "0.035 mg CNT/cm^2, mesh" case. This would support the thought that the regions of no coating created when using the mesh mask allow for a combination of reasonably fast ion transport through the membrane coupled with low electrical resistance. Very little vanadium ion restriction was observed when comparing either of the "0.015 mg CNT/cm^2, mesh" or "0.035 mg CNT/cm^2, mesh" cases to the pristine membrane case.

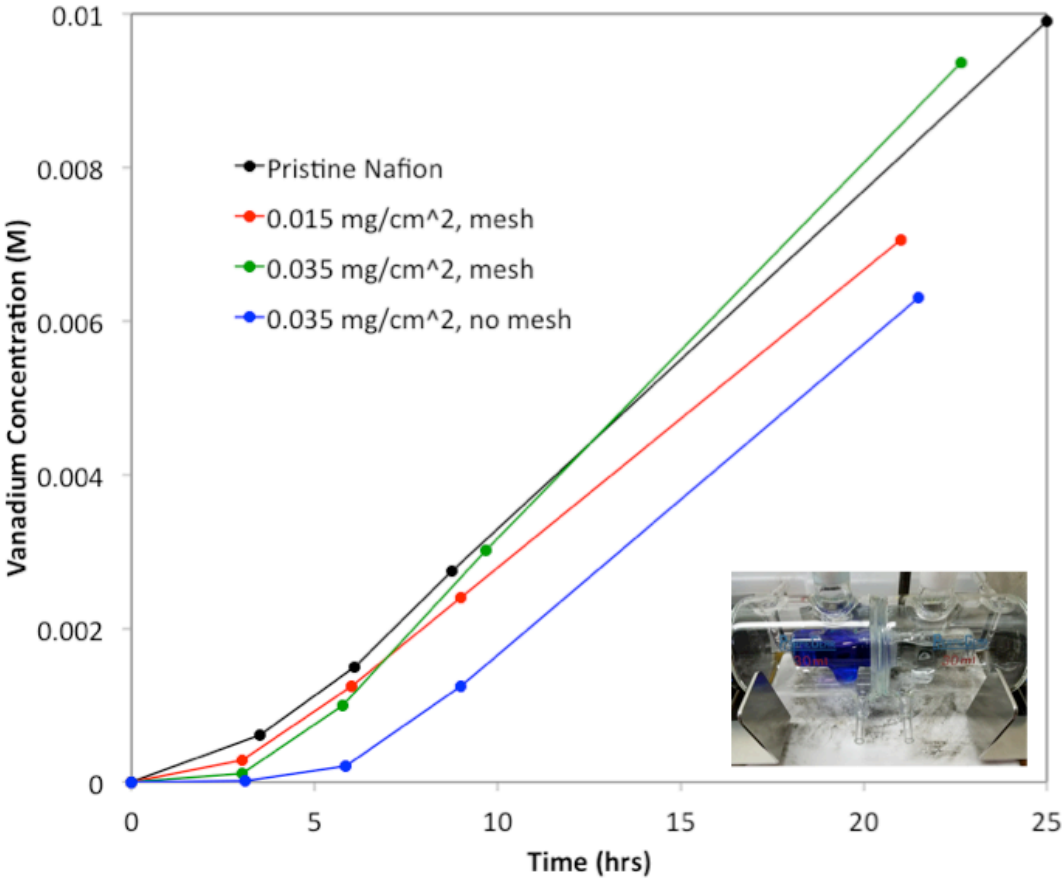

Figure 1.6. Vanadium diffusion across Nafion 117 membranes with varying amounts of conductive ink coating. Diffusion cell setup shown in inset.

1.3.4. Single-Cell Tests. Each membrane was assessed using a single-cell vanadium flow system. This cycling test shows the true utility of any alteration to the VRB – the discharge capacity and efficiencies must be maintained over a large number of cycles, or the battery will face issues regarding potential longevity. Each test consisted of 100 cycles in the voltage window of 0.8 V to 1.7 V. Charge and discharge capacities were monitored over the cycling period. Membranes were tested with varying masses of conductive ink sprayed on them, in order to assess the impact of membrane thickness, mass of CNTs, and ink surface coverage on VRB performance. First, the system was

tested with the pristine Nafion 117 membrane. It was found that the membrane showed good capacity retention and cyclability at lower current densities, around 30 mA/cm^2 and lower. This changed dramatically, however, when current densities were increased. As charge and discharge current densities were increased to between 40 mA/cm^2 and 50 mA/cm^2, discharge capacities dropped precipitously (see Figure 1.7).

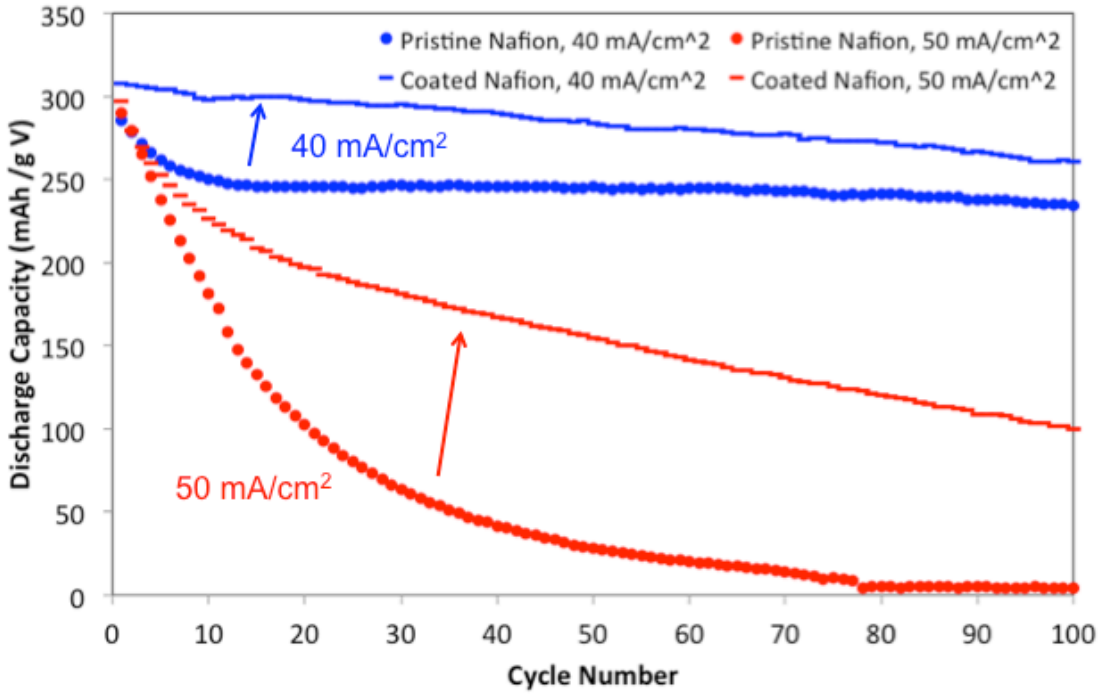

Figure 1.7. Comparison of cycling results using coated and pristine Nafion 117 membranes at different current densities. All coated membranes were electrosprayed with 0.070 mg CNT/cm^2 of conductive ink.

This is attributed to the inability of the vanadium redox reaction to occur quickly enough – limited by slow kinetics of the redox reaction from too few reaction sites or high bulk resistance in the cell. Previous work has theorized that the availability of hydroxyl groups attached to highly electrically conductive material on the electrode can improve the reaction rate of the redox couple, based on reaction mechanisms

proposed in literature.[6] This is also likely the case in this system. Membranes sprayed with the conductive ink were tested at the same current densities for the same number of cycles. Initial tests utilized membranes sprayed with 2.5 mL of the conductive ink on each side of the Nafion 117 membrane. The conductive ink contained 0.13 mg CNT/mL solution. It was found that this led to poor performance of the VRB over time, as the capacity was not retained after many cycles. The capacity retention was diminished at a current density of 30 mA/cm^2 when compared to the pristine Nafion case. It was theorized the thickness and relative hydrophobicity of this coating was negatively impacting the ability of protons to transport easily through the membrane, rapidly increasing cell polarization, and diminishing VRB capacity before the specified cutoff voltage was reached. To address this issue, a two-fold strategy was employed. First, the volume of ink sprayed was reduced to 0.50 mL per side in order to reduce the total overall thickness of the coating. A copper mesh mask, with a grid of 1 mm square holes, was also placed over the membrane during the coating process, in an effort to generate ordered domains of coated and uncoated regions on the surface of the membrane. This was to allow some discrete domains to remain pristine and uncoated, while coating adjacent domains with the conductive ink. The goal was to permit high proton transport, while improving the electrical conductivity between the membrane and the graphite felt. The results of these changes yielded improvements in the capacity retention during cycling, especially at higher current densities (see Figure 1.7). After this improvement, all tests on coated membranes were conducted at the higher rate of 50 mA/cm^2. The volume sprayed was further reduced to approach a lower limit for improvements when reducing CNT loading. Loadings of 0.070 mg

CNT/cm^2, 0.035 mg CNT/cm^2, and 0.015 mg CNT/cm^2 were tested at 50 mA/cm^2 in order to see their effect on capacity retention and battery performance (see Figure 1.8).

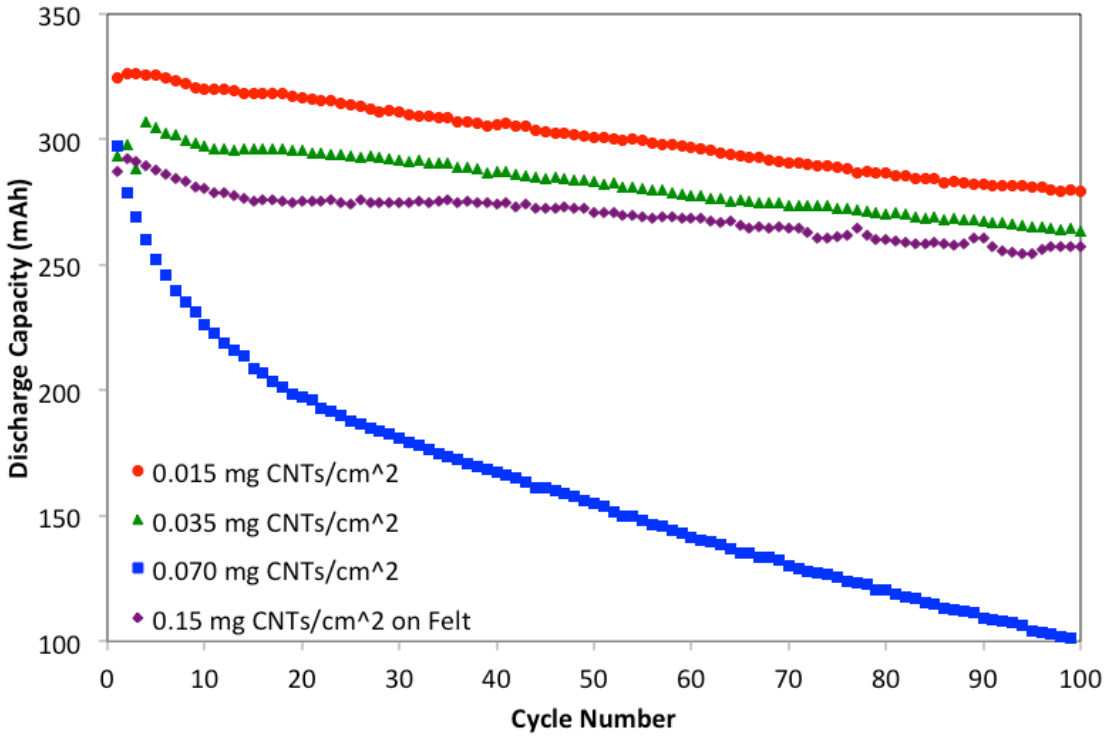

Figure 1.8. Comparison of cycling results (50 mA/cm^2) for different conductive ink coating volumes sprayed onto Nafion 117 membranes and graphite felt.

As the spray volumes were reduced, a lower volume of coating seemed to yield an improvement in initial discharge capacity and capacity retention during cycling. The improvement between loadings of 0.035 mg/cm^2 and 0.015 mg/cm^2 was less pronounced than with larger spray loadings, but still worth noting. This seemed to indicate that there is an important balance between the mass and topology of the coating necessary to improve the overall capacity retention and VRB performance. As the thickness of coating is reduced, proton transport through the membrane likely

approaches rates closer to that in the pristine case (as was demonstrated in diffusion testing), while contributing a highly electrically conductive bridge between the membrane and graphite felt. Single cell tests were conducted wherein the same conductive coating was electrosprayed onto the graphite felt, instead of the membrane surface. This coated felt was paired with a pristine Nafion membrane and tested in the VRB in order to see the impact of electrospraying the conductive ink onto the membrane itself. It was found that even when a loading of 0.15 mg CNT/cm^2 of conductive ink was sprayed onto each piece of graphite felt (ten times the volume that was sprayed onto the best-performing membrane), the VRB single cell tests underperformed those using only 0.015 mg CNT/cm^2 of conductive ink sprayed directly onto the membrane. The coulombic and voltaic efficiencies from each of these tests are shown in Figure 1.9.

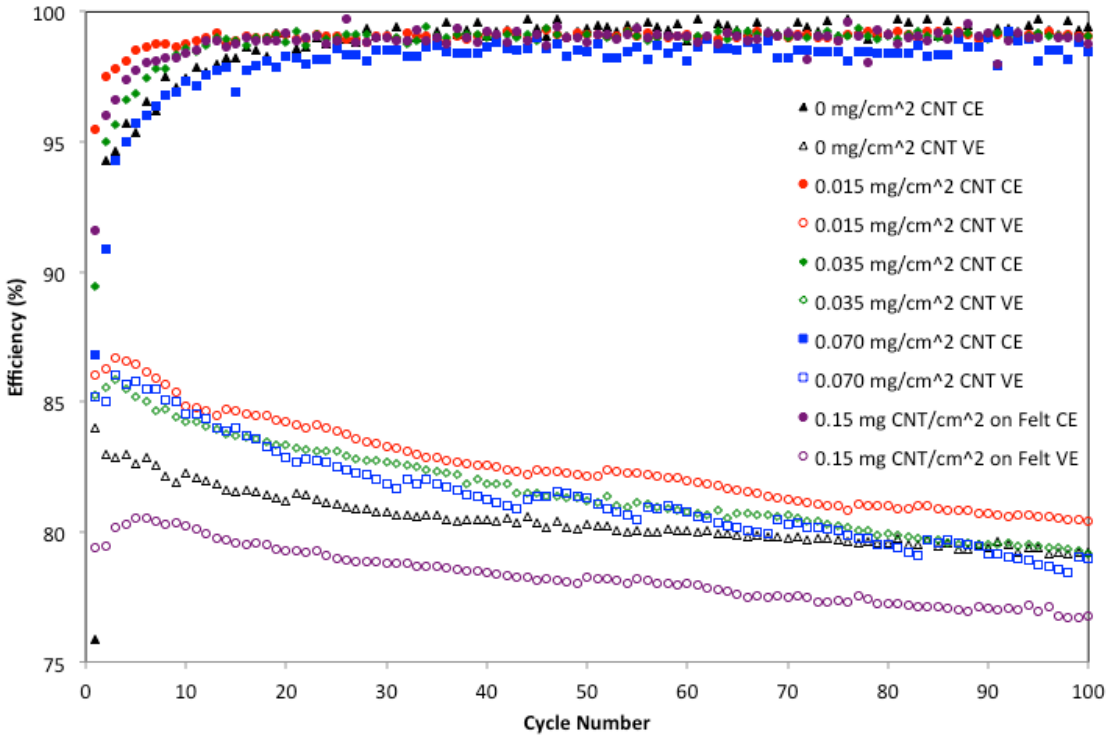

Figure 1.9. Comparison of coulombic and voltaic efficiencies for different conductive ink coating volumes sprayed onto Nafion 117 membranes and graphite felt.

The trends seen in Figure 1.8 are further illustrated here, as each of the tests has a similar coulombic efficiency and differing voltaic efficiencies. The coatings with the highest voltaic efficiencies also tended to have the best capacity retention. This may indicate the importance of focusing the conductive ink at the interface of the VRB, as opposed to simply maximizing the overall mass of conductive ink in the electrodes. It should be noted that the pristine membrane case was unable to adequately discharge at a constant current at 50 mA/cm^2, so the values reflected for the pristine membrane voltaic efficiencies in Figure 1.9 are likely measured in the range of 35-45 mA/cm^2. This choice was made for the sake of comparison at a higher current density, it is expected that these values are higher than they realistically should be for the pristine case. In order to determine the robustness of these coatings, coated membranes were analyzed via SEM and FT-IR both before and after 200 cycles, shown in Figure 1.10. It was found that there was little to no observable change in the surface characteristics of the coating via both the SEM images and the FT-IR spectra. This further demonstrates the promise for the use of these conductive coatings in vanadium redox flow battery applications.

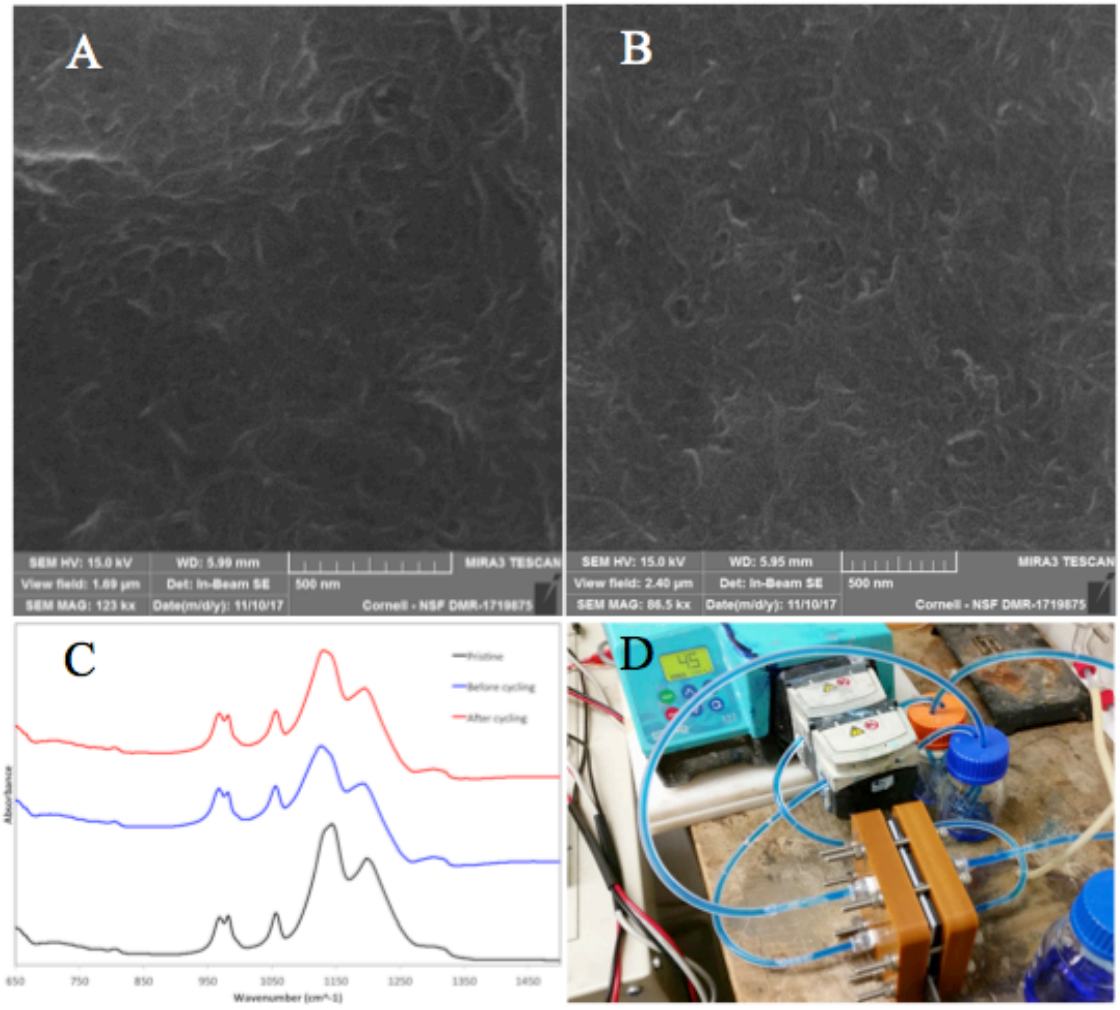

Figure 1.10. Assessment of coated membrane before and after 100 cycles. A. SEM of membrane before cycling, B. SEM of membrane after cycling, C. FT-IR of pristine membrane, coated membrane before cycling, coated membrane after cycling, D. Photo of VRB setup.

1.4. Summary

A very thin CNT-based conductive carbon coating (~ 0.015 mg of CNT/cm^2) onto Nafion 117 membranes can improve the rate capability of vanadium redox flow batteries. Despite a slightly higher electrical surface resistivity, thinner coatings seemed to yield the highest starting discharge capacities and highest capacity retention

over a large number of cycles. The use of a copper mesh mask during the electrospraying process created discrete, ordered domains of coating coverage, which seemed to allow for adequately high proton transport during cycling with still decreasing the surface resistivity of the membrane and thus the interfacial resistance. This coating technique could be used as a fast, stand-alone pretreatment of membranes before use in a vanadium redox flow battery. It could also be used in tandem with other electrode enhancement techniques or on other types of ion-exchange membranes to yield a more efficient battery.

1.5. References

(1) Dunn, B.; Kamath, H.; Tarascon, J. for the Grid : A Battery of Choices. *Science*. **2011**, *334*, 928–935.

(2) Liu, J.; Zhang, J.; Yang, Z.; Lemmon, J. P.; Imhoff, C.; Graff, G. L.; Li, L.; Hu, J.; Wang, C.; Xiao, J.; et al. Materials Science and Materials Chemistry for Large Scale Electrochemical Energy Storage : From Transportation to Electrical Grid. *Adv. Funct. Mater*. **2013**, *23*, 929–946.

(3) Alotto, P.; Guarnieri, M.; Moro, F. Redox flow batteries for the storage of renewable energy : A review. *Renew. Sustain. Energy Rev*. **2014**, *29*, 325–335.

(4) Ulaganathan, M.; Aravindan, V.; Yan, Q.; Madhavi, S.; Skyllas-Kazacos, M.; Lim, T. M. Recent Advancements in All-Vanadium Redox Flow Batteries. *Adv. Mater. Inter*. **2016**, *3*, 1–22.

(5) Parasuraman, A.; Mariana, T.; Menictas, C.; Skyllas-Kazacos, M. Review of material research and development for vanadium redox flow battery applications. *Electrochim. Acta* **2013**, *101*, 27–40.

(6) Park, M.; Jung, Y.; Kim, J.; Cho, J. Synergistic Effect of Carbon Nanofiber/Nanotube Composite Catalyst on Carbon Felt Electrode for High-Performance All-Vanadium Redox Flow Battery. *Nano Lett*. **2013**.

(7) Li, W.; Liu, J.; Yan, C. Modified multiwalled carbon nanotubes as an electrode reaction catalyst for an all vanadium redox flow battery. *J. Solid State Electrochem*. **2013**, *17*, 1369–1376.

(8) Han, P.; Yue, Y.; Liu, Z.; Xu, W.; Zhang, L.; Xu, H. Graphene oxide nanosheets/multi-walled carbon nanotubes hybrid as an excellent electrocatalytic material towards VO^{2+}/VO_2^+ redox couples for vanadium redox flow batteries. *Energy Environ. Sci*. **2011**, 4710–4717.

(9) Chu, Y. Q.; Li, D. D.; Li, W. W.; Ma, C. A. Electrocatalytic Activity of Multi-walled Carbon Nanotubes for VO 2 + / VO 2 + of a Vanadium Redox Flow Battery. *IEEE Conf*. **2013**, 5–8.

(10) Melke, J.; Jakes, P.; Langner, J.; Riekehr, L.; Kunz, U.; Nefedov, A.; Sezen, H.; Wo, C.; Roth, C. Carbon materials for the positive electrode in all-vanadium redox flow batteries. *Carbon*. **2014**, *8*.

(11) Chakrabarti, M. H.; Brandon, N. P.; Hajimolana, S. A.; Tariq, F.; Yu, V.; Hashim, M. A.; Hussain, M. A.; Low, C. T. J.; Aravind, P. V. Application of carbon materials in redox flow batteries. *J. Power Sources* **2014**, *253*, 150–166.

(12) Park, S. M.; Kim, J. H.; Skyllas-Kazacos, M. A technology review of electrodes and reaction mechanisms in vanadium redox flow batteries. *J. Mater. Chem. A* **2015**, *3*, 16913–16933.

(13) Wang, S.; Zhao, X.; Cochell, T.; Manthiram, A. Nitrogen-Doped Carbon Nanotube/Graphite Felts as Advanced Electrode Materials for Vanadium Redox Flow Batteries. *J. Phys. Chem. Lett*. **2012**, *3*, 2164–2167.

(14) Zhu, H. Q.; Zhang, Y. M.; Yue, L.; Li, W. S.; Li, G. L.; Shu, D.; Chen, H. Y. Graphite – carbon nanotube composite electrodes for all vanadium redox flow battery. *J. Power Sources* **2008**, *184*, 637–640.

(15) Wei, G.; Jia, C.; Liu, J.; Yan, C. Carbon felt supported carbon nanotubes catalysts composite electrode for vanadium redox flow battery application. *J. Power Sources* **2012**, *220*, 185–192.

(16) Deng, Q.; Huang, P.; Zhou, W.; Ma, Q.; Zhou, N.; Xie, H.; Ling, W.; Zhou, C.; Yin, Y.; Wu, X.; et al. A High-Performance Composite Electrode for Vanadium Redox Flow Batteries. *Adv. Energy Mater.* **2017**, *1700461*, 1–7.

(17) Ejigu, A.; Edwards, M.; Walsh, D. A. Synergistic Catalyst – Support Interactions in a Graphene – Mn_3O_4 Electrocatalyst for Vanadium Redox Flow Batteries. *ACS Catal.* **2015**, *7130* (1).

(18) Huang, R.; Sun, C.; Tseng, T.; Chao, W.; Hsueh, K. Investigation of Active Electrodes Modified with Platinum / Multiwalled Carbon Nanotube for Vanadium Redox Flow Battery. *J. Electrochem. Soc.* **2012**, *159* (10), 1579–1586.

(19) Li, B.; Gu, M.; Nie, Z.; Shao, Y.; Luo, Q.; Wei, X.; Li, X.; Xiao, J.; Wang, C.; Sprenkle, V.; et al. Bismuth Nanoparticle Decorating Graphite Felt as a High-Performance Electrode for an All-Vanadium Redox Flow Battery. *Nano Lett.* **2013**, *13*, 1330–1335.

(20) Zhang, W.; Xi, J.; Li, Z.; Zhou, H.; Liu, L. Electrochemical activation of graphite felt electrode for VO^{2+}/ VO_2^+ redox couple application. *Electrochim. Acta* **2013**, *89*, 429–435.

(21) Kim, K. J.; Lee, S.; Yim, T.; Kim, J.; Choi, J. W.; Kim, J. H.; Park, M.; Kim, Y. A new strategy for integrating abundant oxygen functional groups into carbon felt electrode for vanadium redox flow batteries. *Sci. Rep.* **2014**, *2*, 1–6.

(22) Kim, K. J.; Kim, Y.; Kim, J.; Park, M. The effects of surface modification on carbon felt electrodes for use in vanadium redox flow batteries. *Mater. Chem. Phys.* **2011**, *131* (1-2), 547–553.

(23) Yue, L.; Li, W.; Sun, F. Highly hydroxylated carbon fibres as electrode materials of all-vanadium redox flow battery. *Carbon.* **2010**, *48* (11), 3079–3090.

(24) Yu, L.; Lin, F.; Xi, J. A recast Nafion / graphene oxide composite membrane for advanced vanadium redox flow batteries. *RSC Adv*. **2016**, *6*, 3756–3763.

(25) Ju, K.; Hwan, Y. Preparation of the graphene oxide (GO)/Nafion composite membrane for the vanadium redox flow battery (VRB) system. *Vacuum* **2014**, *107*, 269–276.

(26) Niu, R.; Kong, L.; Zheng, L.; Wang, H.; Shi, H. Novel graphitic carbon nitride nanosheets / sulfonated poly (ether ether ketone) acid-base hybrid membrane for vanadium redox flow battery. *J. Memb. Sci*. **2017**, *525* (October 2016), 220–228.

(27) Jia, C.; Cheng, Y.; Ling, X.; Wei, G.; Liu, J.; Yan, C. Sulfonated Poly (Ether Ether Ketone)/ Functionalized Carbon Nanotube Composite Membrane for Vanadium Redox Flow Battery Applications. *Electrochim. Acta* **2015**, *153*, 44–48.

(28) Wang, G.; Zhang, J.; Zhang, J.; Chen, J.; Zhu, S. Sulfonated poly(ether ether ketone)/ poly(vinylidene fluoride) / graphene composite membrane for a vanadium redox flow battery. *J. Solid State Electrochem*. **2017**, *21*, 1185–1194.

(29) Jiang, B.; Yu, L.; Wu, L.; Mu, D.; Liu, L.; Xi, J.; Qiu, X. Insights into the Impact of the Nafion Membrane Pretreatment Process on Vanadium Flow Battery Performance. *ACS Mater. Interfaces* **2016**.

(30) Zhou, X. L.; Zhao, T. S.; An, L.; Zeng, Y. K.; Zhu, X. B. Performance of a vanadium redox flow battery with a VANADion membrane. *Appl. Energy* **2016**, *180*, 353–359.

(31) Jiang, B.; Wu, L.; Yu, L.; Qiu, X.; Xi, J. A comparative study of Nafion series membranes for vanadium redox flow batteries. *J. Memb. Sci*. **2016**, *510*, 18–26.

(32) Li, X.; Zhang, H.; Mai, Z.; Zhang, H.; Vankelecom, I. Ion exchange membranes for vanadium redox flow battery (VRB) applications. *Energy Environ. Sci*. **2011**, *4* (4), 1147.

CHAPTER 2

DIRECT ADDITION OF SULFUR AND NITROGEN FUNCTIONAL GROUPS TO GRAPHITE FELT ELECTRODES FOR IMPROVING ALL-VANADIUM REDOX FLOW BATTERY PERFORMANCE

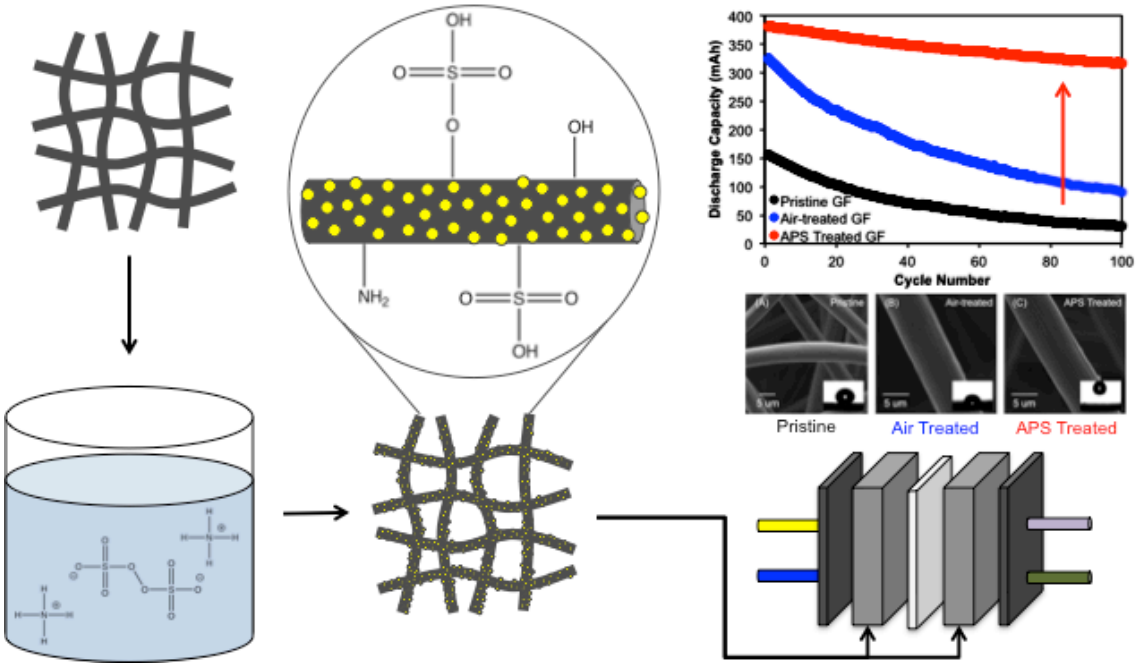

Abstract Figure: Scheme of Process

Sulfur and nitrogen containing groups were bonded to carbon in graphite felt using a hydrothermal synthesis method for use in an aqueous all-vanadium redox flow battery. It was found that the inclusion of these groups improved the voltaic efficiencies, discharge capacities, and capacity retention of these batteries at high current densities. The direct addition of sulfur and nitrogen groups also substantially extended the range

of current densities available to the battery (in excess of 200 mA/cm^2). These results suggest that the direct addition of sulfur and nitrogen containing groups on the graphite felt as a simple and effective method for improving the performance of all-vanadium redox flow batteries.

2.1. Introduction

The need for the development of effective storage methods for renewably generated electricity has become increasingly evident in the past few decades.[1,2] As global energy generation portfolios have begun to burgeon with intermittent generation methods, such as wind and solar power, temporary electrical storage has been researched with greater interest. To date, a large majority of temporary electrical storage exists in the form of mechanical methods. As of 2017, the United States Department of Energy estimated that over 95% of large-scale electrical storage capacity in the United States consisted of a combination of pumped hydroelectric, compressed air, and flywheel storage technologies.[3,4] In an age that is in many ways defined by portable electrical devices, large-scale electrochemical storage technologies play a surprisingly minor role in this portfolio, contributing less than 3% of total electrical storage in the United States.[4] There are a large variety of electrochemical storage technologies that have demonstrated great promise to be deployed at large scales, one of which is redox flow batteries. Redox flow batteries have shown the possibility to be a reasonably low-cost, long-term electrical storage method.[5-7] The all-vanadium aqueous redox flow battery system (VRB) has been of special interest due

to its chemical stability, long cycle life, and potential for high electrical capacity.[8,9] Despite these useful properties, VRBs have struggled to break into major energy markets due to reasonably high fixed costs and relatively low power density compared to other electrical storage methods. Extensive efforts have been taken to investigate and improve these metrics.

The all-aqueous VRB operates using two vanadium based redox couples: VO_2^+ and VO^{2+} in the catholyte, V^{2+} and V^{3+} in the anolyte. These redox couples are simultaneously oxidized and reduced upon charging and discharging, via a one-electron process. A number of factors can impact the performance of these batteries, including the cell configuration, flow properties, and polarization resistance. Polarization resistance is likely the most widely studied area of VRB research, as the overall performance of the battery tends to be most sensitive to changes that impact electrochemical performance. Improvements in electrochemical performance tend to improve metrics such as current density during cycling, which can in turn allow for cell stacks with higher power densities and lower overall capital costs. A number of efforts have been made to improve the electrochemical performance of VRBs by improving the surface properties of the electrodes in a VRB. This has included a large body of work using carbon materials, such as adding various highly conductive carbons to graphite felts[10-19] and membranes[20-24], carbonizing electrodes via specific heat treatments, and synthesizing electrodes out of specially developed high surface area or heteroatom-doped carbon materials. Other work has been focused on decorating carbon materials with metal and metal oxide particles[25-30], either via heat treatments or through direct reduction of soluble salts. Both of these approaches have

shown promise, although issues regarding the stability of some types of added particles have been reported. A large body of work has demonstrated the efficacy of nitrogen-doping carbon-based felts to improve the performance of VRBs. Much of this work has shown that the various forms of amine groups can be used as efficient surface modifiers to act as active sites for vanadium redox reactions.[31-35] It has also been widely demonstrated that adding surface moieties with high oxygen content can improve the reactivity of vanadium redox reactions. This has mainly focused on adding –OH groups to carbon materials, but has also included studies on –COOH and phosphate groups.[36-42] It is logical then, that the combined addition of both amine and sulfur containing groups to carbon-based electrodes should also provide high-quality reaction sites due to high oxygen content and reasonably simple synthetic methods. It seemed that given that the supporting electrolyte in many VRB systems is sulfuric acid, that the use of sulfate groups bonded to the surface of the graphite felt could be more stable over long cycling times than other oxygen containing moieties. Some recent work has investigated the use of sulfate or sulfonate groups in electrolyte additives[43] or in the positive electrode[44-46], but there is little work on the use of nitrogen and sulfur containing functional groups as a direct electrode surface modification to both the anode and cathode of a VRB.

The following work proposes a simple, but potent method of adding both nitrogen and sulfur containing groups to the surface of graphite felt utilizing a one-step hydrothermal treatment with ammonium persulfate (APS) salt dissolved in water. Electrochemical enhancements are observed and examined from a materials based

perspective, to better understand how and why this new method improves VRB performance.

2.2 Methods

2.2.1 Addition of sulfur and nitrogen groups to the surface of graphite felt. Varying masses of ammonium persulfate (APS) were dissolved into 100 mL DI water. About 1g of pristine graphite felt (~3 mm thick) was submerged into this solution, which was subsequently placed in a 200 mL Teflon-lined hydrothermal reactor. The reactor was heated in an air furnace at 180C for 12 hours. The graphite felt was then removed from the reactor, and rinsed thoroughly with DI water to remove residual salt from the surface of the felt. This process was tested with ammonium persulfate solution concentrations of 0.10, 0.25, 0.50, and 0.75M APS in 100 mL water. This process was also tested without the hydrothermal treatment, and simply with graphite felt soaked in the APS solution, and with the hydrothermal treatment alone (no APS added) to serve as control experiments. This process was tested on the graphite felt used as the cathode alone, the anode alone, and in both the cathode and anode.

2.2.2 Single-Cell Testing. The single cell setup consisted of the cell and two glass containers for electrolyte storage. Electrolyte was pumped through ¼" I.D. tubing to and from the flow cell (Tygon 2375 Ultra tubing, Watson-Marlow 323E Pump). Each side of the cell consisted of symmetric acrylic end plates with push-to-connect tube fittings, a graphite current collector, a Viton gasket, a polypropylene flow frame, and an HDPE gasket. These components were separated by a Nafion 212 membrane (50

um thick). The total exposed area of the membrane and graphite current collector was 15 cm^2 (a 5 cm by 3 cm rectangle). Each side of the cell had a 2 mm space between the membrane and current collector, in which a piece of 3 mm thick porous graphite felt (PAN-based, AVCarb) was compressed for good electrical contact. The electrolyte used in all tests was 1M $VOSO_4$ (Alfa Aesar) in 4M H_2SO_4. The electrolyte volume used was 25 mL for the catholyte and anolyte, with a flow rate of 30 mL/min. Each container of electrolyte was purged of air prior to testing by covering the electrolyte with a blanket of argon and sealing well. Current densities between 50 mA/cm^2 and 200 mA/cm^2 were explored. All single-cell cycling testing was carried out using a battery analyzer (3A/5V, MTI). Cycling involved charging and discharging repeatedly at a specified constant current density. The upper cutoff voltage was set at 1.7 V, the lower cutoff voltage was set at 0.8 V. Cycling tests were assessed by coulombic efficiency, voltaic efficiency, energy efficiency, and capacity retention.

2.2.3 Electrochemical Measurements. Electrolytes were assessed using Electrical Impedance Spectroscopy (EIS) testing to measure the changes in resistance in the cell both with and without the addition of APS to the surface of the graphite felt. An electrolyte consisting of 0.20M H_2SO_4 and 0.05M $VOSO_4$ was used for all testing. An AC voltage of 1 mV amplitude was used over a frequency range of 10^4 Hz to 10^{-3} Hz to generate Nyquist plots of the pristine and modified cases. Cyclic voltammetry (CV) was also performed on the electrolytes at rates of 10, 20, 50, and 100 mV/s in a three-electrode glass cell, using the above-mentioned electrolyte. The working electrode consisted of a precisely massed piece of graphite felt, skewered on a narrow glassy

carbon electrode (1 mm diameter) to provide high electrical conductivity. The reference electrode used was Ag/AgCl, the counter electrode used was a platinum mesh (52 mesh, Alfa Aesar) attached to platinum wire to provide a large surface area. A potential range between -1.6 V and +1.4 V was explored.

2.2.4 Materials Characterization. The treated graphite felts were characterized using a variety of analytical techniques. Felts were optically inspected using SEM to observe any visual changes to their surfaces. XPS was used to characterize and quantify the bonding environment on the surface of the felts after the treatment. Raman spectroscopy (using a 488 nm laser) was used to observe the changes in the degree of crystallinity in the carbon network of the graphite felts. Goniometry was employed to determine the contact angle of water on the surface of the felts. Fourier-Transform Infrared Spectroscopy (FT-IR, Bruker Vertex 80v) was used to glean information about bonding groups on the surface of the felts.

2.3. Results and Discussion

The goal of this treatment was to develop a simple method to permanently add reactive nitrogen and sulfur-containing groups to the surface of graphite felt electrodes for use in an aqueous all-vanadium redox flow battery. It was theorized that this would be an elegant method of tethering a high concentration of oxygen sites and ionizable protons on the surface of the graphite felt. The benefits of air-treating graphite felt on VRBs have been well-documented elsewhere[47], but VRBs with air-treated felts alone have limits in their ability to reach high current densities and voltaic efficiencies. It has also been observed that the oxygen groups formed through this process may not be as stable as desired during lengthy cycling processes, such as those necessary in VRB

use. The actual nature of these groups can also vary based on the treatment, but in many cases tend to be a mixture of hydroxyl, carboxyl, and epoxide groups.[36,41,47,48] The proposed treatment uses an inexpensive, highly water-soluble salt as a supply of ammonium and persulfate ions. It has been observed that upon heating in neutral pH, persulfates can decompose to form reactive free radicals, which can add to alkenes and primary alcohols to form both sulfates and sulfonate groups with alkenes[49-53], an example of which is shown in Scheme 2.1.

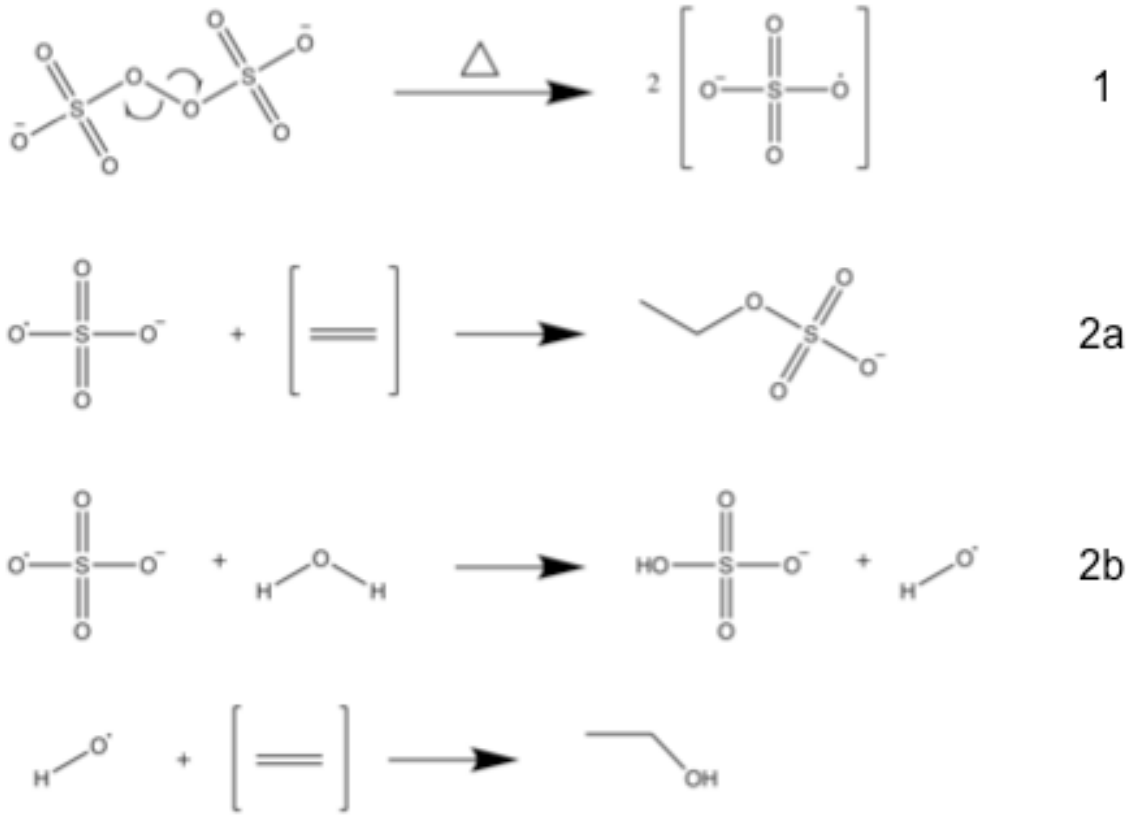

Scheme 2.1. Proposed formation of surface functional moieties. Reaction scheme showing formation of sulfate esters and hydroxyl groups via persulfate radicals. A similar reaction mechanism is expected for the formation of sulfonate groups.

The extent of the contribution from each of these theorized reaction processes was unknown prior to testing, however ammonium persulfate has been long used as an oxidizing agent in a number of unrelated applications.[54-57] Ammonium and ammonia can, in heated aqueous environments, directly substitute nitrogen atoms for carbon atoms in carbon networks.[58-60] There are a number of reagents available for this process. This approach combines the two agents to modify carbon in a single step. Initial range-finding studies were conducted to understand how much APS salt was needed to improve the performance of the graphite felts in the VRB. It was found that concentrations greater that 0.25M APS per gram of graphite felt showed little additional improvement in VRB performance. Hence, all subsequent APS testing was conducted using 0.25M APS solutions to reduce waste of materials and cost. SEM was used to analyze these treated felts, as shown in Figure 2.1.

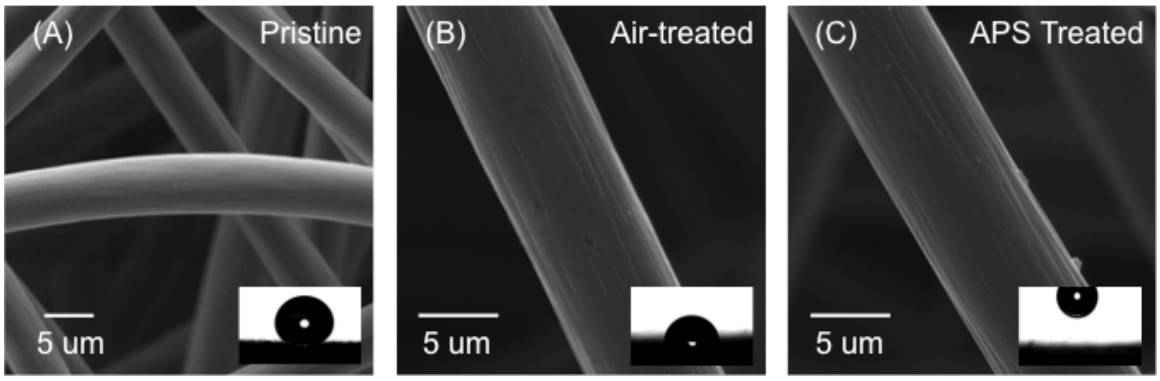

Figure 2.1. FE-SEM images of A. Pristine graphite felt, B. Air-treated graphite felt, and C. APS Treated graphite felt. While no obvious the optical differences can be observed, major differences in hydrophilicity are observed in goniometry measurement (inset). The APS treated felt is so hydrophilic that water droplets immediately wet the felt, prohibiting contact angle measurement.

The felts showed no noticeable visual differences in surface structure. Maintaining the structural integrity of the individual felt fibers is crucial to long-life stability and maintaining high electrical conductivity in VRBs. The APS treatment process showed no evidence of damage to these fibers. Goniometry was conducted using DI water as the working solvent. It was observed that the as-received felts are quite hydrophobic (Figure 2.1A). After air-treatment in a furnace (420C for 10 hours), the felts show a lower contact angle (Figure 2.1B). Following a hydrothermal treatment in a 0.25M APS solution (1.00 g graphite felt: 5.7 g APS salt), the surface was significantly more hydrophilic, evidenced by the rapid wetting of the felt. A contact angle could not be recorded due to the highly hydrophilic nature of the modified felt (Figure 2.1C). The felts were also analyzed using Raman Spectroscopy, as shown in Figure 2.2.

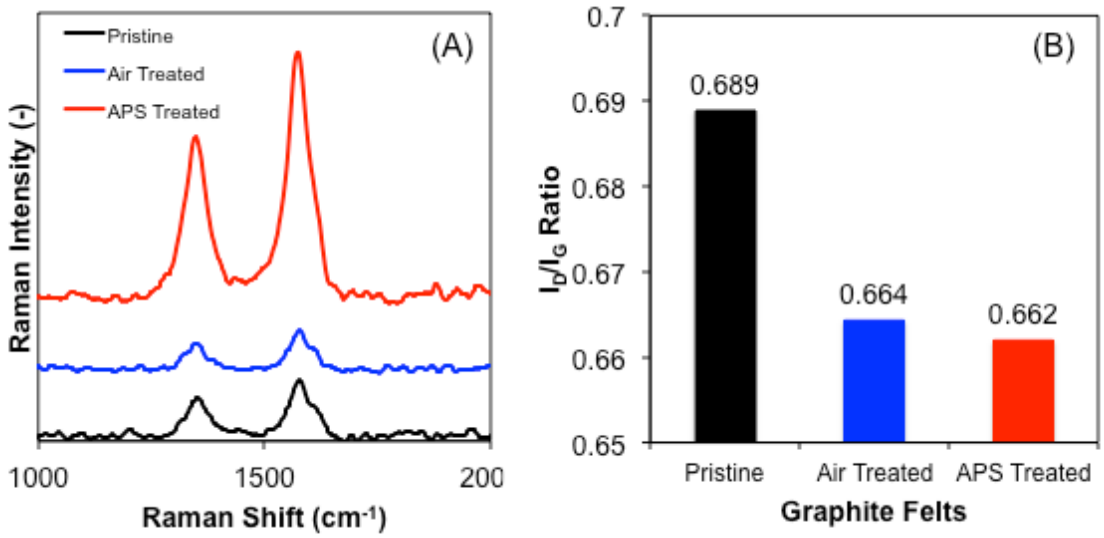

Figure 2.2. A. Raman Spectroscopy showed prominent G and D bands, the relative intensities of which where quantified. B. Summary of relative I_D/I_G intensities showed that the Air-treated and APS Treated felts had a marginally higher degree of crystallinity in the carbon network.

This was conducted to examine the nature of the carbon structure with and without the APS treatment. When observing carbon materials with Raman Spectroscopy, it is common to see two primary signals: the Disorder Band (D Band) and the Graphitic Band (G Band). The relative intensity ratio of these two peaks gives an indication of the degree of crystallinity in the target carbon network.[61] These data show that the D Band occurs at approximately 1350 cm^{-1} and the G Band is found at approximately 1572 cm^{-1}. The I_D/I_G ratios are also summarized in Figure 2.2. The data show that there was an apparent increase in the fraction of crystalline material found in the graphite felt after heat treatment in air. This was attributed to a small amount of carbon oxidation and removal in the form of CO and CO_2 gas during the heat treatment, the majority of which was likely amorphous carbon. The APS treatment seemed to have a minimal impact on the crystallinity of the graphite felt compared to the air-treated felt – an important indicator of the intact structural integrity of the graphite felt. X-ray Photoelectron Spectroscopy (XPS) was used to more accurately quantify the elemental distribution and bonding environment on the surface of the graphite felt. These data are shown in Figure 2.3A. All felts analyzed showed C 1s and O 1s peaks. It is quite clear that the APS treated felt also showed S 2p, S 2s, and N 1s peaks. These peaks indicated a presence of both sulfur and nitrogen on the surface of the graphite felt. The C 1s XPS spectra for each sample was deconvoluted as presented in Figure 2.3. Figure 2.3B shows the pristine felt, which exhibited a majority of C-C bonding at 284 eV, with a minor amount of C-O bonding at 286 eV. The Air-treated case (Figure 2.3C)

showed a larger fraction of C-O bonding, accompanied by substantial C=O bonding at 289 eV. This higher degree of oxidation is expected and is consistent with the overall oxygen content measured, along with the goniometry data. The deconvoluted APS treated felt XPS spectra (Figure 2.3D) showed a series of unique carbon bonds, with the C-C bonding found at 284 eV, C-N bonding at 285 eV, C-O at 287 eV, C-S at 288 eV, and C=O at 290 eV. These fitting assignments are consistent with previous studies on systems containing C, O, N, and S.[38,43,46] They also indicate that a series of sulfur and nitrogen containing compounds are covalently bonded on the surface of the graphite felt as a result of the APS treatment.

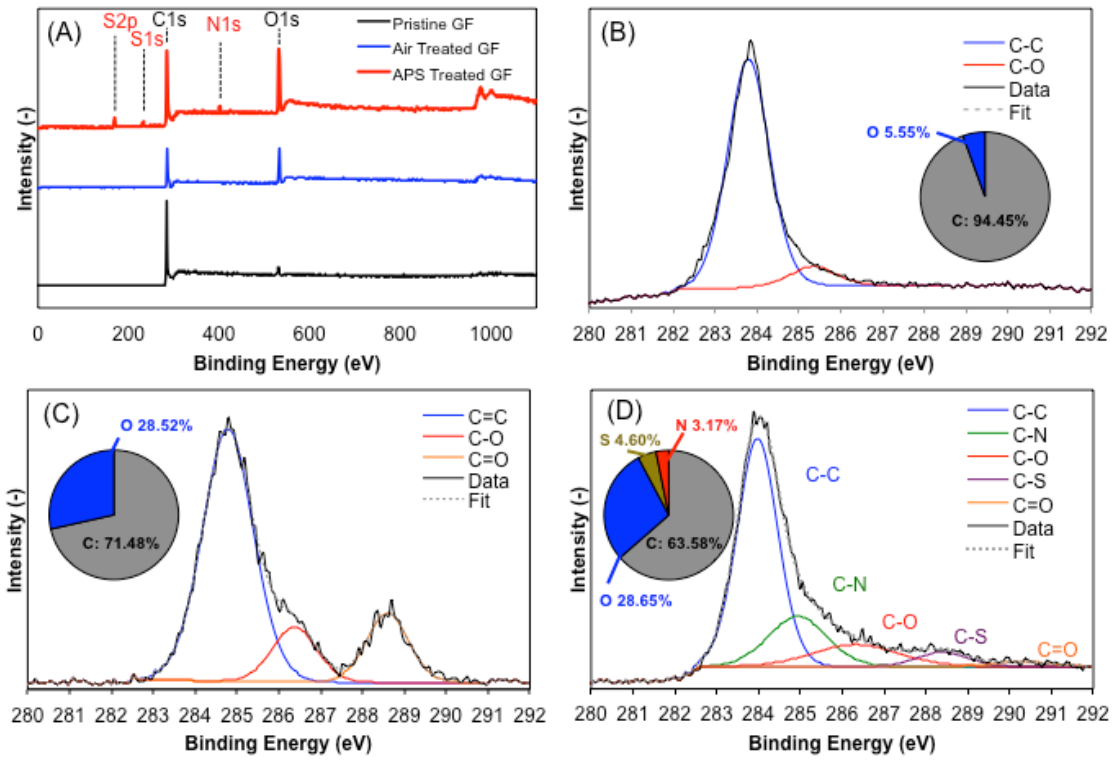

Figure 2.3. A. XPS spectra comparing the three test cases of graphite felt. Both S 2p, S 1s, and N 1s peaks appear clearly in the APS Treated felt spectra. B. C 1s spectra of Pristine felt showed low oxygen content. C. C 1s spectra of Air-treated felt showed a

higher degree of oxidation, evidenced by prominent C-O and C=O bonding. D. C 1s spectra of APS Treated felt showed a series of different carbon bonds. The overall atomic percentages of each sample are reflected by the pie charts.

When the S 1s peak from the APS treated felt was examined in detail (Figure 2.4A), it was shown that it could be deconvoluted into two peaks. Theory dictates that the S 2p peak exist as a doublet due to spin-orbit splitting, and appear in a 1:2 intensity ratio as S $2p_{1/2}$ and S $2p_{3/2}$, respectively.[62] This splitting is demonstrated in the observed S 2p spectra in these data. It is theorized that the S $2p_{3/2}$ peak found at 167 eV is indicative of C-SO_3H groups, whereas the S $2p_{1/2}$ peak found at 169 eV likely represents O-SO_3H groups.[63] These results support the theory that a combination of sulfates and sulfonates are formed during the APS treatment. In Figure 2.4B the N 1s spectra can be deconvoluted into graphitic, pyrrolic, pyridinic, and oxidic groups, based on where the nitrogen atom is inserted into the carbon structure.[31,32] This distribution is observed in the spectra of the APS treated sample, with the graphitic peak found at 401 eV, pyrrolic at 400 eV, pyridinic at 399 eV, and oxidic at 403 eV. It is likely that these groups are formed in a somewhat random nature, although all provide sites for protons available for ion exchange, which are likely used in reaction with the electroactive vanadium species.

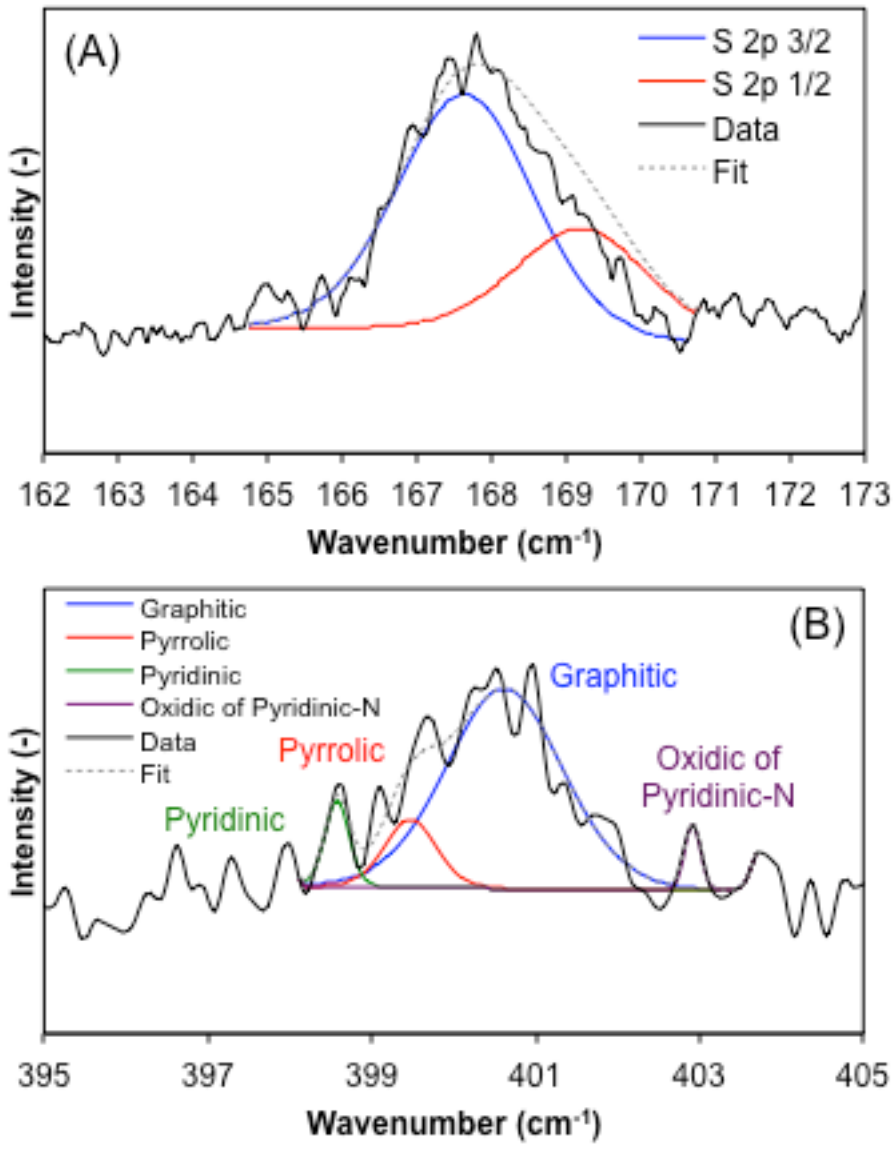

Figure 2.4. A. S 2p XPS spectra from APS Treated felt sample. The peak indicates the presence of S-O and C-S bonding. B. N 1s XPS spectra from APS Treated felt sample. Deconvolution indicates a variety of types of nitrogen bonding to the carbon in the felt.

The three samples of interest were also analyzed using FT-IR Spectroscopy to better understand bonding on the surface of the graphite felts (Figure 2.5). Some peaks were found in all samples tested, and were generally consistent with the carbon-bonding

network of the graphite felt. These included peaks at 1627 cm^{-1} (C=C alkene stretching), 1465 cm^{-1} (C-H alkane bending), 1267 cm^{-1} and 1122 cm^{-1} (likely C-O stretching).[64] Quite a few new peaks were observed and assigned to sulfur containing moieties after the APS treatment. SO_2^- symmetric and asymmetric stretching peaks were observed at 1025 cm^{-1} and 1160 cm^{-1}, respectively.[65-67] Broad peaks centered at 1190 cm^{-1} and 1430 cm^{-1} were also observed, which are both attributed to S=O stretching modes in sulfate or sulfonate groups.[64,67] A peak was also observed at 1052 cm^{-1}, which can likely be attributed to the C-N stretching mode found in amine groups.[64] Interestingly, a reasonably large peak was observed at 877 cm^{-1}, which can be assigned to the stretching mode of a sulfate ester (S-O-C). The expected range for finding a sulfate ester stretching mode is typically between 700 cm^{-1} and 900 cm^{-1}, but previous work has shown that longer carbon based groups tend to shift the peak toward the higher wavenumbers.[68,69] This finding supports the sulfation reaction mechanism proposed via the radical formation process. The most prominent peak in the observed spectra was found at 659 cm^{-1}, which can be attributed to a C-S bond.[70,71] This is indicative of the C-S bond found in sulfonate groups, suggesting that they may exist in greater proportion than the suspected sulfate groups on the surface of the felt.

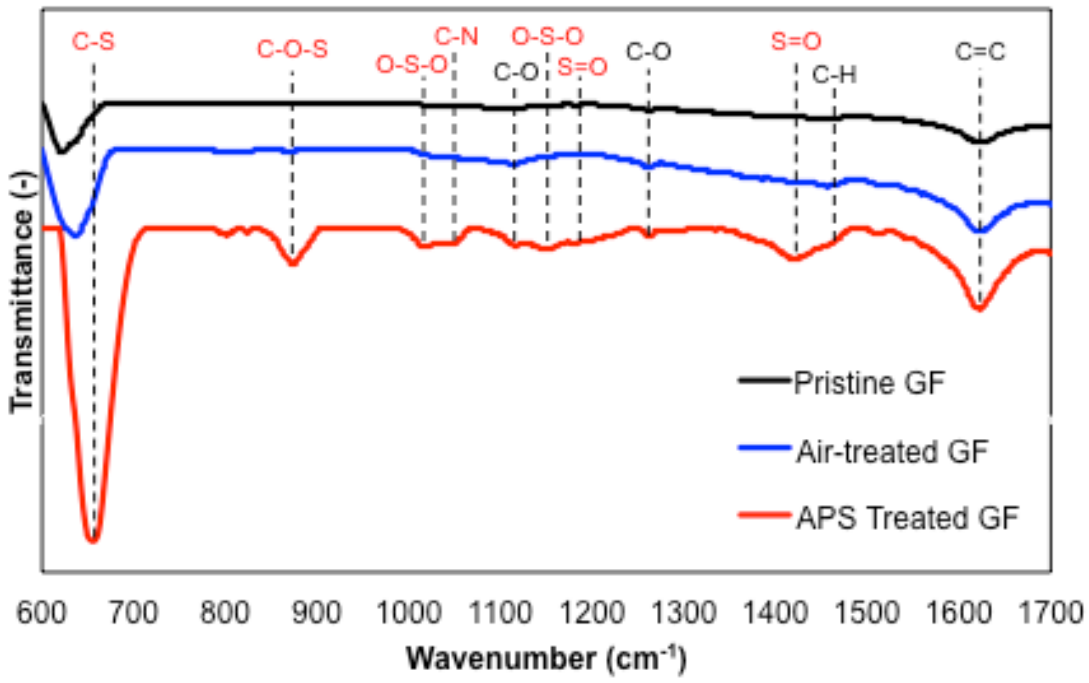

Figure 2.5. FT-IR of graphite felts spectra show a number of peaks indicating presence of various surface functional groups on APS Treated felt.

In order to better understand why this surface modification process works, a reaction scheme was proposed for both the anode and the cathode (Scheme 2.2). Both sulfate and hydroxyl groups are used as instructive examples, but similar reaction mechanisms are expected from sulfonate and amine groups. It is assumed that functional groups on the surface of the felt are fully protonated by the sulfuric acid electrolyte upon contact. During the oxidative charging process in the catholyte, it was theorized that oxygen or nitrogen in the surface functional groups acted as initial reaction sites for the VO^{2+} ion to temporarily bond, displacing a proton. An additional oxygen from water groups in the electrolyte could then bond to the vanadium complex, generating two additional protons and an electron, forming VO_2^+. In the

anolyte, it is theorized that V^{3+} displaced a proton bonded to an oxygen of the functional group, forming an intermediate complex. An electron could then be withdrawn from the graphite felt, subsequently releasing the vanadium ion, now in the V^{2+} state. It is theorized that this process is reversible, using the same mechanism. This assumption, however, may not be completely accurate due to the discrepancies observed in the current density maxima during electrochemical testing, which suggests that one of the steps in this proposed mechanism is slower in the reverse direction, causing loss of capacity over time at higher current densities.

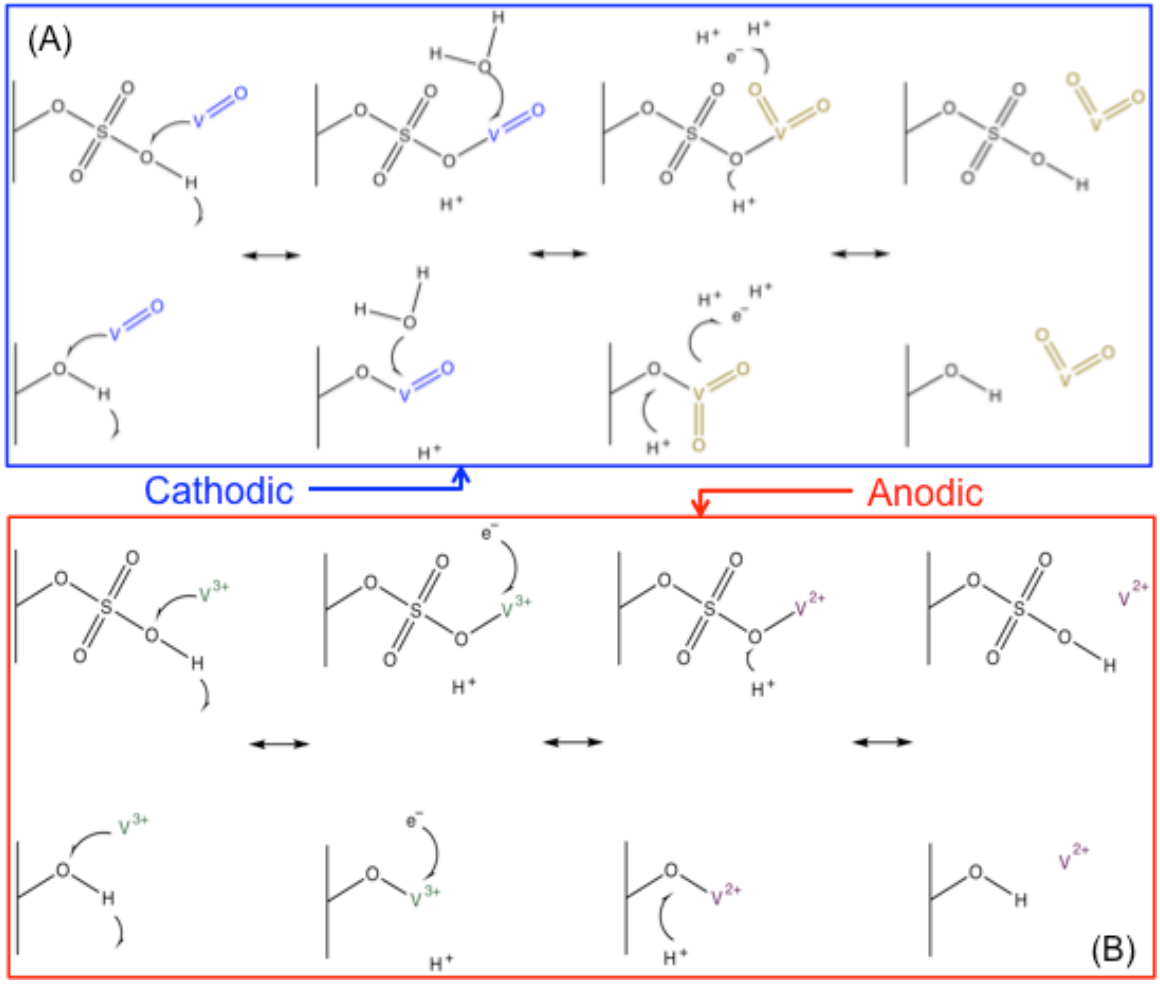

Scheme 2.2. Proposed Vanadium Ion Reaction Mechanism. Sulfate and hydroxyl groups are shown as instructive examples for a suggested reaction mechanism of vanadium ions with surface functional groups from APS Treated felt in the Catholyte (A) and Anolyte (B).

Cyclic voltammetry was conducted to test the electrochemical effects of the APS graphite felt treatment on the relevant VRB reactions. Figure 2.6 shows the CV of the different graphite felts in the catholyte at a potential scan rates of 10, 20, 50, and 100 mV/s. It can be seen that the treatment has minimal impact on the cathodic peak (V(IV) to V(V) reaction) with the use of the APS treated felt. The maximum current density of the air-treated and APS treated felts and the peak position are similar, and both improve upon the pristine felt. There was, however, a substantial improvement in the reverse reaction in the catholyte (V(V) to V(IV)). The maximum current density for the APS treated felt occurred at a higher potential as compared to the pristine and air-treated felts. This indicated a drop in the overpotential of the reaction, which generally suggests more favorable reaction kinetics. This was coupled with the observation that the maximum peak height was greater in the reverse reaction with the use of the APS treated felt. This again indicates favorable reaction kinetics, as a greater generated current signifies an increase in the number of electroactive groups reacting and transferring electrons during the potential sweep. These effects are attributed to the increased number of vanadium reaction sites from oxygen in the sulfate, sulfonate and hydroxyl groups and nitrogen in the amine groups on the surface of the graphite felt. The reversibility of this reaction (in terms of current density) seems to be limited by the reverse reaction (V(V) to V(IV)). It seems that the increased number of surface moieties in the cathode plays a more important role in the reverse reaction than in the forward reaction. This is indicative of either more sluggish

reaction kinetics, which are improved by additional reaction sites, or a reverse reaction mechanism that is different than that of the forward reaction.

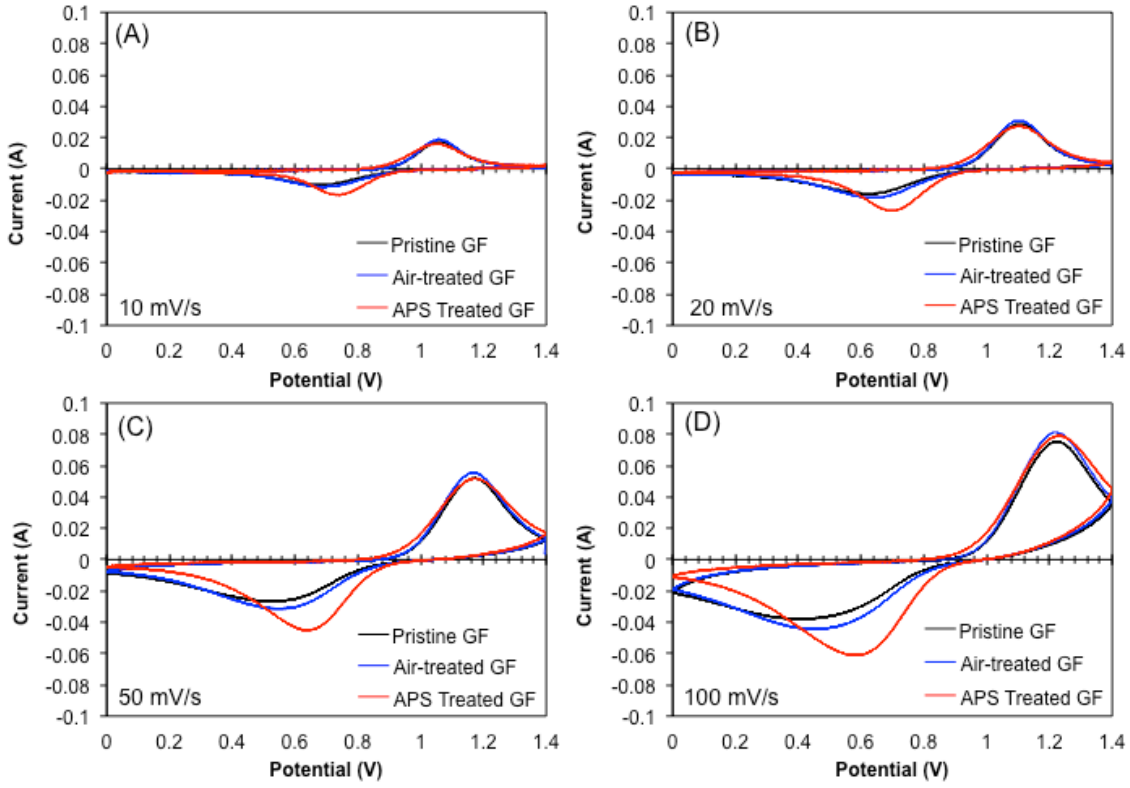

Figure 2.6. CV data is compared for potential scan rates of 10, 20, 50, and 100 mV/s using different graphite felts in the catholyte. Data presented by individual felt type can be found in Figure 2.S1.

Figure 2.7 shows CV data of the graphite felts in the anolyte. The improvements in reversibility of these reactions are more pronounced in these data. The use of APS treated felt causes a large shift in the peak position of the cathodic peak in the anolyte as compared to both the Pristine and Air-treated cases. The observed current is also substantially greater at all measured sweep rates. The differences in the observed anodic peaks are even more striking. The anodic peak in the anolyte is difficult to measure in either the Pristine or Air-treated cases, especially at higher current

densities, due to the onset of gas generation experienced during the more reducing potentials. This peak is much more pronounced in the APS Treated felt case, as is demonstrated by the peak shoulder near -1.0 V. These results indicate superior activity and reversibility of the anodic reaction with the use of the APS treated felt.

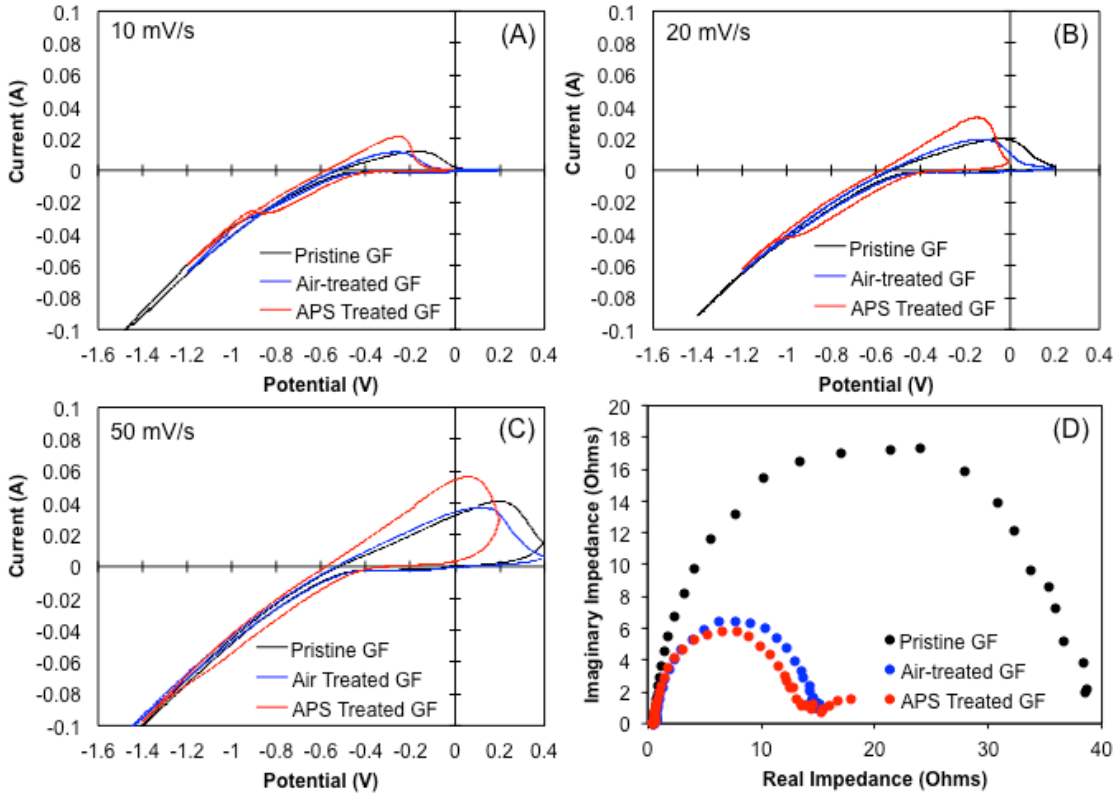

Figure 2.7. Plots A, B, and C show CV data collected at potential scan rates of 10, 20, and 50 mV/s for different graphite felts in the anolyte. Data presented by individual felt type can be found in Figure 2.S2. D. EIS spectra comparison of the three felts in the vanadium electrolyte.

In order to better understand the diffusive characteristics of the vanadium species in the presence of the different types of felt, the Randles-Sevcik equation was used to plot the CV peak current density versus the square root of the potential scan rate.[72] The resulting plots are shown in Figure 2.8 and were plotted based on Equation 2.1:

$$i_p = (2.69 \times 10^5) n^{3/2} A D_o^{1/2} C_o^* v^{1/2} \quad (2.1)$$

where i_p is peak current (A), n is number of electrons transferred (1), A is electrode area (cm^2), D_o is the apparent diffusion coefficient (cm^2/s), C_o^* is the bulk electrolyte concentration (mol/cm^3), and v is the potential sweep rate (V/s).

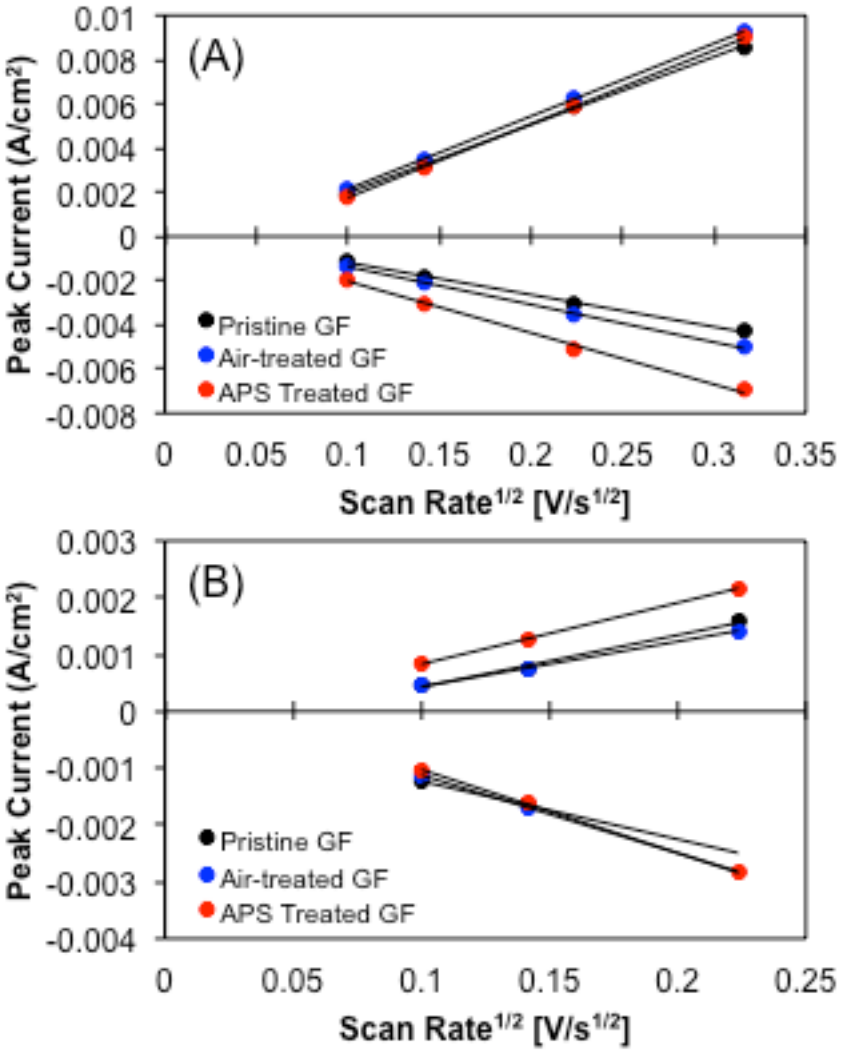

Figure 2.8. Plots of Peak Current (measured from CV testing) vs. potential scan rate$^{1/2}$. Data was plotted to calculate effective vanadium ion diffusion coefficients in the presence of the different felts.

The apparent diffusion coefficients for the different felts in the anolyte and catholyte are tabulated in Table 1. In the catholyte, the mass transfer of the forward reaction is not greatly impacted by the treated APS felt or the air-treated felt. The reverse reaction, however, shows that the apparent diffusion coefficient of the APS treated felt is nearly double that of the air-treated felt and greater than double that of the pristine felt. The diffusion coefficients are all smaller in the anolyte, which is consistent with slower reaction kinetics. The APS treated felt again shows larger diffusion coefficients as compared to the pristine or air-treated felts, indicative of a more favorable surface for the relevant reactions.

Table 2.1. Calculated effective vanadium ion diffusion coefficients

	Catholyte (10^{-6} cm^2/s)		**Anolyte** (10^{-6} cm^2/s)	
	Positive	Negative	Positive	Negative
Pristine GF	5.24	1.18	0.46	0.58
Air-treated GF	6.02	1.62	0.35	1.04
APS Treated GF	6.13	3.00	0.65	1.19

Electrical Impedance Spectroscopy (EIS) was performed in a 3-probe cell using each of the graphite felts as a working electrode. These data (Figure 2.7D) supported the results from the CV testing, showing an evident decrease in charge transfer resistance

with both the APS and air-treated felts as compared to the pristine felt. The APS treated felt showed an even smaller charge transfer resistance than the air-treated felt, as was expected. The Ohmic resistance was unchanged for each test, as expected.

Finally, the felts were assessed in single cell tests. Each test consisted of a series of charge-discharge cycles at various current densities to measure the discharge capacities and coulombic, voltaic, and energy efficiencies. The current densities tested ranged from 50 mA/cm^2 to 200 mA/cm^2 in increments of 25 mA/cm^2. The tested cases were: Pristine GF (anode and cathode), Air-treated GF (anode and cathode), APS Treated GF (cathode only, Air-treated anode), APS Treated GF (anode only, Air-treated cathode), and APS Treated (anode and cathode). The coulombic efficiencies were largely unaffected by the changes in surface treatment (Figure 2.9A). The voltaic efficiencies show the true impact of the APS treatment on the felts. The Pristine GF was unable to cycle past 75 mA/cm^2. The Air-treated GF showed an improvement to the pristine case, but was limited to a current density range of 100 mA/cm^2. The use of an APS Treated GF in the cathode with an Air-treated anode resulted in a modest improvement in the voltaic efficiency compared to the all Air-treated case, consistent with CV data. The use of an APS Treated GF anode with an Air-treated GF cathode showed a major improvement in the voltaic efficiency of the VRB, and extended the current density range to 175 mA/cm^2. The best results were seen when the APS treated GF was used on both sides of the VRB, resulting in a voltaic efficiency of ~75% at a high current density of 200 mA/cm^2. This translates to an energy efficiency improvement of over 25% when compared to the Pristine felt case at 50 mA/cm^2.

These results suggest that the APS treatment has a much greater impact in the anode than the cathode of the VRB, but demonstrate an improvement on both sides of the battery. The corresponding discharge capacities of these tests were also reported (Figure 2.9D), demonstrating that the measured capacities correspond well to the voltaic and energy efficiencies.

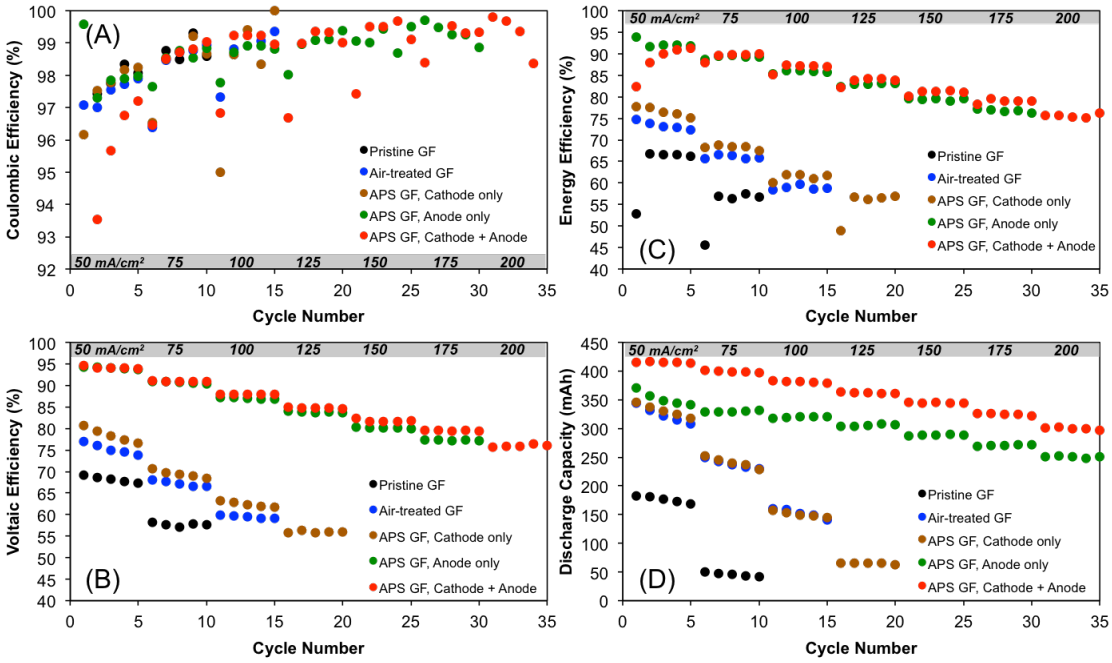

Figure 2.9. Results of ramping study of different graphite felts at increasing current density. Each current density increment lasted 5 cycles. A. Coulombic efficiency comparison, B. Voltaic efficiency comparison, C. Energy efficiency comparison, D. Discharge capacity comparison.

In order to probe the capacity retention in these systems, cycling tests at a modest current density of 50 mA/cm^2 were conducted on the Pristine, Air-treated, and APS Treated (anode and cathode) VRBs. These data (Figure 2.10) show that the APS treated case has a capacity retention of 83.1% over 100 cycles, compared to 19.7% (Pristine) and 27.9% (Air-treated).

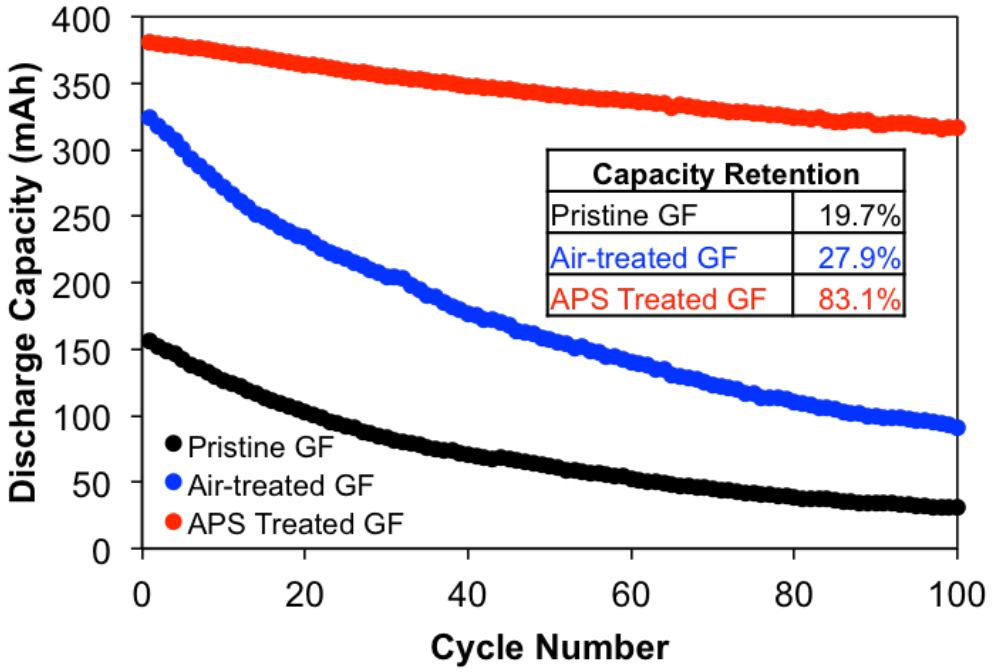

Figure 2.10. Capacity retention comparison of different felts, tested at 50 mA/cm^2 for 100 cycles.

A series of tests were taken to better understand how much the APS treatment contributed to the improvement of the performance of each single cell test. This included control tests with hydrothermally treating the felts in water alone (no APS addition), soaking the felts in APS solution for 12 hours (no hydrothermal treatment), and hydrothermally treating the felts in 9M H_2SO_4 instead of in the APS solution. This series of tests was compared to tests with the air-treated felts in both the anode and the cathode, and with pristine felts in both the anode and the cathode. The voltaic efficiencies of ramping data for the various cases of felts are shown in Figure 2.S3. The data show that hydrothermally treating with sulfuric acid shows a minor improvement in performance, likely due to mild oxidation or sulfation of the graphite felt. This case shows less impressive data than the Air-treated base case. When the

felts are hydrothermally treated in water alone, the voltaic efficiencies are similar to the Air-treated case. This is also explained by mild oxidation of the felts from the water treatment, although perhaps in a way that does less damage to the electrically conductive network of the felt. Finally, a room-temperature soak in the APS solution showed the most positive results, and readily outperformed the Air-treated felt. This is likely due to the unstable radical nature of the persulfate groups in the APS salt. Some small amount of reaction with the felt likely occurs to cause a noticeably large improvement in both voltaic efficiency and accessible current densities. It is important to note that none of these cases come close to performing as well as the hydrothermally treated APS felt, especially when the treatment is to both sides of the felt. It is clear that a larger thermal activation is necessary for the surface reactions to occur to a greater extent.

2.4. Conclusions

Sulfur and nitrogen containing functional groups were successfully added to graphite felt electrodes for use in a VRB via a simple hydrothermal method. The use of APS salt allowed for the formation of persulfate radicals, which tethered sulfate, sulfonate, and hydroxyl groups to the carbon surface. Ammonium ions also caused the formation of amine groups of various types. As a result, major improvements in voltaic and energy efficiency were achieved by using APS Treated felt in both the anode and the cathode, attributed to a large amount of active oxygen and nitrogen surface sites on the graphite felt electrodes. These improvements were studied and characterized using various electrochemical and materials analyses, which revealed improvements in both

charge transfer and mass transfer of the vanadium redox couples. The vanadium reactions in the anolyte proved to be the limiting factor in the overall performance of the VRB. In conclusion, this method created a stable, oxygen-rich, hydrophilic surface that greatly improved the overall performance of an aqueous vanadium redox flow battery.

2.5. Acknowledgements

This work made use of the Cornell Center for Materials Research Shared Facilities which are supported through the NSF MRSEC program (DMR-1719875). This work was performed in part at the Cornell NanoScale Facility, a member of the National Nanotechnology Coordinated Infrastructure (NNCI), which is supported by the National Science Foundation (Grant ECCS-1542081).

2.6. Supporting Information

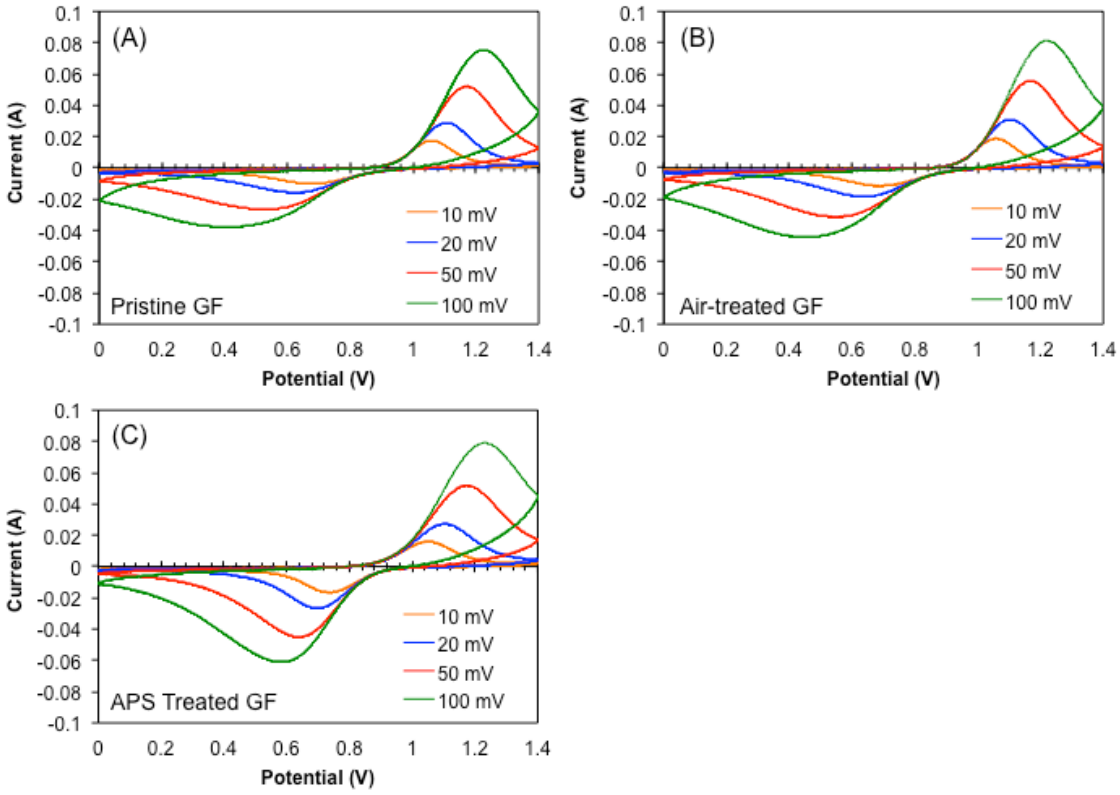

Figure 2.S1. CV data compared for potential scan rates of 10, 20, 50, and 100 mV/s in catholyte using A. Pristine felt, B. Air-Treated felt, C. APS Treated felt

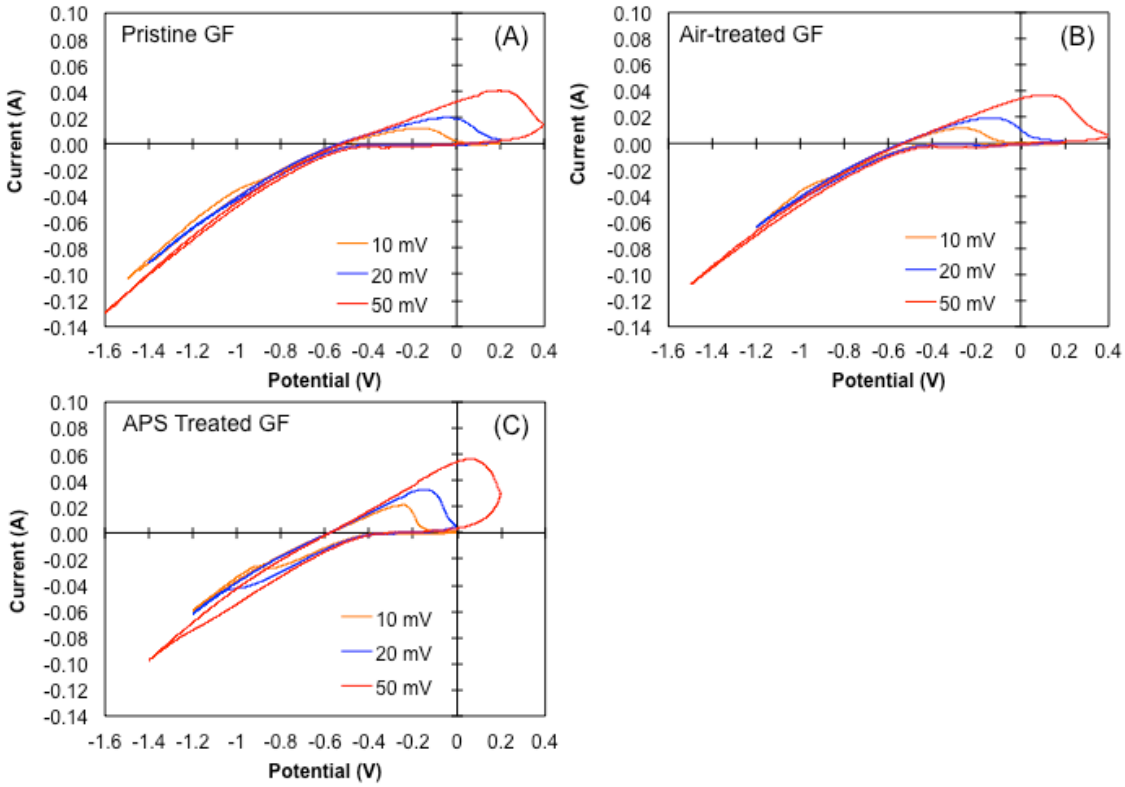

Figure 2.S2. CV data compared for potential scan rates of 10, 20, and 50 mV/s in anolyte using A. Pristine felt, B. Air-Treated felt, C. APS Treated felt

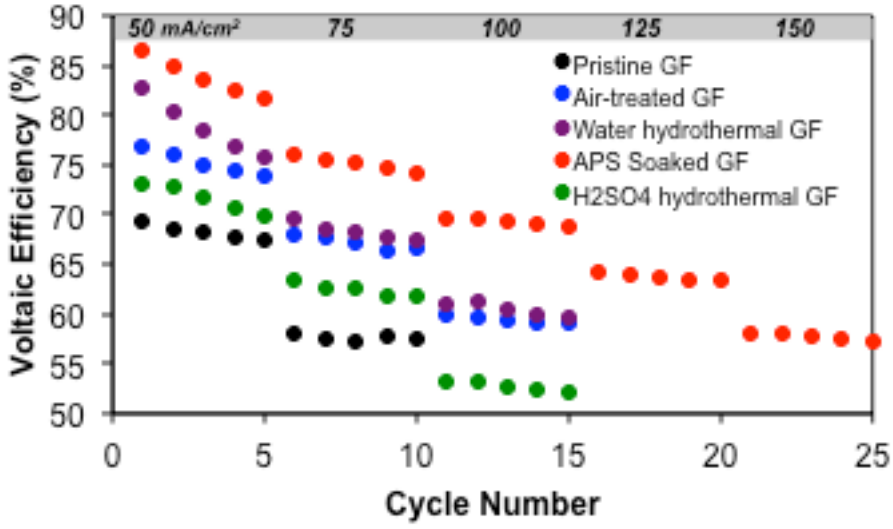

Figure 2.S3. Voltaic efficiencies from ramping study of control case graphite felts. All cases underperformed use of APS hydrothermally treated felts.

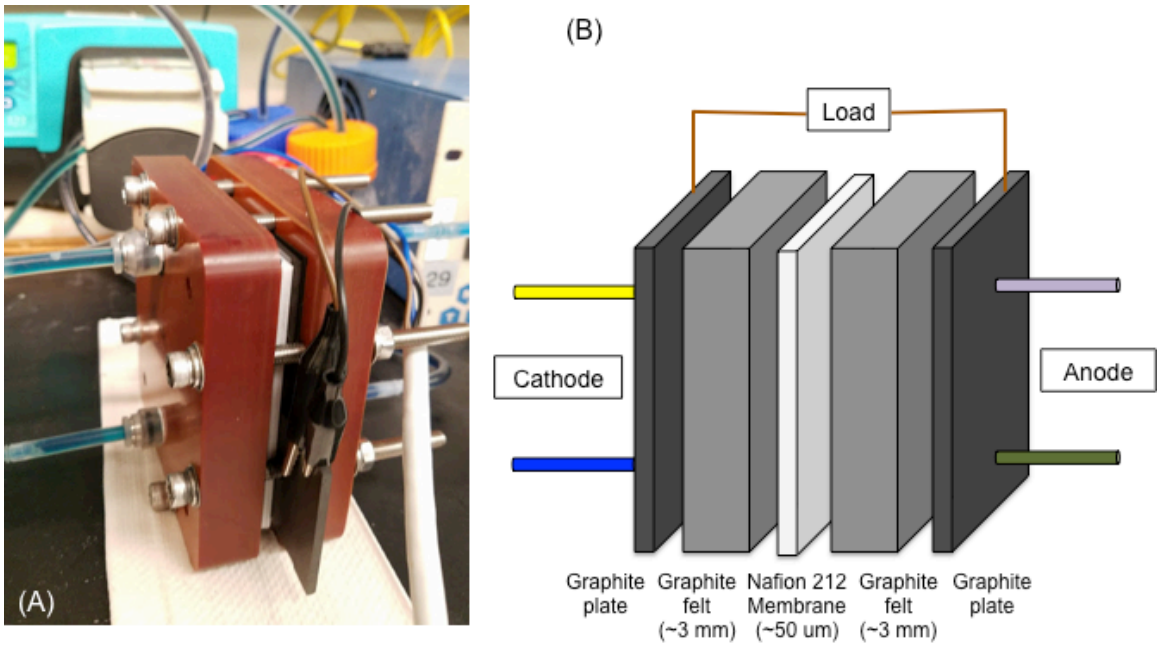

Figure 2.S4. A. Photo of VRB single-cell setup. B. Schematic of VRB single-cell setup.

2.7. References

(1) Dunn, B.; Kamath, H.; Tarascon, J. for the Grid : A Battery of Choices. *Science*. **2011**, *334*, 928–935.

(2) Liu, J.; Zhang, J.; Yang, Z.; Lemmon, J. P.; Imhoff, C.; Graff, G. L.; Li, L.; Hu, J.; Wang, C.; Xiao, J.; et al. Materials Science and Materials Chemistry for Large Scale Electrochemical Energy Storage : From Transportation to Electrical Grid. *Adv. Funct. Mater.* **2013**, *23*, 929–946.

(3) Center for Sustainable Systems, University of Michigan. 2017. "U.S. Grid Energy Storage Factsheet." Pub. No. CSS15-17.

(4) U.S. Department of Energy *Grid Energy Storage*. 2013.

(5) Huskinson, B.; Marshak, M. P.; Suh, C.; Er, S.; Gerhardt, M. R.; Galvin, C. J.; Chen, X.; Aspuru-Guzik, A.; Gordon, R.; Aziz, M. A metal-free organic–inorganic aqueous flow battery. *Nature* **2014**, *505*, 195–198.

(6) Janoschka, T.; Martin, N.; Martin, U.; Friebe, C.; Morgenstern, S.; Hiller, H.; Hager, M. D.; Schubert, U. S. An aqueous, polymer-based redox-flow battery using non-corrosive, safe, and low-cost materials. *Nature* **2015**, *527*, 78–81.

(7) Alotto, P.; Guarnieri, M.; Moro, F. Redox flow batteries for the storage of renewable energy : A review. *Renew. Sustain. Energy Rev.* **2014**, *29*, 325–335.

(8) Ulaganathan, M.; Aravindan, V.; Yan, Q.; Madhavi, S.; Skyllas-Kazacos, M.; Lim, T. M. Recent Advancements in All-Vanadium Redox Flow Batteries. *Adv. Mater. Inter.* **2016**, *3*, 1–22.

(9) Parasuraman, A.; Mariana, T.; Menictas, C.; Skyllas-Kazacos, M. Review of material research and development for vanadium redox flow battery applications. *Electrochim. Acta* **2013**, *101*, 27–40.

(10) Park, M.; Jung, Y.; Kim, J.; Cho, J. Synergistic Effect of Carbon Nanofiber/Nanotube Composite Catalyst on Carbon Felt Electrode for High-Performance All-Vanadium Redox Flow Battery. *Nano Lett.* **2013**.

(11) Li, W.; Liu, J.; Yan, C. Modified multiwalled carbon nanotubes as an electrode reaction catalyst for an all vanadium redox flow battery. *J. Solid State Electrochem.* **2013**, *17*, 1369–1376.

(12) Han, P.; Yue, Y.; Liu, Z.; Xu, W.; Zhang, L.; Xu, H. Graphene oxide nanosheets/multi-walled carbon nanotubes hybrid as an excellent electrocatalytic material towards VO^{2+}/VO_2^+ redox couples for vanadium redox flow batteries. *Energy Environ. Sci.* **2011**, 4710–4717.

(13) Chu, Y. Q.; Li, D. D.; Li, W. W.; Ma, C. A. Electrocatalytic Activity of Multi-walled Carbon Nanotubes for VO 2 + / VO 2 + of a Vanadium Redox Flow Battery. *IEEE Conf*. **2013**, 5–8.

(14) Melke, J.; Jakes, P.; Langner, J.; Riekehr, L.; Kunz, U.; Nefedov, A.; Sezen, H.; Wo, C.; Roth, C. Carbon materials for the positive electrode in all-vanadium redox flow batteries. *Carbon*. **2014**, *8*.

(15) Chakrabarti, M. H.; Brandon, N. P.; Hajimolana, S. A.; Tariq, F.; Yu, V.; Hashim, M. A.; Hussain, M. A.; Low, C. T. J.; Aravind, P. V. Application of carbon materials in redox flow batteries. *J. Power Sources* **2014**, *253*, 150–166.

(16) Park, S. M.; Kim, J. H.; Skyllas-Kazacos, M. A technology review of electrodes and reaction mechanisms in vanadium redox flow batteries. *J. Mater. Chem. A* **2015**, *3*, 16913–16933.

(17) Zhu, H. Q.; Zhang, Y. M.; Yue, L.; Li, W. S.; Li, G. L.; Shu, D.; Chen, H. Y. Graphite – carbon nanotube composite electrodes for all vanadium redox flow battery. *J. Power Sources* **2008**, *184*, 637–640.

(18) Wei, G.; Jia, C.; Liu, J.; Yan, C. Carbon felt supported carbon nanotubes catalysts composite electrode for vanadium redox flow battery application. *J. Power Sources* **2012**, *220*, 185–192.

(19) Deng, Q.; Huang, P.; Zhou, W.; Ma, Q.; Zhou, N.; Xie, H.; Ling, W.; Zhou, C.; Yin, Y.; Wu, X.; et al. A High-Performance Composite Electrode for Vanadium Redox Flow Batteries. *Adv. Energy Mater*. **2017**, *1700461*, 1–7.

(20) Shah, A. B.; Zhou, X.; Brezovec, P.; Markiewicz, D.; Joo, Y. L. Conductive Membrane Coatings for High-Rate Vanadium Redox Flow Batteries. *ACS Omega* **2018**, *3*, 1856–1863.

(21) Yu, L.; Lin, F.; Xi, J. A recast Nafion / graphene oxide composite membrane for advanced vanadium redox flow batteries. *RSC Adv*. **2016**, *6*, 3756–3763.

(22) Ju, K.; Hwan, Y. Preparation of the graphene oxide (GO)/Nafion composite membrane for the vanadium redox flow battery (VRB) system. *Vacuum* **2014**, *107*, 269–276.

(23) Niu, R.; Kong, L.; Zheng, L.; Wang, H.; Shi, H. Novel graphitic carbon nitride nanosheets / sulfonated poly (ether ether ketone) acid-base hybrid membrane for vanadium redox flow battery. *J. Memb. Sci.* **2017**, *525* (October 2016), 220–228.

(24) Jia, C.; Cheng, Y.; Ling, X.; Wei, G.; Liu, J.; Yan, C. Sulfonated Poly (Ether Ether Ketone)/ Functionalized Carbon Nanotube Composite Membrane for Vanadium Redox Flow Battery Applications. *Electrochim. Acta* **2015**, *153*, 44–48.

(25) Ejigu, A.; Edwards, M.; Walsh, D. A. Synergistic Catalyst – Support Interactions in a Graphene – Mn_3O_4 Electrocatalyst for Vanadium Redox Flow Batteries. *ACS Catal.* **2015**, *7130* (1).

(26) Huang, R.; Sun, C.; Tseng, T.; Chao, W.; Hsueh, K. Investigation of Active Electrodes Modified with Platinum / Multiwalled Carbon Nanotube for Vanadium Redox Flow Battery. *J. Electrochem. Soc.* **2012**, *159* (10), 1579–1586.

(27) Li, B.; Gu, M.; Nie, Z.; Shao, Y.; Luo, Q.; Wei, X.; Li, X.; Xiao, J.; Wang, C.; Sprenkle, V.; et al. Bismuth Nanoparticle Decorating Graphite Felt as a High-Performance Electrode for an All-Vanadium Redox Flow Battery. *Nano Lett.* **2013**, *13*, 1330–1335.

(28) Wei, L.; Zhao, T. S.; Zeng, L.; Zhou, X. L.; Zeng, Y. K. Copper nanoparticle-deposited graphite felt electrodes for all vanadium redox flow batteries. *Appl. Energy* **2016**, *180*, 386–391.

(29) Li, B.; Gu, M.; Nie, Z.; Wei, X.; Wang, C.; Sprenkle, V.; Wang, W. Nanorod Niobium Oxide as Powerful Catalysts for an All Vanadium Redox Flow Battery. *Nanoletters* **2014**, *14*, 158–165.

(30) Wang, W. H.; Wang, X. D. Investigation of Ir-modified carbon felt as the positive electrode of an all-vanadium redox flow battery. *Electrochim. Acta* **2007**, *52*, 6755–6762.

(31) Wang, S.; Zhao, X.; Cochell, T.; Manthiram, A. Nitrogen-doped carbon nanotube/graphite felts as advanced electrode materials for vanadium redox flow batteries. *J. Phys. Chem. Lett.* **2012**, *3*, 2164–2167.

(32) Kim, J.; Lim, H.; Jyoung, J.; Lee, E.; Yi, J. S.; Lee, D. High electrocatalytic performance of N and O atomic co-functionalized carbon electrodes for vanadium redox flow battery. *Carbon*. **2017**, *111*, 592–601.

(33) Shao, Y.; Wang, X.; Engelhard, M.; Wang, C.; Dai, S.; Liu, J.; Yang, Z.; Lin, Y. Nitrogen-doped mesoporous carbon for energy storage in vanadium redox flow batteries. *J. Power Sources* **2010**, *195* (13), 4375–4379.

(34) Shi, L.; Liu, S.; He, Z.; Shen, J. Nitrogen-doped graphene : effects of nitrogen species on the properties of the vanadium redox flow battery. *Electrochim. Acta* **2014**, *138*, 93–100.

(35) Park, M.; Ryu, J.; Kim, Y.; Cho, J. Corn protein-derived nitrogen-doped carbon materials with oxygen-rich functional groups : a highly efficient electrocatalyst for all-vanadium redox flow batteries. *Energy Environ. Sci.* **2014**, *7*, 3727–3735.

(36) Zhang, W.; Xi, J.; Li, Z.; Zhou, H.; Liu, L. Electrochemical activation of graphite felt electrode for VO^{2+}/ VO_2^+ redox couple application. *Electrochim. Acta* **2013**, *89*, 429–435.

(37) Kim, K. J.; Lee, S.; Yim, T.; Kim, J.; Choi, J. W.; Kim, J. H.; Park, M.; Kim, Y. A new strategy for integrating abundant oxygen functional groups into carbon felt electrode for vanadium redox flow batteries. *Sci. Rep.* **2014**, *2*, 1–6.

(38) Kim, K. J.; Kim, Y.; Kim, J.; Park, M. The effects of surface modification on carbon felt electrodes for use in vanadium redox flow batteries. *Mater. Chem. Phys.* **2011**, *131* (1-2), 547–553.

(39) Yue, L.; Li, W.; Sun, F. Highly hydroxylated carbon fibres as electrode materials of all-vanadium redox flow battery. *Carbon*. **2010**, *48* (11), 3079–3090.

(40) Bourke, A.; Miller, M. A.; Lynch, R. P.; Gao, X.; Landon, J.; Wainright, J. S.; Savinelli, R. F.; Buckley, D. N. Electrode kinetics of vanadium flow batteries : contrasting responses of V(II) -V(III) and V(IV) -V(V) to electrochemical pretreatment of carbon. *J. Electrochem. Soc.* **2016**, *163* (1), A5097–A5105.

(41) Goulet, M.-A.; Skyllas-Kazacos, M.; Kjeang, E. The importance of wetting in carbon paper electrodes for vanadium redox reactions. *Carbon*. **2016**, *101*, 390–398.

(42) Kim, K. J.; Lee, H. S.; Kim, J.; Park, M.; Kim, J. H.; Kim, Y.; Skyllas-Kazacos, M. Superior Electrocatalytic Activity of a Robust Carbon-Felt Electrode with Oxygen-Rich Phosphate Groups for All-Vanadium Redox Flow Batteries. *ChemSusChem* **2016**, *9* (11), 1329–1338.

(43) Hwang, J.; Kim, B.; Moon, J.; Mehmood, A.; Ha, H. Y. A highly efficient and stable organic additive for the positive electrolyte in vanadium redox flow batteries: taurine biomolecules containing -NH_2 and – SO_3H functional groups. *J. Mater. Chem. A* **2018**, *6*, 4695–4705.

(44) He, Z.; Jiang, Y.; Li, Y.; Wang, L. Boosting the electrocatalytic performance of carbon nanotubes toward V(V) / V(IV) reaction by sulfonation treatment. *Int. J. Energy Res.* **2018**, 1–10.

(45) He, Z.; Jiang, Y.; Li, Y.; Zhu, J.; Zhou, H.; Meng, W. Carbon layer-exfoliated, wettability-enhanced, SO_3H-functionalized carbon paper : A superior positive electrode for vanadium redox flow battery. *Carbon.* **2018**, *127*, 297–304.

(46) Li, C.; Xie, B.; Chen, J.; He, J.; He, Z. Enhancement of nitrogen and sulfur co-doping on the electrocatalytic properties of carbon nanotubes. *RSC Adv.* **2017**, *7*, 13184–13190.

(47) Sun, B.; Skyllas-Kazacos, M. Modification of graphite electrode materials for vanadium redox flow battery application - I. Thermal treatment. *Electrochim. Acta* **1992**, *37* (7), 1253–1260.

(48) Li, W.; Liu, J.; Yan, C. Reduced graphene oxide with tunable C / O ratio and its activity towards vanadium redox pairs for an all vanadium redox flow battery. *Carbon.* **2013**, *55*, 313–320.

(49) Neta, P.; Madhavan, V.; Zemel, H.; Fessenden, W. Rate constants and mechanism of reaction of SO_4.- with aromatic compounds. *J. Am. Chem. Soc.* **1977**, *99*, 163–164.

(50) Geroge, C.; El Rassy, H.; Chovelon, J.-M. Reactivity of Selected Volatile Organic Compounds (VOCs) Toward the Sulfate Radical. *Int. J. Chem. Kinet.* **2001**, *33* (9), 539–547.

(51) Zhang, B.; Zhang, Y.; Teng, Y.; Fan, M. Sulfate radical and its application in decontamination technologies. *Crit. Rev. Environ. Sci. Technol.* **2015**, *45* (16), 1756–1800.

(52) Matzek, L. W.; Carter, K. E. Activated persulfate for organic chemical degradation : A review. *Chemosphere* **2016**, *151*, 178–188.

(53) McBride, E. Sulfonation Process. U.S. Patent 5,117,041, May 26, 1992.

(54) Liu, P.; Wang, T. Ultrasonic-assisted chemical oxidative cutting of multiwalled carbon nanotubes with ammonium persulfate in neutral media. *Appl. Phys. A* **2009**, *97*, 771–775.

(55) Moreno-Castilla, C.; Ferro-Garcia, M. A.; Joly, J. P.; Bautista-Toledo, I.; Carrasco-Marin, F.; Rivera-Utrilla, J. Activated Carbon Surface Modifications by Nitric Acid, Hydrogen Peroxide, and Ammonium Peroxydisulfate Treatments. *Langmuir* **1996**, No. 11, 4386–4392.

(56) An, D.; Westerhoff, P.; Zheng, M.; Wu, M.; Yang, Y.; Chiu, C.-A. UV-activated persulfate oxidation and regeneration of NOM-Saturated granular activated carbon. *Water Res.* **2015**, *73*, 304–310.

(57) Peyton, G. R. The free-radical chemistry of persulfate-based total organic carbon analyzers. *Mar. Sci.* **1993**, *41*, 91–103.

(58) Yang, Z.; Minghan, X.; Liu, Y.; He, F.; Gao, F.; Su, Y.; Wei, H.; Zhang, Y. Nitrogen-doped, carbon-rich, highly photoluminescent carbon dots from ammonium citrate. *Nanoscale* **2014**, *6*, 1890–1895.

(59) Long, D.; Li, W.; Ling, L.; Miyawaki, J.; Mochida, I.; Yoon, S. Preparation of nitrogen-doped graphene sheets by a combined chemical and hydrothermal reduction of graphene oxide. *Langmuir* **2010**, *26* (20), 16096–16102.

(60) Chen, P.; Xiao, T.; Qian, Y.; Li, S.; Yu, S. A nitrogen-doped graphene/carbon nanotube nanocomposite with synergistically enhanced electrochemical activity. *Adv. Mater*. **2013**, *25*, 3192–3196.

(61) Krishnamoorthy, K.; Veerapandian, M.; Yun, K.; Kim, S.-J. The chemical and structural analysis of graphene oxide with different degrees of oxidation. *Carbon*. **2012**, *53*, 38–49.

(62) Zotti, G.; Zecchin, S.; Schiavon, G.; Crispin, X.; Osikowicz, W.; Salaneck, W.; Fahlman, M. Electrochemical and XPS studies toward the role of monomeric and polymeric sulfonate counterions in the synthesis, composition, and properties of poly(3,4-ethylenedioxythiophene). *Macromolecules* **2003**, *36*, 3337–3344.

(63) Wei, B.; Xu, X.; Jin, Z.; Tian, Y. Surface chemical compositions and dispersity of starch nanocrystals formed by sulfuric and hydrochloric acid hydrolysis. *PLoS One* **2014**, *9* (2), 1–7.

(64) Coates, J. Interpretation of Infrared Spectra , A Practical Approach. In *Encyclopedia of Analytical Chemistry: Applications, Theory and Intrumentation, 1*; Meyers, R. A., Ed.; Wiley: Chichester, 2000; pp 10815–10837.

(65) Rao, B. V. S. K.; Mouli, K. C.; Rambabu, N.; Dalai, A. K.; Prasad, R. B. N. Carbon-based solid acid catalyst from de-oiled canola meal for biodiesel production. *Catal. Commun.* **2015**, *14* (1), 20–26.

(66) Rao, C.; Venkataraghavan, R.; Kasturi, T. R. Contribution to the infrared spectra of organosuphur compounds. *Can. J. Chem.* **1964**, *42*, 36–42.

(67) Zhou, J.; Sui, Z.; Zhu, J.; Li, P.; Chen, D. Characterization of surface oxygen complexes on carbon nanofibers by TPD, XPS and FT-IR. *Carbon*. **2007**, *45*, 785–796.

(68) Chihara, G. Medical and biochemical application of infrared spectroscopy. V. Infrared absorption spectra of organic sulfate esters. *Chem. Pharm. Bull.* **1960**, *8* (11), 988–994.

(69) Lloyd, A. G.; Tudball, N.; Dodgson, K. S. Infrared studies on sulphate esters III. O-sulphate esters of alcohols, amino alcohols and hydroxylated amino acids. *Biochim. Biophys. Acta* **1961**, *52*, 413–419.

(70) Kaneko, M.; Kumagai, S.; Nakamura, T.; Sato, H. Study of sulfonation mechanism of low-density polyethylene films with fuming sulfuric acid. *J. Appl. Polym. Sci.* **2004**, *91*, 2435–2442.

(71) Bakker, B. H.; Cerfontain, H. Sulfonation of alkenes by chlorosulfuric acid, acetyl sulfate, and trifluoroacetyl sulfate. *European J. Org. Chem.* **1999**, 91–96.

(72) Bard, A. J.; Faulkner, L.R. *Electrochemical Methods: Fundamentals and Applications,* 2nd ed.; Wiley: New York, 2001; pp 226-255.

CHAPTER 3

DIRECT REDUCTION OF METAL SALTS AS ANODIC ELECTROCATALYSTS FOR AQUEOUS VANADIUM REDOX FLOW BATTERIES

ABSTRACT: Low concentrations of Sn^{2+} and Cu^{2+} salts were dissolved in the anolyte of an aqueous all-vanadium redox flow battery to form tin and copper nanoparticles to improve the reactivity of the V(II)/V(III) reaction. The presence of tin and copper nanoparticles showed improvements in both the discharge capacity (> 40%) and the energy efficiency (> 9%) at a high current density of 150 mA/cm^2. The addition of tin and copper also substantially extended the range of current densities available to the battery. These results suggest the use of tin and copper nanoparticles as a simple and effective method for improving the performance of all-vanadium redox flow batteries.

3.1. Introduction

The need for the development of effective storage methods for renewably generated electricity has become increasingly evident in the past few decades.[1,2] As global energy generation portfolios have begun to burgeon with intermittent generation methods, such as wind and solar power, temporary electrical storage has been researched with greater interest. The all-vanadium aqueous redox flow battery system (VRB) has been of special interest due to its chemical stability, long cycle life, and potential for high electrical capacity.[8,9] Despite these useful properties, VRBs have struggled to break into major energy markets due to reasonably high fixed costs and

relatively low power density compared to other electrical storage methods. Extensive efforts have been taken to investigate and improve these metrics.

The all-aqueous VRB operates using two vanadium based redox couples: VO_2^+ and VO^{2+} in the catholyte, V^{2+} and V^{3+} in the anolyte. These redox couples are simultaneously oxidized and reduced upon charging and discharging, via a one-electron process. A number of factors can impact the performance of these batteries, including the cell configuration, flow properties, and polarization resistance. Polarization resistance is likely the most widely studied area of VRB research, as the overall performance of the battery tends to be most sensitive to changes that impact electrochemical performance. Improvements in electrochemical performance tend to improve metrics such as current density during cycling, which can in turn allow for cell stacks with higher power densities and lower overall capital costs. A number of efforts have been made to improve the electrochemical performance of VRBs by improving the surface properties of the electrodes in a VRB. This has included a large body of work using carbon materials, such as adding various highly conductive carbons to graphite felts[10-19] and membranes[20-24], carbonizing electrodes via specific heat treatments, and synthesizing electrodes out of specially developed high surface area or heteroatom-doped carbon materials. Other work has been focused on decorating carbon materials with metal and metal oxide particles[25-44], either via heat treatments or through direct reduction of soluble salts. Some of the initial work in this area was first conducted using directly reduced Bi^{3+} particles in the anode of the VRB. Other work has tested direct reduction of different elements, but with little explanation as to why certain elements work better than others. The general requirements for this

methodology remain the same – the metal ion of the added salt must have a standard reduction potential between +1.00V and -0.26V, versus the Standard Hydrogen Electrode (SHE). To form a metal particle and play a role in the catalysis of the vanadium reduction reaction, the metal salt must be reduced to a solid form during the charging cycle of the VRB, but at a redox potential that is more positive than -0.26V.

The following work proposes a simple method of adding small masses of tin and copper salts to the anolyte of a VRB for the purpose of direct reduction of metal particles on the surface of graphite felt during charge cycles. Electrochemical enhancements are observed and examined from a materials based perspective, to better understand how and why this new method improves VRB performance.

3.2. Methods

3.2.1 Addition of $SnCl_2$ and $CuCl_2$ to the Electrolyte

Varying amounts of $SnCl_2$ were added to the anolyte of the discharged VRB (in the V(III)/V(IV) state). The amounts of salts tested equated to concentrations of 0.005 M, 0.01 M, 0.02 M, and 0.04M of $SnCl_2$, and concentrations of 0.005M, 0.01M, and 0.02M $CuCl_2$ in the anolyte. Both salts were observed to be readily soluble in the electrolyte.

3.2.2 Single-Cell Testing. The single cell setup consisted of the cell and two glass containers for electrolyte storage. Electrolyte was pumped through ¼" I.D. tubing to and from the flow cell (Tygon 2375 Ultra tubing, Watson-Marlow 323E Pump). Each side of the cell consisted of symmetric acrylic end plates with push-to-connect tube

fittings, a graphite current collector, a Viton gasket, a polypropylene flow frame, and an HDPE gasket. These components were separated by a Nafion 212 membrane (50 um thick). The total exposed area of the membrane and graphite current collector was a 5 cm by 3 cm rectangle, totaling 15 cm^2. Each side of the cell had a 2 mm space between the membrane and current collector, in which a piece of 3 mm thick porous graphite felt (PAN-based, AVCarb) was compressed for good electrical contact. The graphite felt was pretreated by heating in air for 10 hrs at 420C to improve wettability. The electrolyte used in all tests was 1M $VOSO_4$ (Alfa Aesar) in 4M H_2SO_4. The electrolyte volume used was 25 mL for the catholyte and anolyte, with a flow rate of 30 mL/min. Each container of electrolyte was purged of air prior to testing by flowing in a blanket of argon and sealing well. Current densities between 30 mA/cm^2 and 200 mA/cm^2 were explored. All single-cell cycling testing was carried out using a battery analyzer (3A/5V, MTI). Cycling involved charging and discharging repeatedly at a specified constant current density. The upper cutoff voltage was set at 1.7 V, the lower cutoff voltage was set at 0.8 V. Cycling tests were assessed by coulombic efficiency (CE), voltaic efficiency (VE), energy efficiency (EE), and discharge capacity. These metrics were defined as follows:

$$CE = \frac{Discharge\ Capacity}{Charge\ Capacity} \tag{1}$$

$$VE = \frac{Mid-Cycle\ Discharge\ Voltage}{Mid-Cycle\ Charge\ Voltage} \tag{2}$$

$$EE = CE + VE \quad (3)$$

These were plotted versus current density, which is a measure of the charge and discharge current of the test, divided by the surface area of the membrane. All of the tests discussed in this study used membranes that were 15 cm^2 in area.

3.2.3 Electrochemical Measurements. Electrolytes were assessed using Electrical Impedance Spectroscopy (EIS) testing to measure the changes in resistance in the cell both with and without the addition of $SnCl_2$ to the electrolyte. An electrolyte consisting of 4M H_2SO_4 and 1M $VOSO_4$ was used for all testing. An AC voltage of 1mV amplitude was used over a frequency range of 10^4 Hz to 10^{-3} Hz to generate Nyquist plots of the pristine and modified cases. Cyclic voltammetry (CV) was also performed on the electrolytes at a rate of 20 mV/s in a three-electrode glass cell, using the above-mentioned electrolyte. The reference electrode used was Ag/AgCl, the counter electrode used was a platinum wire. A 3.0 mm diameter circle of polished Glassy Carbon Electrode (GCE) was used as the working electrode. A potential range between -0.85 V and 1.4 V was explored.

3.2.4 Materials Characterization. The modified graphite felts were characterized using a variety of analytical techniques. Felts were optically inspected using SEM to observe any visual changes in the form of metal particles on their surfaces. EDX was used to confirm the existence of the metals of interest.

3.3. Results and Discussion

3.3.1 SEM Analysis of Directly Reduced Tin and Copper Salts

The purpose of this modification was to develop a simple, inexpensive method to temporarily attach nano-scale and micron-scale particles to the surface of graphite felt electrodes for use in an aqueous all-vanadium redox flow battery. The principle of direct reduction in VRBs has been previously explored by other researchers, but the metal salts which have been explored were limited at the time of testing. Tin and copper salts were investigated as they had not been previously studied at the time of experimentation, and they fit the selection criteria. The selection criteria first involved choosing metal salts that had standard reduction potentials that were within the voltage window of the VRB system, that is between -0.26V and 1.00V vs. the SHE. The principle of this scheme relies on the metal salt being reduced from its ionic form to its zero-state metallic form upon charging of the VRB. As the anode is exposed to increasingly negative potentials, the majority of the salt will plate in small particles on the surface of the graphite felt. Previous work has shown that this process can produce highly-active reaction sites upon which the anodic vanadium reaction can occur. Another important selection detail was the need for the salt to be highly soluble and stable in aqueous media and 4M sulfuric acid (the working electrolyte). If the salt was not soluble, the particles would likely fail to properly adhere to the surface of the felt, and would not contribute to the performance of the battery. The salts needed to be reasonably inexpensive for this process to be worthwhile. It was acknowledged that precious noble metals could potentially be used in this scheme, but the main thrust of this work is to decrease the overall cost of the RFB assembly. Many noble metals (Pt, Pd, Ru, etc.) also tend to be too effective when splitting water into H_2 and O_2 gasses in reducing or oxidizing environments, a problem which is of great concern in aqueous

RFBs. When the results of these screening criteria were combined, both copper and tin stood out as interesting candidates. Both metals are reasonably resistant to corrosion, are inexpensive, are highly electrically conductive, and exist in salt forms that are readily soluble in sulfuric acid. With this knowledge in mind, various concentrations of each salt ($SnCl_2$ and $CuCl_2$) were dissolved into the anolyte of a VRB. The VRBs were cycled, data was collected, and the felts were analyzed after cycling. SEM images of the Pristine and Air-treated graphite felts are shown in Figure 3.1.

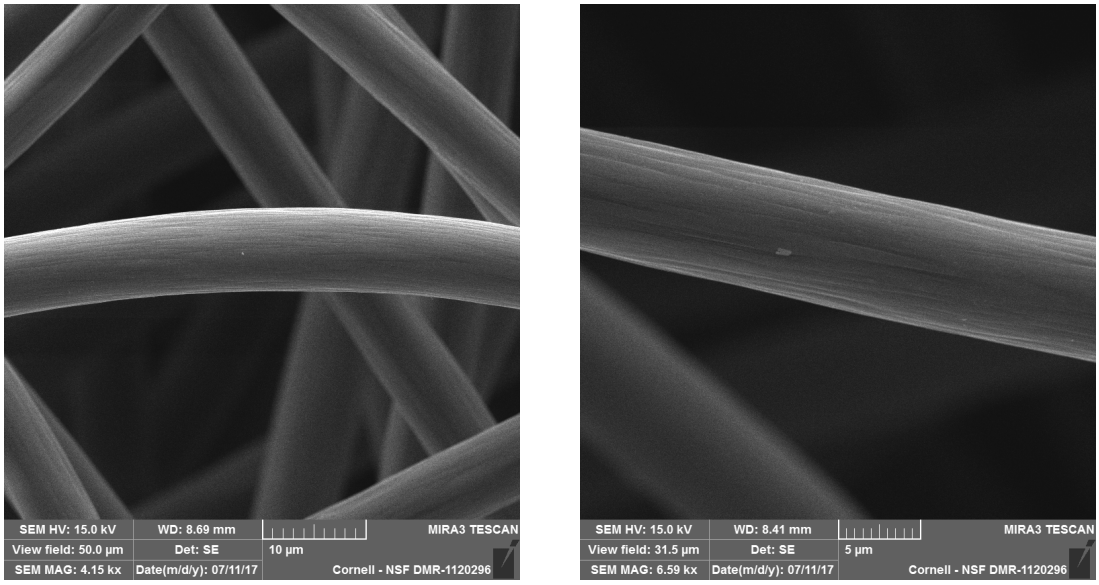

Figure 3.1. SEM of unmodified felts: Left: Pristine graphite felt; Right: Air-treated Graphite felt

It can be seen that the pristine felt is void of any obvious damage, the surface appearing smooth and unmodified. The Air-treated felt appears to have visible lines, parallel to the axial direction of each fiber, from which some material has been removed via thermal oxidation. This material is likely removed in the form of CO, CO_2 and N_2 gases from the degradation of the poly(acrylonitrile) polymer from which

the fibers were originally synthesized. This burn-off is designed to introduce an abundance of hydrophilic surface groups, which can act as reaction sites for the aforementioned vanadium redox reactions in both the anode and the cathode. It is important for the structural integrity of the fibers to be maintained after this process has been completed, as the electrical conductivity of the graphite felt network has an important impact on the overall performance of the battery. Based on the Air-Treated SEM image in Figure 3.1, this seems to be the case with this particular thermal treatment. SEM images of graphite felts modified with 0.005M concentrations of $SnCl_2$ salt are shown in Figure 3.2.

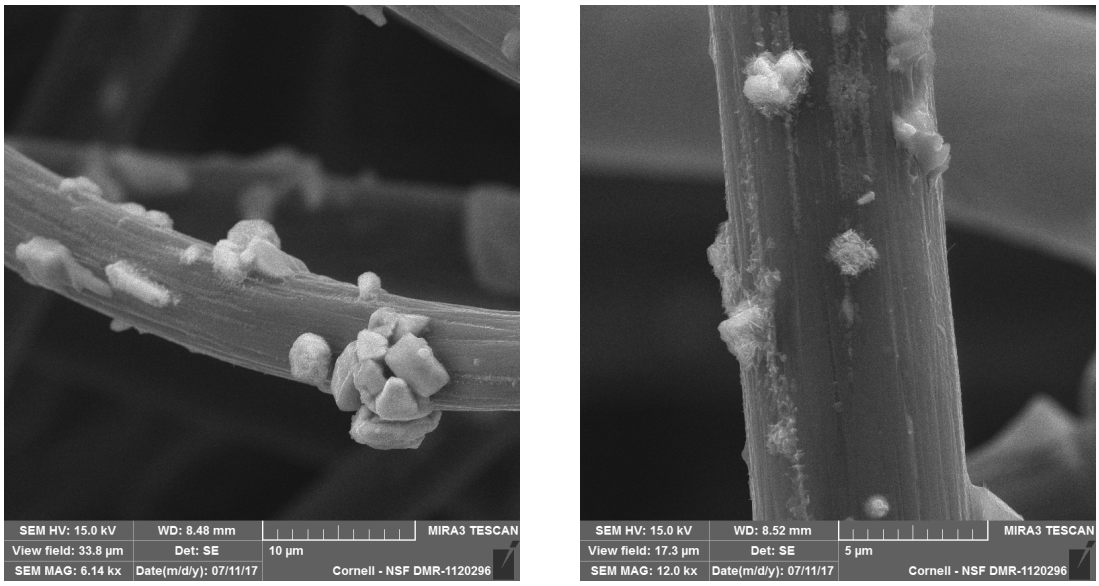

Figure 3.2. SEM images of graphite felts, modified by adding 0.005M concentrations of $SnCl_2$ to the anolyte before cycling. Images show felts after cycling analysis.

It is evident that the addition of $SnCl_2$ shows the formation of Sn crystals on the surface of the graphite felt. This process works because the reduction of $Sn^{2+}_{(aq)}$ to $Sn^{0}_{(s)}$ occurs at a potential of -0.13V compared to the SHE, whereas the reduction of

$V^{3+}_{(aq)}$ to $V^{2+}_{(aq)}$ occurs at -0.26V compared to the SHE. In theory, a majority of the small amount of tin in solution will reduce to the elemental form before the vanadium is reduced in solution. This creates the observed crystals, and enables their use as solid, electroactive metal catalysts. The crystals formed from the tin reduction process tend to be dispersed randomly, and in general seem to aggregate to sizes between 500 nm and 5 um. It is theorized that better controlled crystal formation could yield better performing anodes, as much of the interior of the observed tin crystals is likely not used for catalysis. A similar approach was taken using 0.005M $CuCl_2$ dissolved into the anolyte. SEM images of the cycled anodes are shown in Figure 3.3 and Figure 3.4.

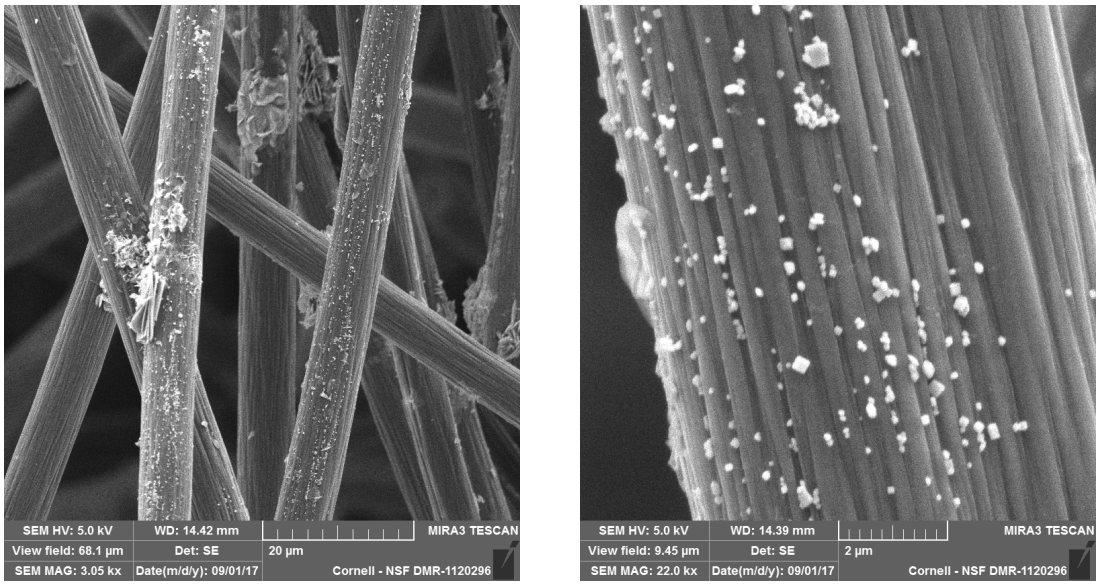

Figure 3.3. SEM images of VRB anodes with 0.005M $CuCl_2$ added to the anolyte

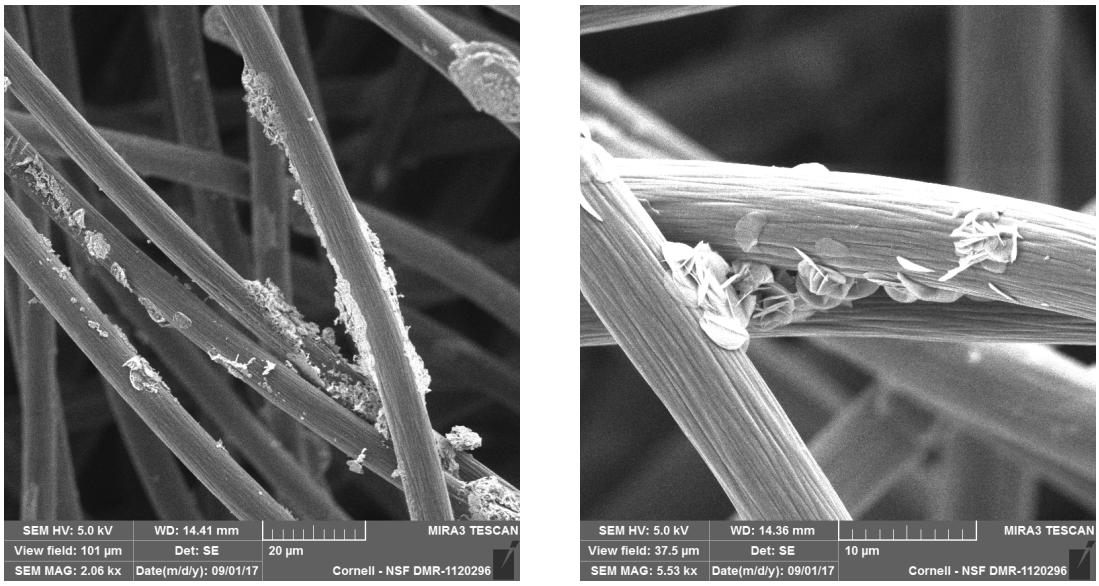

Figure 3.4. SEM images of VRB anodes with 0.005M $CuCl_2$ added to the anolyte

These images show distinctly different crystal structures when compared to the 0.005M $SnCl_2$ images. They show a combination of nanoscale block-like structures and flat disc-like structures. These crystals were scattered randomly throughout the sample. It was unclear why the crystals formed in the observed structures, as there are quite a few variables affecting their growth (salts concentration, local graphite felt environment, shear from electrolyte convection, incomplete redissolution upon discharge, etc.). Ideally, the individual contribution from these different crystals structures could be determined, however it was decided that this was outside the scope of this study. The interesting images in Figures 3.3 and 3.4 led to testing a higher concentration of $CuCl_2$ addition to the anolyte, in an effort to probe the effects on the performance of the battery and accompanying crystal formation. A concentration of 0.01M $CuCl_2$ was dissolved into the anolyte, and the resulting SEM images from the cycled battery are shown in Figure 3.5 and Figure 3.6.

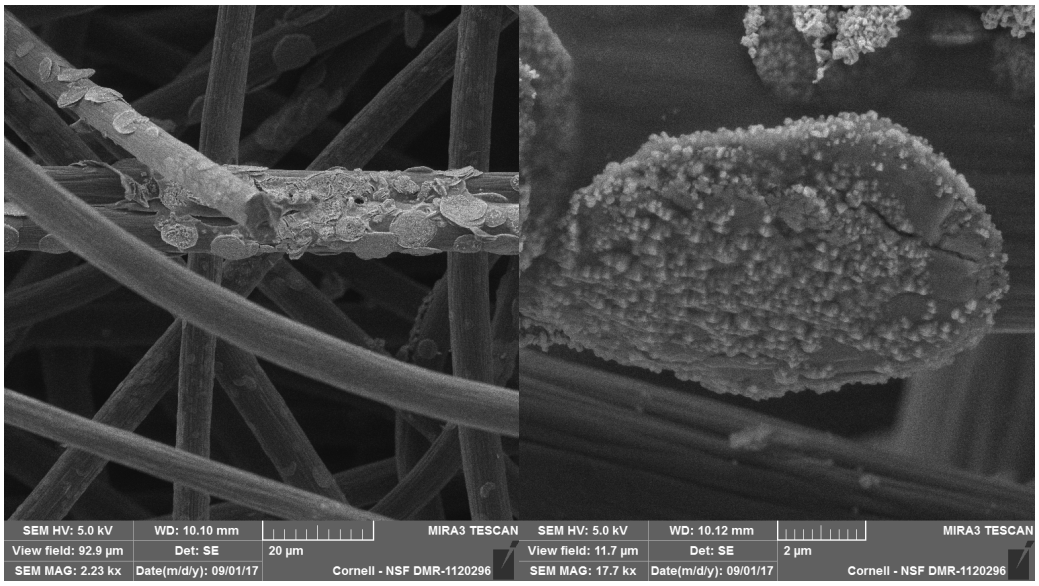

Figure 3.5. SEM images of VRB anodes with 0.01M $CuCl_2$ added to the anolyte

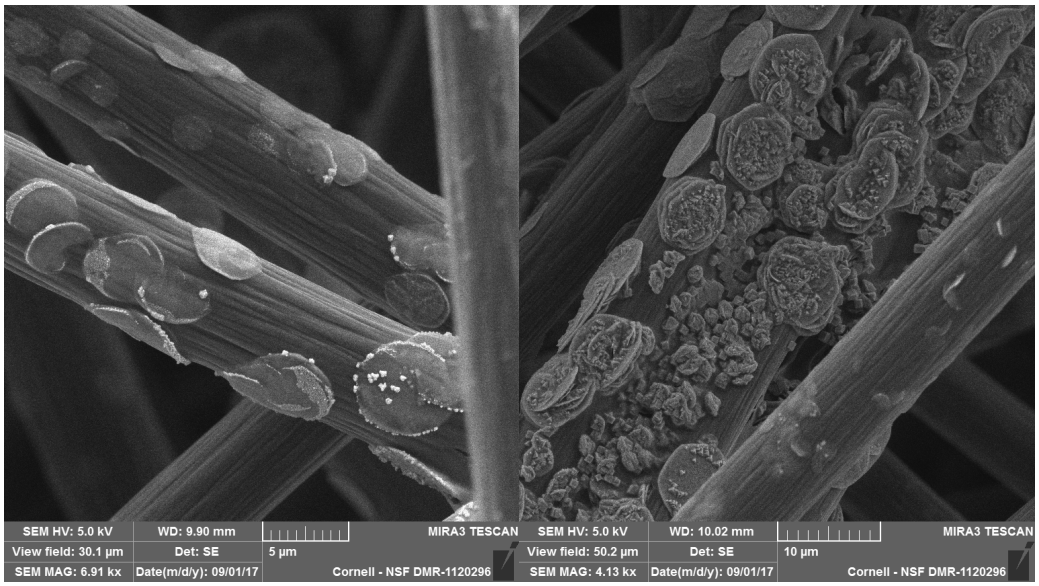

Figure 3.6. SEM images of VRB anodes with 0.01M $CuCl_2$ added to the anolyte

The images in these figures show a greater density of disc-like crystal structures formed upon the surface of the felt. Many of the discs show the beginning of nucleation of greater crystal growth on their surfaces. Regions in which individual

graphite felt fibers touch show the highest degree of crystal growth, indicating a locally low surface energy that is favorable to nucleation and growth of copper crystals. This observation leads to a broader conclusion – the use of anode templates that have a more uniformly ordered structure may lead to better distributed crystal growth. In general, it is acknowledged that smaller particles tend to be more active for catalysis than larger particles, as a greater fraction of their mass is on the surface and not obscured in the bulk of the particle. Better-ordered conductive templates, such as those from graphitized block copolymer monoliths or the like, could lead to better particle distribution and likely better overall performance of VRBs.

A bimetallic system was investigated in an effort to discover some synergistic effects related to crystal structure. The premise for this investigation stemmed from both battery cycling results and observations made from SEM imaging of the crystal structure. The optimal molar concentrations of the added salts (reported below) from a battery performance perspective were different. This was an interesting conclusion, as it indicated that there was more than total surface area at play in this system – the resulting crystal structure and elements making up said structure may play a larger role on the performance. This conclusion led to studies in which small concentrations of both $SnCl_2$ and $CuCl_2$ salts were dissolved into the anolyte of the VRB. The first study tested concentrations of 0.005M $SnCl_2$ and 0.005M $CuCl_2$. The SEM images from the cycled anode from this study are shown in Figure 3.7 and Figure 3.8.

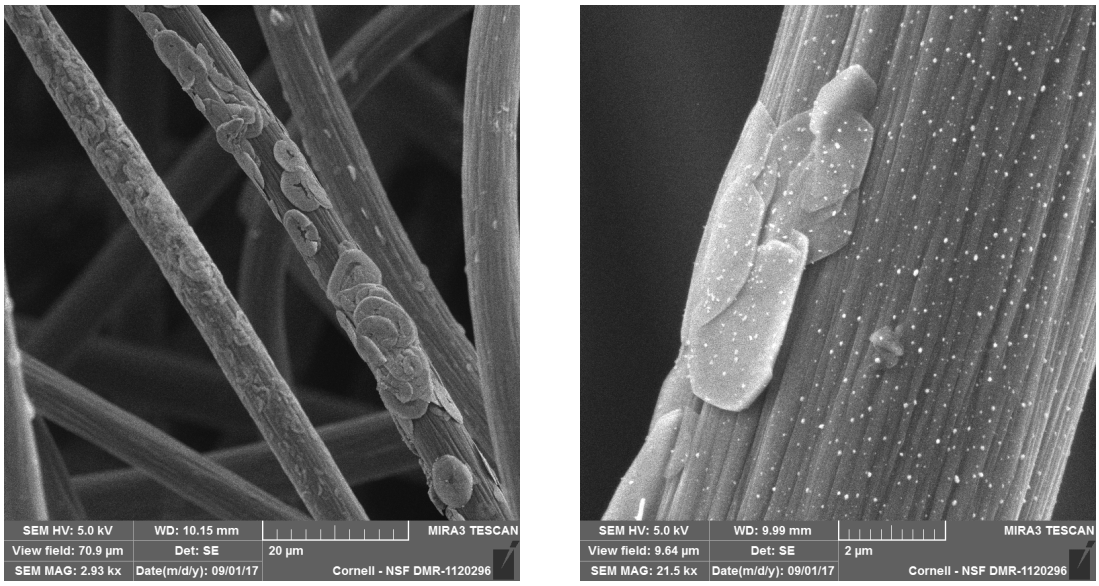

Figure 3.7. SEM images of VRB anodes with 0.005M $CuCl_2$ and 0.005M $SnCl_2$ added to the anolyte

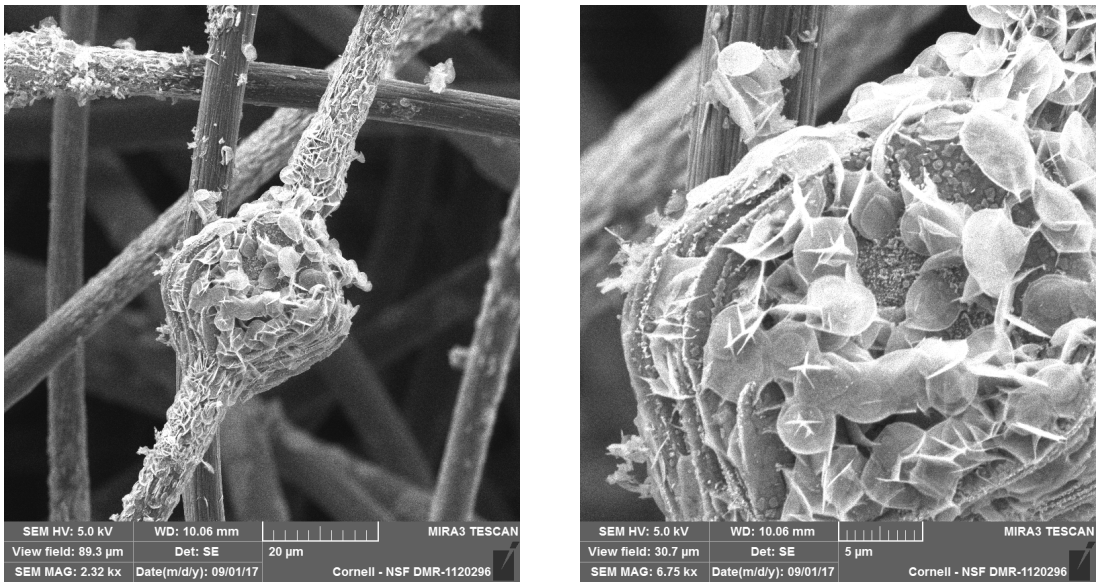

Figure 3.8. SEM images of VRB anodes with 0.005M $CuCl_2$ and 0.005M $SnCl_2$ added to the anolyte

These images show some of the characteristic features observed in the single element studies, although they are closer to resembling the copper images than the tin images. Both disc-like crystal structures and nanoscale crystals are observed, intermingling

together. It is expected that the metal that is closest to the surface of the felt will be copper, as the standard reduction potential of the Cu^{2+} ion is less negative compared to that of the Sn^{2+} ion. However, hybrid particles could still be formed due to non-idealities in the system, such as locally high or low surface energies, mass transport effects, etc. An additional test was conducted using the same concentration of $CuCl_2$ (0.005M), but a higher concentration of $SnCl_2$ (0.02M). The SEM images from this cycled felt are shown in Figure 3.9 and Figure 3.10.

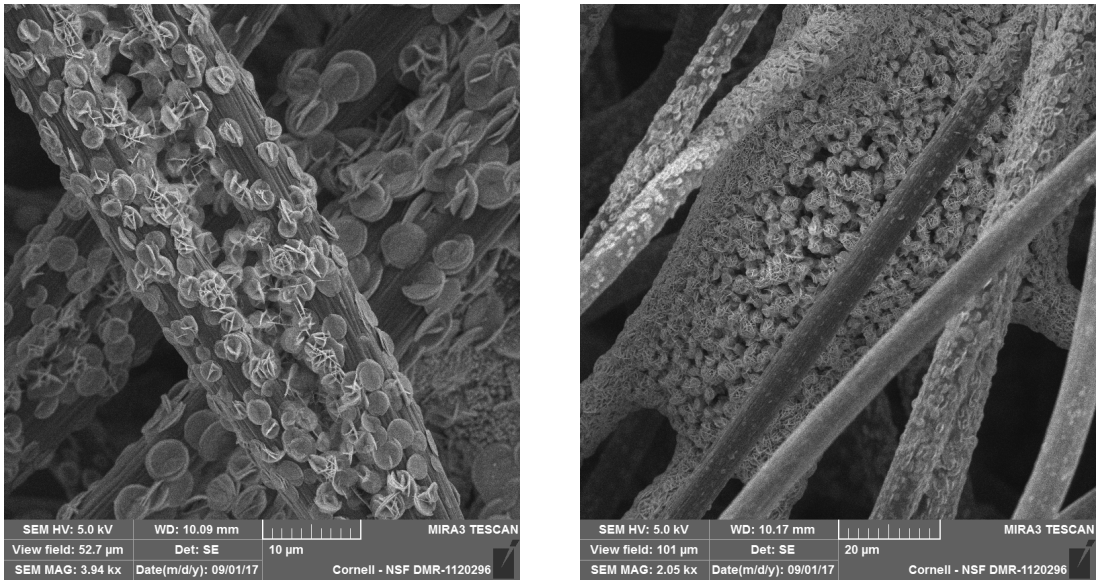

Figure 3.9. SEM images of VRB anodes with 0.005M $CuCl_2$ and 0.02M $SnCl_2$ added to the anolyte

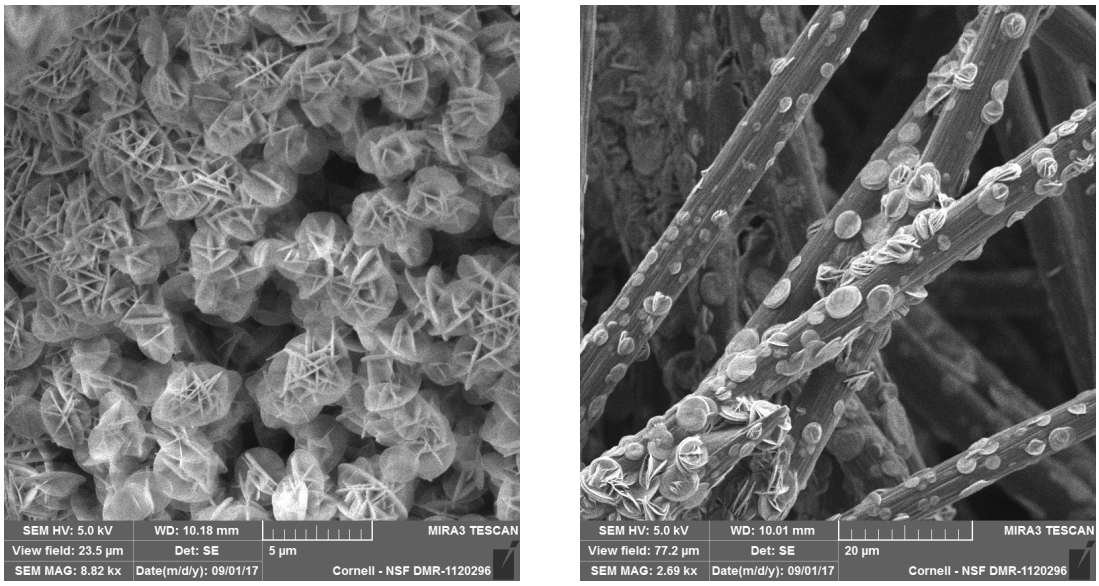

Figure 3.10. SEM images of VRB anodes with 0.005M $CuCl_2$ and 0.02M $SnCl_2$ added to the anolyte

It is evident that the dominant crystal structure in these tests has shifted to primarily the disc-like structure. The crystals are distributed broadly and seem to easily grow adjacent to one another. The corresponding performances of all of these tests are shown in the "Single Cell Testing" part of this report.

3.3.2 SEM Analysis of Tin and Copper Particles Synthesized Using Different Treatments

Tin and copper salts were thermally treated in an effort to compare the resulting morphology of crystals with the directly reduced salts. About ~1g of graphite felt was soaked in a 0.01M aquoues solution of copper (II) acetate for 1 hour, after which it was heat treated at 400C for 2 hours under flowing N_2 gas. The purpose of this treatment was to introduce an inert atmosphere, allowing for the reduction of the

copper (II) acetate to copper metal. The resulting SEM images are shown in Figure 3.11.

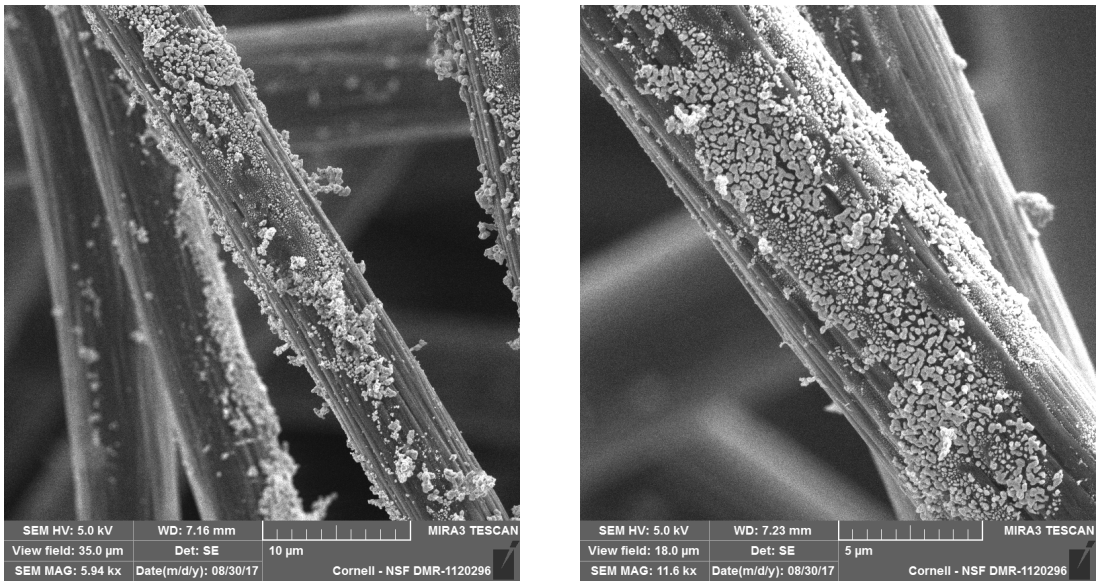

Figure 3.11. SEM images of 0.01M CuAc, after heat treatment under flowing N_2 at 400C for 2 hours.

The morphology of the copper particles formed from this method is distinctly different than those formed from direct reduction. The disc-like structures from the direct reduction studies do not appear, in their place are a series of submicron-sized particles, found in clusters on the surface of the felt. These particles seem to be less strongly attached to the surface of the felt when compared to the directly reduced case. The small particle size is likely a result of the rapid evaporation of solvent and subsequent reduction of salt during the heat treatment process. A similar approach was taken with tin (II) acetate. Graphite felt was soaked in a solution of 0.01M tin acetate for 1 hour, then heat-treated under flowing N_2 at 400C for 2 hours. The resulting SEM images are shown in Figure 3.12.

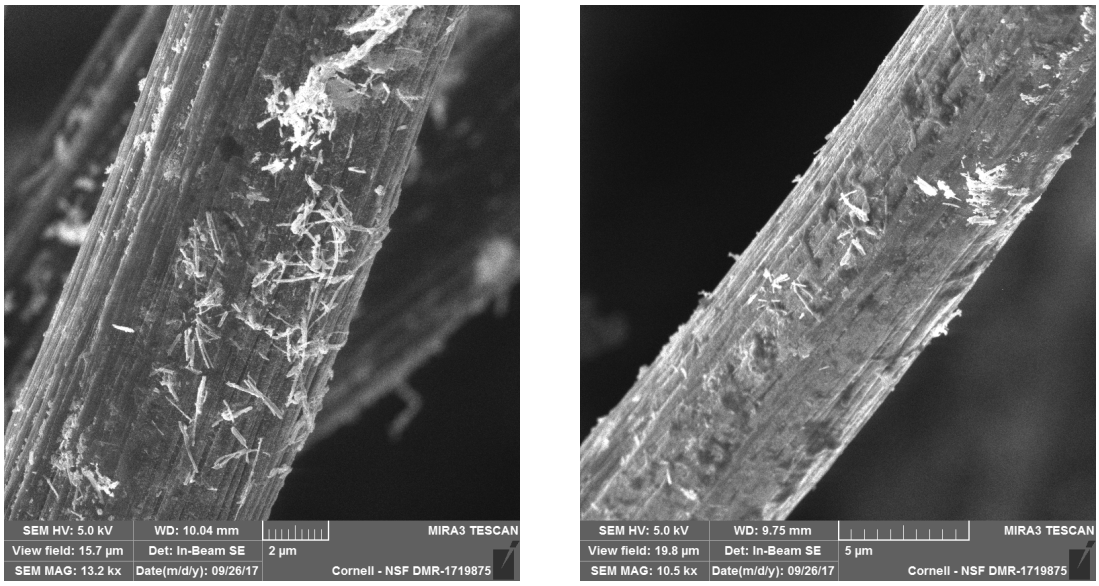

Figure 3.12. SEM images of 0.01M SnAc, after heat treatment under flowing N_2 at 400C for 2 hours.

The morphology of the formed crystals is again very different from that formed by the direct reduction method. The surface of the felt looks visibly smoother, with some micron-sized crystals on the surface. This is likely due to the fact that the melting point of tin is about 232C, and the heat treatment used was at 400C. Any formed tin crystals likely partially melted and spread along the surface of the graphite felt, greatly lowering the surface area of both the felt and the formed tin crystals. This observation does give some information about the heat treatment process – it likely indicates that the heat treatment does indeed fully reduce the acetate forms of the salts to their metallic states, instead of simply drying the solvent or forming oxide forms of the salts.

Great improvements in the performance of the VRBs were realized from the use of directly reduced copper salts (see "Single Cell Testing" section), so addition of copper

to the system was attempted by using less conventional means. A small amount of copper mesh was added to the anode of a VRB and cycled, in an effort to introduce a simple copper source. The battery performed poorly, and SEM imaging of the resulting felt (see Figure 3.13 and Figure 3.14) showed that the felt was nearly completely covered with either copper or copper oxide.

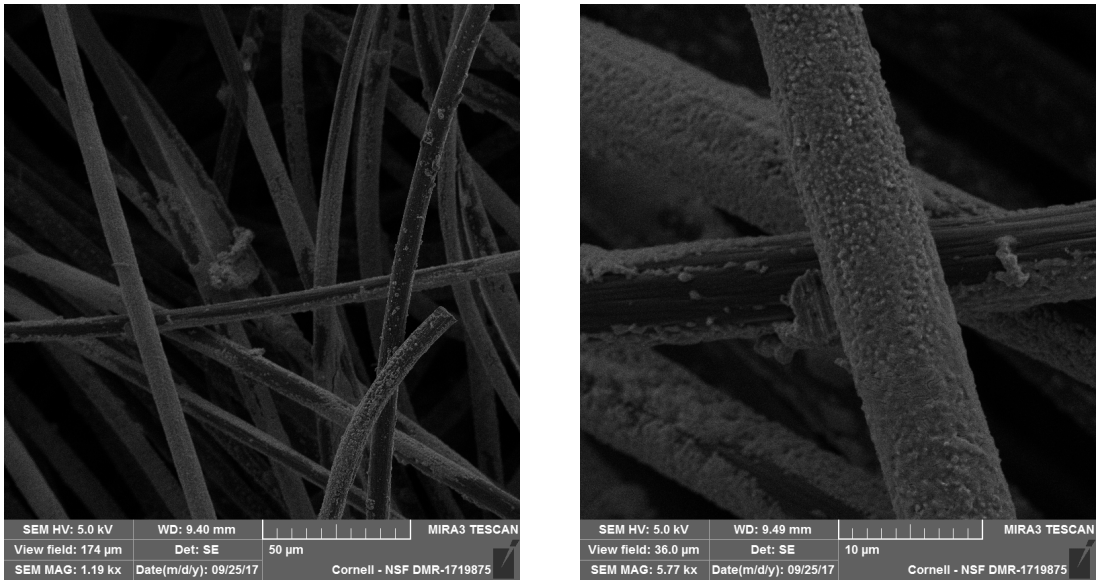

Figure 3.13. SEM images of graphite felt from anode after cycling from test using addition of 0.1g copper mesh

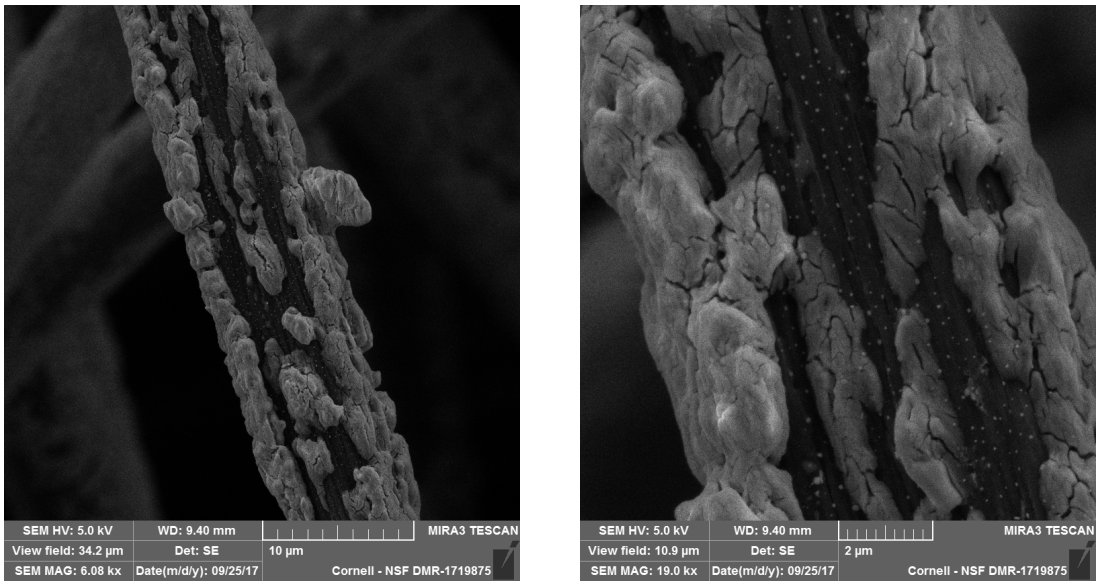

Figure 3.14. SEM images of graphite felt from anode after cycling from test using addition of 0.1g copper mesh

It is evident from this result that nearly complete coverage of the anode in electroactive material is undesirable for battery performance. Much of the copper formed a bulky and likely impermeable layer of the surface of the felt from excessive reduction of copper ions, which likely increased the internal resistance of the battery.

3.3.3 SEM Analysis of the Impact of Directly Reduced Tin and Copper Salts on the Ion-Exchange Membrane

Throughout the course of this testing, it was noticed that the addition of small amounts of tin and copper salts was affecting the ion-exchange membrane. The membranes used in this testing were Nafion 212 membranes, part of a family of perfluorinated-sulfonated cation exchange membranes. Initial observations occurred when disassembling the batteries to which the metal salts were added – the membranes had very small color changes compared to previous tests. To study this, the membranes

were removed from the batteries, dried, and observed using SEM. Images from a membrane from one of the tests using 0.005M $CuCl_2$ in the anolyte is shown in Figure 3.15 and Figure 3.16.

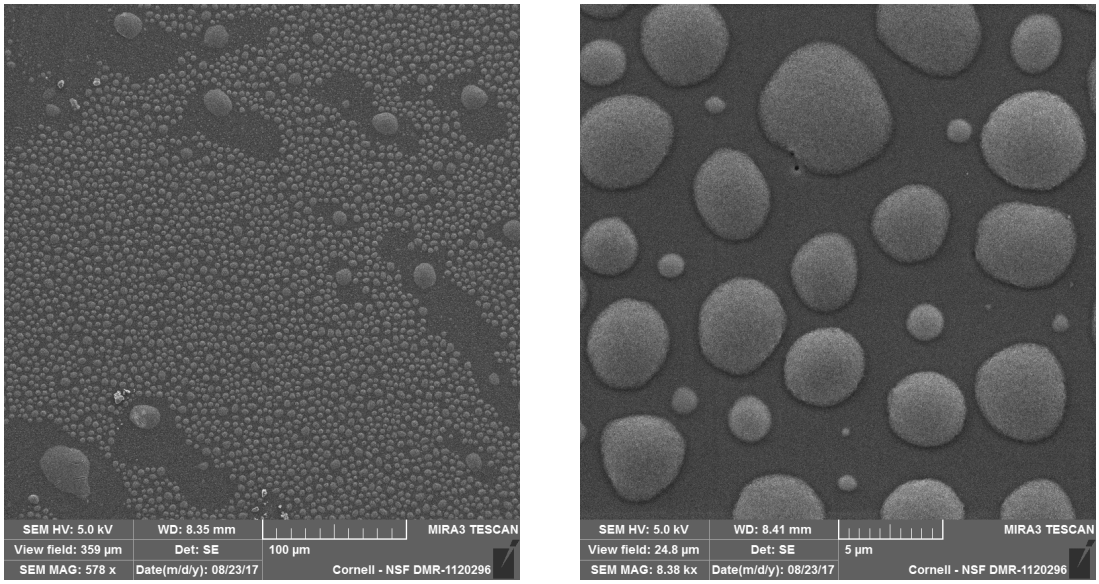

Figure 3.15. SEM images of anode side of Nafion 212 membrane from test where 0.005M $CuCl_2$ was added to the anolyte.

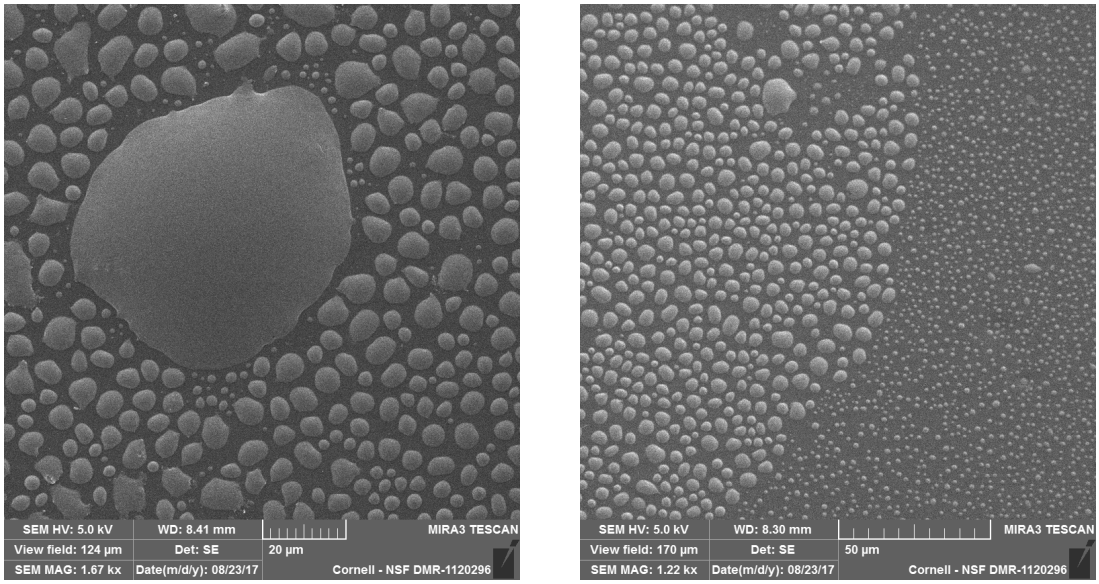

Figure 3.16. SEM images of anode side of Nafion 212 membrane from test where 0.005M $CuCl_2$ was added to the anolyte.

These images all show a series of smooth, circular regions on the surface of the membrane. These are believed to be metallic copper, which has been directly reduced onto the surface of the membrane instead of the graphite felt. Some of these regions have coalesced into larger metallic structures. This is expected, as the reducing potential in the anode of the battery is impose on anything in contact with the electrode. During the construction of the battery, the membrane is pressed firmly against the surface of the electrodes in order to reduce internal resistances. Hence, this is an inevitable outcome of this modification. This is not a desirable outcome, however, as any solid that even temporarily blocks any part of the membrane limits the flux of protons through the Nafion, and in turn limits the achievable current densities of the battery. This could also pose longer-term negative effects, as it is unclear as to how easily these regions are removed upon oxidation (discharging the battery). In an effort to mitigate the effects of this phenomenon, a 0.10 mL spray of a 5% CNT solution in water was sprayed onto the surface of the membrane, which was covered by a mash mask in order to create regions of covered and uncovered surface. The theory was that the specific regions of covered surface could act as growth templates for the copper metal, and the growth could potentially be guided into these regions and away from the majority of the membrane. The resulting SEM images from this study are shown in Figure 3.17 and Figure 3.18.

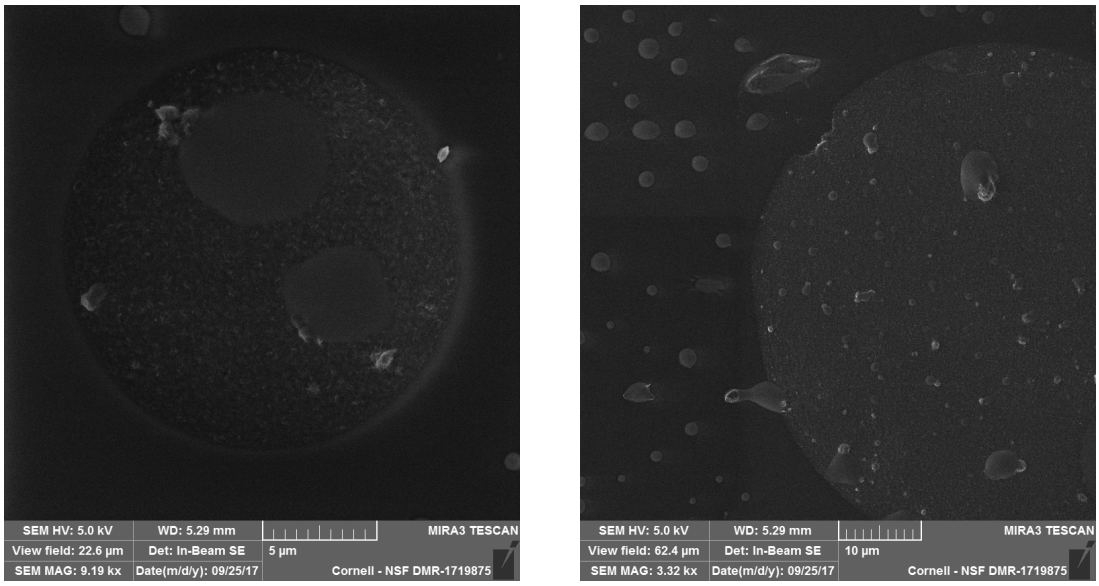

Figure 3.17. SEM images of anode side of Nafion 212 membrane from test where 0.005M $CuCl_2$ was added to the anolyte, and a CNT-based spray was used to help template the membrane.

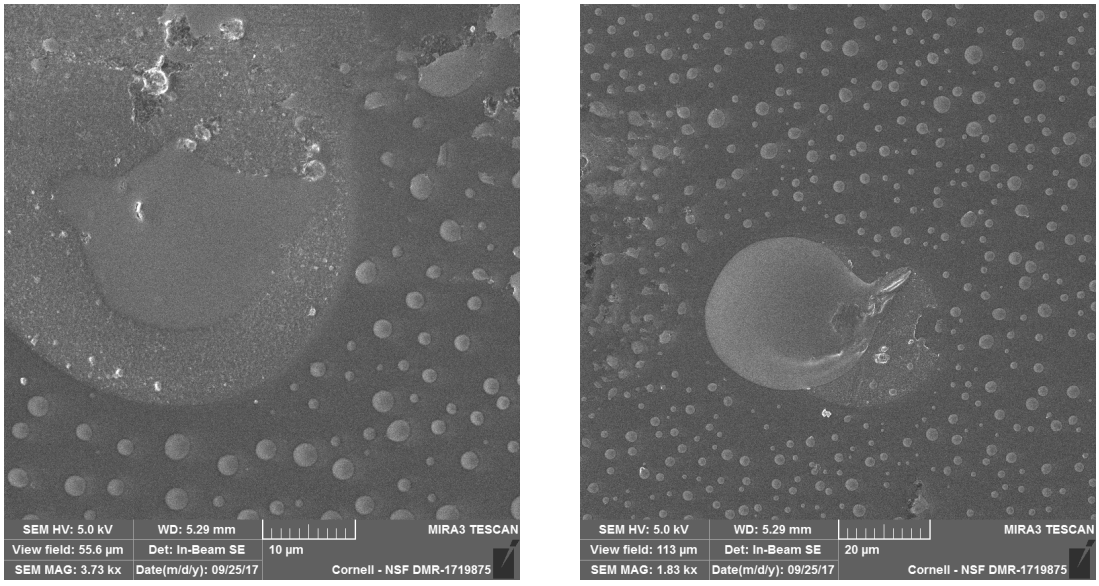

Figure 3.18. SEM images of anode side of Nafion 212 membrane from test where 0.005M $CuCl_2$ was added to the anolyte, and a CNT-based spray was used to help template the membrane.

After analysis using SEM, it is clear that some of the reduced metal ends up covering the CNT-coated surfaces of the Nafion membrane. However, the reduced copper still

seems to cover other parts of the membrane surface with nearly as much potency as was seen without the CNT treatment. This method seems ineffective at addressing this issue, although this issue is still worth considering using other means.

3.3.4 Electrochemical Testing Results – Direct Reduction of Tin

Each of the aforementioned direct reduction schemes was tested using both cyclic voltammetry and electrical impedance spectroscopy to help quantify the impact of the additives. Figure 3.19 shows the proof-of-concept CV curves for adding $SnCl_2$ to the anolyte of the VRB.

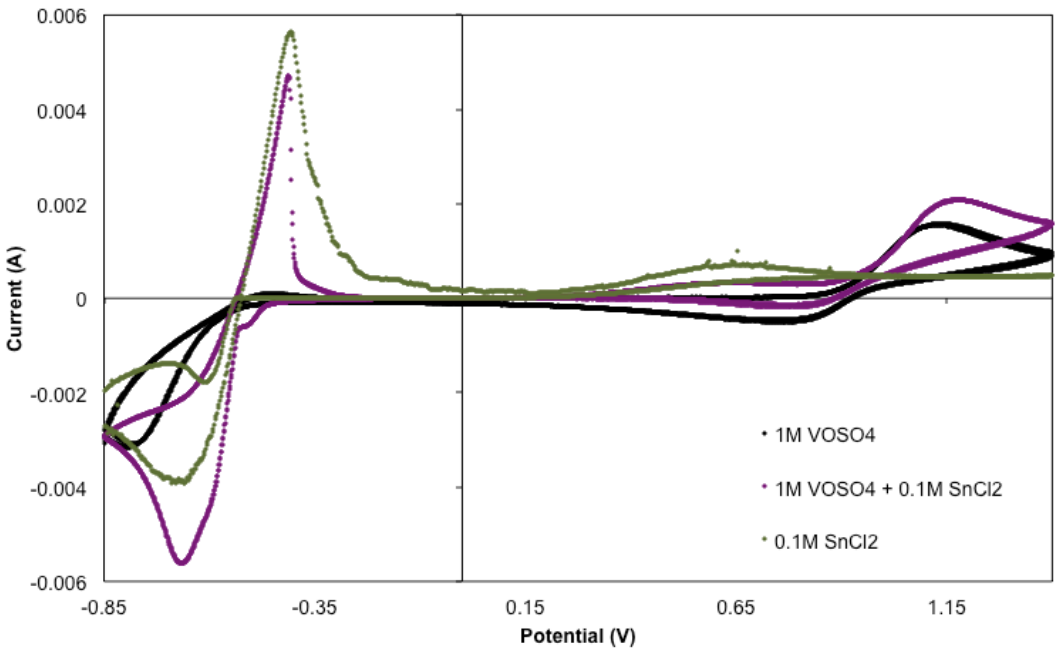

Figure 3.19. CV curves of the unmodified VRB electrolyte, the VRB electrolyte with 0.1M $SnCl_2$ added, and of only 0.1M $SnCl_2$ dissolved in 4M H_2SO_4. (Scan rate: 20 mV/s, vs. Ag/AgCl reference electrode)

The anodic reaction occurs at about -0.80V (reduction, V^{3+} to V^{2+}) and -0.45V (oxidation, V^{2+} to V^{3+}) in the unmodified electrolyte. The peak height of the oxidation

reaction is minimal, and difficult to measure. When 0.1M $SnCl_2$ alone is dissolved into the same supporting acid (4M H_2SO_4), the resulting CV curve shows Sn^{2+} reduction occurs at about -0.69V and the subsequent oxidation back to Sn^0 occurs at about -0.41V. There is no observed cathodic peak (in the positive region) from the $SnCl_2$ only test, as there is no vanadium in the system. When the same concentration of $SnCl_2$ was dissolved into the vanadium-based electrolyte, a few interesting changes were noted in the CV curve. First, the maximum negative current from the reduction peak of the potential sweep was much greater in magnitude than the either the vanadium or tin cases individually. This is partially due to the fact that this reduction peak is now a convoluted peak of both Sn^{2+} reduction and V^{3+} reduction. More importantly, the maximum peak potential shifts slightly to the right of the original tin peak, and far to the right of the original vanadium peak, likely indicating that the overpotential of the vanadium reduction reaction has been greatly reduced. Decreasing the overpotential of this reaction is an important indicator that the overall performance of the battery will be improved. The kinetics of the vanadium reduction have likely been improved by the plating of the tin on the surface of the working electrode. In order to move from this proof-of-concept study to more realistic concentrations, another set of CV tests were conducted, this time investigating concentrations of 0.005M, 0.01M, and 0.02M $SnCl_2$ dissolved in 1M $VOSO_4$ and 4M H_2SO_4. These curves are shown in Figure 3.20.

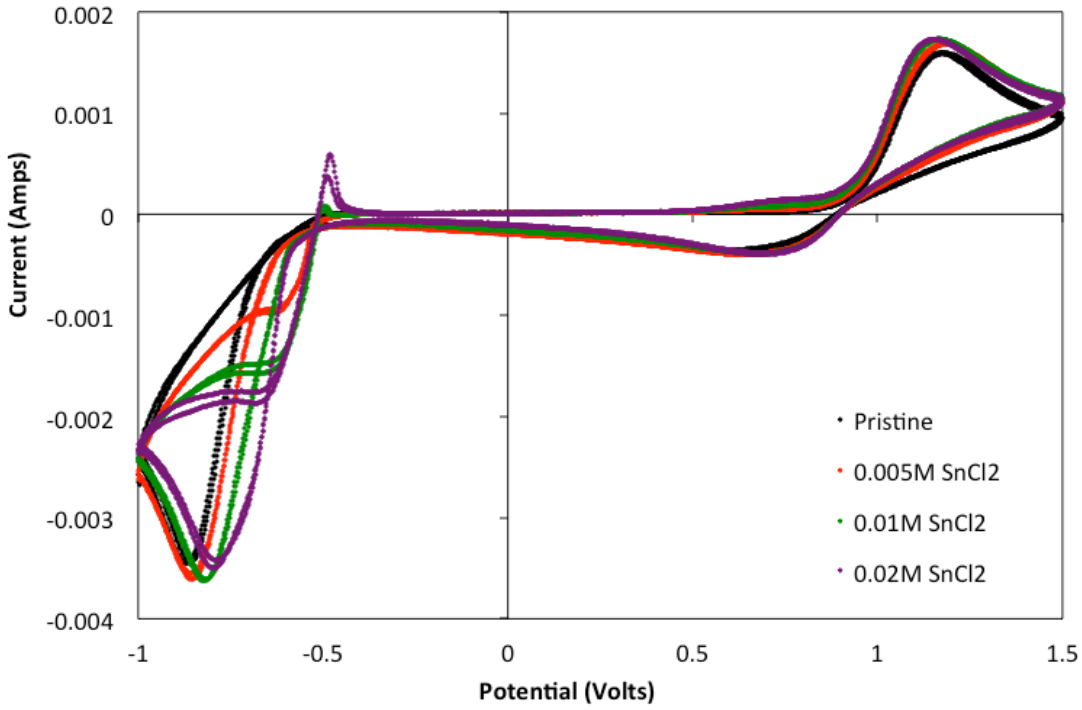

Figure 3.20. CV curves of the electrolytes consisting of 0.005M, 0.01M, and 0.02M $SnCl_2$ dissolved in 1M $VOSO_4$ and 4M H_2SO_4. (Scan rate: 20 mV/s, vs. Ag/AgCl reference electrode)

The data shown in Figure 3.20 demonstrate that in the tested range of 0.005M to 0.02M $SnCl_2$, the addition of 0.02M $SnCl_2$ shows the greatest improvement on the performance of the VRB. The anodic reduction peak shifts from the unmodified position of -0.85V to progressively less negative potentials with the inclusion of addition tin salt, indicating a drop in the overpotential of the reaction. The cathodic peak is mostly unchanged, as expected, as the $SnCl_2$ will how redissolved into the electrolyte as the potential is swept through increasingly positive potentials. These results suggest that $SnCl_2$ can be added to the VRB to improve performance. In order to further probe these effects, EIS testing was conducted on the 0.005M $SnCl_2$ case to

see the impact on the internal resistances of the cell. The results are shown in Figure 3.21.

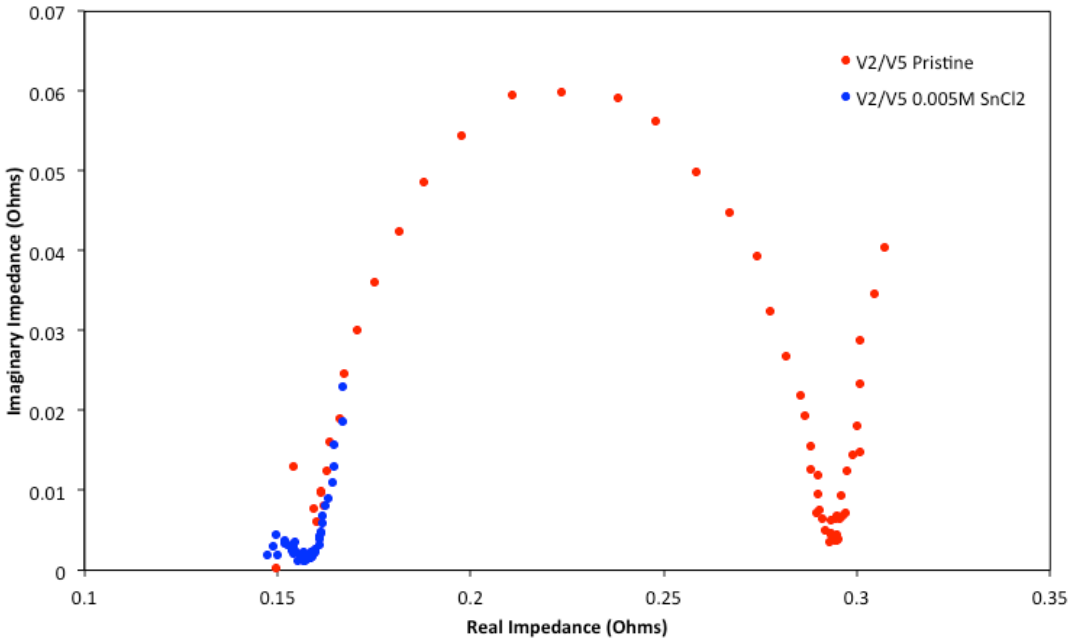

Figure 3.21. Electrical Impedance Spectroscopy of the unmodified (pristine) vanadium electrolyte and vanadium electrolyte with 0.005M $SnCl_2$ added. (AC Voltage: 1mV, Frequency range: 10^4 Hz to 10^{-2} Hz)

The results from EIS testing show that the ohmic resistance in the cell is nearly the same for both of the cases, and is estimated to be about 0.15 Ohms. This is expected, as this represents a lumped term for all of the internal resistances in the cell. The charge transfer resistance, however, is very clearly different for the two cases. The charge transfer resistance for the pristine case is about 0.15 Ohms, while it is closer to 0.01 Ohms for the case with $SnCl_2$ added. This indicates a much lower resistance to charge transfer as a result of the addition of $SnCl_2$.

3.3.5 Electrochemical Testing Results – Direct Reduction of Copper

A similar procedure was used to investigate the use of $CuCl_2$ salt in the anolyte of the VRB. CV testing was conducted on the VRB electrolyte, a solution of 0.1M $CuCl_2$ dissolved into 4M H_2SO_4, and 0.1M $CuCl_2$ dissolved into the VRB electrolyte. The results are shown in Figure 3.22.

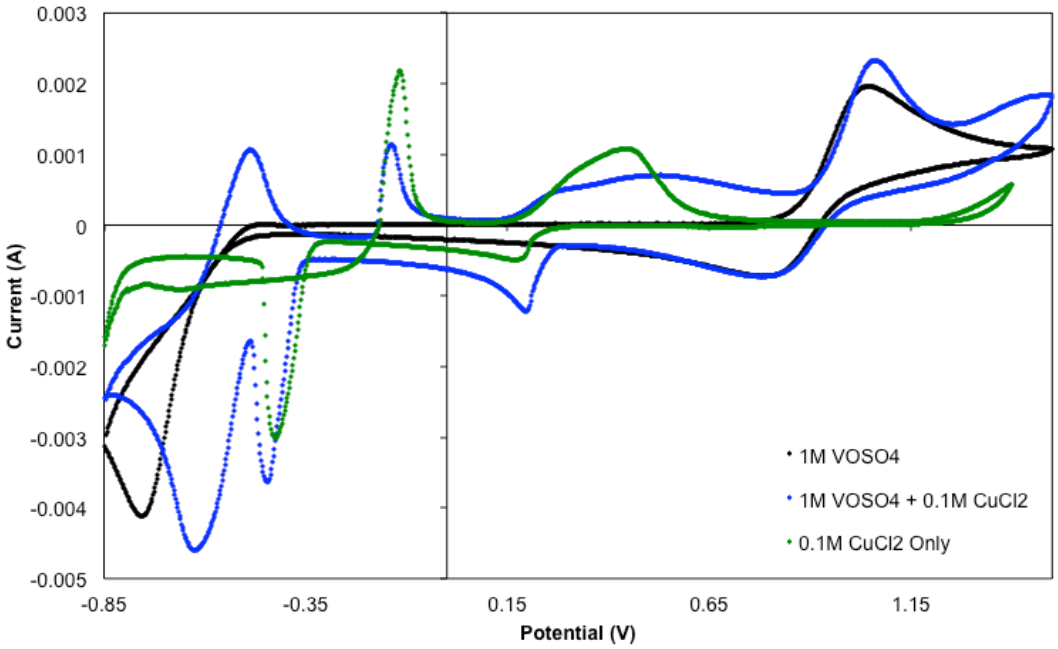

Figure 3.22. CV curves of the unmodified VRB electrolyte, the VRB electrolyte with 0.1M $CuCl_2$ added, and of only 0.1M $CuCl_2$ dissolved in 4M H_2SO_4. (Scan rate: 20 mV/s, vs. Ag/AgCl reference electrode)

It is evident that the $CuCl_2$ greatly improves the kinetics of the anodic reaction, as shown by the large shift in the overpotential. The unmodified electrolyte has an anodic reduction peak at about -0.75V, this peak shifts to nearly -0.60V upon the addition of 0.1M $CuCl_2$. There is also a much more prominent oxidation peak associated with the anodic reaction, as seen at about -0.50V. This indicates a large improvement in the kinetics of the oxidation of V^{2+} to V^{3+} as compared to the unmodified electrolyte. There are two sets of oxidation and reduction peaks from the $CuCl_2$, which occur due

to the $Cu^{2+} \Leftrightarrow Cu^{+}$ reaction, and the $Cu^{2+} \Leftrightarrow Cu^{0}$ reaction. The peaks from the vanadium reaction are still apparent. The cathodic peak (+1.05V) seems to increase with the addition of the $CuCl_2$; this may be a contribution from some of the $CuCl_2$ not fully redissolving into the electrolyte upon oxidation. CV curves of more realistic concentration of $CuCl_2$ were collected, including 0.005M, 0.01M, and 0.02M $CuCl_2$. These data are presented in Figure 3.23.

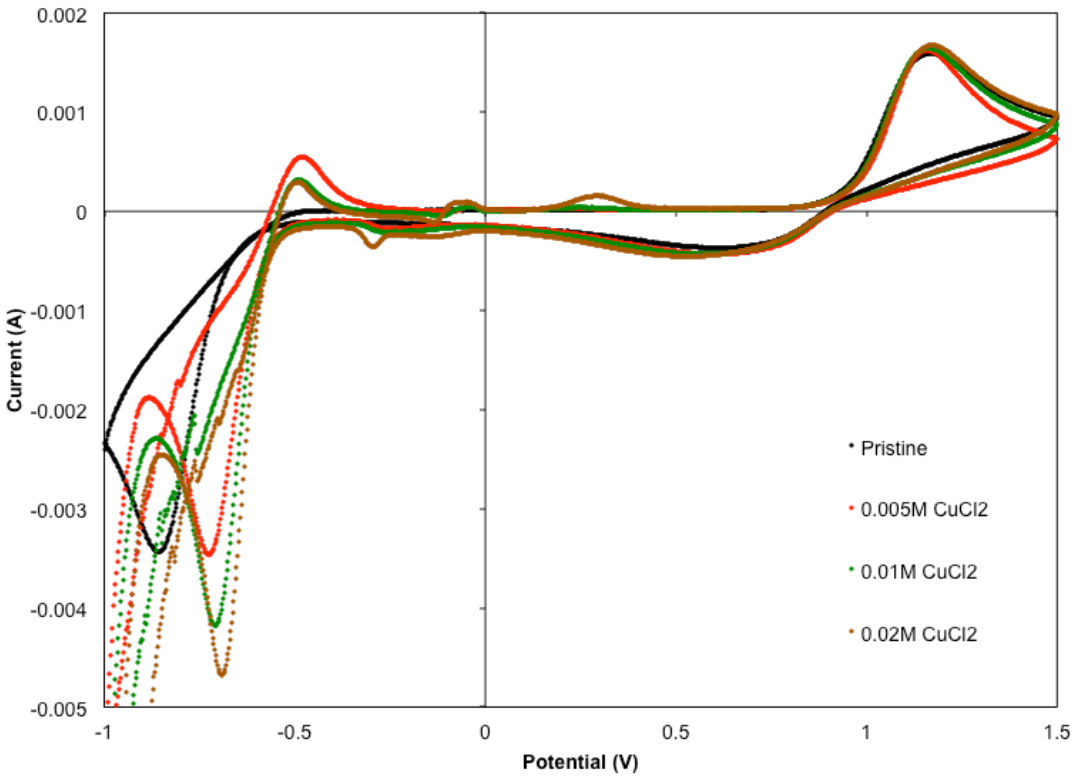

Figure 3.23. CV curves of the electrolytes consisting of 0.005M, 0.01M, and 0.02M $CuCl_2$ dissolved in 1M $VOSO_4$ and 4M H_2SO_4. (Scan rate: 20 mV/s, vs. Ag/AgCl reference electrode)

The impact of the $CuCl_2$ on the vanadium anodic reaction differs slightly from the $SnCl_2$ case. The trend of the reduction part of the anodic reaction is as expected – as more $CuCl_2$ is added, the peak height increases and the peak potential shifts to the

right, indicating a drop in the overpotential of the reaction. However, the oxidation part of the anodic reaction shows a different trend – the peak height of the 0.005M $CuCl_2$ case is the highest, compared to the cases with additional $CuCl_2$ this may indicate that the lowest concentration of $CuCl_2$ tested may allow for the best reversibility of vanadium redox reaction, which is indicative of better overall VRB performance. The peak from the reduction part of the anodic reaction seems to indicate that additional $CuCl_2$ increases the current from the reduction reaction. It is possible for both of these phenomena to be occurring simultaneously, although their holistic impact will be convoluted in the overall performance of the battery. The lower concentrations of $CuCl_2$ tested do not seem to have any impact on the cathodic reaction.

3.3.6 Electrochemical Testing Results – Direct Reduction of Hybrid System of Tin and Copper

A hybrid of these two approaches was tested by adding equilmolar amounts of both salts to a dilute version of the vanadium electrolyte. The purpose of this test was to explore whether any synergistic effects could be realized by including salts of both elements. In theory, the copper should reduce before the tin, which should both be in a fully reduced form before the vanadium reduction occurs. The CV curves from this study are shown in Figure 3.24.

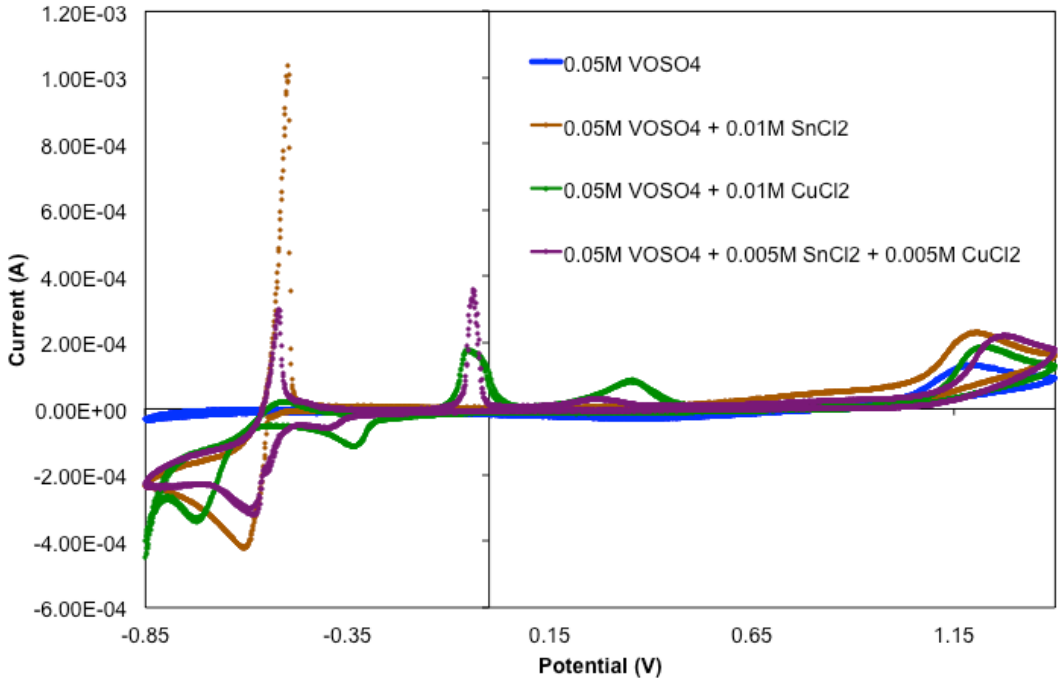

Figure 3.24. CV curves of the electrolytes consisting of 0.05M $VOSO_4$ in 4M H_2SO_4, 0.01M $SnCl_2$ + 0.05M $VOSO_4$ in 4M H_2SO_4, 0.01M $CuCl_2$ + 0.05M $VOSO_4$ in 4M H_2SO_4, 0.005M $CuCl_2$ + 0.005M $SnCl_2$ + 0.05M $VOSO_4$ in 4M H_2SO_4. (Scan rate: 20 mV/s, vs. Ag/AgCl reference electrode)

The data from CV testing indicate that a hybrid system of $SnCl_2$ and $CuCl_2$ should be an effective additive system to the VRB electrolyte. This is shown in the large shift in peak potential in the anodic reaction. The analysis of the hybrid system is somewhat less trivial than the single salt systems, as the tin reduction peak occurs very close to the vanadium reduction peak, nearly obscuring it. A careful examination of the peaks shows that the reduction of tin occurs at about -0.55V, whereas the reduction of vanadium occurs at about -0.58V. There is a small shoulder on the larger peak where these data are observed. While the potential of the hybrid peak has shifted to the right from the pristine and copper only cases, the height of the peak has also dropped slightly, indicating a limitation on the corresponding current generated from the

vanadium reduction reaction. The oxidation peak of the anodic reaction is convoluted in the oxidation peak from the tin oxidation reaction, and the magnitude of the impact on the vanadium reaction is difficult to discern. The overarching message from these data is that a hybrid system may improve the kinetics, although potentially lower the overall capacity of a VRB.

3.3.7 Single Cell Testing Results – Direct Reduction of Tin

A series of small amounts of $SnCl_2$ were dissolved into the vanadium electrolyte to make solutions of concentrations 0.005M, 0.01M, 0.02M, and 0.04M $SnCl_2$. Under normal circumstances, the VRB goes through a two-step process to begin cycling. The first step involves starting with equal volumes of 1M $VOSO_4$ dissolved in 4M H_2SO_4 as the anolyte and catholyte. Both the anolyte and catholyte consist of vanadium in the V^{4+} state. The battery is then cycled under constant current conditions (at the low current density of 30 mA/cm^2) to convert the V^{4+} in the anode to V^{3+}, and the V^{4+} in the cathode to V^{5+}. The V^{5+} in the cathode is then removed and replaced with a equal volume of V^{4+}, and normal charging and discharging can commence. This is one approach to ensuring the battery has V^{2+} in the anode and V^{5+} in the cathode when it is fully charged. The tin salt additives were added *after* the initial charge step, after removal and replacement of the catholyte had occurred. The tests using the various concentrations of $SnCl_2$ were analyzed using Colombic Efficiency, Voltaic Efficiency, Energy Efficiency, and Discharge Capacity as evaluation metrics. The plots showing these data are in Figure 3.25, Figure 3.26, Figure 3.27, and Figure 3.28, respectively.

Each data point shown for the various efficiencies represents the average of five cycles at the given current density, for purposes of clarity.

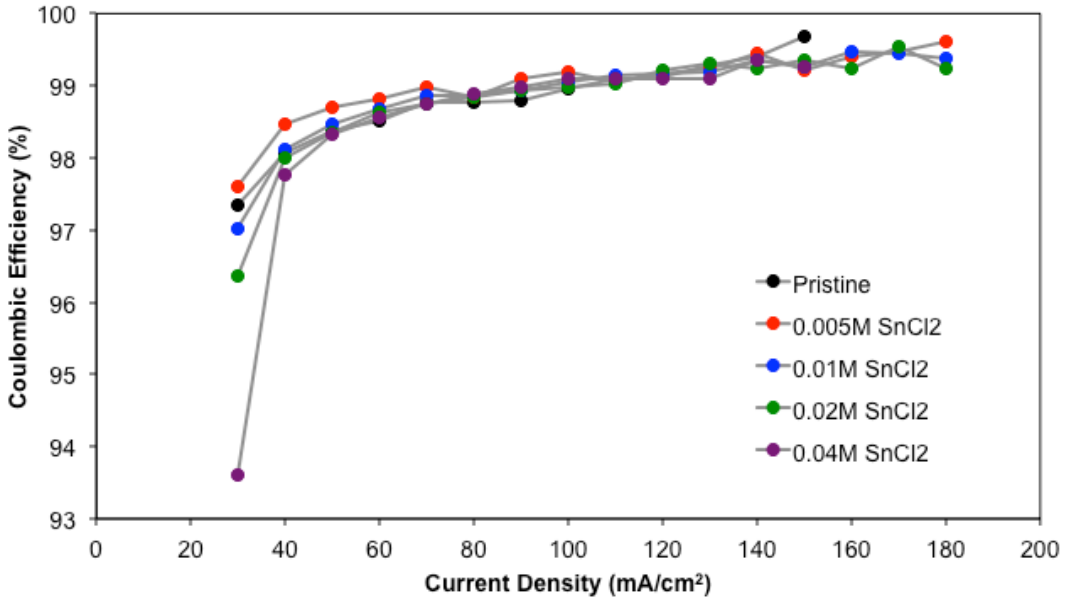

Figure 3.25. Coulombic Efficiency vs. Current Density for various concentrations of $SnCl_2$ added to the anolyte.

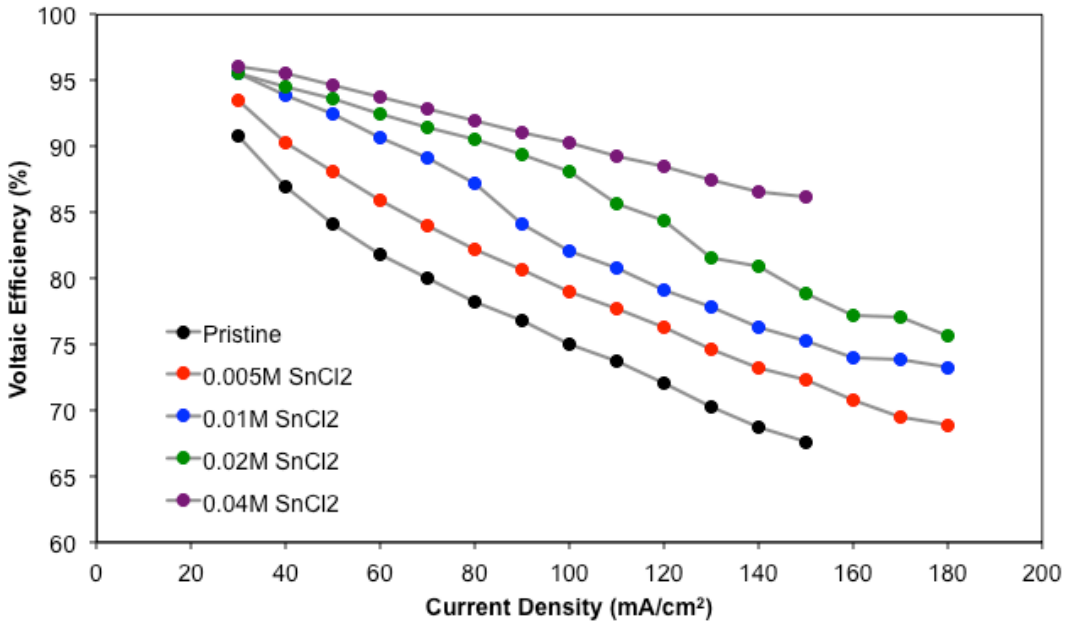

Figure 3.26. Voltaic Efficiency vs. Current Density for various concentrations of $SnCl_2$ added to the anolyte.

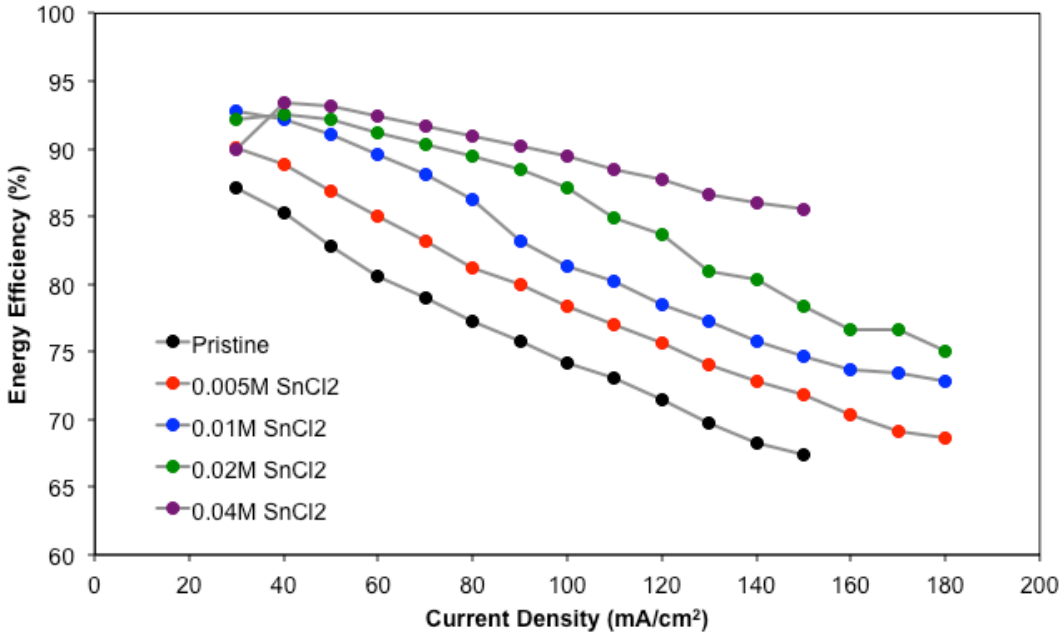

Figure 3.27. Energy Efficiency vs. Current Density for various concentrations of $SnCl_2$ added to the anolyte.

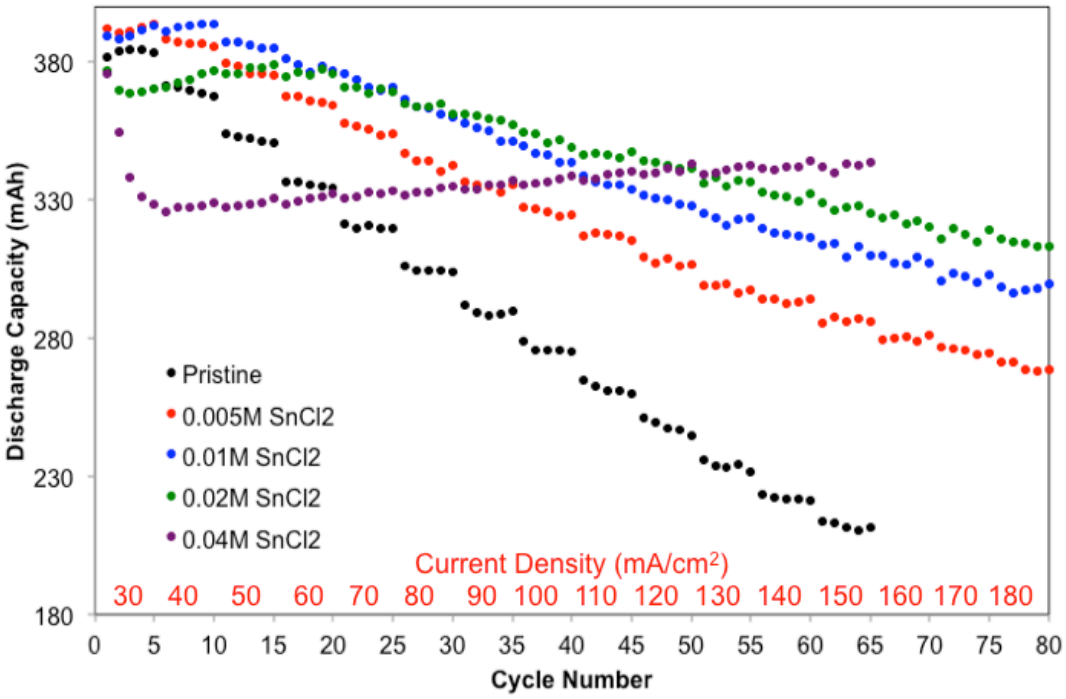

Figure 3.28. Discharge Capacity vs. Cycle Number (Current Density) for various concentrations of $SnCl_2$ added to the anolyte. Cycle number is listed below the x-axis; Current Density for each block of five cycles is listed above the x-axis, in red.

The Coulombic Efficiencies (Figure 3.25) are largely unchanged by the addition of $SnCl_2$. They show the characteristic trend of steadily increasing as a function of current density. This phenomenon is likely due to the shorter time during charge and discharge cycles, which limits the amount of vanadium ion crossover through the Nafion membrane. For instance, the total time for a single charge and discharge cycle at 30 mA/cm^2 is about 120 minutes, the equivalent for 180 mA/cm^2 is about 13 minutes. The difference in diffusion across the membrane during that time is not negligible, and is observed in the Coulombic Efficiency data. Another point to note is the relatively low Coulombic Efficiencies at low current densities, which trend to lower values with increasing $SnCl_2$ concentration. This is likely due to capacity contributions from the reduction of tin that are not realized in the discharge capacity, as they either are not reoxidized into the salt form, or they are lost via shear from the electrolyte convection. The Voltaic Efficiency data (Figure 3.26) shows the true impact of the addition of $SnCl_2$ to the system. There is a clear trend of increasing Voltaic Efficiency as a function of adding additional $SnCl_2$ at the current densities tested. This trend is accompanied by an extension of the accessible current density ranges, as the battery is able to charge and discharge at constant currents up to 180 mA/cm^2. This is a clear improvement over the previous ranges observed in the pristine case. As the concentration of $SnCl_2$ is increased, the Voltaic Efficiency increases accordingly, but this trend seems to reach a maximum at between 0.02M $SnCl_2$ and 0.04M $SnCl_2$, as observed by the loss of current density range. The 0.04M $SnCl_2$ case

could only discharge at a maximum of 150 mA/cm^2. This is likely due to the formation of tin crystals that have grown larger than is useful for the system. In general, it is believed that small, uniform distributions of metal crystals create ideal templates upon which the vanadium redox reaction can occur. As these crystals grow in size, much of the potential reaction site surface area is lost in the bulk of the crystals, causing a drop in overall activity. Another theory is that larger crystals are easier to remove via shear from electrolyte convection. The voltaic efficiency may also be artificially high due to the tin reduction and oxidation contributing to the overall voltage of the battery at higher $SnCl_2$ concentrations, but are in practice actually limiting reaction sites. The Energy Efficiency (Figure 3.27) shows the overall effect of the $SnCl_2$ treatment. The Coulombic Efficiencies are nearly identical for the various cases tested, so the Energy Efficiency data tend to resemble identical trends as those seen in the Voltaic Efficiency data. When examining the discharge capacity data (Figure 3.28), a trend of increasing capacity as a function of $SnCl_2$ concentration is found. This trend continues for increasing current densities, up to 180 mA/cm^2. This trend stops abruptly with the addition of 0.04M $SnCl_2$, which shows a very different discharge capacity profile. It is common to see the discharge capacity of a battery decrease as a function of increasing current density, and this trend is seen for the majority of these data. The case of 0.04M $SnCl_2$ is peculiar, as the capacity increases with increasing current density, until it stops at 150 mA/cm^2. The development of this behavior is seen in the early cycles of the 0.02M $SnCl_2$ case, and very mild effects are seen during very early cycles of the 0.01M and 0.005M cases as well. This effect is attributed to the incomplete reduction of the $SnCl_2$ upon the surface of the graphite felt anode. It is theorized that at 0.04M

$SnCl_2$, the concentration of added salt is high enough that the reduction occurs over a series of cycles, instead of all during each cycle. The metallic tin is not reoxidized into an ionic form effectively, but unreduced $SnCl_2$ adds metallic tin to the existing crystals with each cycle. Thus, the discharge capacity that is measured for each cycle includes a contribution from additional tin reduction. This effect continues until the ionic tin cycling through the cell has been depleted. The lower discharge capacity observed in the 0.04M $SnCl_2$ case is likely due to limited contributions from vanadium reduction, as the high amount of tin deposited on the surface of the graphite felt causes large clusters of crystals which begin to inhibit the vanadium redox reaction due to their density. This claim is supported by the fact that the current density range in the 0.04M $SnCl_2$ case is limited compared to lower concentrations tested – too much tin deposition increases internal resistances in the cell. Based on these results, it can be concluded that an ideal concentration of $SnCl_2$ to add to the anolyte of a VRB is between 0.02M and 0.04M.

3.3.8 Single Cell Testing Results – Direct Reduction of Copper

A series of small amounts of $CuCl_2$ were dissolved into the vanadium electrolyte to make solutions of concentrations 0.005M, 0.01M, and 0.02M $CuCl_2$. As with the $SnCl_2$ testing, the copper salt additives were added after the initial charge step during the VRB setup. The tests were analyzed using Colombic Efficiency, Voltaic Efficiency, Energy Efficiency, and Discharge Capacity as evaluation metrics. The plots showing these data are in Figure 3.29, Figure 3.30, Figure 3.31, and Figure 3.32,

respectively. Each data point shown for the various efficiencies represents the average of five cycles at the given current density.

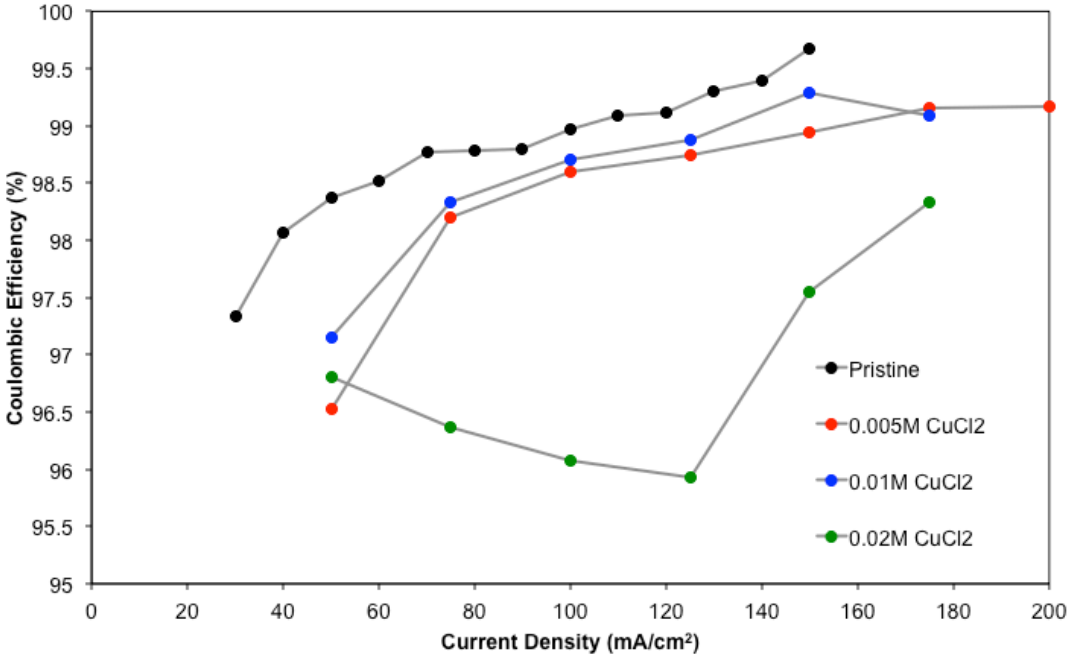

Figure 3.29. Coulombic Efficiency vs. Current Density for various concentrations of $CuCl_2$ added to the anolyte.

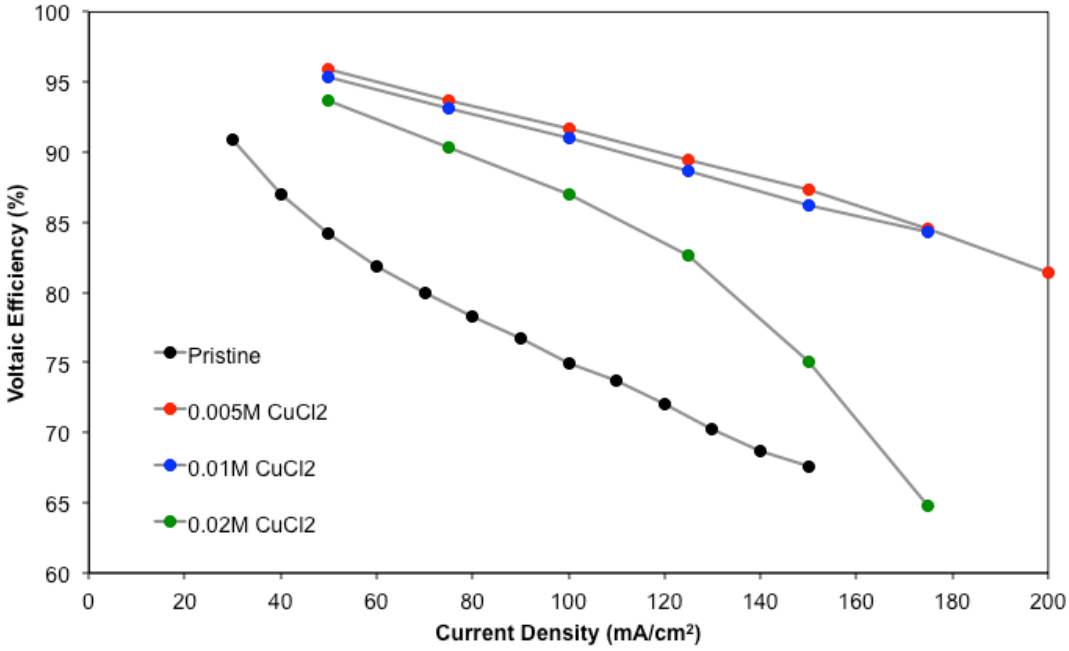

Figure 3.30. Voltaic Efficiency vs. Current Density for various concentrations of $CuCl_2$ added to the anolyte.

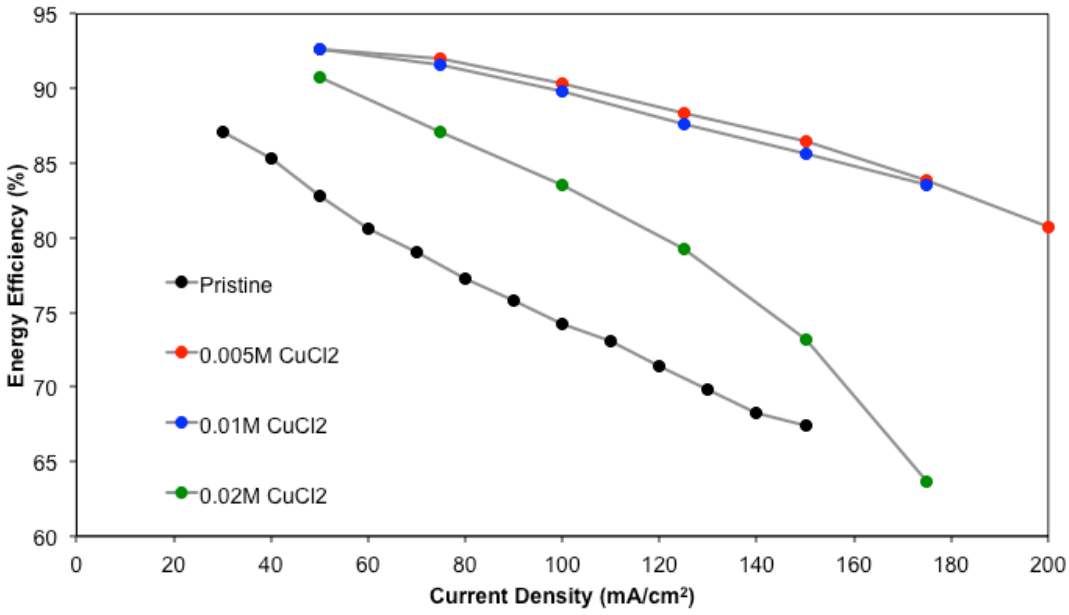

Figure 3.31. Energy Efficiency vs. Current Density for various concentrations of $CuCl_2$ added to the anolyte.

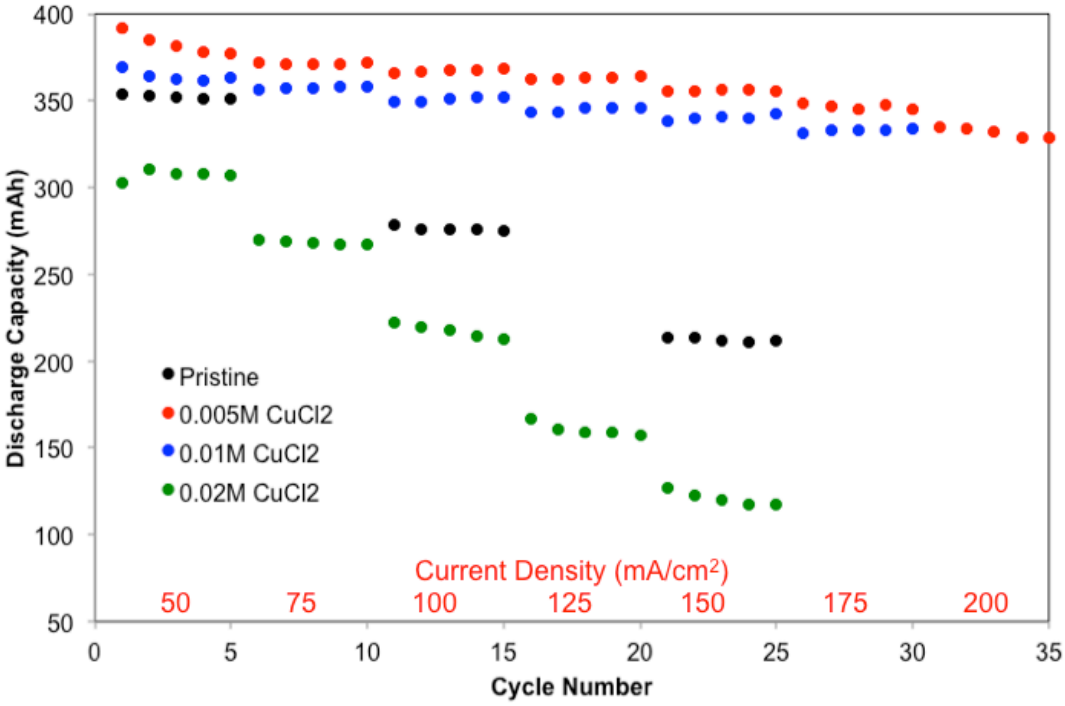

Figure 3.32. Discharge Capacity vs. Cycle Number (Current Density) for various concentrations of $CuCl_2$ added to the anolyte. Cycle number is listed below the x-axis; Current Density for each block of five cycles is listed above the x-axis, in red.

The Coulombic Efficiencies (Figure 3.29) generally increase as a function of current density, as expected. The highest concentration tested, 0.02M $CuCl_2$, shows a small drop in efficiency during lower current densities. This is due to a loss in discharge capacity during the first cycle after every increase in current density during the ramping study, which is likely caused by capacity from additional copper deposition that is not redissolved upon discharge. This phenomenon is not observed in the lower concentrations tested. The Voltaic Efficiencies (Figure 3.30) show that lower concentrations of $CuCl_2$ yield higher voltaic efficiencies. The difference in Voltaic Efficiency between the 0.005M and 0.01M cases is minor, but it seems that the lower concentration case yields slightly higher values, and extends the current density range

to 200 mA/cm^2. The Voltaic Efficiencies from the 0.02M are clearly lower than that of the other two cases tested. Similar to the $SnCl_2$ case, the Energy Efficiencies (Figure 3.31) show nearly identical trends as seen in the Voltaic Efficiencies. The discharge capacities show similar trends as seen in the efficiency data, with the 0.005M $CuCl_2$ case showing the highest capacities. Interestingly, the 0.02M $CuCl_2$ case shows lower discharge capacities than the Pristine case. This is likely due to excessive coverage of the surface of the graphite felt with metallic copper, which may limit performance. It could also be due to a larger charge capacity contribution from forming copper particles, which could be removed via shear from convective flow of electrolyte, limiting their ability to reoxidize and contribute to the discharge capacity.

3.3.9 Single Cell Testing Results – Direct Reduction of Tin + Copper Hybrid Systems

Based on the promising results from using $SnCl_2$ and $CuCl_2$ as anodic catalysts in the VRB, hybrid systems were tested to probe for any synergistic effects from bimetallic systems. The general approach used for these tests was to take the best case observed from the $CuCl_2$ system, the use of 0.005M $CuCl_2$, and test a series of varying amount of $SnCl_2$. As with the $SnCl_2$ and $CuCl_2$ testing, the salt additives were added after the initial charge step during the VRB setup. The tests were analyzed using Colombic Efficiency, Voltaic Efficiency, Energy Efficiency, and Discharge Capacity as evaluation metrics. The plots showing these data are in Figure 3.33, Figure 3.34, Figure 3.35, and Figure 3.36, respectively. Each data point shown for the various efficiencies represents the average of five cycles at the given current density.

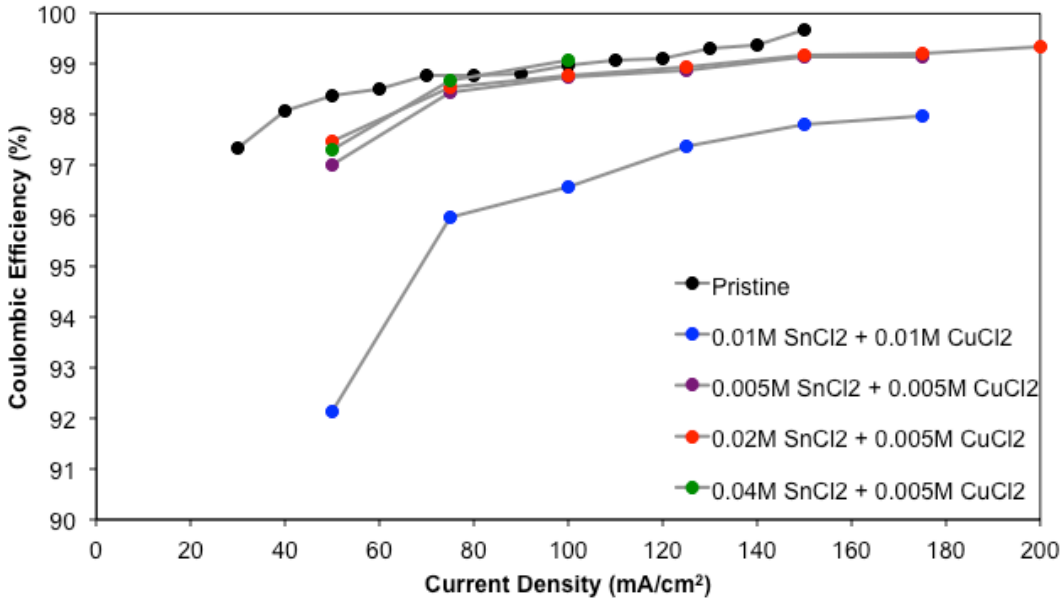

Figure 3.33. Coulombic Efficiency vs. Current Density for various concentrations of $CuCl_2$ + $SnCl_2$ added to the anolyte.

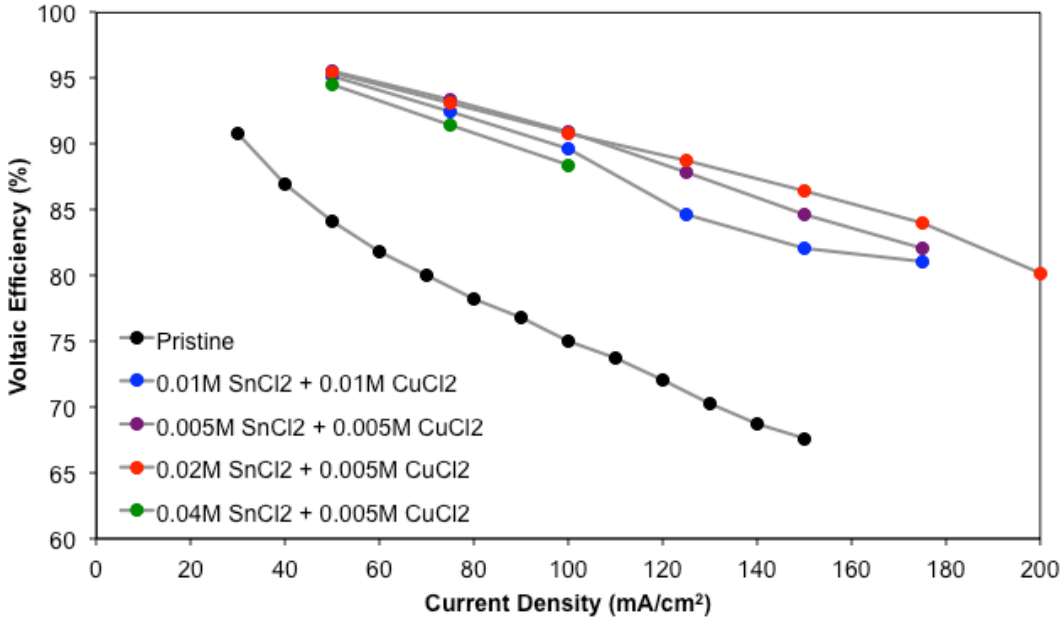

Figure 3.34. Voltaic Efficiency vs. Current Density for various concentrations of $CuCl_2$ + $SnCl_2$ added to the anolyte.

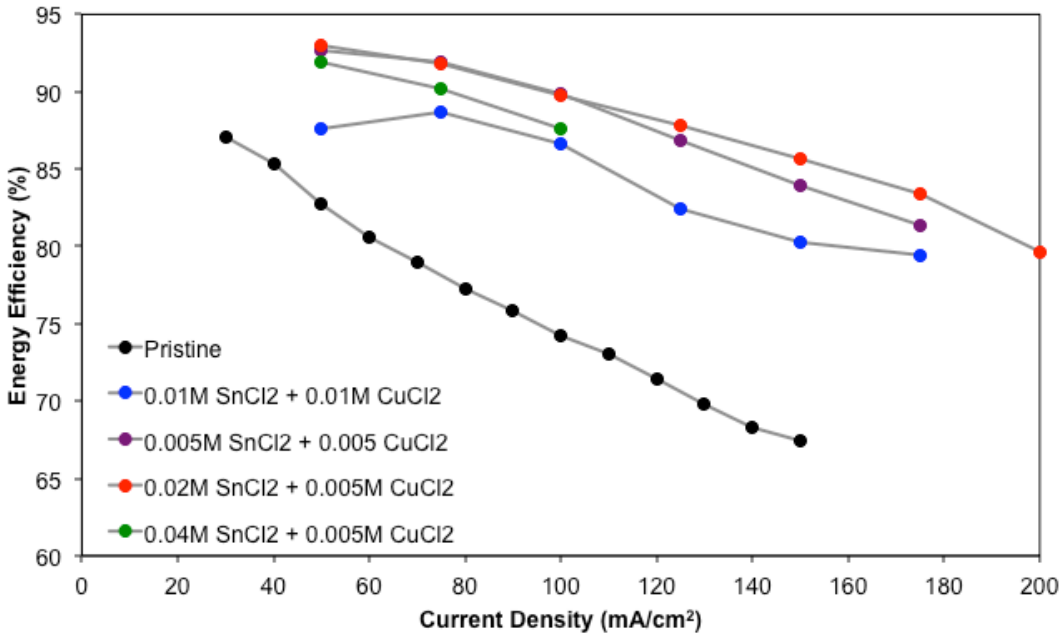

Figure 3.35. Energy Efficiency vs. Current Density for various concentrations of $CuCl_2$ + $SnCl_2$ added to the anolyte.

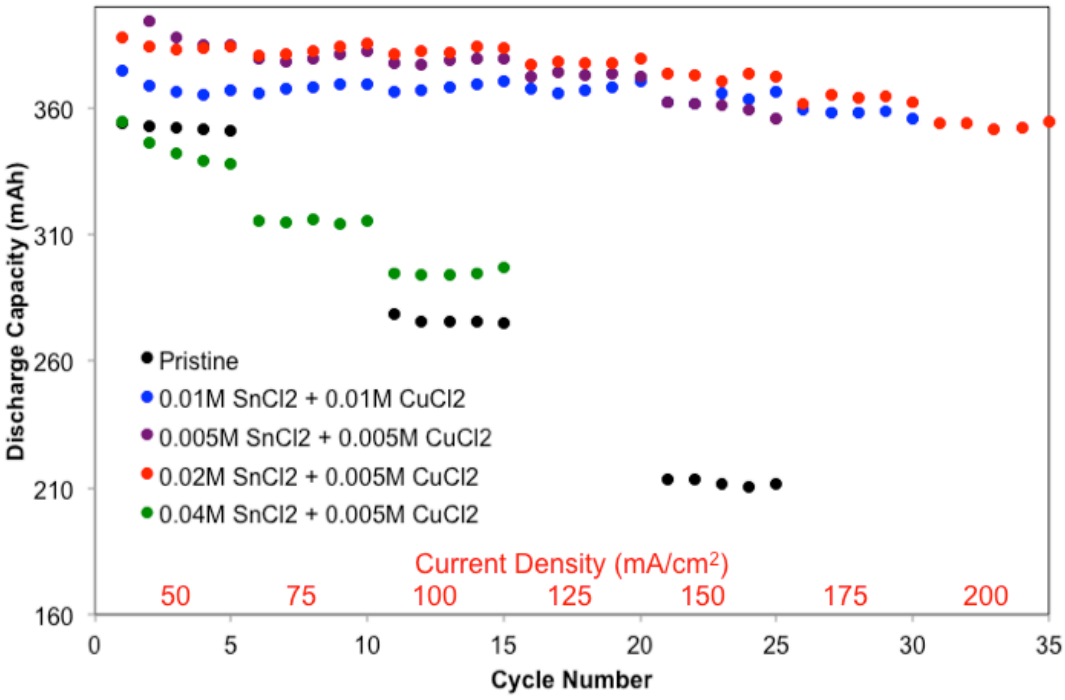

Figure 3.36. Discharge Capacity vs. Cycle Number (Current Density) for various concentrations of $SnCl_2$ and $CuCl_2$ added to the anolyte. Cycle number is listed below the x-axis; Current Density for each block of five cycles is listed above the x-axis, in red.

The Coulombic Efficiencies (Figure 3.33) generally increase as a function of current density, as seen in previous cases. The equimolar case of 0.01M $SnCl_2$ + 0.01 $CuCl_2$ is the case that shows any discernable difference from other tests. This is also the only test that uses 0.01M $CuCl_2$ instead of 0.005M $CuCl_2$, which may be contributing to irreversible copper deposition contributing to the charge capacities. The Voltaic Efficiencies (Figure 3.34) show reasonably similar values for the various cases tested. Interested observations include the limited current density range for the case with 0.005M $CuCl_2$ + 0.04M $SnCl_2$. This limited range is similar to the test using 0.04M $SnCl_2$ only, which was theorized to reduce at a slower rate during cycling as a result of excess $SnCl_2$. The addition of 0.005M $CuCl_2$ seemed to exacerbate the issues with current density, lowering the range from 150 mA/cm^2 to 100 mA/cm^2. Another observation is of the case with the highest Voltaic Efficiency, 0.005M $CuCl_2$ + 0.02M $SnCl_2$. These concentrations are the same as the cases with the highest Voltaic Efficiencies in the single salt testing, indicating that these concentrations are local optimums, even when coupled with another element. The performance of the 0.005M $CuCl_2$ + 0.02M $SnCl_2$ case outperforms the 0.02M $SnCl_2$ case, but shows very similar Voltaic Efficiencies compared to the 0.005M $CuCl_2$ case, indicating that the $SnCl_2$ is not inhibiting performance, but not necessarily helping it. The Energy Efficiencies (Figure 3.35) show similar results as the Voltaic Efficiencies. The discharge capacities (Figure 3.36) show similar results to the Voltaic Efficiencies, with the 0.005M $CuCl_2$

+ 0.02M $SnCl_2$ case demonstrating the highest discharge capacities of the hybrid tests. When looking at these tests from a holistic perspective, the 0.005M $CuCl_2$ + 0.02M $SnCl_2$ case shows the highest Energy Efficiency and discharge capacity, and can be deemed the most favorable result from the hybrid tests. When compared to the single salt tests, the 0.005M $CuCl_2$ + 0.02M $SnCl_2$ case has a very similar Voltaic Efficiency profile to the best single element case (0.005M $CuCl_2$), and a slightly higher discharge capacity. The higher discharge capacity may be a function of contributions from the additional $SnCl_2$ added, instead of contributions from additional vanadium reduction. Based on these results, it is recommended that the 0.005M $CuCl_2$ + 0.02M $SnCl_2$ case be used, although the 0.005M $CuCl_2$ case is only subtly less impressive in performance. In any case, nearly all of the salts and salt combinations tested in the direct reduction studies of tin and copper greatly improved the performance of the VRB.

3.3.10 Single Cell Testing Results – Tin and Copper Particles Synthesized Using Different Treatments

In an effort to test if the method by which the metallic particles were formed has an impact on their performance in the VRB, copper and tin particles were formed using different treatments. These treatments primarily involved using copper (II) acetate and tin (II) acetate, and testing their effects in tandem with varying concentrations of $CuCl_2$. The main goal of these experiments was to attempt to seed the crystal growth from the directly reduced $CuCl_2$ based particles with crystals growth using thermal reduction treatments. Typically, these treatments involved soaking the graphite felt in

an aqueous copper acetate solution, followed by a heat treatment under an inert gas to reduce the metal. These felts were then put in the anode of the VRB, to which varying amounts of $CuCl_2$ was added for direct reduction. It was thought that the thermal treatments could provide more controlled morphological control over the direction of the growth of the crystals, and limit the randomness that was observed from SEM imaging. This was thought to potentially yield better overall VRB performance. As with the previous studies, battery tests were analyzed using Colombic Efficiency, Voltaic Efficiency, Energy Efficiency, and Discharge Capacity as evaluation metrics. The plots showing these data are in Figure 3.37, Figure 3.38, Figure 3.39, and Figure 3.40, respectively. They are presented with the original $CuCl_2$ only data, for the purposes of comparison. Each data point shown for the various efficiencies represents the average of five cycles at the given current density.

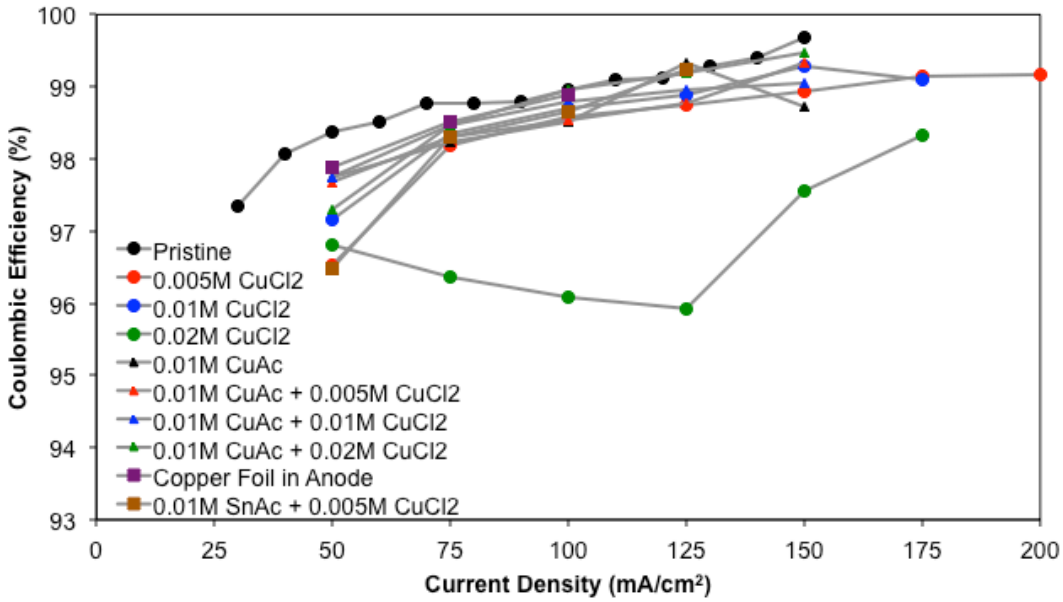

Figure 3.37. Coulombic Efficiency vs. Current Density for various concentrations of $CuCl_2$, thermally reduced Copper acetate + directly reduced $CuCl_2$, and other methods of particle growth.

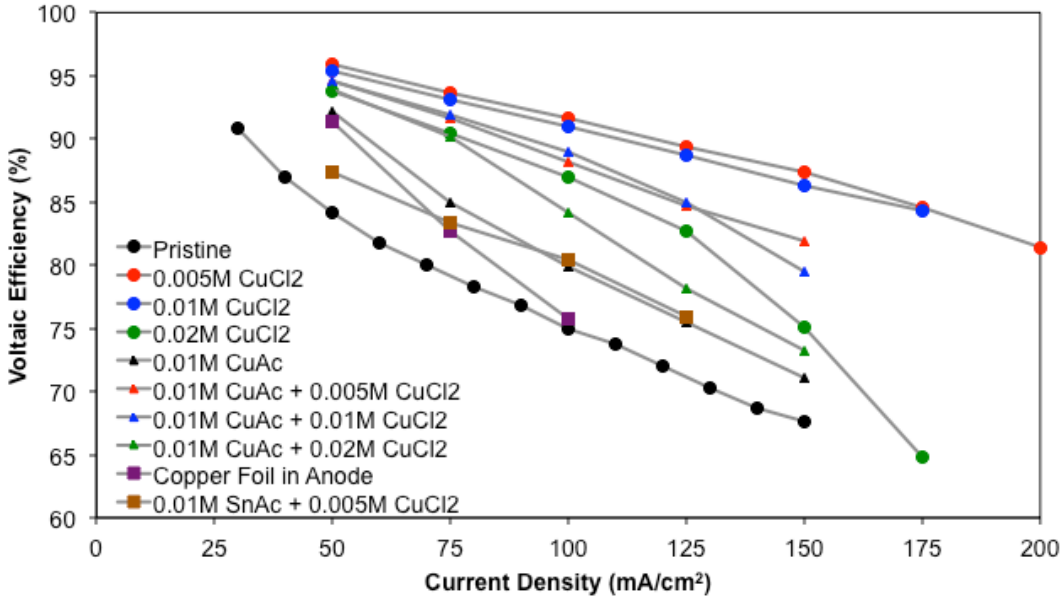

Figure 3.38. Voltaic Efficiency vs. Current Density for various concentrations of $CuCl_2$, thermally reduced Copper acetate + directly reduced $CuCl_2$, and other methods of particle growth.

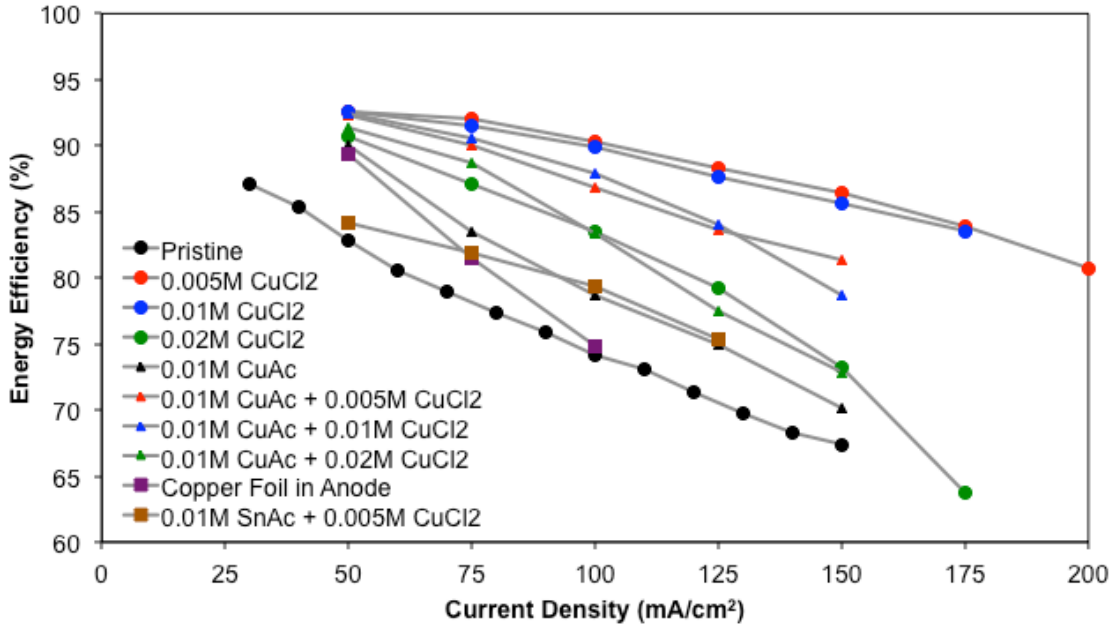

Figure 3.39. Energy Efficiency vs. Current Density for various concentrations of $CuCl_2$, thermally reduced Copper acetate + directly reduced $CuCl_2$, and other methods of particle growth.

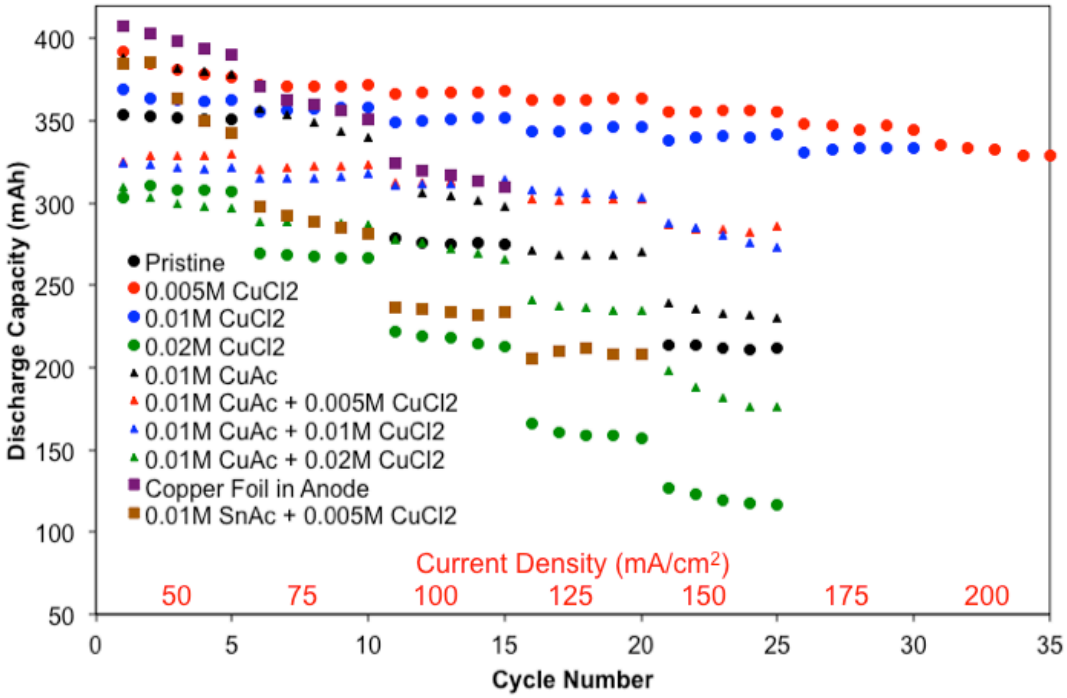

Figure 3.40. Discharge Capacity vs. Cycle Number (Current Density) for various concentrations of $CuCl_2$, thermally reduced Copper acetate + directly reduced $CuCl_2$, and other methods of particle growth. Cycle number is listed below the x-axis; Current Density for each block of five cycles is listed above the x-axis, in red.

The Coulombic Efficiencies (Figure 3.37) are reasonably high during every current density for the test cases with copper acetate added. This is likely due to the fact that there is less irreversible deposition of copper on the graphite felt during each cycle. This could either indicate that some fraction of the added $CuCl_2$ is staying in solution, or that there are reasonably high levels of reoxidation of copper metal into ionic form. The fact that there are not coulombic efficiency levels greater than 100% also could indicate there are minimal contributions to the discharge capacity of the battery from the preformed copper particles. An examination of the Voltaic Efficiencies (Figure

3.38) shows that nearly every case tested with a combination of copper acetate and $CuCl_2$ performed less well than the equivalent $CuCl_2$ test. This indicates that the use of copper particles formed via thermal reduction from copper acetate underperform copper crystals formed through direct reduction. The exact reason for this is likely found in the formation process – the thermal reduction process forms crystals reasonably quickly, and potentially does not completely reduce the crystals to copper, but to forms of copper oxide. The direct reduction process also allows for a slower, more controlled crystal growth process, which may yield more highly active copper particles when compared to the thermal reduction. The trends in the CuAc + $CuCl_2$ data confirm the trends seen in the $CuCl_2$ data alone – the addition of more $CuCl_2$ is detrimental to the Voltaic Efficiency of the VRB. There is also a clear drop-off in performance between both sets of 0.01M $CuCl_2$ and 0.02M $CuCl_2$, indicating some saturation threshold at which the formation of solid copper particles starts to inhibit vanadium reduction. The data from the copper acetate alone also demonstrates poor performance compared to all cases tested, with the exception of the Pristine case. The tin acetate and copper foil cases both performed unremarkably, and were not pursued further. The Energy Efficiencies (Figure 3.39) show similar results to the Voltaic Efficiencies. The discharge capacities (Figure 3.40) show predictably similar data when compared to the Voltaic Efficiencies. The copper foil case shows relatively high discharge capacities during early cycles, likely because the foil is readily oxidized upon discharge, contributing to the discharge capacity. The free copper ions then redeposit on the surface of the graphite felt in large quantities upon charging,

saturating the surface with copper (see Figures 3.13 and 3.14) and limiting surface area of the anode and hence current density range of the VRB.

3.4. Conclusions

A series of tests using various concentrations of $SnCl_2$, $CuCl_2$, CuAc, SnAc, and hybrid systems thereof were used to improve the kinetics of the anodic reaction in a VRB. Nearly every system tested improved the performance of the VRB when compared to the Pristine case. It was found that the case using 0.005M $CuCl_2$ dissolved into the anolyte for the purposes of direct reduction showed the best performance in terms of Energy Efficiency and current density range. A hybrid system using 0.005M $CuCl_2$ and 0.02M $SnCl_2$ showed a similarly high Voltaic Efficiency, and a slightly high discharge capacity, making the case for the exploration of local optimization in bimetallic systems. The direct reduction tests outperformed the thermal reduction tests in every circumstance observed, indicating that while the concentration of starting metal salt may be the same, the quality and performance of the metal particles depends strongly on the process used to create them. Further investigation is needed to fully understand what is occurring at a chemical and crystallographic level in these cases. Another general observation was that lower concentrations of particles can often yield better results, through highly-active small particles contributing to a large surface area. It is clear that exposure of at least some part of the graphite felt to the electrolyte is necessary for successful performance. It is also recommended that investigation into the impact of direct reduction of metal particles on the ion flux through the Nafion membrane be considered, based on wide-

ranging metal particle deposition on the surface of the membrane as observed through SEM imaging. The use of directly reduced copper and tin particles show great promise for improving VRB performance.

3.5 Acknowledgments

This work made use of the Cornell Center for Materials Research Shared Facilities which are supported through the NSF MRSEC program (DMR-1719875). This work was performed in part at the Cornell NanoScale Facility, a member of the National Nanotechnology Coordinated Infrastructure (NNCI), which is supported by the National Science Foundation (Grant ECCS-1542081).

3.6 References

(1) Dunn, B.; Kamath, H.; Tarascon, J. for the Grid : A Battery of Choices. *Science*. **2011**, *334*, 928–935.

(2) Liu, J.; Zhang, J.; Yang, Z.; Lemmon, J. P.; Imhoff, C.; Graff, G. L.; Li, L.; Hu, J.; Wang, C.; Xiao, J.; et al. Materials Science and Materials Chemistry for Large Scale Electrochemical Energy Storage : From Transportation to Electrical Grid. *Adv. Funct. Mater*. **2013**, *23*, 929–946.

(3) Center for Sustainable Systems, University of Michigan. 2017. "U.S. Grid Energy Storage Factsheet." Pub. No. CSS15-17.

(4) U.S. Department of Energy *Grid Energy Storage*. 2013.

(5) Huskinson, B.; Marshak, M. P.; Suh, C.; Er, S.; Gerhardt, M. R.; Galvin, C. J.; Chen, X.; Aspuru-Guzik, A.; Gordon, R.; Aziz, M. A metal-free organic–inorganic aqueous flow battery. *Nature* **2014**, *505*, 195–198.

(6) Janoschka, T.; Martin, N.; Martin, U.; Friebe, C.; Morgenstern, S.; Hiller, H.; Hager, M. D.; Schubert, U. S. An aqueous, polymer-based redox-flow battery using non-corrosive, safe, and low-cost materials. *Nature* **2015**, *527*, 78–81.

(7) Alotto, P.; Guarnieri, M.; Moro, F. Redox flow batteries for the storage of renewable energy : A review. *Renew. Sustain. Energy Rev.* **2014**, *29*, 325–335.

(8) Ulaganathan, M.; Aravindan, V.; Yan, Q.; Madhavi, S.; Skyllas-Kazacos, M.; Lim, T. M. Recent Advancements in All-Vanadium Redox Flow Batteries. *Adv. Mater. Inter.* **2016**, *3*, 1–22.

(9) Parasuraman, A.; Mariana, T.; Menictas, C.; Skyllas-Kazacos, M. Review of material research and development for vanadium redox flow battery applications. *Electrochim. Acta* **2013**, *101*, 27–40.

(10) Park, M.; Jung, Y.; Kim, J.; Cho, J. Synergistic Effect of Carbon Nanofiber/Nanotube Composite Catalyst on Carbon Felt Electrode for High-Performance All-Vanadium Redox Flow Battery. *Nano Lett.* **2013**.

(11) Li, W.; Liu, J.; Yan, C. Modified multiwalled carbon nanotubes as an electrode reaction catalyst for an all vanadium redox flow battery. *J. Solid State Electrochem.* **2013**, *17*, 1369–1376.

(12) Han, P.; Yue, Y.; Liu, Z.; Xu, W.; Zhang, L.; Xu, H. Graphene oxide nanosheets/multi-walled carbon nanotubes hybrid as an excellent electrocatalytic material towards VO^{2+}/VO_2^+ redox couples for vanadium redox flow batteries. *Energy Environ. Sci.* **2011**, 4710–4717.

(13) Chu, Y. Q.; Li, D. D.; Li, W. W.; Ma, C. A. Electrocatalytic Activity of Multi-walled Carbon Nanotubes for VO 2 + / VO 2 + of a Vanadium Redox Flow Battery. *IEEE Conf*. **2013**, 5–8.

(14) Melke, J.; Jakes, P.; Langner, J.; Riekehr, L.; Kunz, U.; Nefedov, A.; Sezen, H.; Wo, C.; Roth, C. Carbon materials for the positive electrode in all-vanadium redox flow batteries. *Carbon*. **2014**, *8*.

(15) Chakrabarti, M. H.; Brandon, N. P.; Hajimolana, S. A.; Tariq, F.; Yu, V.; Hashim, M. A.; Hussain, M. A.; Low, C. T. J.; Aravind, P. V. Application of carbon materials in redox flow batteries. *J. Power Sources* **2014**, *253*, 150–166.

(16) Park, S. M.; Kim, J. H.; Skyllas-Kazacos, M. A technology review of electrodes and reaction mechanisms in vanadium redox flow batteries. *J. Mater. Chem. A* **2015**, *3*, 16913–16933.

(17) Zhu, H. Q.; Zhang, Y. M.; Yue, L.; Li, W. S.; Li, G. L.; Shu, D.; Chen, H. Y. Graphite – carbon nanotube composite electrodes for all vanadium redox flow battery. *J. Power Sources* **2008**, *184*, 637–640.

(18) Wei, G.; Jia, C.; Liu, J.; Yan, C. Carbon felt supported carbon nanotubes catalysts composite electrode for vanadium redox flow battery application. *J. Power Sources* **2012**, *220*, 185–192.

(19) Deng, Q.; Huang, P.; Zhou, W.; Ma, Q.; Zhou, N.; Xie, H.; Ling, W.; Zhou, C.; Yin, Y.; Wu, X.; et al. A High-Performance Composite Electrode for Vanadium Redox Flow Batteries. *Adv. Energy Mater*. **2017**, *1700461*, 1–7.

(20) Shah, A. B.; Zhou, X.; Brezovec, P.; Markiewicz, D.; Joo, Y. L. Conductive Membrane Coatings for High-Rate Vanadium Redox Flow Batteries. *ACS Omega* **2018**, *3*, 1856–1863.

(21) Yu, L.; Lin, F.; Xi, J. A recast Nafion / graphene oxide composite membrane for advanced vanadium redox flow batteries. *RSC Adv*. **2016**, *6*, 3756–3763.

(22) Ju, K.; Hwan, Y. Preparation of the graphene oxide (GO)/Nafion composite membrane for the vanadium redox flow battery (VRB) system. *Vacuum* **2014**, *107*, 269–276.

(23) Niu, R.; Kong, L.; Zheng, L.; Wang, H.; Shi, H. Novel graphitic carbon nitride nanosheets / sulfonated poly (ether ether ketone) acid-base hybrid membrane for vanadium redox flow battery. *J. Memb. Sci*. **2017**, *525* (October 2016), 220–228.

(24) Jia, C.; Cheng, Y.; Ling, X.; Wei, G.; Liu, J.; Yan, C. Sulfonated Poly (Ether Ether Ketone)/ Functionalized Carbon Nanotube Composite Membrane for Vanadium Redox Flow Battery Applications. *Electrochim. Acta* **2015**, *153*, 44–48.

(25) Ejigu, A.; Edwards, M.; Walsh, D. A. Synergistic Catalyst – Support Interactions in a Graphene – Mn_3O_4 Electrocatalyst for Vanadium Redox Flow Batteries. *ACS Catal*. **2015**, *7130* (1).

(26) Huang, R.; Sun, C.; Tseng, T.; Chao, W.; Hsueh, K. Investigation of Active Electrodes Modified with Platinum / Multiwalled Carbon Nanotube for Vanadium Redox Flow Battery. *J. Electrochem. Soc*. **2012**, *159* (10), 1579–1586.

(27) Li, B.; Gu, M.; Nie, Z.; Shao, Y.; Luo, Q.; Wei, X.; Li, X.; Xiao, J.; Wang, C.; Sprenkle, V.; et al. Bismuth Nanoparticle Decorating Graphite Felt as a High-Performance Electrode for an All-Vanadium Redox Flow Battery. *Nano Lett*. **2013**, *13*, 1330–1335.

(28) Wei, L.; Zhao, T. S.; Zeng, L.; Zhou, X. L.; Zeng, Y. K. Copper nanoparticle-deposited graphite felt electrodes for all vanadium redox flow batteries. *Appl. Energy* **2016**, *180*, 386–391.

(29) Li, B.; Gu, M.; Nie, Z.; Wei, X.; Wang, C.; Sprenkle, V.; Wang, W. Nanorod Niobium Oxide as Powerful Catalysts for an All Vanadium Redox Flow Battery. *Nanoletters* **2014**, *14*, 158–165.

(30) Wang, W. H.; Wang, X. D. Investigation of Ir-modified carbon felt as the positive electrode of an all-vanadium redox flow battery. *Electrochim. Acta* **2007**, *52*, 6755–6762.

(31) He, Z.; Dai, L.; Liu, S.; Wang, L.; Li, C. Mn_3O_4 anchored on carbon nanotubes as an electrode reaction catalyst of V(IV) / V(V) couple for vanadium redox flow batteries. *Electrochim. Acta* **2015**, *176*, 1434–1440.

(32) Bayeh, A. W.; Kabtamu, D. M.; Chang, Y.; Chen, G.; Chen, H.; Lin, G.; Liu, T.; Wondimu, T. H.; Wang, K.; Wang, C. Ta 2 O 5 - Nanoparticle-Modified Graphite Felt As a High-Performance Electrode for a Vanadium Redox Flow Battery. *ACS Sustain. Chem. Eng.* **2018**, *6*, 3019–3028.

(33) Cao, L.; Skyllas-kazacos, M.; Wang, D. Modification Based on MoO3 as Electrocatalysts for High Power Density Vanadium Redox Flow Batteries. *ChemElectroChem* **2017**, *4*, 1836–1839.

(34) Wang, S. C. Three-dimensional annealed WO3 nanowire/graphene as an electrocatalytic material for all vanadium redox flow batteries. *Sustain. Energy Fuels* **2017**, *1*, 2091–2100.

(35) Mehboob, S.; Mehmood, A.; Lee, J.; Hwang, J.; Abbas, S.; Ha, H. Y.; Shin, H. Excellent electrocatalytic effects of tin through in situ electrodeposition on the performance of all-vanadium redox flow batteries. *J. Mater. Chem. A* **2017**, *5*, 17388–17400.

(36) Wei, L.; Zhao, T.; Zeng, L.; Zhou, X.; Zeng, Y. Titanium Carbide Nanoparticle-Decorated Electrode Enables Significant Enhancement in Performance of All-Vanadium Redox Flow Batteries. *Energy Technol.* **2016**, *4*, 990–996.

(37) Zhou, H.; Shen, Y.; Xi, J.; Qiu, X.; Chen, L. ZrO2 - Nanoparticle-Modified Graphite Felt : Bifunctional Effects on Vanadium Flow Batteries. *ACS Appl. Mater. Interfaces* **2016**, *8*, 15369–15378.

(38) Gobal, F.; Faraji, M. RuO2/MWCNT/stainless steel mesh as a novel positive electrode in vanadium redox flow batteries. *RSC Adv.* **2015**, *5*, 68378–68384.

(39) Shen, J.; Liu, S.; He, Z.; Shi, L. Influence of antimony ions in negative electrolyte on the electrochemical performance of vanadium redox flow batteries. *Electrochim. Acta* **2015**, *151*, 297–305.

(40) Tseng, T.; Huang, R.; Huang, C.; Liu, C. Carbon Felt Coated with Titanium Dioxide / Carbon Black Composite as Negative Electrode for Vanadium Redox Flow. *J. Electrochem. Soc.* **2014**, *161* (6), 1132–1138.

(41) Zhou, H.; Xi, J.; Li, Z.; Zhang, Z.; Yu, L.; Liu, L.; Qiu, X.; Chen, L. CeO2 decorated graphite felt as a high-performance electrode for vanadium redox flow batteries. *RSC Adv.* **2014**, *4*, 61912–61918.

(42) Tseng, T.; Huang, R.; Huang, C.; Hsueh, K. A Kinetic Study of the Platinum/Carbon Anode Catalyst for Vanadium Redox Flow Battery. *J. Electrochem. Soc.* **2013**, *160* (4), 690–696.

(43) Kim, K. J.; Park, M.; Kim, J.; Hwang, U.; Lee, N. J.; Jeong, G.; Kim, Y. Novel catalytic effects of Mn3O4 for all vanadium redox flow batteries. *ChemComm* **2012**, *48*, 5455–5457.

CHAPTER 4

LEAD-BASED PARTICLES AS HIGHLY ACTIVE ELECTROCATALYSTS FOR ALL-VANADIUM AQUEOUS REDOX FLOW BATTERY ANODES

ABSTRACT: A series of synthetic methods were investigated for creating lead-based particles on the surface of graphite felts for use in the anode of aqueous all-vanadium redox flow batteries. This involved using chemical means to create both metallic lead and lead oxide particles deposited on the surface of graphite felts. The various methods were first analyzed using electrochemical characterization, to help determine the most favorable state of oxidation of the lead-based particles. The performance of these felts was then assessed in a single cell vanadium redox flow battery at a series of current densities. It was found that the formation of tetragonal lead monoxide (litharge) particles yielded the best results of all tested systems, with a voltaic efficiency of 77.2% at a high current density of 200 mA/cm^2. The best cases observed showed stable cycling for longer periods of time, again demonstrating the subtle but important differences in the state of oxidation of lead-based particles in reducing acidic environments. This work suggests the use of lead monoxide particles as simple and effective electrocatalysts for use in an aqueous vanadium redox flow battery.

4.1. Introduction

Redox flow batteries have demonstrated the promise to be stable, reasonably low-cost, long-term electrical storage methods.[1-7] The aqueous all-vanadium redox flow battery system (VRB) has been of special interest for many years due to its chemical stability, long cycle life, and potential for high electrical capacity. Despite these advantageous properties, VRBs have consistently been handicapped by their reasonably high capital costs and relatively low power density compared to other large-scale electrical storage methods. Wide-ranging studies have been conducted to investigate and improve these metrics.[8,9]

The all-aqueous VRB operates using two vanadium based redox couples: VO_2^+ and VO^{2+} in the catholyte, V^{2+} and V^{3+} in the anolyte. These redox couples are simultaneously oxidized and reduced upon charging and discharging, via a one-electron process. A number of factors can impact the performance of these batteries, including the cell configuration, flow properties, and polarization resistance.

From a chemical perspective, one of the main limitations of a VRB is the comparatively slow kinetics of the vanadium redox reaction in the anolyte. The anodic reaction has been determined to be the rate-limiting step during cycling in VRBs. Balancing the reaction rates in the anode and cathode is likely one of the most essential advances that can be made at the laboratory scale to advance this technology. To that end, a number of efforts have been made to improve the electrochemical performance of the VRB by changing the surface properties of the anode. This has included a large body of work using carbon materials, such as adding various highly conductive carbons to graphite felts[10-19] and membranes[20-24], carbonizing electrodes via specific heat treatments, and synthesizing electrodes out of specially developed high

surface area carbon materials. Carbon felts have been modified via nitrogen doping[25-29], and with stable, oxygen-rich surface groups, such as –OH, $–OSO_3$, and $–OPO_3$.[30-42] Other work has been focused on decorating carbon materials with metal particles, including Pt[43,44], Bi[45], Cu[46], Ir[47], Sn[48], Sb[49], and Ti[50]. Many of these treatments are not particularly stable over many cycles, as particles can have poor adherence to carbon electrodes. In some of the testing using directly reduced soluble salts, the reduced salts will slowly deposit on the surface of the ion-exchange membrane, limiting lifespan. Some work has been conducted to examine less costly metal oxide particles used in the anode, including Mn_3O_4[51,52], NiO[53], Ta_2O_5[54], MoO_3[55], WO_3[56], ZrO_2[57], RuO_2[58], TiO_2[59], and CeO_2[60]. Many of these treatments make use of expensive transition metal oxides, and some approaches use lengthy synthesis techniques that are not particularly scalable. An ideal candidate for this application is an inexpensive, electrochemically active metal oxide that can be synthesized through a simple scheme.

Lead and lead oxides have been used in electrochemical devices dating to the mid-19th century. They have long been used as reliable components of lead-acid batteries, but have only found limited use in other electrochemical systems.[61-63] Lead has a series of distinctive oxide forms, each with properties that can be explored and exploited in other systems.[64] Some of these oxides have reasonably high electrical conductivity, and adhere well to carbon surfaces.[65] Lead is inexpensive, abundant, and is already widely supplied throughout the world, making it an interesting candidate for use as an additive to VRB systems.[62,63] Little work has been investigated using forms of lead in VRBs.[66] To our knowledge, no work has been previously conducted on using lead-based particles in VRB anodes.

The following work investigates the chemistry, performance, and stability of lead-based particles as electrocatalysts used in the anode of the VRB. Dramatic improvements in the energy efficiency and discharge capacity of VRBs are observed, and potential explanations for this enhanced performance are discussed.

4.2. Methods

4.2.1 Various synthetic methods for creating lead-based particles. Three different synthetic schemes were used to create lead-based particles on the surface of pristine graphite felts. These methods were designed to test the efficacy of different types of lead compounds and crystal structures to better elucidate their effects on kinetic activity in the anolyte of the VRB. Each method used 1.0g of 3mm thick graphite felt placed in a 200mL Teflon-lined reaction vessel, to which 0.1g $Pb(NO_3)_2$ dissolved in 100mL DI water was added as a starting step. This was followed by dropwise addition of a 1M NaOH solution to increase the alkalinity of the water to pH 9, usually about 20-30 drops. The subsequent treatments are summarized in Figure 4.1.

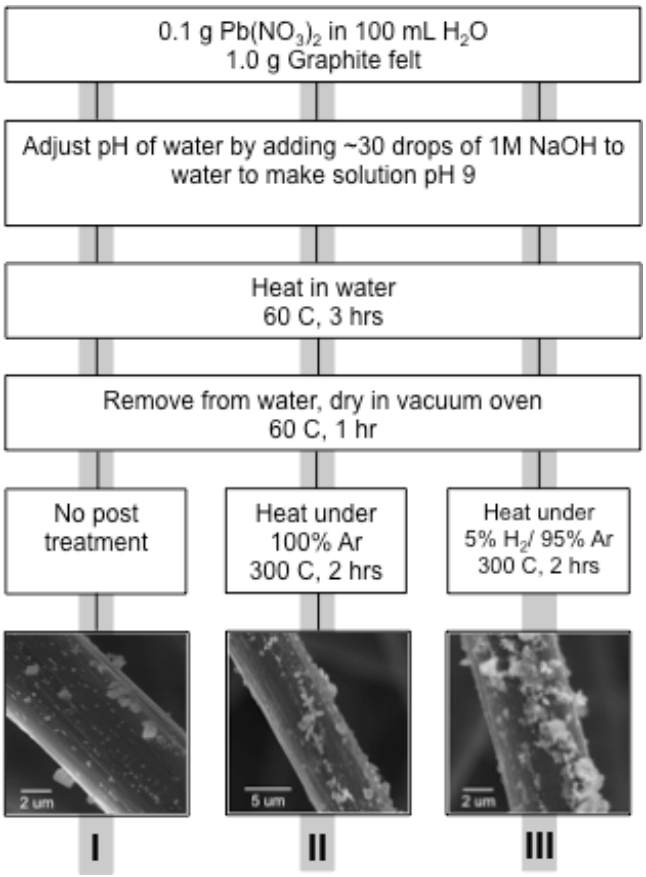

Figure 4.1. Post-Treatment Methods. Lead hydroxide particles were formed on all felts, then underwent no post treatment (I), heating under flowing Argon (II), and heating under flowing H_2/Argon (III).

Method I used a modest heating step (60C for 3 hours), followed by drying in a vacuum oven at 60C for 1 hour. Method II used the same initial heating step, followed by drying, followed by a short heat treatment under flowing Argon at 300C for 2 hours. Method III is identical to Method II, but instead is heat-treated using a 5% H_2: 95% Argon gas mixture at 300C for 2 hours. Each of these felts was put directly in the VRB anode upon completion of modification.

4.2.2 Single-Cell Testing. The single cell setup consisted of the cell and two glass containers for electrolyte storage. Electrolyte was pumped through ¼" I.D. tubing to

and from the flow cell (Tygon 2375 Ultra tubing, Watson-Marlow 323E Pump). Each side of the cell consisted of symmetric acrylic end plates with push-to-connect tube fittings, a graphite current collector, a Viton gasket, a polypropylene flow frame, and an HDPE gasket. These components were separated by a Nafion 212 membrane (50 um thick). The total exposed area of the membrane and graphite current collector was 15 cm^2 (a 5 cm by 3 cm rectangle). Each side of the cell had a 2 mm space between the membrane and current collector, in which a piece of 3 mm thick porous graphite felt (PAN-based, AVCarb) was compressed for good electrical contact. The electrolyte used in all tests was 1M $VOSO_4$ (Alfa Aesar) in 4M H_2SO_4. The electrolyte volume used was 25 mL for the catholyte and anolyte, with a flow rate of 30 mL/min. Each container of electrolyte was purged of air prior to testing by covering the electrolyte with a blanket of argon and sealing well. Current densities between 50 mA/cm^2 and 200 mA/cm^2 were explored. All single-cell cycling testing was carried out using a battery analyzer (3A/5V, MTI). Cycling involved charging and discharging repeatedly at a specified constant current density. The upper cutoff voltage was set at 1.7 V, the lower cutoff voltage was set at 0.8 V. Cycling tests were assessed by coulombic efficiency, voltaic efficiency, energy efficiency, and capacity retention.

4.2.3 Electrochemical Measurements. Electrolytes were assessed using Electrical Impedance Spectroscopy (EIS) testing to measure the changes in resistance in the cell both with and without the addition of APS to the surface of the graphite felt. An electrolyte consisting of 0.20M H_2SO_4 and 0.05M $VOSO_4$ was used for all testing. An AC voltage of 1 mV amplitude was used over a frequency range of 10^4 Hz to 10^{-3} Hz

to generate Nyquist plots of the pristine and modified cases. Cyclic voltammetry (CV) was also performed on the electrolytes at rates of 10, 20, and 50 mV/s in a three-electrode glass cell, using the above-mentioned electrolyte. The working electrode consisted of a precisely massed piece of graphite felt, skewered on a platinum wire to provide high electrical conductivity. The mass of graphite felt used was 25 mg, a mass that was chosen out of convenience based on the corresponding size of graphite felt. The platinum wire was always kept out of the electrolyte, leaving 5mm of the graphite felt out of the solution. This procedure allowed for consistent analytical testing. The reference electrode used was Ag/AgCl, the counter electrode used was a platinum mesh (52 mesh, Alfa Aesar) attached to platinum wire to provide a large surface area. A potential range between -1.2 V and +0.4 V was explored.

4.2.4 Materials Characterization. The treated graphite felts were characterized using a variety of analytical techniques. Felts were optically inspected using SEM to observe any visual changes to their surfaces, and to analyze particle formation. XRD was used to determine the lead-based particle composition and state of oxidation after each treatment. High-resolution XPS analysis was used to determine the bonding environment of particles formed on the surface of the graphite felt, and the relative concentrations of the different elements.

4.3. Results and Discussion

The purpose of these treatments was to probe the effects of using different post-treatments on lead-based particles to improve the kinetics of the anodic reaction in the

aqueous VRB. The idea for using lead-based particles came in part from the wide usage of lead as a component in lead-acid batteries. Lead is widely abundant, inexpensive, and readily available when compared to various other metals. There are large supplies of used lead from retired lead-acid batteries that can be repurposed for use in other electrochemical systems.[61-63] Lead salts also happen to be highly insoluble in sulfuric acid, forming lead sulfate as described in equation 1:

$$Pb^{2+}_{(aq)} + SO_4{}^{2-}_{(aq)} \leftrightarrow PbSO_{4(s)} \quad (1)$$

This reaction was viewed with an interest in the formation of these particles, as lead sulfate tends to have low electrical conductivity, but a high oxygen content, which has been shown to be beneficial to the vanadium reduction reaction in previous works.[31-33,35,36] The initial strategy was to avoid the direct synthesis of lead sulfate, although it was expected that some amount would form during cycling, regardless of synthetic method. This limited the ability to directly dissolve a lead salt into the electrolyte, as has been investigated in previous studies using soluble metal salts in the anolyte of VRBs.[45,46,48,49] While metallic lead has reasonably high electrical conductivity, it was assumed that its stability in an acidic, reducing environment is limited. The formation of lead sulfate on the surface of lead particles is highly likely in an environment such as a VRB. The standard reduction potential of metallic lead is shown in equation 2,

$$Pb^{2+}_{(aq)} + 2e^- \leftrightarrow Pb_{(s)} \quad \text{E = -0.126V vs. SHE} \quad (2)$$

$$V^{3+}_{(aq)} + e^- \leftrightarrow V^{2-}_{(aq)} \qquad \text{E = -0.255V vs. SHE} \quad (3)$$

which is a more positive potential than the anodic reaction (equation 3) in the VRB.[67] This implies that should any metallic lead be present in the system, it is susceptible to oxidation upon discharging of the VRB, leading to the formation of Pb^{2+} ions. It was theorized that these ions would rapidly form $PbSO_4$, and may be detrimental to VRB performance. To that end, a synthesis strategy utilizing more stable lead oxides was pursued. Theory shows that forms of PbO_2 tend to have reasonably positive standard reduction potentials to form undesirable products, as shown in equations 4 and 5:

$$PbO_{2\,(s)} + 4H^+ + 2e^- \leftrightarrow Pb^{2-}_{(aq)} + 2H_2O \qquad \text{E = 1.455V vs. SHE} \quad (4)$$

$$PbO_{2\,(s)} + SO_4^{2-} + 4H^+ + 2e^- \leftrightarrow PbSO_{4\,(s)} + 2H_2O \qquad \text{E = 1.691V vs. SHE} \quad (5)$$

Alternatively, PbO is more stable and requires a strong negative potential to reduce it to metallic lead, as shown in equation 6:

$$PbO_{(s)} + H_2O + 2e^- \leftrightarrow Pb_s + 2OH^- \qquad \text{E = -0.580V vs. SHE} \quad (6)$$

The standard reduction potential of PbO is more negative than that required for the vanadium reduction reaction, and should therefore not be greatly affected by the cycling process. In order to test this theory, lead particles were made using chemical means. The initial synthetic step of using a simple base to create lead particles in a water solution has been previously demonstrated to be effective at precipitating metal

hydroxide particles from aqueous solutions.[68,69] The choice to adjust the alkalinity of the lead salt bath to pH 9 is due to the fact that an excessively alkaline conditions in solution will limit the formation of the desired product, insoluble lead hydroxide (equation 7), and will begin to form soluble plumbate ions (equation 8), which are less desirable for this application.[70]

$$Pb^{2-}{}_{(aq)} + 2OH^{-}{}_{(aq)} \leftrightarrow Pb(OH)_{2\,(s)} \tag{7}$$

$$Pb(OH)_{2\,(s)} + 2OH^{-}{}_{aq} \leftrightarrow [Pb(OH)_4]^{2-}{}_{(aq)} \tag{8}$$

Once the lead hydroxide particles have formed on the surface of the graphite felt, three methods were used as post-treatment. Method I simply dried the graphite felt and used it in the lead hydroxide form. Method II consisted of a heat-treatment step under flowing Argon. Argon is an inert gas that can be used as a mild reducing agent in elevated temperatures without greatly affecting the graphite felt. The purpose of this step was to create PbO particles. Method III used a similar heat-treatment step under a mixture of 5% H_2 and 95% Argon gasses. This was used as a more aggressively reducing step to further convert the particles from lead hydroxide to metallic lead. The temperature of this step was also an important consideration, as metallic lead melts at about 327C. While the various lead oxides melt at much higher temperatures, this treatment was conducted at 300C to prevent melting of the particles upon conversion to their metallic forms. This decision was made with the goal of maintaining the surface morphology of the particles during the heat treatment.

SEM images of modified graphite felts are shown in Figure 4.2.

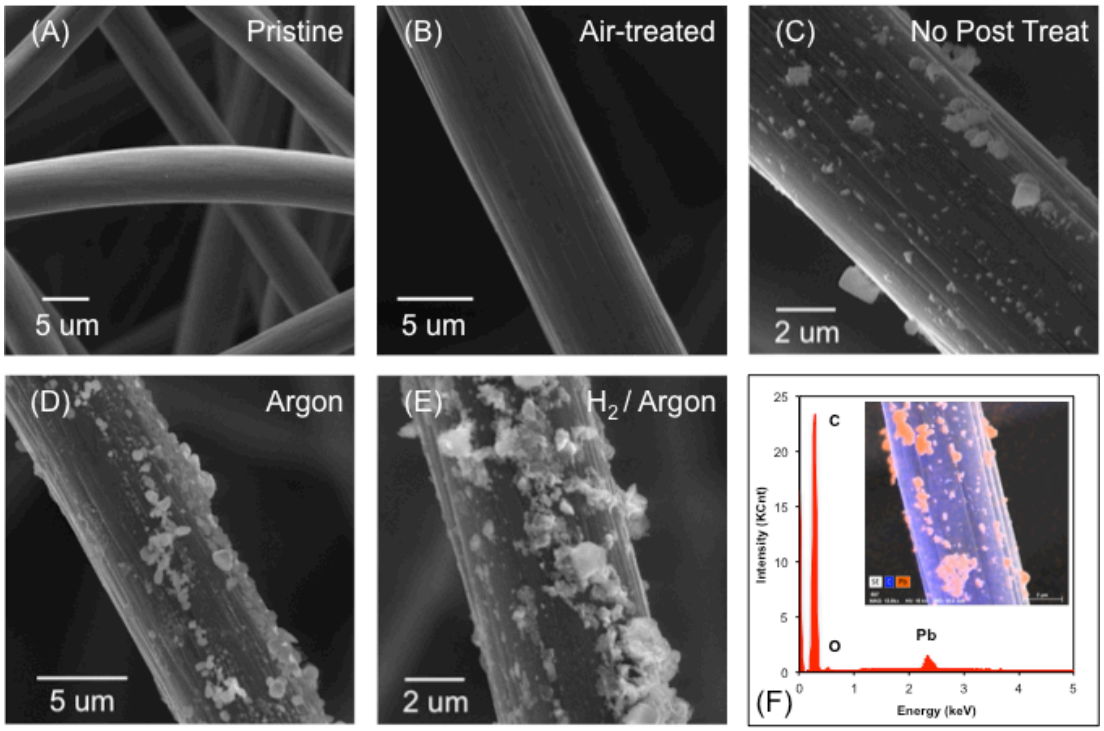

Figure 4.2. FE-SEM images of A. Pristine graphite felt, B. Air-treated graphite felt, C. Method I felt, D. Method II felt, E. Method III felt, F. EDX image of cycled Method III felt with corresponding spectra. There were no obvious the optical differences can be observed in images A and B, but clear particle formation in images C, D, and E. Particles tended to be randomly distributed and optically similar. EDX shows lead-based particles on the surface of a felt after cycling, and identifies C, Pb, and O as major elements in the system.

There are few noticeable differences between the Pristine and Air-Treated felts. The felt from Method I (no post treatment) shows the formation of a reasonable density of nanoscale lead hydroxide particles. The particles tend to be randomly dispersed on the surface of the felt, and vary in size. Figure 4.2D shows felt made using Method II (Argon heat-treatment). The density of particles on the surface of the felt seems to be slightly higher, with the particles still varying in size. Figure 4.2E shows felt made using Method III (H_2/Argon heat-treatment). There seems to be a reasonably high

density of particles on the surface of this felt as well, with a greater fraction of large particles. These images were chosen to represent each case, as they were deemed representative of each sample on the whole, although some spatial variation in particle distribution was observed. Figure 4.2F shows EDX imaging and spectra from a piece of Argon-treated graphite felt (Method II) that has been through 100 cycles in the VRB. It is important to notice that there is still a high distribution of lead-based particles on the surface of the felt, despite exposure to shear from electrolyte convection. This is in contrast to some other metal and metal oxide electrocatalyst systems that have been previously investigated, in which the particles have a poorer adherence to the surface of the felt. The EDX spectra indicate the presence of carbon, oxygen, and lead. Interestingly, there is very little sulfur detected in the sample, suggesting that the lead-based particles have minimal formation of lead sulfate, and exist only in lead oxide forms, even after cycling. This claim can only apply to the depths at which EDX probes, which tends to be on the micron scale. XPS gives more information about the surfaces, and the nanometer depth. Additional EDX images can be found in Figure 4.S1. In general, the density and visual appearance of the particles from the different synthetic methods tend to be similar, as is expected. The total mass of lead on the surface of the graphite felts should be very similar due to the use of the same initial processing steps to create the starting lead hydroxide particles. XRD analysis was conducted on collected particles in order to probe the corresponding state of oxidation from each method. Figure 4.3 shows XRD spectra for Methods I through III.

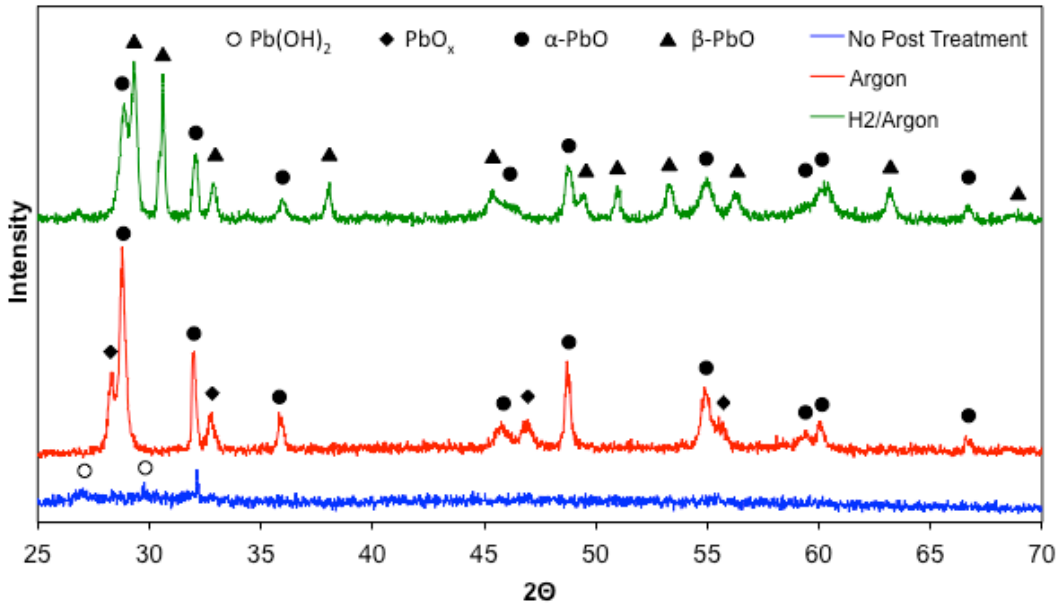

Figure 4.3. XRD spectra of particles on the felts created using Methods I, II, and III. Residual particles were collected during synthesis and exposed to the same conditions as the felts before analysis. Method I (No Post Treatment) shows the formation of $Pb(OH)_2$ and compounds of the like, Method II (Argon) shows the formation of α-PbO and various non-stoichiometric ratios of PbO_x, Method III (H_2/Argon) shows the formation of both α-PbO and β-PbO. A version of this figure including the formation of metallic lead from further reduction treatments is found in Figure 4.S2.

Method I shows very little coherent crystal structure, and appeared to be more of an amorphous solid powder, in the form of $Pb(OH)_2$ and $Pb(NO)_3OH$. Previous work has shown that the speciation from purported $Pb(OH)_2$ solids is likely more complex than stated, but this rather simplistic assignment was deemed adequate for these purposes.[71] Spectra of particles from Method II showed much more clear crystal structures, predominantly in the form of tetragonal α-PbO (known commonly as litharge) and a non-stoichiometric lead oxide compound, identified most closely as $PbO_{1.44}$.[72] Various ratios of oxygen to lead content are common in lead oxide compounds, and the

resulting oxygen vacancies have been exploited for their electron-conducting properties in other applications.[73] The Argon heat-treatment partially reduced the former $Pb(OH)_2$ species into primarily oxide forms. Spectra from Method III (H_2/Argon) show that some α-PbO still exists in the sample. The other known polymorph of lead monoxide, orthorhombic β-PbO (commonly known as massicot), is also found in the sample.[72] No other oxides were observed, and no metallic lead was observed, despite the more reducing environment. Further testing at more elevated H_2/Argon heat-treatment temperatures times was explored, and XRD results confirmed that the majority of particles had converted to metallic lead in these cases (see Figure 4.S2).[74] However, the results from these tests were unimpressive compared to the performance from their lead oxide counterparts (see Figure 4.S3) in terms of energy efficiency and stability over time. This could be in part due to loss of surface area during heat-treatment due to particles melting, but warrants further investigation. X-ray Photoelectron Spectroscopy (XPS) was used to more accurately quantify the elemental distribution and bonding environment on the surface of the graphite felt. These data are shown in Figure 4.4.

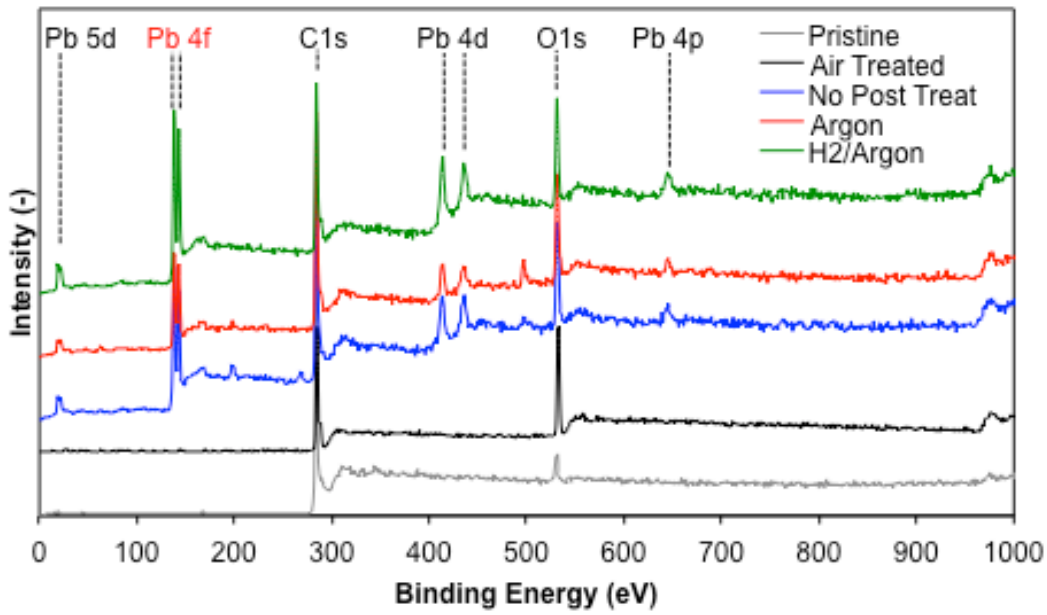

Figure 4.4. High-resolution XPS survey scan showing the five different felts tested in this study. Lead peaks are identified; the Pb 4f is of particular interest.

All felts analyzed showed C 1s and O 1s peaks. It is quite clear that each of the methods using lead treatments also show a series of Pb peaks, as indicated on the figure. The peak used for analysis of the different types of lead bonding observed was the Pb 4f peak. This peak appears as a doublet due to spin orbital splitting, as Pb $4f_{7/2}$ and Pb $4f_{5/2}$.[76] The Pb $4f_{7/2}$ peak was used for analysis in each of these samples. Figure 4.5 shows XPS spectra of this peak in each of the samples both before and after cycling in the VRB.

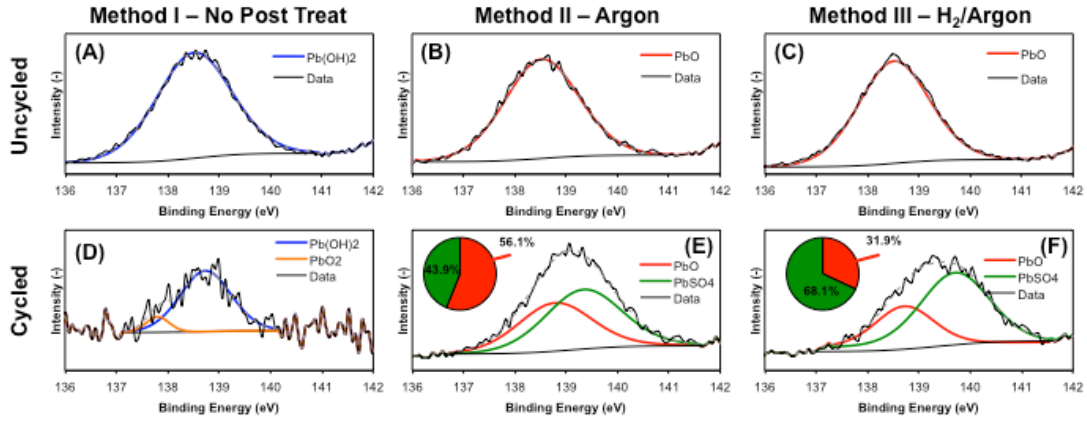

Figure 4.5 XPS spectra of the Pb $4f_{7/2}$ peak observed in felts created with the three post treatment methods, before and after cycling in the VRB. A. Method I, uncycled; B. Method II, uncycled; C. Method III, uncycled; D. Method I, cycled; E. Method II, cycled; F. Method III, cycled. Uncycled XPS spectra support XRD results. Cycled XPS show some conversion of original species to new species, mainly $PbSO_4$.

Figure 4.5A shows the major $Pb(OH)_2$ peak is found at about 138.5 eV, while Figures 4.5B and 4.5C show a PbO peak at 138.6 eV.[77] These peaks are very similar in position, however the previous XRD analysis supports these assignments. The α-PbO and β-PbO peaks were deemed to close in position to reasonably deconvolute, and were lumped into a single PbO peak. After cycling, the samples were removed from the VRB, were gently rinsed with DI water to remove the electrolyte, and were dried at low temperature in a vacuum oven. Figure 4.5D shows that there is likely still some lead in the form of $Pb(OH)_2$, although some seems to have oxidized to form PbO_2. A large fraction of the lead compounds that were originally on the surface in this sample were no longer detected after cycling, which may explain the performance of this sample. It could also indicate that $Pb(OH)_2$ is somewhat soluble in sulfuric acid, and dissolved into the electrolyte during the cycling process. Figure 4.5E shows that after cycling, the Pb $4f_{7/2}$ peak has shifted to slightly higher binding energies. This peak was

deconvoluted into PbO (138.5 eV) and $PbSO_4$ (139.5 eV) peaks, as per literature references.[78] The deconvolution indicates that about 44% of the PbO on the surface of the felt has been converted to $PbSO_4$. This result should again be examined with caution, as this pertains to only the first few nanometers of penetration depth that XPS analysis allows. Figure 4.5F shows that the peak from the felt from Method III has shifted to even higher binding energies after cycling. It is thought that this represents a greater conversion of PbO to $PbSO_4$, about 68%. The main difference between Methods I and II (according to XRD) was the state of oxidation from the post-treatment. This indicates that more reduced samples (such as those from Method III) may be more susceptible to sulfation in the environment of the VRB, especially over long exposure times.[75] Cyclic voltammetry was conducted to test the electrochemical effects of the various lead-based particles on the relevant VRB reactions. Figure 4.6 shows the CV of the different graphite felts in the anolyte at a potential scan rates of 10, 20, 30, and 50 mV/s.

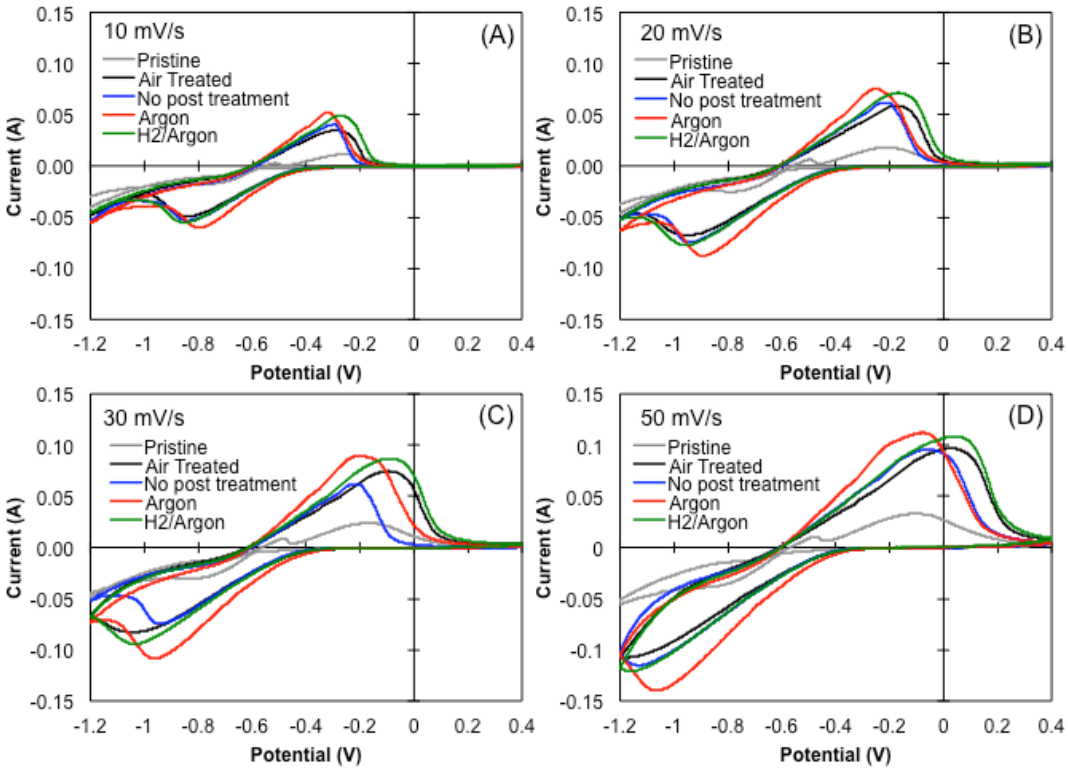

Figure 4.6. Cyclic Voltammetry testing of the five felts of interest. The anodic vanadium reaction was probed at scan rates of 10, 20, 30, and 50 mV/s. Data presented by individual felt type can be found in Figure 4.S4.

It can be seen that Pristine felt has very poor kinetics, due to the hydrophobicity and lack of surface sites available for reaction. The Air Treated felt improves upon the Pristine felt, as demonstrated by a large increase in the peak maxima for both the oxidation and reduction reactions in the anolyte. The graphite felt synthesized using Method I shows a limited impact on the vanadium reactions compared to the Air Treated felt. The peak separation is lowered marginally, likely due to the additional hydrophilic reaction sites from the lead hydroxide particles on the surface of the felt. The felt using Method II (Argon) shows a clear improvement on the Air Treated felt. At 10 mV/s, the peak potential separation is decreased from 560 mV in the Air

Treated case to 479 mV in the Argon-treated case. This is a clear indication of enhanced electrochemical activity due to the presence of the PbO particles. Both the oxidation and reduction reaction peak heights have also increased as a result of the treatment. The results from Method III (H_2/Argon) are quite interesting, as the maximum peak potentials are actually quite similar to the Air Treated results, but show peak heights comparable to those seen in Method II. The higher peaks are attributed to the increase in surface area from the crystalline particles formed during the treatment. However, there is a minimal drop in the overpotential provided by the particles, despite being only marginally chemically different than the particles from Method II. This subtle but important difference is attributed to the lower band gap (1.9 eV) in the α-PbO polymorph that primarily makes up the sample from Method II, as compared to the higher band gap (2.8 eV) in the β-PbO that is found in the sample from Method III.[79,80] Electrical conductivity information from the various non-stoichiometric phases of of PbO_x is not known, but in general the phases of lead oxide with higher degrees of oxidation tend to have lower band gaps.[80] This information must be balanced with the expectation that polymorphs of PbO_2 will be too easily reduced to Pb^{2+}. The vacancies provided by the non-stoichiometric phases of PbO_x (where $1 < x < 2$) confirmed from XRD of samples from Method II could also provide greater electron mobility during cycling of the VRB. In any case, the observed currents from both the oxidation and reduction reaction are noticeably higher with either form of PbO. These results indicate high electrochemical activity and reversibility of the anodic reaction with the use of Methods II and III, with samples from Method II showing the most favorable results.

In order to better understand the diffusive characteristics of the vanadium species in the presence of graphite felt from each of the treatment methods, the Randles-Sevcik equation was used to plot the CV peak current density versus the square root of the potential scan rate.[81] The resulting plots are shown in Figure 4.7 and were plotted based on Equation 9:

$$i_p = (2.69 \times 10^5) n^{3/2} A D_o^{1/2} C_o^* \upsilon^{1/2} \quad (9)$$

where i_p is peak current (A), n is number of electrons transferred (1), A is electrode area (cm^2), D_o is the apparent diffusion coefficient (cm^2/s), C_o^* is the bulk electrolyte concentration (mol/cm^3), and υ is the potential sweep rate (V/s). The apparent diffusion coefficients for the different felts in the anolyte are tabulated in Table 1.

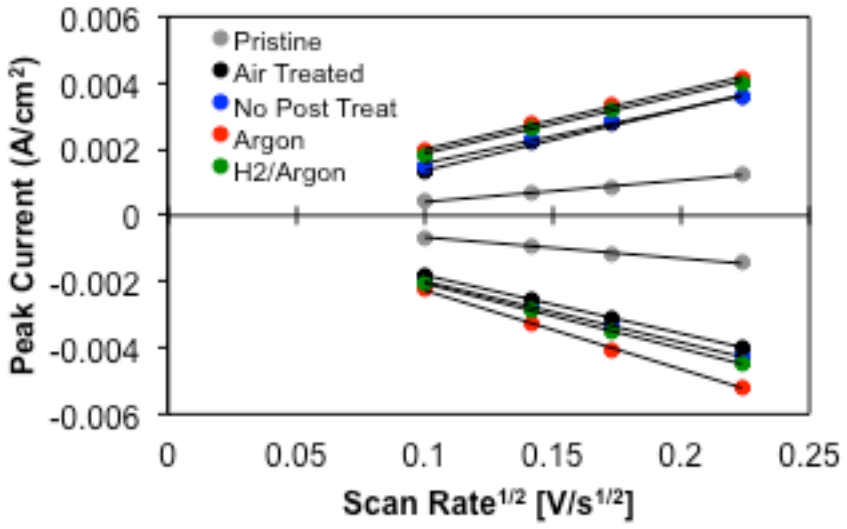

Figure 4.7. Plots of Peak Current (measured from CV testing) vs. potential scan rate$^{1/2}$. Data was plotted to calculate effective vanadium ion diffusion coefficients in the presence of the different felts.

Table 1. Calculated diffusion coefficients (10^{-6} cm^2/s)		
	Positive	Negative
Pristine	0.23	0.23
Air Treated	1.89	1.71
No Post Treat	1.49	1.89
Argon Post Treat	1.71	3.16
H_2/Argon Post Treat	1.71	2.12

The mass transfer of the oxidation reaction is not greatly impacted by the treatments from Methods II and III compared to the Air Treated felt. The reduction reaction, however, shows clear differences in the diffusion coefficients of all three of the methods investigated. There is a marginal improvement from Method I, a more clear improvement from Method III, and a diffusion coefficient that is nearly double that of the Air Treated felt from Method II. All of these modifications are indicative of an improvement in the surface properties of the felts for the vanadium redox reactions.

Electrical Impedance Spectroscopy (EIS) was performed in a 3-probe cell using each of the modified felts as a working electrode. These data (Figure 4.8) are consistent with the results from the CV testing, showing an apparent decrease in charge transfer resistance from felts made with all three post-treatment methods, when compared to the Air Treated felt. The felts from Methods I and III showed similar Ohmic resistances (first intercept with the x-axis), and both were lower than the Air Treated felt. This is explained by an improvement in the hydrophilicity of the felt due to the lead-based particles covering the surfaces. This improvement in Ohmic resistance is

even more pronounced with the felt from Method II, which again is attributed to a drop in the contact resistance of the solution to the felt.

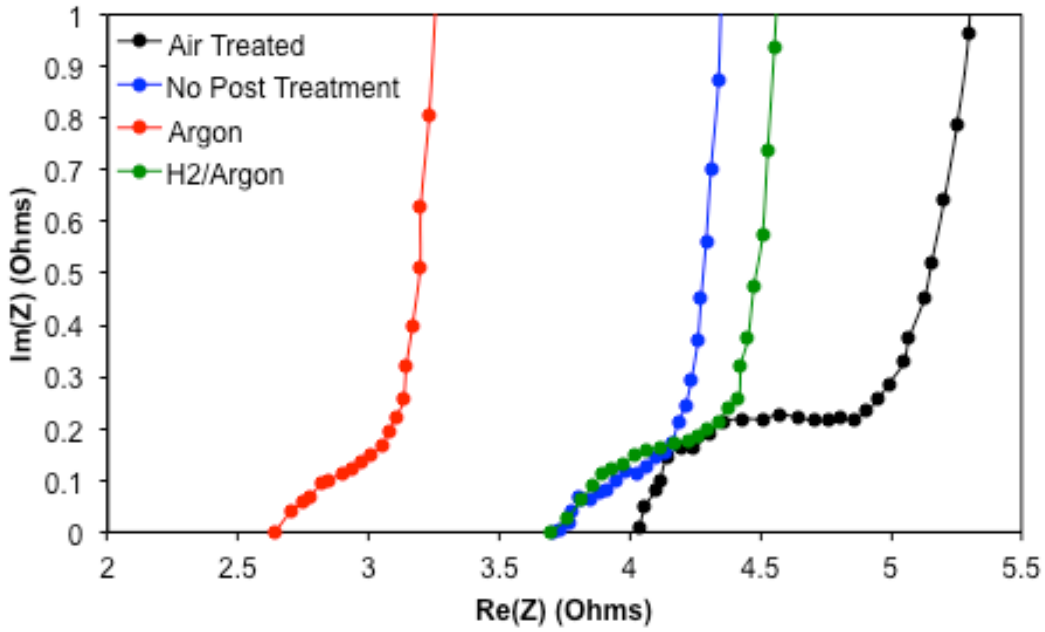

Figure 4.8. EIS spectra comparison of the felts of interest in the vanadium electrolyte.

To test the actual performance of these felts in a VRB, the felts were assessed in single cell tests. Each test consisted of a series of charge-discharge cycles at increasing current densities to measure the discharge capacities and coulombic, voltaic, and energy efficiencies. The current densities tested ranged from 50 mA/cm^2 to 200 mA/cm^2, increasing by increments of 25 mA/cm^2. The coulombic efficiencies were fairly similar, regardless of treatment, as seen in Figure 4.9A.

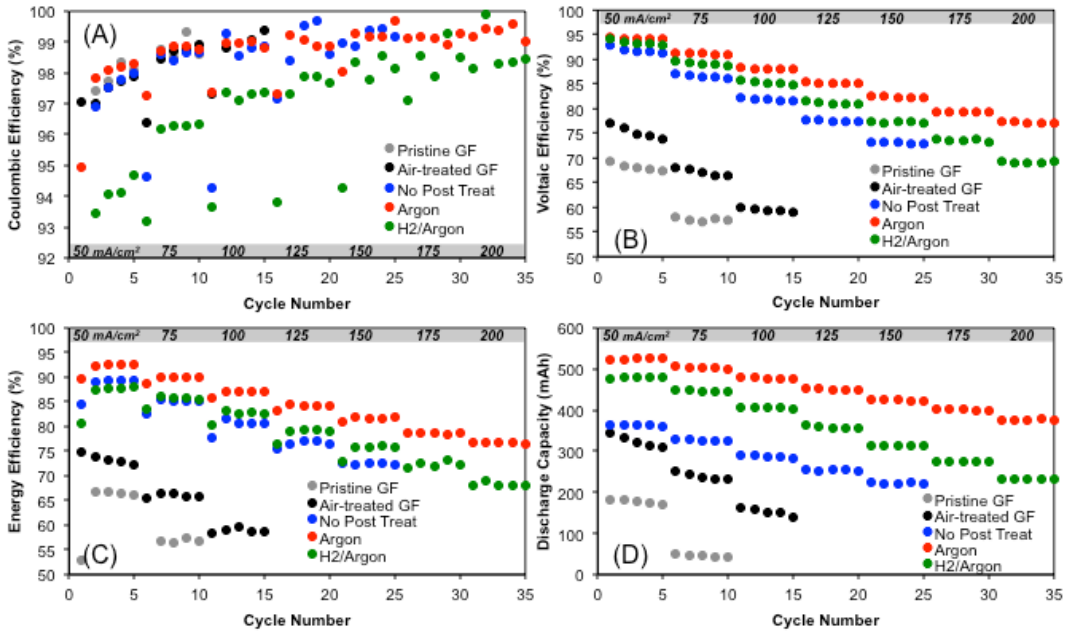

Figure 4.9 Results of ramping study of different graphite felts at increasing current density. Each current density increment lasted 5 cycles. A. Coulombic efficiency comparison, B. Voltaic efficiency comparison, C. Energy efficiency comparison, D. Discharge capacity comparison.

One noteworthy observation was that the coulombic efficiencies from the felt treated using Method III (H_2/Argon) were consistently lower than the other cycles tested. This implies that there exists some sort of change in the electrode that is contributing to the charge capacity, but is not contributing to the discharge capacity during each cycle. Each charge cycle imposes a reducing environment in the anode, thus it would follow that some small amount of the lead oxide particles in the sample from Method III are being reduced to a new state upon charging, but are not re-oxidized upon discharging. It is believed that some of the β-PbO is reduced to metallic lead, which is not re-oxidized to a form of lead oxide, at least electrochemically. It is more likely that any metallic lead formed will react chemically with the sulfuric acid electrolyte, forming lead sulfate, and will not contribute to discharge capacity and corresponding

coulombic efficiency. None of the other samples examined seemed to exhibit this behavior. In all samples tested the coulombic efficiency increased as a function of current density, as expected, likely due to shorter cycle times, which limits the time for diffusive vanadium ion crossover through the membrane. The voltaic efficiencies (Figure 4.9B) more clearly demonstrate the differences between the various post-treatment methods. Both Pristine GF and Air-treated GF were limited in their performance, as has been frequently demonstrated. When the graphite felt from Method I was used in the anode, the current density range was extended to 150 mA/cm^2 at a voltaic efficiency of 73.0%. The felt from Method III (H_2/Argon) improved upon this result, further extending the current density range to 200 mA/cm^2 at a voltaic efficiency of 69.2%. Finally, the most impressive result was demonstrated by the case using the felt from Method II (Argon), which showed a voltaic efficiency of 77.2% at 200 mA/cm^2. In the cases of both Method II and Method III, the current density was limited by the capabilities of the setup, and both are expected to be able to perform at even higher current densities. The trends seen in these data further confirm the results from preliminary electrochemical testing. The corresponding energy efficiencies (Figure 4.9C) show similar trends to the voltaic efficiencies, with the performance of the felt from Method II exhibiting an improvement in energy efficiency of over 20% when compared to the Air Treated felt and nearly 27% when compared to the Pristine felt at 50 mA/cm^2. Figure 4.9D shows the discharge capacities for each of these ramping studies. The discharge capacities correspond well with the efficiency data. A sample set of charge-discharge curves can be seen in Figure HHH.

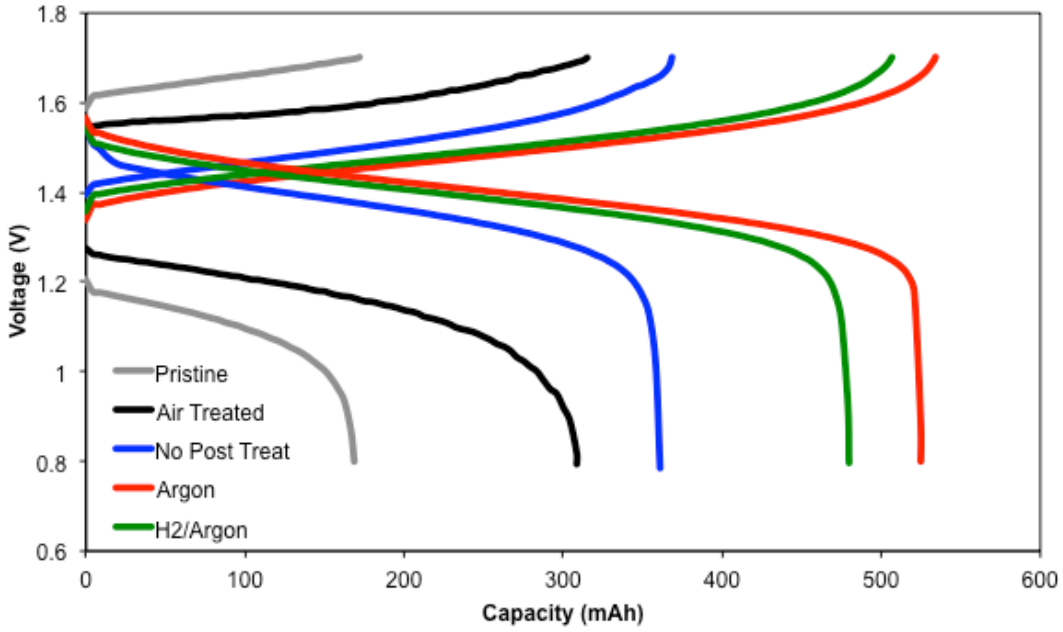

Figure 4.10 Sample set of charge-discharge curves of the five felts tested at 50 mA/cm^2.

It should be noted again, that despite a very minor difference in post-treatment, the sample from Method II showed a discharge capacity that was over 60% greater than the sample from Method III at 200 mA/cm^2. This is a remarkable difference in performance. The capacity retention of the VRB using each of these felts was measured using cycling tests at a current density of 50 mA/cm^2. These data (Figure 4.11A) show that the felt from Method II has a capacity retention of 93.49% over 25 cycles, compared to 92.40% (Method III) and 92.53% (Method I). All of these retention rates were higher than the Air Treated case (84.21%) and the Pristine case (58.59%). Figure 4.11B shows the corresponding Voltaic Efficiency over the same cycling period. The felt treated using Method II (Argon) exhibits extremely high voltaic efficiency retention at 99.79%. This equates to a very low voltaic efficiency decay rate of 0.0084% per cycle. The felts treated using both Method I and Method III

also display impressive voltaic efficiency retention at 95.27% and 96.47%, respectively. All of these results outperform that of the Air Treated felt, at 93.97%. This difference in decay rates may be attributed to relative instability of hydroxyl groups on the surface of the graphite felt as compared to more chemically stable metal oxide particles. This also demonstrates that there is minimal impact on performance from loss of particles from the surface of the felt due to convection. SEM images of the felts before and after cycling can be found in Figure 4.S5.

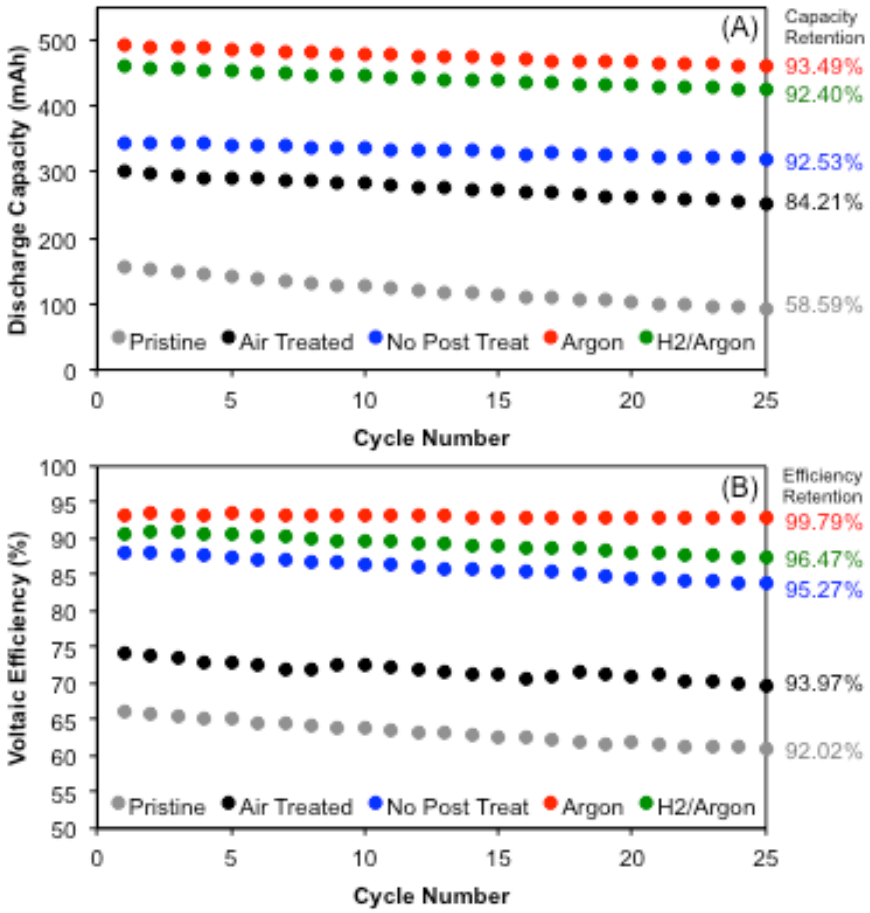

Figure 4.11 Cycling Stability Studies of the various felts. A. Discharge capacity retention over 25 cycles; B. Voltaic Efficiency retention over 25 cycles.

In an effort to probe the effects of concentration of $Pb(NO_3)_2$ on the performance of the VRB, felts were synthesized using Method II with masses of 0.05g and 0.2g $Pb(NO_3)_2$, in addition to the original case of 0.1g $Pb(NO_3)_2$. SEM images from all three of these loadings are shown in Figure 4.12.

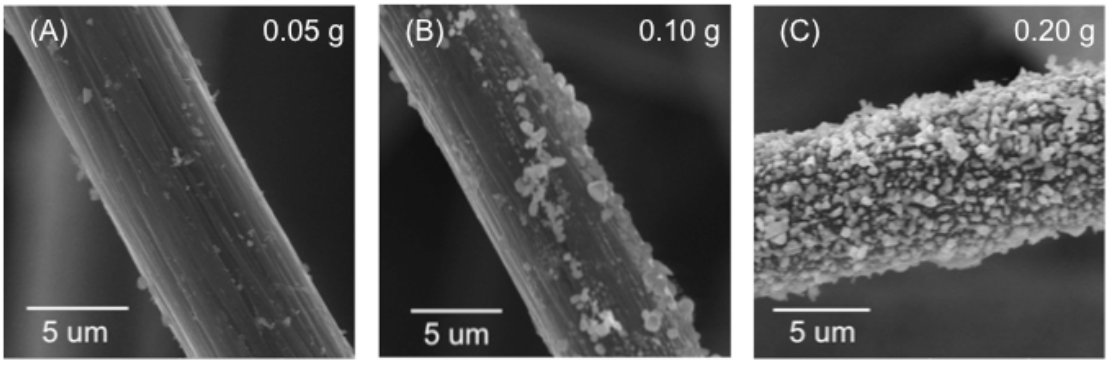

Figure 4.12. SEM images of felts created using Method II with $Pb(NO_3)_2$ loadings of A. 0.05g; B. 0.10g; C. 0.20g per 1.0g of graphite felt.

The visual difference in PbO loading is quite apparent between the three samples. The different loadings were assessed using the same efficiency and capacity retention metrics as previously described, and are presented in Figure 4.13.

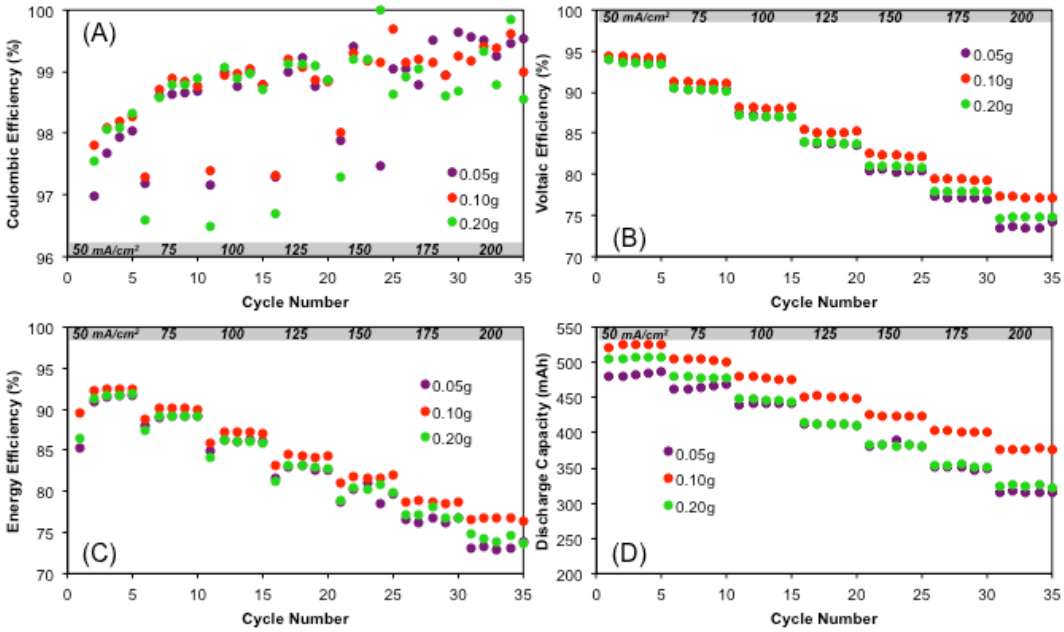

Figure 4.13 Results of ramping study of felts created using Method II with various loadings of $Pb(NO_3)_2$, at increasing current density. Each current density increment lasted 5 cycles. A. Coulombic efficiency comparison, B. Voltaic efficiency comparison, C. Energy efficiency comparison, D. Discharge capacity comparison.

The coulombic efficiencies from the various felts are predictably similar. The voltaic efficiencies are clustered together throughout cycling, but indicate that the original case tested with a loading of 0.10g $Pb(NO_3)_2$ seems to have the most impressive performance. The loading of 0.20g $Pb(NO_3)_2$ seems to perform marginally better than the case with 0.05g $Pb(NO_3)_2$. All of the tested samples were able to reach a maximum current density of 200 mA/cm^2, and the energy efficiencies of all loadings were higher than any of the other original methods investigated. This is further evidence of a clear difference in performance using the post-treatment from Method II as compared to the other methods.

4.4. Conclusions

A series of graphite felts with lead-based particles were synthesized for use in the anode of a VRB. Different post-treatments provided chemically unique starting configurations in an effort to see the impact of their various chemistries on the performance of a single cell VRB. It was found that the case which comprised mainly of tetragonal α-PbO and other non-stoichiometric forms of PbO_x showed the best performance, with major improvements in energy efficiency, current density range, and discharge capacity. The case comprising of both α-PbO and β-PbO also performed quite well. Both cases showed some conversion of PbO to $PbSO_4$ during cycling, although this had a remarkably minimal impact on the overall performance. This indicates that either the premise that $PbSO_4$ would be detrimental to the performance was incorrect, or that the mechanism of improvement in this system is a stronger function of particle surface area than of chemical structure and electrical conductivity. Sulfate groups have been shown to be beneficial to vanadium reduction kinetics in other studies, and they may still be useful to some lesser extent than the different forms of PbO. These results suggest that additional studies using aqueous hybrid vanadium and lead battery systems may be worth investigating, as they share many similar characteristics which could lead to interesting synergies. In conclusion, lead-based particles provide an interesting means to create electrocatalyts that greatly improved the overall performance of an aqueous vanadium redox flow battery.

4.5 Supporting Information

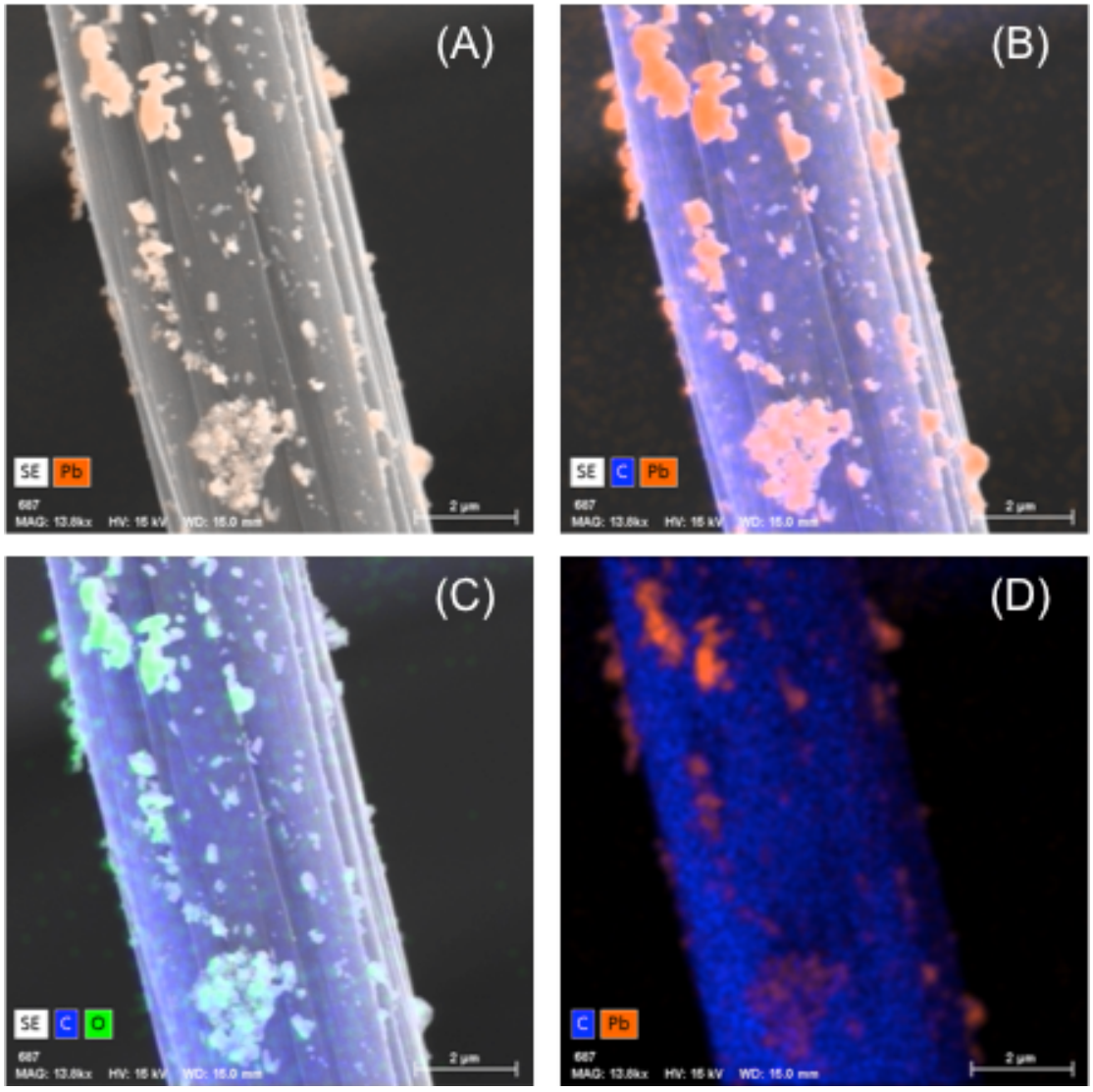

Figure 4.S1. EDX images of cycled felt from Method III. A. SEM and Pb mapping; B. SEM and C + Pb mapping; C. SEM and C + O mapping; D. Only C + Pb mapping. Pb is shown in orange, C in blue, and O in green.

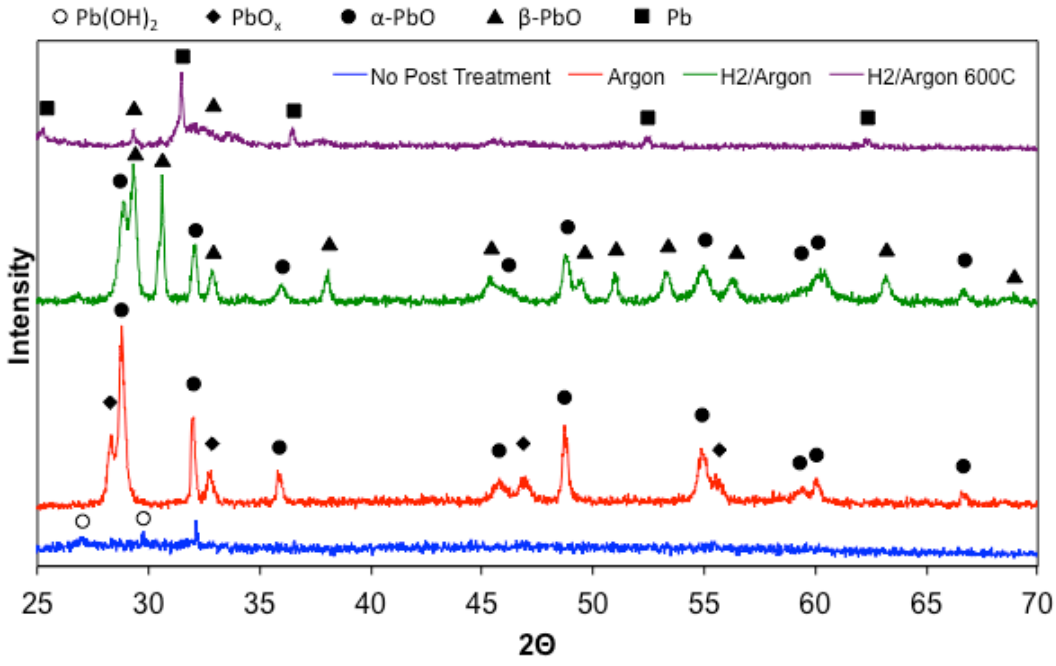

Figure 4.S2. XRD spectra showing felts from the three methods, in addition to a felt heat-treated under H_2/Argon at 600C for 2 hours. The spectra from this felt showed that most of the PbO species had reduced to metallic Pb.

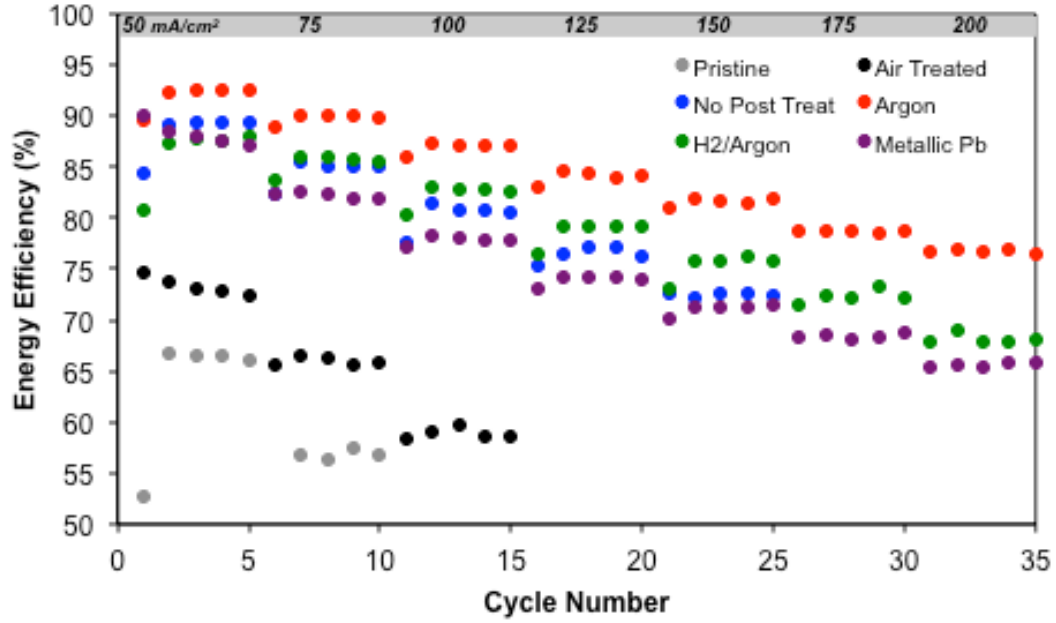

Figure 4.S3. Energy efficiency from ramping study of felts, including a felt with mainly metallic Pb particles formed after post-treatment at 600C under H_2/Argon. The case with metallic Pb is able to extend to a high current density, but at a lower energy efficiency when compared to the PbO counterparts.

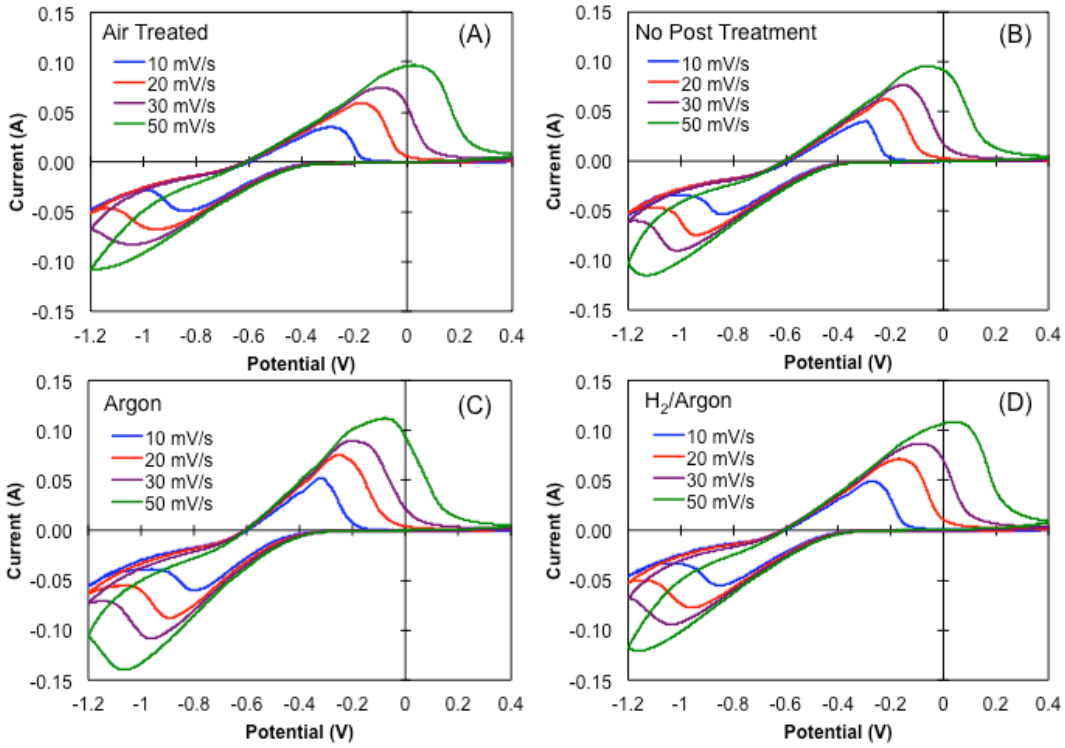

Figure 4.S4. CV data compared for potential scan rates of 10, 20, 30 and 50 mV/s in anolyte using A. Air-Treated felt, B. Method I felt, C. Method II felt, D. Method III felt.

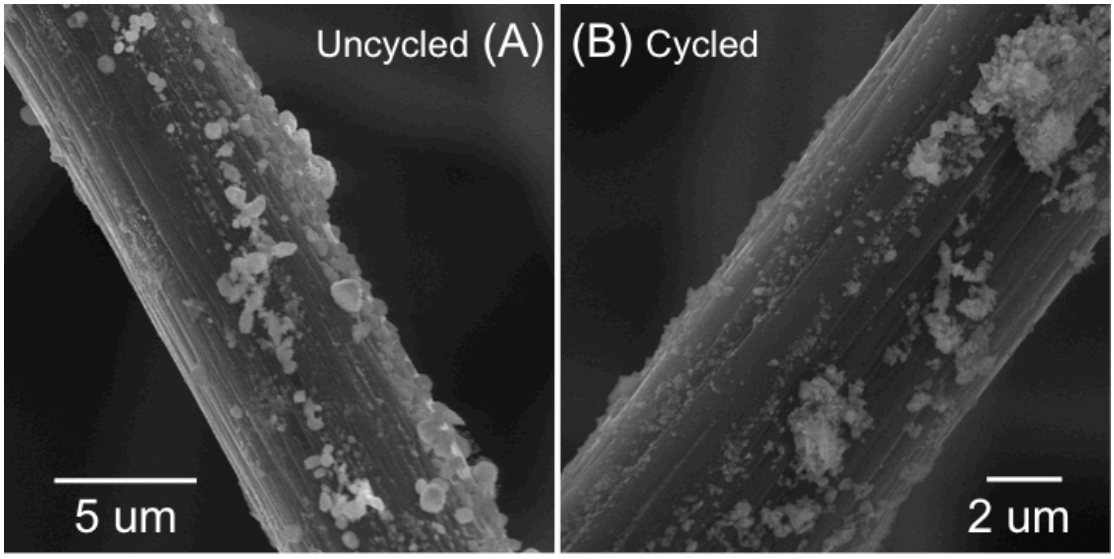

Figure 4.S5. SEM images of felts made using Method II, both A. uncycled and B. cycled.

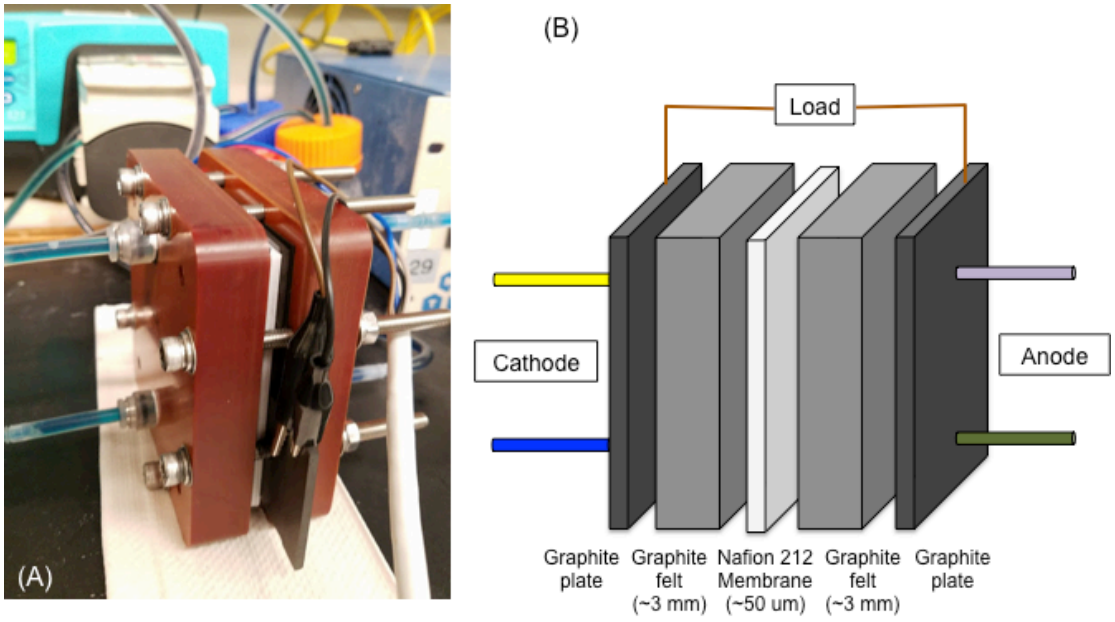

Figure 4.S6. A. Photo of VRB single-cell setup. B. Schematic of VRB single-cell setup.

4.6 Acknowledgments

This work made use of the Cornell Center for Materials Research Shared Facilities which are supported through the NSF MRSEC program (DMR-1719875).

4.7 References

(1) Dunn, B.; Kamath, H.; Tarascon, J. for the Grid : A Battery of Choices. *Science*. **2011**, *334*, 928–935.

(2) Liu, J.; Zhang, J.; Yang, Z.; Lemmon, J. P.; Imhoff, C.; Graff, G. L.; Li, L.; Hu, J.; Wang, C.; Xiao, J.; et al. Materials Science and Materials Chemistry for Large Scale Electrochemical Energy Storage : From Transportation to Electrical Grid. *Adv*. *Funct*. *Mater*. **2013**, *23*, 929–946.

(3) Center for Sustainable Systems, University of Michigan. 2017. "U.S. Grid Energy Storage Factsheet." Pub. No. CSS15-17.

(4) U.S. Department of Energy *Grid Energy Storage*. 2013.

(5) Huskinson, B.; Marshak, M. P.; Suh, C.; Er, S.; Gerhardt, M. R.; Galvin, C. J.; Chen, X.; Aspuru-Guzik, A.; Gordon, R.; Aziz, M. A metal-free organic–inorganic aqueous flow battery. *Nature* **2014**, *505*, 195–198.

(6) Janoschka, T.; Martin, N.; Martin, U.; Friebe, C.; Morgenstern, S.; Hiller, H.; Hager, M. D.; Schubert, U. S. An aqueous, polymer-based redox-flow battery using non-corrosive, safe, and low-cost materials. *Nature* **2015**, *527*, 78–81.

(7) Alotto, P.; Guarnieri, M.; Moro, F. Redox flow batteries for the storage of renewable energy : A review. *Renew*. *Sustain*. *Energy Rev*. **2014**, *29*, 325–335.

(8) Ulaganathan, M.; Aravindan, V.; Yan, Q.; Madhavi, S.; Skyllas-Kazacos, M.; Lim, T. M. Recent Advancements in All-Vanadium Redox Flow Batteries. *Adv. Mater. Inter.* **2016**, *3*, 1–22.

(9) Parasuraman, A.; Mariana, T.; Menictas, C.; Skyllas-Kazacos, M. Review of material research and development for vanadium redox flow battery applications. *Electrochim. Acta* **2013**, *101*, 27–40.

(10) Park, M.; Jung, Y.; Kim, J.; Cho, J. Synergistic Effect of Carbon Nanofiber/Nanotube Composite Catalyst on Carbon Felt Electrode for High-Performance All-Vanadium Redox Flow Battery. *Nano Lett.* **2013**.

(11) Li, W.; Liu, J.; Yan, C. Modified multiwalled carbon nanotubes as an electrode reaction catalyst for an all vanadium redox flow battery. *J. Solid State Electrochem.* **2013**, *17*, 1369–1376.

(12) Han, P.; Yue, Y.; Liu, Z.; Xu, W.; Zhang, L.; Xu, H. Graphene oxide nanosheets/multi-walled carbon nanotubes hybrid as an excellent electrocatalytic material towards VO^{2+}/VO_2^+ redox couples for vanadium redox flow batteries. *Energy Environ. Sci.* **2011**, 4710–4717.

(13) Chu, Y. Q.; Li, D. D.; Li, W. W.; Ma, C. A. Electrocatalytic Activity of Multi-walled Carbon Nanotubes for VO 2 + / VO 2 + of a Vanadium Redox Flow Battery. *IEEE Conf.* **2013**, 5–8.

(14) Melke, J.; Jakes, P.; Langner, J.; Riekehr, L.; Kunz, U.; Nefedov, A.; Sezen, H.; Wo, C.; Roth, C. Carbon materials for the positive electrode in all-vanadium redox flow batteries. *Carbon*. **2014**, *8*.

(15) Chakrabarti, M. H.; Brandon, N. P.; Hajimolana, S. A.; Tariq, F.; Yu, V.; Hashim, M. A.; Hussain, M. A.; Low, C. T. J.; Aravind, P. V. Application of carbon materials in redox flow batteries. *J. Power Sources* **2014**, *253*, 150–166.

(16) Park, S. M.; Kim, J. H.; Skyllas-Kazacos, M. A technology review of electrodes and reaction mechanisms in vanadium redox flow batteries. *J. Mater. Chem. A* **2015**, *3*, 16913–16933.

(17) Zhu, H. Q.; Zhang, Y. M.; Yue, L.; Li, W. S.; Li, G. L.; Shu, D.; Chen, H. Y. Graphite – carbon nanotube composite electrodes for all vanadium redox flow battery. *J. Power Sources* **2008**, *184*, 637–640.

(18) Wei, G.; Jia, C.; Liu, J.; Yan, C. Carbon felt supported carbon nanotubes catalysts composite electrode for vanadium redox flow battery application. *J. Power Sources* **2012**, *220*, 185–192.

(19) Deng, Q.; Huang, P.; Zhou, W.; Ma, Q.; Zhou, N.; Xie, H.; Ling, W.; Zhou, C.; Yin, Y.; Wu, X.; et al. A High-Performance Composite Electrode for Vanadium Redox Flow Batteries. *Adv. Energy Mater.* **2017**, *1700461*, 1–7.

(20) Shah, A. B.; Zhou, X.; Brezovec, P.; Markiewicz, D.; Joo, Y. L. Conductive Membrane Coatings for High-Rate Vanadium Redox Flow Batteries. *ACS Omega* **2018**, *3*, 1856–1863.

(21) Yu, L.; Lin, F.; Xi, J. A recast Nafion / graphene oxide composite membrane for advanced vanadium redox flow batteries. *RSC Adv.* **2016**, *6*, 3756–3763.

(22) Ju, K.; Hwan, Y. Preparation of the graphene oxide (GO)/Nafion composite membrane for the vanadium redox flow battery (VRB) system. *Vacuum* **2014**, *107*, 269–276.

(23) Niu, R.; Kong, L.; Zheng, L.; Wang, H.; Shi, H. Novel graphitic carbon nitride nanosheets / sulfonated poly (ether ether ketone) acid-base hybrid membrane for vanadium redox flow battery. *J. Memb. Sci.* **2017**, *525* (October 2016), 220–228.

(24) Jia, C.; Cheng, Y.; Ling, X.; Wei, G.; Liu, J.; Yan, C. Sulfonated Poly (Ether Ether Ketone)/ Functionalized Carbon Nanotube Composite Membrane for

Vanadium Redox Flow Battery Applications. *Electrochim. Acta* **2015**, *153*, 44–48.

(25) Wang, S.; Zhao, X.; Cochell, T.; Manthiram, A. Nitrogen-doped carbon nanotube/graphite felts as advanced electrode materials for vanadium redox flow batteries. *J. Phys. Chem. Lett.* **2012**, *3*, 2164–2167.

(26) Kim, J.; Lim, H.; Jyoung, J.; Lee, E.; Yi, J. S.; Lee, D. High electrocatalytic performance of N and O atomic co-functionalized carbon electrodes for vanadium redox flow battery. *Carbon*. **2017**, *111*, 592–601.

(27) Shao, Y.; Wang, X.; Engelhard, M.; Wang, C.; Dai, S.; Liu, J.; Yang, Z.; Lin, Y. Nitrogen-doped mesoporous carbon for energy storage in vanadium redox flow batteries. *J. Power Sources* **2010**, *195* (13), 4375–4379.

(28) Shi, L.; Liu, S.; He, Z.; Shen, J. Nitrogen-doped graphene : effects of nitrogen species on the properties of the vanadium redox flow battery. *Electrochim. Acta* **2014**, *138*, 93–100.

(29) Park, M.; Ryu, J.; Kim, Y.; Cho, J. Corn protein-derived nitrogen-doped carbon materials with oxygen-rich functional groups : a highly efficient electrocatalyst for all-vanadium redox flow batteries. *Energy Environ. Sci.* **2014**, *7*, 3727–3735.

(30) Zhang, W.; Xi, J.; Li, Z.; Zhou, H.; Liu, L. Electrochemical activation of graphite felt electrode for VO^{2+}/ VO_2^+ redox couple application. *Electrochim. Acta* **2013**, *89*, 429–435.

(31) Kim, K. J.; Lee, S.; Yim, T.; Kim, J.; Choi, J. W.; Kim, J. H.; Park, M.; Kim, Y. A new strategy for integrating abundant oxygen functional groups into carbon felt electrode for vanadium redox flow batteries. *Sci. Rep.* **2014**, *2*, 1–6.

(32) Kim, K. J.; Kim, Y.; Kim, J.; Park, M. The effects of surface modification on carbon felt electrodes for use in vanadium redox flow batteries. *Mater. Chem. Phys.* **2011**, *131* (1-2), 547–553.

(33) Yue, L.; Li, W.; Sun, F. Highly hydroxylated carbon fibres as electrode materials of all-vanadium redox flow battery. *Carbon*. **2010**, *48* (11), 3079–3090.

(34) Bourke, A.; Miller, M. A.; Lynch, R. P.; Gao, X.; Landon, J.; Wainright, J. S.; Savinelli, R. F.; Buckley, D. N. Electrode kinetics of vanadium flow batteries : contrasting responses of V(II) -V(III) and V(IV) -V(V) to electrochemical pretreatment of carbon. *J. Electrochem. Soc.* **2016**, *163* (1), A5097–A5105.

(35) Goulet, M.-A.; Skyllas-Kazacos, M.; Kjeang, E. The importance of wetting in carbon paper electrodes for vanadium redox reactions. *Carbon*. **2016**, *101*, 390–398.

(36) Kim, K. J.; Lee, H. S.; Kim, J.; Park, M.; Kim, J. H.; Kim, Y.; Skyllas-Kazacos, M. Superior Electrocatalytic Activity of a Robust Carbon-Felt Electrode with Oxygen-Rich Phosphate Groups for All-Vanadium Redox Flow Batteries. *ChemSusChem* **2016**, *9* (11), 1329–1338.

(37) Hwang, J.; Kim, B.; Moon, J.; Mehmood, A.; Ha, H. Y. A highly efficient and stable organic additive for the positive electrolyte in vanadium redox flow

batteries: taurine biomolecules containing -NH_2 and – SO_3H functional groups. *J. Mater. Chem. A* **2018**, *6*, 4695–4705.

(38) He, Z.; Jiang, Y.; Li, Y.; Wang, L. Boosting the electrocatalytic performance of carbon nanotubes toward V(V) / V(IV) reaction by sulfonation treatment. *Int. J. Energy Res.* **2018**, 1–10.

(39) He, Z.; Jiang, Y.; Li, Y.; Zhu, J.; Zhou, H.; Meng, W. Carbon layer-exfoliated, wettability-enhanced, SO_3H-functionalized carbon paper : A superior positive electrode for vanadium redox flow battery. *Carbon*. **2018**, *127*, 297–304.

(40) Li, C.; Xie, B.; Chen, J.; He, J.; He, Z. Enhancement of nitrogen and sulfur co-doping on the electrocatalytic properties of carbon nanotubes. *RSC Adv*. **2017**, *7*, 13184–13190.

(41) Sun, B.; Skyllas-Kazacos, M. Modification of graphite electrode materials for vanadium redox flow battery application - I. Thermal treatment. *Electrochim. Acta* **1992**, *37* (7), 1253–1260.

(42) Li, W.; Liu, J.; Yan, C. Reduced graphene oxide with tunable C / O ratio and its activity towards vanadium redox pairs for an all vanadium redox flow battery. *Carbon*. **2013**, *55*, 313–320.

(43) Huang, R.; Sun, C.; Tseng, T.; Chao, W.; Hsueh, K. Investigation of Active Electrodes Modified with Platinum / Multiwalled Carbon Nanotube for Vanadium Redox Flow Battery. *J. Electrochem. Soc*. **2012**, *159* (10), 1579–1586.

(44) Tseng, T.; Huang, R.; Huang, C.; Hsueh, K. A Kinetic Study of the Platinum/Carbon Anode Catalyst for Vanadium Redox Flow Battery. *J. Electrochem. Soc.* **2013**, *160* (4), 690–696.

(45) Li, B.; Gu, M.; Nie, Z.; Shao, Y.; Luo, Q.; Wei, X.; Li, X.; Xiao, J.; Wang, C.; Sprenkle, V.; et al. Bismuth Nanoparticle Decorating Graphite Felt as a High-Performance Electrode for an All-Vanadium Redox Flow Battery. *Nano Lett.* **2013**, *13*, 1330–1335.

(46) Wei, L.; Zhao, T. S.; Zeng, L.; Zhou, X. L.; Zeng, Y. K. Copper nanoparticle-deposited graphite felt electrodes for all vanadium redox flow batteries. *Appl. Energy* **2016**, *180*, 386–391.

(47) Wang, W. H.; Wang, X. D. Investigation of Ir-modified carbon felt as the positive electrode of an all-vanadium redox flow battery. *Electrochim. Acta* **2007**, *52*, 6755–6762.

(48) Mehboob, S.; Mehmood, A.; Lee, J.; Hwang, J.; Abbas, S.; Ha, H. Y.; Shin, H. Excellent electrocatalytic effects of tin through in situ electrodeposition on the performance of all-vanadium redox flow batteries. *J. Mater. Chem. A* **2017**, *5*, 17388–17400.

(49) Shen, J.; Liu, S.; He, Z.; Shi, L. Influence of antimony ions in negative electrolyte on the electrochemical performance of vanadium redox flow batteries. *Electrochim. Acta* **2015**, *151*, 297–305.

(50) Wei, L.; Zhao, T.; Zeng, L.; Zhou, X.; Zeng, Y. Titanium Carbide Nanoparticle-Decorated Electrode Enables Significant Enhancement in Performance of All-Vanadium Redox Flow Batteries. *Energy Technol*. **2016**, *4*, 990–996.

(51) Ejigu, A.; Edwards, M.; Walsh, D. A. Synergistic Catalyst – Support Interactions in a Graphene – Mn_3O_4 Electrocatalyst for Vanadium Redox Flow Batteries. *ACS Catal*. **2015**, *7130* (1).

(52) He, Z.; Dai, L.; Liu, S.; Wang, L.; Li, C. Mn_3O_4 anchored on carbon nanotubes as an electrode reaction catalyst of V(IV) / V(V) couple for vanadium redox flow batteries. *Electrochim. Acta* **2015**, *176*, 1434–1440.

(53) Li, B.; Gu, M.; Nie, Z.; Wei, X.; Wang, C.; Sprenkle, V.; Wang, W. Nanorod Niobium Oxide as Powerful Catalysts for an All Vanadium Redox Flow Battery. *Nanoletters* **2014**, *14*, 158–165.

(54) Bayeh, A. W.; Kabtamu, D. M.; Chang, Y.; Chen, G.; Chen, H.; Lin, G.; Liu, T.; Wondimu, T. H.; Wang, K.; Wang, C. Ta_2O_5 - Nanoparticle-Modified Graphite Felt As a High-Performance Electrode for a Vanadium Redox Flow Battery. *ACS Sustain. Chem. Eng*. **2018**, *6*, 3019–3028.

(55) Cao, L.; Skyllas-Kazacos, M.; Wang, D. Modification Based on MoO3 as Electrocatalysts for High Power Density Vanadium Redox Flow Batteries. *ChemElectroChem* **2017**, *4*, 1836–1839.

(56) Wang, S. C. Three-dimensional annealed WO_3 nanowire/graphene as an electrocatalytic material for all vanadium redox flow batteries. *Sustain. Energy Fuels* **2017**, *1*, 2091–2100.

(57) Zhou, H.; Shen, Y.; Xi, J.; Qiu, X.; Chen, L. ZrO_2 - Nanoparticle-Modified Graphite Felt : Bifunctional Effects on Vanadium Flow Batteries. *ACS Appl. Mater. Interfaces* **2016**, *8*, 15369–15378.

(58) Gobal, F.; Faraji, M. RuO_2/MWCNT/stainless steel mesh as a novel positive electrode in vanadium redox flow batteries. *RSC Adv.* **2015**, *5*, 68378–68384.

(59) Tseng, T.; Huang, R.; Huang, C.; Liu, C. Carbon Felt Coated with Titanium Dioxide / Carbon Black Composite as Negative Electrode for Vanadium Redox Flow. *J. Electrochem. Soc.* **2014**, *161* (6), 1132–1138.

(60) Zhou, H.; Xi, J.; Li, Z.; Zhang, Z.; Yu, L.; Liu, L.; Qiu, X.; Chen, L. CeO_2 decorated graphite felt as a high-performance electrode for vanadium redox flow batteries. *RSC Adv.* **2014**, *4*, 61912–61918.

(61) May, G. J.; Davidson, A.; Monahov, B. Lead batteries for utility energy storage : A review. *J. Energy Storage* **2018**, *15*, 145–157.

(62) Zhang, W.; Yang, J.; Wu, X.; Hu, Y.; Yu, W.; Wang, J.; Dong, J.; Li, M.; Liang, S.; Hu, J.; et al. A critical review on secondary lead recycling technology and its prospect. *Renew. Sustain. Energy Rev.* **2016**, *61*, 108–122.

(63) Sun, Z.; Cao, H.; Zhang, X.; Lin, X.; Zheng, W.; Cao, G.; Sun, Y. Spent lead-acid battery recycling in China – A review and sustainable analyses on mass flow of lead. *Waste Manag.* **2017**, *64* (1), 190–201.

(64) Poll, C. G.; Payne, D. J. Electrochemical Synthesis of PbO 2 , Pb 3 O 4 and PbO Films on a Transparent Conducting Substrate. *Electrochim. Acta* **2015**, *156* (3), 283–288.

(65) Wang, H.; Yu, J.; Zhao, Y.; Guo, Q. A facile route for PbO@C nanocomposites : An electrode candidate for lead-acid batteries with enhanced capacitance. *J. Power Sources* **2013**, *224*, 125–131.

(66) Wu, X.; Xu, H.; Lu, L.; Zhao, H.; Fu, J.; Shen, Y.; Xu, P. PbO2-modified graphite felt as the positive electrode for an all-vanadium redox flow battery. *J. Power Sources* **2014**, *250*, 274–278.

(67) Atkins, P. W.; Paula, J. D. *Physical chemistry*; W.H. Freeman: New York, 2010.

(68) Nejati, L.; Sousan, M.; Masoud, G.; Niasari, S. Hydrothermal synthesis and characterization of lead oxide nanocrystal in presence of tetradentate Schiff-base and degradation investigation of organic pollutant in waste water. *J. Mater. Sci. Mater. Electron.* **2017**, *28* (13), 9919–9926.

(69) Cao, M.; Hu, C.; Peng, G.; Qi, Y.; Wang, E. Selected-Control Synthesis of PbO_2 and Pb_3O_4 Single-Crystalline Nanorods. *J. Am. Chem. Soc.* **2003**, *125*, 4982–4983.

(70) Carr, J. (1972). *Studies of the electrochemistry of lead dioxide*. Ph.D. Loughborough University.

(71) Cheng, J.; Zou, X.; Meng, X.; Yang, G.; Lü, X.; Wei, C.; Sun, Z.; Feng, H.; Yang, Y. Lead Hydroxide Nanowires Obtained from Lead Nitrate Solution by Adding Chloride Ions. *Adv. Mater. Res.* **2010**, *123*, 719–722.

(72) Stillman, R.; Robins, R.; Skyllas-Kazacos, M. Quantitative X-ray Diffraction Analysis of alpha-PbO/beta-PbO in Lead-acid Battery Primary Oxide. *J. Power Sources* **1984**, *13*, 171–180.

(73) Ganduglia-Pirovano, M. V.; Hofmann, A.; Sauer, J. Oxygen vacancies in transition metal and rare earth oxides : Current state of understanding and remaining challenges. *Surf. Sci. Rep.* **2007**, *62*, 219–270.

(74) Volpe, M.; Oliveri, D.; Ferrara, G.; Salvaggio, M.; Piazza, S.; Italiano, S.; Sunseri, C. Metallic lead recovery from lead-acid battery paste by urea acetate dissolution and cementation on iron. *Hydrometallurgy* **2009**, *96* (1-2), 123–131.

(75) Ruetschi, P.; Sklarchuk, J.; Angstadt, R. T. Stability and Reactivity of Lead Oxides. *Electrochim. Acta* **1963**, *8*.

(76) Rondon, S.; Sherwood, P. M. A. Core Level and Valence Band Spectra of PbO by XPS. *Surf. Sci. Spectra* **2014**, *5*, 97–103.

(77) Kim, K. S.; Leary, T. J. O.; Winograd, N. X-Ray Photoelectron Spectra of Lead Oxides. *Anal. Chem.* **1973**, *45* (13).

(78) Li, X.; Liu, X.; Dong, C.; Deem, N. X-Ray Photoelectron Spectroscopy Study of Passive Layers Formed on Pb-Sn and Pb-Sb Alloys. *Metall. Mater. Trans. A* **2005**, *36A*, 2175–2190.

(79) Keezer, R. C.; Bowman, D. L.; Becker, J. H. Electrical and Optical Properties of Lead Oxide Single Crystals. *J. Appl. Phys.* **2013**, *39* (4), 2062–2066.

(80) Evarestov, R. A.; Veryazov, V. A. The Electronic Structure of Crystalline Lead Oxides. *Phys. Stat. Sol.* **1991**, *165*, 401–410.

(81) Bard, A. J.; Faulkner, L.R. *Electrochemical Methods: Fundamentals and Applications,* 2nd ed.; Wiley: New York, 2001; pp 226-255.

CHAPTER 5

MEMBRANE SYNTHESIS FOR METAL-FREE REDOX FLOW BATTERY SYSTEMS: PRELIMINARY STUDIES AND FUTURE PERSPECTIVES

5.1. Introduction

For the past few decades, the majority of research on redox flow batteries has focused systems that rely on solubilizing metal salts in either aqueous or organic solvents. This push has yielded a large variety of redox flow battery chemistries, nearly all focused on harnessing power from the reduction and oxidation of metals with multiple oxidation states. This was a practical starting point for the field, as the chemistries were reasonably simple and predictable, and the materials easy to acquire and test. However, there are questions about the long-term viability of this class of redox flow batteries. These potential pitfalls can be categorized into two major issues: sustainability and cost.

5.1.2 Sustainability Issues with Metal-Based Redox Flow Batteries

There are long-term sustainability issues associated with many types of metal-based battery systems. There is an inherent supply issue associated with mining large quantities of any type of element. Metal-based redox flow batteries often require many tons of elements such as V, S, Zn, Fe, Cr, Cu, Ni, Mn, and others. The acquisition of these amounts of pure metal salts is often not only costly, but environmentally damaging and practically challenging.[1-8] The geographic regions in which the

elements are naturally found may not be conducive to long-term mining operations. There are limited easily accessible metal resources to employ for these types of batteries. This information has caused researchers to look for more sustainable alternatives in recent years.

5.1.3 Cost Issues with Metal-Based Redox Flow Batteries

Nearly every type of redox flow battery has similar fixed costs: electrolyte materials, electrode materials, pumping costs, and others are somewhat unavoidable in this type of technology. One of the main costs, however, is the cost of the ion-exchange membrane that separates the anolyte and catholyte containers. The performance of this membrane is critical to the success of most redox flow batteries, as this membrane must play a unique role in separating specific types of metal ions, while allowing for rapid transport of charge-balancing ions, often protons from supporting acids. These membranes must be robust – withstanding contact with corrosive acids and salts for months or years, resisting deformation from electrolyte convection, and maintaining their basic structure without swelling or shrinking. The solution that has been employed thus far has been to use costly perfluorinated sulfonated ion-exchange membranes, such as those in the Nafion family of membranes. This choice was made due to the reliability of these membranes in acidic environments, and the high proton conductivity exhibited when these membranes are in their hydrated forms. A large body of work has been investigated in order to create less expensive versions of these membranes. Much of this work has focused on using inexpensive bulk polymers and utilizing a variety of processing techniques to make microporous or nanoporous

membranes with morphologies that are suitable for redox flow battery applications. Many of these methodologies have been successfully used to make membranes for other applications in the past, such as filtration membranes, porous battery separators, and dialysis membranes. These approaches have only found limited success when used with most metal-based redox flow battery systems. This is due to the inherent difficulty in separating ions of very similar sizes over long periods of time. For instance, the ionic radius of a vanadium ion is between 50 pm and 80 pm, depending on oxidation state, whereas the effective ionic radius of a hydrogen ion is about 10 pm. While the vanadium ion is a few times larger than the hydrogen ion, both are quite small. This leads to an inherent challenge in membrane design for metal-based redox flow batteries: design a very precise membrane at a high production cost, or design an acceptable membrane and realize that there will be capacity losses via electrolyte diffusion through the membrane. A more appealing reality would involve a greater difference in ionic size between the electroactive material and the supporting counter-ion.

5.2. Metal-free Battery Systems

The past few years has seen the rapid discovery and development of metal-free redox flow battery systems. These systems use the same original principles as metal-based flow battery systems, save for the fact that the electroactive material does not contain any metal. Most electroactive materials are completely synthetic, in that they are often small aqueous-soluble organic molecules that can be readily synthesized at large scales. The most promising systems of this new class of batteries are quinone-based

redox flow batteries. These batteries are a much newer technology compared to VRBs, as is shown in Figure 5.1, a plot of publications found on Web of Science with the phrase “quinone redox flow battery” in the title shown by year of publication.

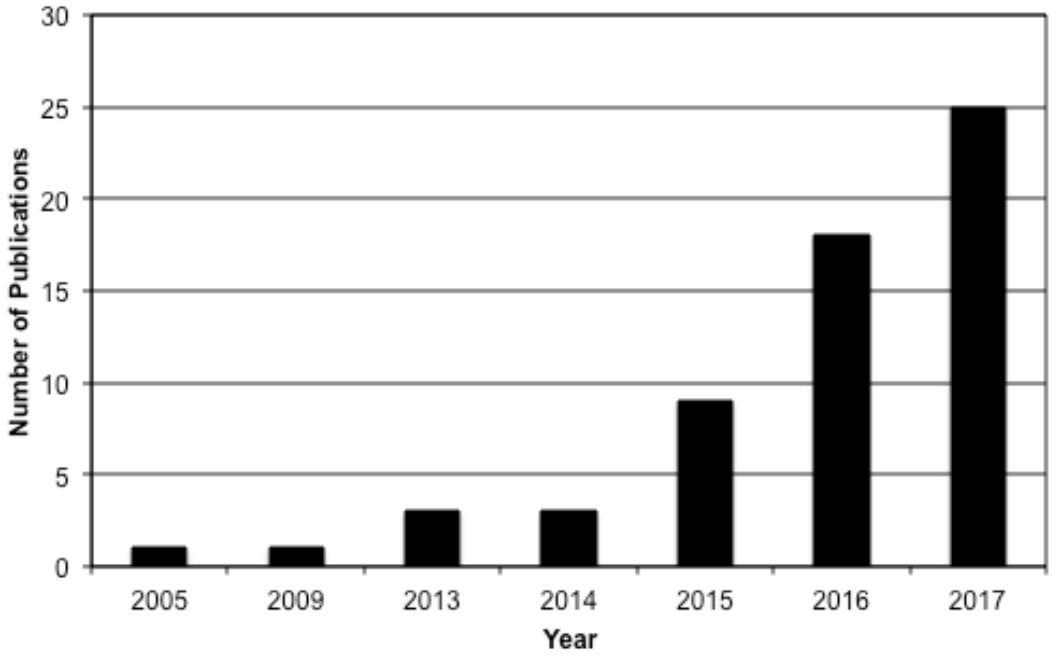

Figure 5.1. A plot generated by searching Web of Science for the number of articles containing the phrase “quinone redox flow battery” in their title, shown by year of publication.

These molecules were originally discovered as parts of the electron transport chain in photosynthetic processes, however they have been created synthetically at scale for other applications as well. These compounds consist of one or more aromatic rings, with at least one C=C bond converted to a C=O bond. This C=O can be reduced to a C-OH bond, and re-oxidized back to a C=O with some degree of reliability. Based on the conjugation site of the oxygen group on the ring, the standard reduction potential will change. Different versions of these compounds can be used simultaneously to create a battery. An example of two compounds that can be used together in a Metal-

free redox flow battery are anthraquinones and benzoquinones. Versions of these molecules are shown in Figure 5.2.

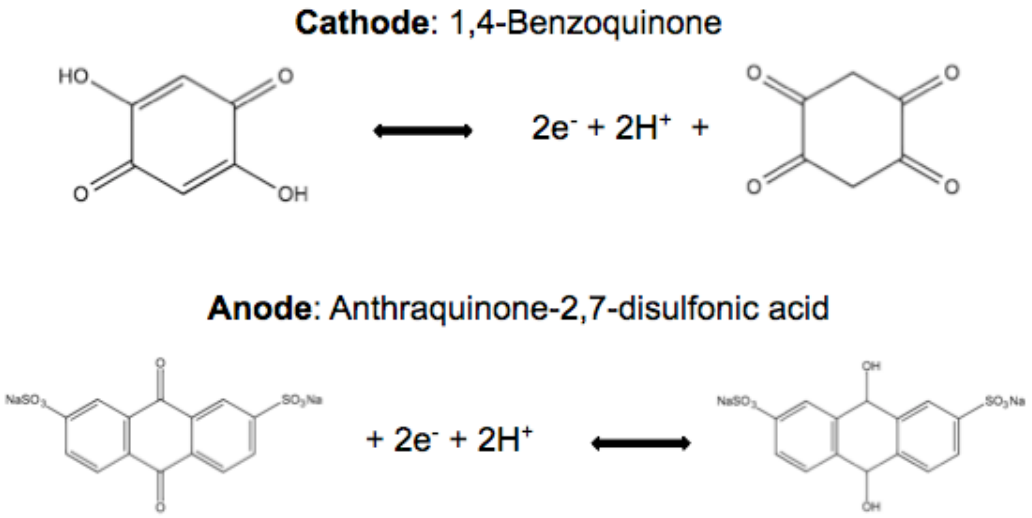

Figure 5.2. An example of a possible coupling of quinones for use in a metal-free redox flow battery.

The upsides of these types of batteries are their renewability, and potential for very high current densities. The organic nature of the electroactive material is conducive to use with hydrophobic graphite felts, and difficulties with the kinetics of reaction have not been observed. The challenges of this chemistry are similar to some metal-based systems. These batteries typically have even lower nominal cell voltages than many of the metal-based systems. This implies even lower power densities than with many metal-based systems. See Figure 5.3 for CV curves using the molecules shown in Figure 5.2, dissolved in 1M H_2SO_4 at concentrations of 0.2M.

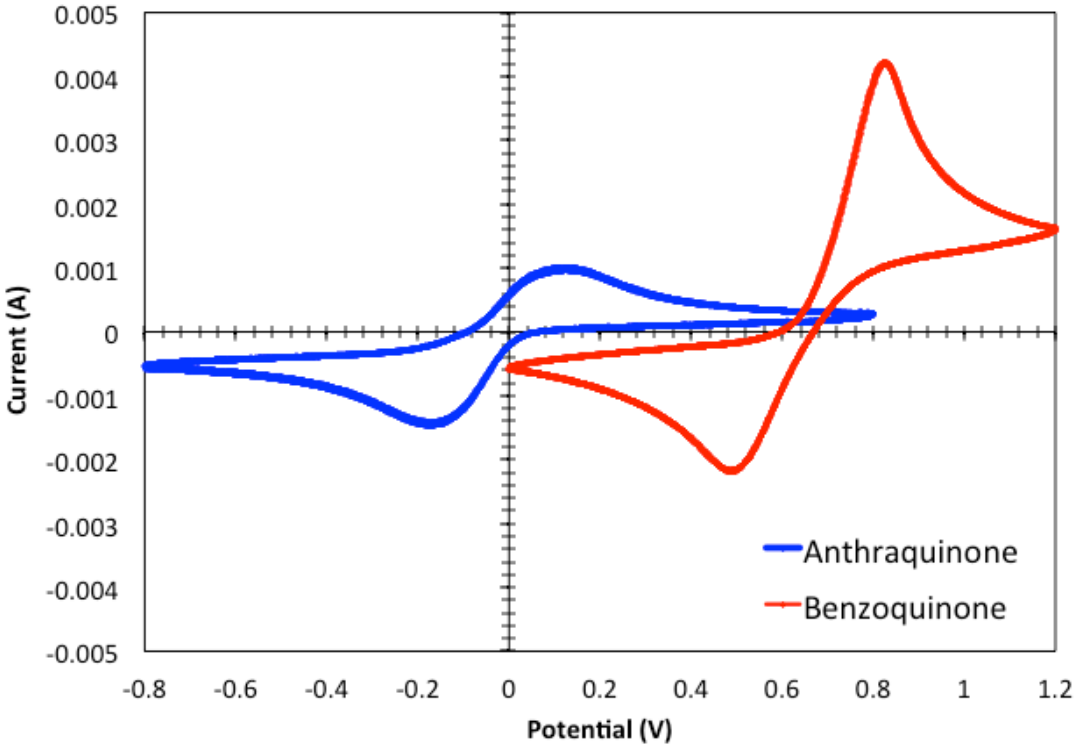

Figure 5.3. Cyclic Voltammetry of 0.2M concentrations of 1,4-Benzoquinone and Anthraquinone-2,7-disulfonic acid dissolved in 1M H_2SO_4. Scan rate of 10 mV/s.

Because the quinones must be chemically different to build up a potential, any crossover through the membrane results in permanent capacity losses, rather than temporary losses as seen in the VRB. There are also issues with energy density due to the relatively low solubility of organic molecules in aqueous solvents. The membrane used in these systems still tends to be a type of Nafion membrane. While these membranes still work well for this application, they add substantially to the total cost of the battery.

5.3. Membrane Synthesis for Metal-free Battery Systems

The advent of newer metal-free flow battery systems opens the door for new uses for existing membrane technology. The molecules involved in these systems are much larger than metal salts, and thus the need for very precise membranes is less important for the battery to cycle efficiently. Methods of microporous membrane synthesis have had limited success in many metal-based redox flow battery systems, but have the potential to be used in metal-free systems. One membrane synthetic method that could be a useful is using phase inversion of bulk polymers to create microporous and mesoporous coatings on existing porous membranes. In this method, an inexpensive porous substrate is coated with a thin layer of polymer solution. The coated assembly is then submerged in an antisolvent, the function of which is to rapidly precipitate the polymer coating out of solution, and onto the surface of the substrate. This method causes the rapid formation of a thin layer of polymer with a uniform pore structure. This pore structure can then be tuned with the addition of additives, such as surfactants, ceramic precursors, and other hydrophilic media. These additives can help aid in the hydrophilicity of the system, while affecting the nature of the pore formation in the membrane. A schematic of this process using polyvinylidene fluoride as a sample system is shown in Figure 5.4. The process outlines various methods of the coating process, including dip coating, spin coating, and spray coating. Each of these methods can make coatings at various levels of scalability.

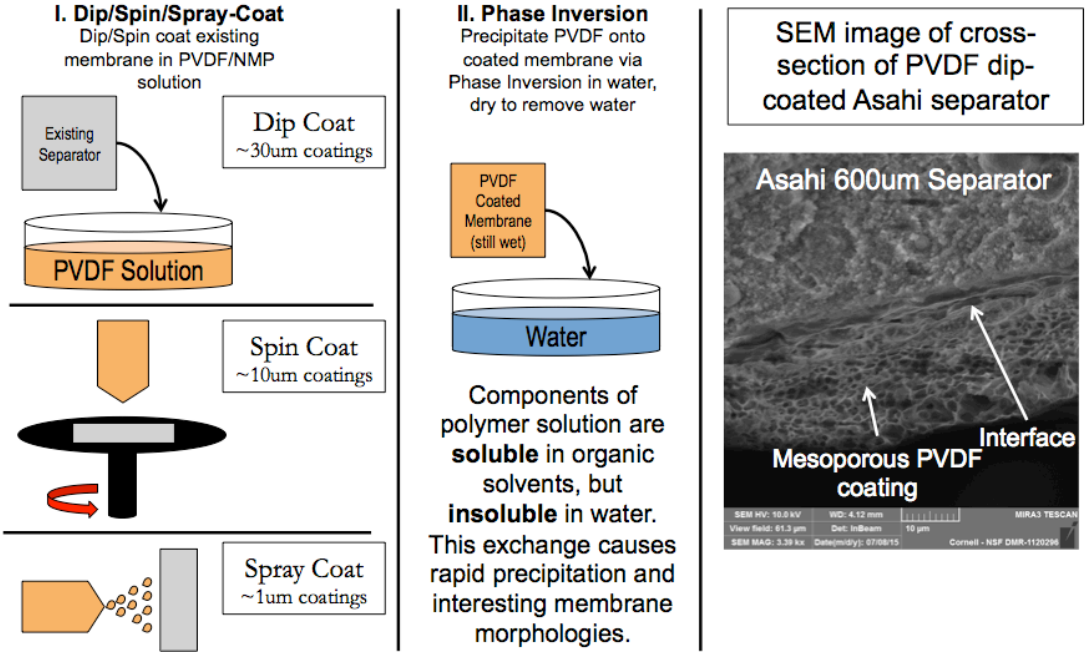

Figure 5.4. Schematic of polymer coating process (step I), followed by a phase inversion in an antisolvent (step II). Right panel shows an SEM image of a sample coating on a porous substrate separator.

This process could help reduce the costs of using a metal-free redox flow battery system, while having a limited negative impact on the overall performance of the battery. As research on metal-free redox flow batteries begins to progress, inexpensive microporous membranes could be a valuable asset for the widespread adoption of these systems.

5.4. References

(1) Huskinson, B.; Marshak, M. P.; Suh, C.; Er, S.; Gerhardt, M. R.; Galvin, C. J.; Chen, X.; Aspuru-Guzik, A.; Gordon, R.; Aziz, M. A metal-free organic–inorganic aqueous flow battery. *Nature* **2014**, *505*, 195–198.

(2) Hoober-Burkhardt, L.; Krishnamoorthy, S.; Yang, B.; Murali, A.; Nirmalchandar, A.; Prakash, G. K. S.; Narayanan, S. R. A New Michael-Reaction-Resistant Benzoquinone for Aqueous Organic Redox Flow Batteries. *J. Electrochem. Soc.* **2017**, *164* (4), 600–607.

(3) Esquivel, J. P.; Alday, P.; Ibrahim, O. A.; Fernández, B.; Kjeang, E. A Metal-Free and Biotically Degradable Battery for Portable Single-Use Applications. *Adv. Energy Mater.* **2017**, *7*.

(4) Shimizu, A.; Takenaka, K.; Handa, N.; Nokami, T.; Itoh, T. Liquid Quinones for Solvent-Free Redox Flow Batteries. *Adv. Mater.* **2017**, *1606592*, 1–5.

(5) Mukhopadhyay, A.; Hamel, J.; Katahira, R.; Zhu, H. Metal-Free Aqueous Flow Battery with Novel Ultrafiltered Lignin as Electrolyte. *ACS Sustain. Chem. Eng.* **2018**, *6*, 5394–5400.

(6) Yang, B.; Hoober-Burkhardt, L.; Wang, F.; Prakash, G. K. S.; Narayanan, S. R. An Inexpensive Aqueous Flow Battery for Large-Scale Electrical Energy Storage Based on Water-Soluble Organic Redox Couples. *J. Electrochem. Soc.* **2014**, *161* (9).

(7) Lin, K.; Chen, Q.; Gerhardt, M. R.; Tong, L.; Kim, S. B.; Eisenach, L.; Valle, A. W.; Hardee, D.; Gordon, R. G.; Aziz, M. J.; et al. Alkaline quinone flow battery. *Science*. **2015**, *349* (6255), 2013–2017.

(8) Sueleyman, E.; Suh, C.; Michael Marshak; Aspuru-guzik, A. Computational design of molecules for an all-quinone redox flow battery. *Chem. Sci.* **2015**, *6* (2), 885–893.

CHAPTER 6

SUMMARY AND FUTURE WORK

Aqueous redox flow batteries are compelling candidates for use in large-scale energy storage systems. Their long life cyclability and recyclability have the potential to complement renewable electricity generation for many years at a time. Vanadium redox flow batteries are arguably one of the most mature forms of this technology, and many of the technical issues are in the process of being addressed. It has been demonstrated that the power density of a VRB can be improved through reasonably simple and inexpensive membrane and electrode modifications, alterations that can lead to prodigious cost savings at full scale. Highly conductive carbon materials can serve as a useful template from which high surface area and excellent electrical conductivity can be coupled to improve vanadium redox reaction rates. Both metals and metal oxides can also address this issue, acting as solid electrocatalysts that can improve the kinetics of the anodic vanadium reaction. The wettability of the electrodes is also an important consideration, and the inclusion of heteroatoms and oxygen-rich functional groups clearly can have a major positive impact on the reaction rates of the vanadium redox reaction. More recent work has shown that aqueous organic redox flow battery systems have shown great promise, with a large variety of molecular options available for testing and discovery. There is an opportunity to reduce the barrier to entry for market acceptance by using coated microporous membranes in these batteries. It would also be worth investigating hybrids of these systems, and

perhaps membrane-less systems, in which the electrolytes separate based solely on solubility. In all of these systems, the primary goal is to reduce internal resistances in the battery setup, thus minimizing both solvent and membrane resistances is likely the next step in the progression of these batteries. There are inherent difficulties in this regard, however success in these research directions could make truly major strides in making aqueous electrochemical flow systems more energy dense.